PROCESSING AND PROPERTIES OF ADVANCED CERAMICS AND GLASSES

workshop

Book of extended abstracts

November 20-22, 2019
Ráztočno, Slovak Republic

ISBN 978-80-971648-8-1

ORGANIZING INSTITUTION

Slovak Silicate Scientific-Technological Society

Institute of Inorganic Chemistry SAS

Slovak Academy of Sciences

SCIENTIFIC BOARD

prof. RNDr. Ján Dusza, DrSc.	*IMR SAS Košice*
prof. Ing. Dušan Galusek, DrSc.	*VILA Trenčín*
prof. RNDr. Pavol Šajgalík, DrSc.	*IIC SAS Bratislava*

ORGANIZING COMMITTEE

Ing. Ondrej Hanzel, PhD.	*IIC SAS Bratislava*
doc. Ing. Miroslav Hnatko, PhD.	*IIC SAS Bratislava*
Anna Jurová	*SSiVTS*

Ráztočno, November 20-22, 2019, Slovak Republic

PREFACE

Engineering ceramics are the class of materials which steadily occupy a larger portion of the industrial applications. The reason for this positive development is that engineering ceramics found applications which are not only mechanistic. Presently developed engineering ceramic materials move from the pure engineering applications requiring “only” the mechanical performance of the material to the more sophisticated applications.

The orientation of research to surface modification of different materials and bio-materials was supported not only by interest from academia but also by demands from industry but also from the society and showed that ceramic materials have the potential to be useful for the improving of the life of society. The ultra-high temperature ceramics, ceramics for lighting, ceramic implants, 3D printed materials etc. are examples of ceramic devices which make the new technologies possible. The achievements of the science of ceramics are remarkable and, as described above, they are targeted towards new technologies which affect everyday life in a positive sense.

The present workshop on Processing and Properties of Advanced Ceramics is a consequence of this development. More than 20 contributions collected in the present book of abstracts cover whole variety of research performed in Slovakia, Czech Republic, Germany, Italy, Serbia and Austria with a great potential for the application. The Slovak teams dealing with the ceramics unified under the umbrella of the Slovak Silicate Society, together with the research groups from the other countries are regularly get together just to interact and exchange the experiences with the newest development in this exciting research area. Three days of discussions usually results in the co-ordination of the ceramic research in Slovakia, co-operation with the other European countries as well as the planning of the new perspective project on the national/European level.

prof. RNDr. Pavol Šajgalík, DrSc.

CONTENTS

3D PRINTING

TEPELNÉ SPRACOVANIE KOMPOZITU PRE 3D TLAČ KERAMIKY

THERMAL PROCESSING OF COMPOSITE MATERIAL FOR 3D PRINTING OF CERAMICS

P. Veteška[1], Z. Hajdúchová[1], Ľ. Bača[1], J. Feranc[2], J. Milde[3], M. Kritikos[3], M. Janek[1]

[1] *Oddelenie anorganických materiálov FCHPT STU*
[2] *Oddelenie plastov, kaučuku a vlákien FCHPT STU*
[3] *Katedra obrábania a počítačovej podpory technológií MTF STU*

ABSTRACT

Ceramic-polymer composite filament was used for the production of model ceramic object by means of additive manufacturing using Fused Filament Fabrication (FFF) technique. The composite specimens were subjected to single-stage thermal debinding and sintering with final temperatures in range from 1200°C to 1400°C. Objects with well-defined details without major shape deformations were obtained after sintering. The overall shape and shrinkage of model objects was evaluated by means of computer tomography scanning technique. Volumetric shrinkage for temperature 1400°C was determined to be 49 vol. %.

Keywords: additive manufacturing, ceramics, sintering, debinding

INTRODUCTION

Additive manufacturing (AM) has gained a lot of attention since the expiration of Stratasys patents for Fused Deposition Modelling (FDM) technology in 2009. Since then, the popularity and application range for this technology has greatly expanded, specifically of FDM, alternatively called Fused Filament Fabrication technique (FFF). Although some authors have already published papers dealing with AM of ceramics using FFF technique, the filaments produced usually has several limitations: brittleness, special nozzle materials, requirement for minimal nozzle diameter to be larger than average nozzle diameter used for polymer AM, etc. Thus, the FFF of ceramics still cannot be considered as end-user-friendly and generally established technology. At the same time, the most prominent use of FFF for ceramic or ceramic composite [1] production is the combination of PLA and hydroxyapatite for bioresorbable and bioactive ceramic composite [2, 3] preparations. Other verification studies in the AM literature include manufacturing of ceramic components, either by sacrificial template route - covering the FFF template with a alumina or porcelain slurry and subsequent removal of polymer [4] or by direct FFF of polymer/ceramic composite and subsequent debinding of the polymer [5-7]. The aim of this work is to prepare cylindrical test objects from ceramic/polymer composite filament by additive manufacturing and to verify debinding and sintering behaviour of these test objects.

EXPERIMENTAL

The extrusion of composite ceramic/polymer material into 1.75 mm filament was performed from pre-mixed materials using single screw extruder (Brabender, Germany). The ceramic powder loading of composite was at the level of 65 wt. %. For production of cylindrical samples with diameter of 30 mm, commercial AM device Leapfrog Creatr (Leapfrog, Netherlands) with modified extruder nozzle of 0.4 mm diameter was used. The printing parameters used for AM of green bodies are listed in Table 1.

Table 1: Printing parameters for ceramic/polymer composite filament

Parameter	**Value**
Printing speed	5 mm.s^{-1}
Filament extrusion multiplier	1.00
Filament temperature at 1st layer	215°C
Filament temperature after 1st layer	215°C
Bed temperature	55°C
Vertical shell perimeter count	2
Infill density	35%

To determine temperature range necessary for direct polymer removal during heating, thus debinding the composite system, DTA/TG analysis was performed using TG/DTA Exstar 6300 (Seiko Instruments USA Inc., USA). The ceramic powder was pressed into small pellets with diameter of approx. 3 mm and subjected to thermal analysis using heating microscope 1A (Leitz Wetzlar, Germany) coupled with camera EOS 700D (Canon Inc., Japan) to obtain data regarding sintering behaviour of the system for sintering temperature optimization. The heating rate of 10 K.min^{-1} was used in temperature interval 25-1500°C. Computer tomography (CT) scans were collected on a Metrotom® (Carl Zeiss, Germany) instrument with the scanning parameters: 150 kV, 450 μA, integration time 1000 ms, and voxel size of 74 μm. Obtained CT images were analysed using GOM Inspect 2018 software (GOM GmbH, Germany).

Thermal processing of prepared composite samples was done using commercial laboratory furnace type 1013 (Clasic s.r.o., Czech Republic). Temperature program chosen for debinding and sintering was optimized using TGA/DTA data shown below. The average heating rate during debinding was 10°C.hour^{-1}, the heating rate in interval between 850°C (debinding temperature) and final sintering temperature was 10°C.min^{-1}.

RESULTS

TGA analysis

Following the thermal analysis of ceramic powder on heating microscope, the prepared ceramic/polymer composite material was subjected to TGA analysis to obtain data for tuning of the debinding process (Figure 1).

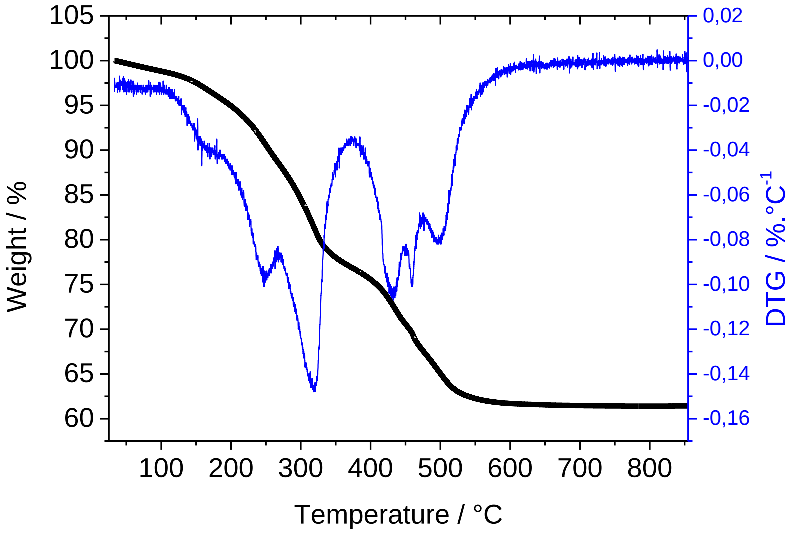

Figure 1: TGA analysis of prepared composite

The analysis shows rapid mass loss in three main temperature intervals: 125-170°C, 200-350°C and 400-550°C. The TGA curve indicates the decomposition of polymer matrix is complete after reaching temperature of approx. 600°C and no further mass loss is observed after this point. These results point to multi-stage decomposition of used polymer matrix which is the main limiting factor in the debinding processing step. At the same time, the debinding process can be accelerated if operating outside the main three decomposition zones, thus decreasing energy cost of the process. As a result, the proposed debinding process used in further experiments involves low heating rates in area below 600°C (6.0 °C.min^{-1}).

Heating microscope analysis

Following the thermal analysis of ceramic/polymer composite, the results of ceramic powder sintering behaviour analysis can be seen below in Figure 2. The sample shrinkage rapidly increases at temperatures above 1100°C, while exhibiting first signs of softening at temperature of 1500°C, accompanied by partial fusion to alumina substrate used for analysis at this temperature.

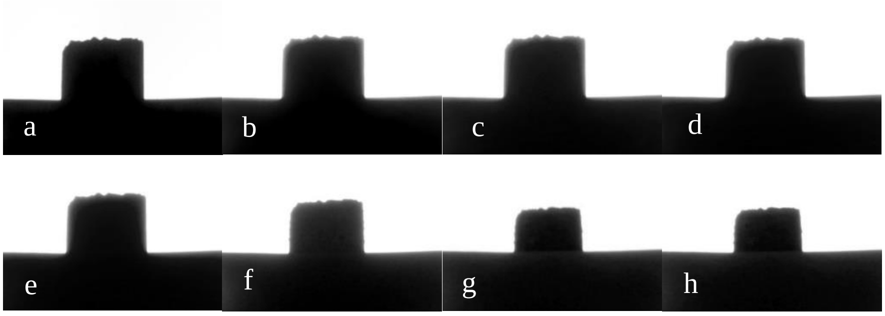

Figure 2: Sample during experiment at different temperatures: a) 25°C, b) 850°C, c) 1000°C, d)1100°C, e) 1200°C, f) 1300°C, g) 1400°C, h) 1500°C

Values of sample shrinkage at selected temperatures are shown in Table 2.

Table 2: Overall shrinkage during thermal analysis of ceramic powder

Temperature / °C	Shrinkage / %
25	0.0
850	0.1
1000	1.6
1100	1.0
1200	7.7
1300	21.7
1400	41.5
1500	35.3

It can be seen that at temperature of 850°C which lies above the temperature required for complete elimination of polymer matrix, the ceramic body does not change its external dimensions. First signs of ongoing sintering can be clearly seen at temperature 1200°C, where we observe shrinkage of approx. 7.5-8%. Based on these experiments, the temperature region of interest for sintering of composite produced from this type of ceramics is expected to be in range from 1200 to 1400°C. Temperatures above 1400°C were not further included into the experimental plan to avoid problems with fusion of sample to the furnace experimental alumina base plate used for thermal processing, as well as to avoid deformations caused by the proximity of sintering temperature to the melting point of the ceramic system.

Processing of composite material

Green bodies of cylindrical shape manufactured from ceramic/polymer composite material were successfully prepared using commercial FFF device. The as-prepared green body as well as model objects sintered at temperatures of 850, 1200, 1300 and 1400°C can be seen in Figure 3.

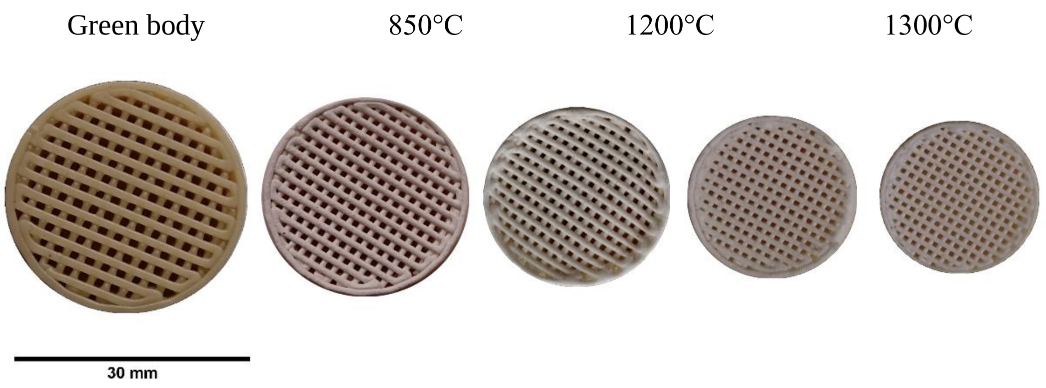

Figure 3: Macro photographs of as-prepared green body and samples after thermal processing

The samples do not exhibit any visible signs of deformation in any direction and maintained their internal infill structure created during AM process. No fractures, delamination or other defects have been observed.

CT measurements

To obtain information on internal defects and/or testing printout inhomogeneities, both green body as well as sintered species up to 1400°C were analysed using computer tomography (CT). Achieved visualisation of selected sample sintered to 1400°C is shown in the Figure 4.

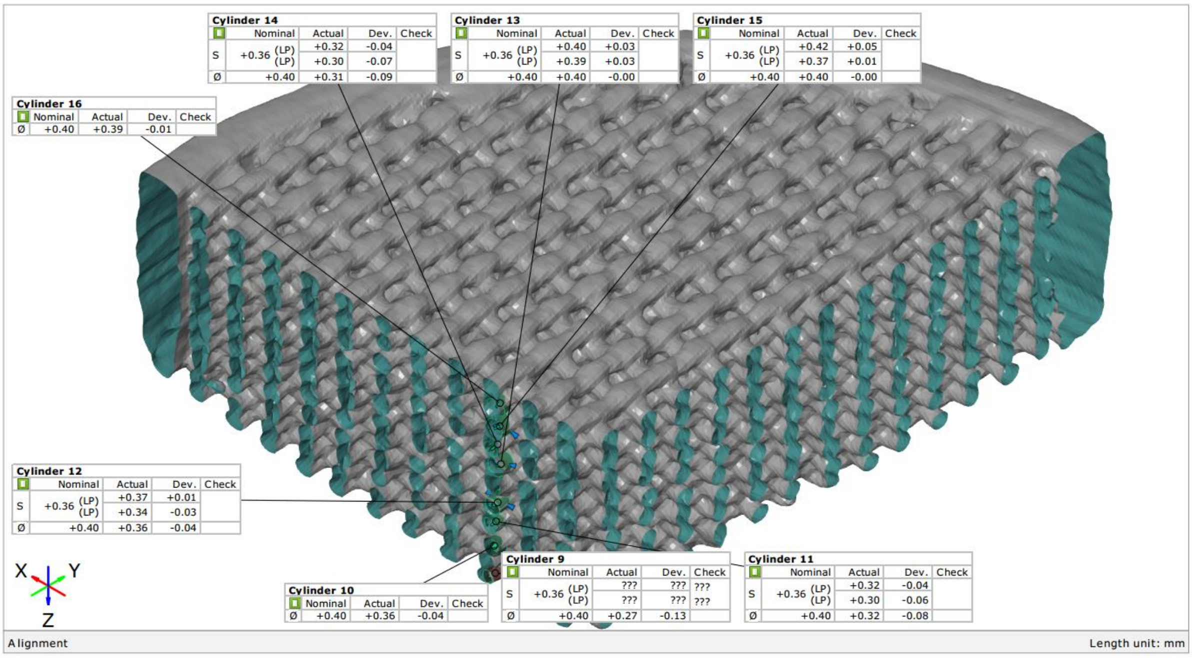

Cylinder 14

🟩	Nominal	Actual	Dev.	Check
S	+0.36 (LP)	+0.32	-0.04	
	(LP)	+0.30	-0.07	
Ø	+0.40	+0.31	-0.09	

Cylinder 13

🟩	Nominal	Actual	Dev.	Check
S	+0.36 (LP)	+0.40	+0.03	
	(LP)	+0.39	+0.03	
Ø	+0.40	+0.40	-0.00	

Cylinder 15

🟩	Nominal	Actual	Dev.	Check
S	+0.36 (LP)	+0.42	+0.05	
	(LP)	+0.37	+0.01	
Ø	+0.40	+0.40	-0.00	

Cylinder 16

🟩	Nominal	Actual	Dev.	Check
Ø	+0.40	+0.39	-0.01	

Cylinder 12

🟩	Nominal	Actual	Dev.	Check
S	+0.36 (LP)	+0.37	+0.01	
	(LP)	+0.34	-0.03	
Ø	+0.40	+0.36	-0.04	

Cylinder 10

🟩	Nominal	Actual	Dev.	Check
Ø	+0.40	+0.36	-0.04	

Cylinder 9

🟩	Nominal	Actual	Dev.	Check
S	+0.36 (LP)	???	???	???
	(LP)	???	???	???
Ø	+0.40	+0.27	-0.13	

Cylinder 11

🟩	Nominal	Actual	Dev.	Check
S	+0.36 (LP)	+0.32	-0.04	
	(LP)	+0.30	-0.06	
Ø	+0.40	+0.32	-0.08	

Figure 4: Computer tomography scan of sample sintered at 1400°C

The CT scan of sintered sample shows well-defined internal structure of interconnected infill filament paths without visible deformation. The internal pathways within the infill structure are well-defined and no delamination or vacant spaces within the structure have been detected. CT analysis has also been used for precise determination of volumetric shrinkage. The CT images showed a decrease in total object volume (volume of filament paths within the sample) from 2622.43 mm^{-3} to approx. 1330 mm^{-3}. This corresponds to volumetric shrinkage of 49 vol. %, which is well within the volumetric loading level of prepared green body material (50 vol. %).

CONCLUSIONS

Green bodies of ceramic/polymer materials were successfully prepared using commercial additive manufacturing device from the composite filament developed and produced in our laboratory. Prepared specimens were subjected to single-step thermal debinding and sintering and analysed using computer tomography. Thermal analysis of the ceramic powder shows the suitable thermal processing interval for sintering of this type of ceramic material is between 1200°C and 1400°C. The sintered bodies did not contain any delaminated or cracked layers. The computer tomography analysis confirmed shape stability in this temperature interval and good interconnection of outside perimeters and internal infill structures within the prepared object. Total volumetric shrinkage of sample annealed at 1400°C was close to volume fraction of ceramic powder filling grade within the ceramic/polymer composite material.

ACKNOWLEDGMENT

The financial support of the Slovak Grant Agency for Science VEGA grant No. 1/0906/17 and Slovak Research and Development Agency APVV-16-0341, as well as financial support of project "Center for Applied Research of New Materials and Technology Transfer", ITMS 26240220088, supported by the Science and Research Operational Program by the European Regional Development Fund are gratefully acknowledged.

REFERENCES

[1] L. Sang, S. Han, X. Peng, X. Jian, J. Wang, Development of 3D-printed basalt fiber reinforced thermoplastic honeycombs with enhanced compressive mechanical properties, Compos. Part A Appl. Sci. Manuf. 125 (2019) 105518. doi:10.1016/j.compositesa.2019.105518.

[2] C. Esposito Corcione, F. Scalera, F. Gervaso, F. Montagna, A. Sannino, A. Maffezzoli, One-step solvent-free process for the fabrication of high loaded PLA/HA composite filament for 3D printing, J. Therm. Anal. Calorim. 134 (2018) 575–582. doi:10.1007/s10973-018-7155-5.

[3] F.S. Senatov, K. V. Niaza, M.Y. Zadorozhnyy, A. V. Maksimkin, S.D. Kaloshkin, Y.Z. Estrin, Mechanical properties and shape memory effect of 3D-printed PLA-based porous scaffolds, J. Mech. Behav. Biomed. Mater. 57 (2016) 139–148. doi:10.1016/j.jmbbm.2015.11.036.

[4] L. Fiocco, B. Michielsen, E. Bernardo, Silica-bonded apatite scaffolds from calcite-filled preceramic polymers, J. Eur. Ceram. Soc. 36 (2016) 3211–3218. doi:10.1016/J.JEURCERAMSOC.2016.05.013.

[5] L. Gorjan, R. Tonello, T. Sebastian, P. Colombo, F. Clemens, Fused deposition modeling of mullite structures from a preceramic polymer and γ-alumina, J. Eur. Ceram. Soc. 39 (2019) 2463–2471. doi:10.1016/J.JEURCERAMSOC.2019.02.032.

[6] A.S. M. Allahverdi, S.C. Danforth, M. Jafari, Processing of advanced electroceramic components by fused deposition technique, Ferroelectrics. 263 (2001) 45–54. doi:10.1080/00150190108225177.

[7] D. Nötzel, R. Eickhoff, T. Hanemann, Fused filament fabrication of small ceramic components, Materials (Basel). 11 (2018) 1–10. doi:10.3390/ma11081463.

3D PRINTING

SPEKANIE Al_2O_3 KERAMIKY PRIPRAVENEJ POMOCOU 3D TLAČE

SINTERING OF 3D PRINTED ALUMINA CERAMICS

M. Orlovská[1], Z. Chlup[2], Ľ. Bača[1], M. Janek[1], M. Kitzmantel[3], E. Neubauer[3]

[1] *Department of Inorganic Materials, Institute of inorganic chemistry, technology and materials FCHPT STU, Radlinského 9, 812 37 Bratislava, Slovakia*
[2] *CEITEC IPM, Institute of Physics of Materials, Academy of Sciences of the Czech Republic, Žižkova 22, 616 62 Brno, Czech Republic*
[3] *RHP-Technology GmbH, Forschungszentrum, 2444 Seibersdorf, Austria*

ABSTRACT

Fused filament fabrication (FFF) as the most used and a novel fabrication technique, widely known as 3D printing, played the primary role in the preparation of alumina ceramics. In this work, a composite ceramic filament with 50 vol. % of high purity alumina powder was used for 3D printing of cylindrical samples with different printing parameters (infill density and layer thickness). The effect of printing variables and debinding step on the sintering of prepared 3D parts has been investigated. After properly optimized debinding cycle (up to 850 °C for 1 h) and sintering at 1600 °C for 1 h, 54 % and 94 % of theoretical density were obtained after debinding and sintering, respectively.

Keywords: fused filament fabrication, alumina, debinding, roughness, 3D printing

INTRODUCTION

The design and development of advanced ceramic materials for high-performance applications in automotive, aerospace, defence, energy or the environmental and biomedical field are one of the most challenging tasks of modern engineering. Because ceramic materials provide a full scale of excellent physical and chemical properties, such as chemical and high-temperature resistance, refractoriness, biocompatibility, hardness and more, it is an incontrovertible fact that the extensive industrial use depends on the fabrication variability of complex-shaped three-dimensional ceramic parts [2-3]. Because anisotropy of printed parts is the general problem of additive manufacturing technologies, printing parameters need to be optimized to obtain 3D objects with at least comparable results as it is for traditional manufacturing [1]. As one of the most used and high - performance ceramic material is aluminium oxide or alumina. Under optimized conditions of preparation and heat treatment, alumina is a hard material, and additional machining with diamond tools is necessary to fabricate complex or near-net-shaped products.

Three - dimensional (3D) printing is a relatively new, cost-effective and unique technique that allows to directly fabricate complex structures and is expected to solve the limitations of traditional methods [3-4]. During the additive manufacturing process a three-dimensional object is built layer-by-layer from a Computer-Aided Design (CAD) files by controlled extrusion of composite thermoplastic filament onto the build platform [2, 5]. Some attempts have been undertaken to prepare ceramic products via 3D printing, while lack of report concerns high dense alumina ceramic. Most of the current research in three-dimensional ceramics printing is focused on using different techniques according to the form of the pre-processed feedstock prior to printing.

In this work, the main focus is centred on the preparation of complex-shaped ceramic objects via FFF technology using composite high-filled alumina filament (50 vol. %), main technical aspects including printability and post-treatment (debinding and sintering).

EXPERIMENTAL

Alumina filament of diameter 1.75 mm and solid loading 50 vol. % of pure alpha-Al_2O_3 powder (primary particle size 0.4 – 0.7 μm) was used for printing objects with defined dimensions suitable for measurements of physical (cylinders) and mechanical (bars) properties. Printer provider, a program for three-dimensional modelling and slicing of objects together with printing parameters are in Tab. 1. Printing variables used for further investigation of mechanical properties were different layer height (0.1, 0.2 and 0.3 mm) and infill density (65, 80 and 95 %). Debinding mode after proper optimization was performed by the 2-step regime – in a suitable solvent and thermally up to 850 °C. Sintering was done at 1600 °C for 1 hour.

Table1: Software and printer variables used for the preparation of samples

FFF commercial desktop printers	Leapfrog
3D modelling program	Tinkercad
Slicing program	Repetier-Host with Slic3r software
Bed (platform) temperature	60 °C
Extruder temperature	230 °C
Print speed	5 – 20 mm / s
Nozzle diameter	0.35 mm

RESULTS

FFF green parts (objects after printing) with a high polymer content require special attention through the debinding process. This critical step can either proceed solely thermally or be aided by solvent debinding out of the printed body. The thermal debinding methods are based on evaporation of components with low molecular weights, or that of products of thermal decomposition and their removal through the porous medium of the already partially debinded body by diffusion or permeation. Solvent debinding is based on extraction by immersion during which one component of the binder is dissolved, thus creating a porous structure suitable for subsequent thermal extraction. In this phase remaining open pores support further thermal decomposition of the binder.

For the preparation of high dense alumina, proper optimization of debinding cycle is a crucial part because of the risk of volume expansion or presence of inner cracks. In Fig.1 we can find results from the DTA / TG analysis for the composite filament in its printed form. From the graph, we can see critical temperature areas for debinding cycle in the temperature range 160 – 450 °C.

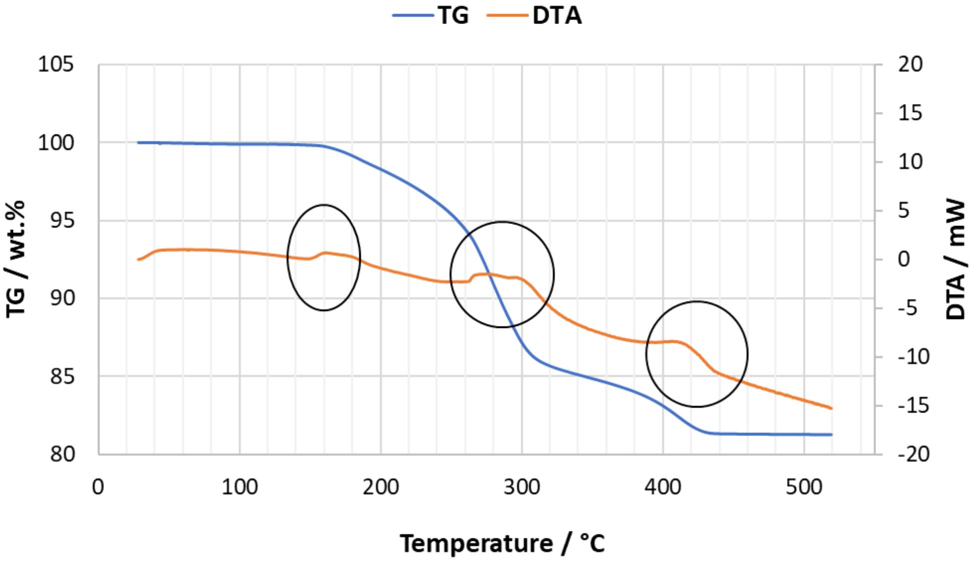

Figure 1: DTA / TG analysis of the as printed filament

According to results from DTA / TG analysis, many debinding modes were performed and evaluated. It was found that the thermal debinding alone caused deformations if the infill density was higher than 60 %. On the other hand, if a combination of solvent and thermal debinding was used, the risk of damaging the 3D objects was minimized. Moreover, with correctly optimized debinding cycle, relative densities up to 54 % can be obtained directly after this step in comparison to the only thermally debinded samples (40 – 42 % depending on the infill density). For illustration in the Fig.2, the cross-section of cylindrical samples printed with the infill 95 % and debinded in two different modes are compared.

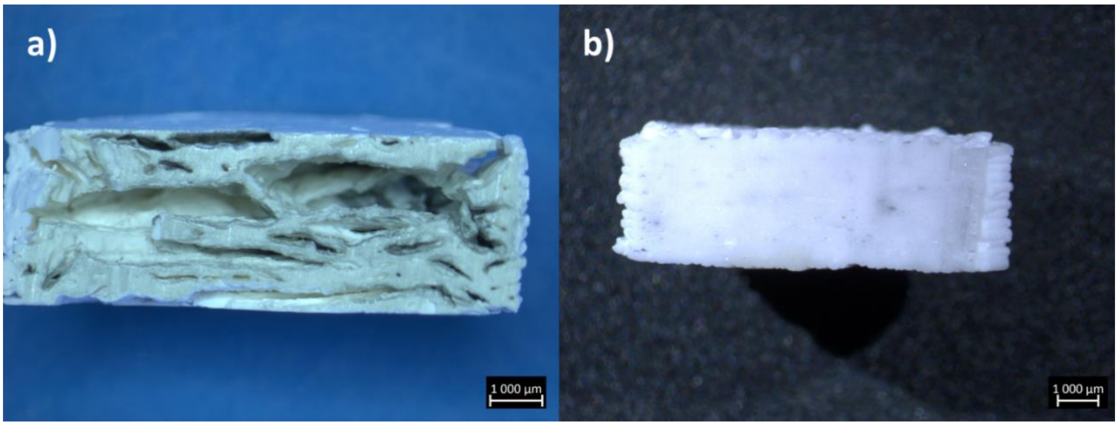

Figure 2: Cross section of sample printed with the infill 95 % a) thermally debinded b) solvent + thermally debinded

Bulk density measurements of sintered cylindrical samples at 1600 °C for 1 h revealed that with the highest applied infill it is possible to prepare relative dense (94 % of theoretical density) alumina ceramics without visible inner cracks or voids. As expected, an application of lower infill density results in the lower bulk density after sintering. The bulk density of samples prepared with the 65 % infill reached only around 80 % of theoretical density. However, the distribution of voids in the structure was homogeneously reflecting the printing model. A change of layer thickness (height) did not affect the bulk density results though may influence the aesthetical quality of the print, mechanical properties or surface roughness. In the Tab. 2, results of open porosity and bulk density measurements of sintered cylindrical samples (1600 °C, 1 h) can be seen.

Table 2: Results of open porosity and bulk density measurements

Infill density / Layer height		***0.3 mm***	***0.2 mm***	***0.1 mm***	***Cross section***
95 %	**Rel. density**	94 %	94 %	93 %	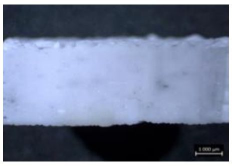
	Absorptivity	0.2 %	0.5 %	0.1 %	
80 %	**Rel. density**	92 %	86 %	93 %	
	Absorptivity	0.5 %	3.0 %	0.4 %	
65 %	**Rel. density**	82 %	78 %	86 %	
	Absorptivity	3.9 %	4.3 %	3.0 %	

As a future outlook, manufactured 3D printed bars and pillars with same printing variables as for cylindrical specimens and depicted in Fig. 3 will be used for measurement of three-point bending strength, Young's modulus as well as fracture and microstructure analysis.

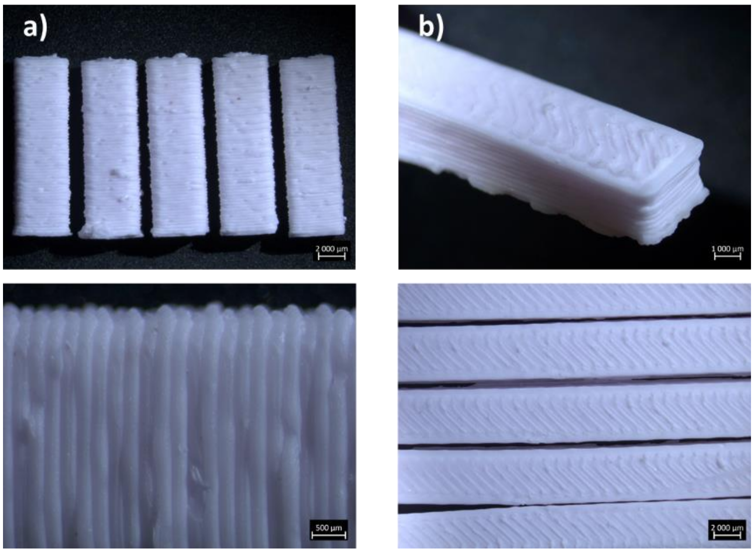

Figure 3: Samples prepared for measurements of mechanical properties a) pillars b) bars

CONCLUSIONS

In this work, a new technique for the fabrication of ceramics, 3D printing by Fused Filament Fabrication, was used for the preparation of dense alumina ceramics. After properly optimized debinding cycle and sintering at 1600 °C for 1 h it was possible to prepare nearly dense alumina depending on used printing parameters – 94 % of theoretical density. For the characterization of physical and mechanical properties, printing variables such as infill density and layer height are being used. As a future outlook, mechanical properties such as elastic modulus or 3-point bending strength will be measured on samples of bars and pillars 3D printed in x-y and z-direction, respectively.

ACKNOWLEDGMENT

The authors are grateful to the JECS Trust for funding [the visit of 25/02/2019-25/03/2019] (Contract No. 2018192). The financial support of the Slovak Grant Agency for Science VEGA grant No. 1/0906/17 and Slovak Research and Development Agency APVV-16-0341 are also greatly appreciated.

REFERENCES

[1] A. Zocca et al., Additive Manufacturing of Ceramics: Issues, Potentialities, and Opportunities J. Am. Ceram. Soc. 98 (2015) 1983–2001.

[2] N. Travitzky et al., Additive Manufacturing of Ceramic-Based Materials, in Advanced Engineering Materials 2014, doi: 10.1002 / adem.201400097.

[3] X. Li et al., Microstructure and mechanical properties of porous alumina ceramic prepared by a combination of 3–D printing and sintering, in Ceramic International 42 (2016) 12531 – 12535.

[4] J. Maurath et al., 3D printing of open-porous cellular ceramics with high specific strength, Journal of the European Ceramic Society 37 (2017) 4833 – 4842.

[5] X. Wang et al., 3D printing of polymer matrix composites: A review and prospective, Composites Part B 110 (2017) 442 – 458.

3D PRINTING

MECHANICKÉ VLASTNOSTI FILAMENTOV NA BÁZE HAP A SIMULÁCIA ICH VZPERNÉHO TLAKU AKO INDIKÁTOR TLAČITEĽNOSTI POMOCOU FDC

MECHANICAL PROPERTIES OF HAP BASED FILAMENTS AND BUCKLING SIMULATION AS INDICATOR OF PRINTABILITY IN FDC

M. Janek*[1,2], T. Gabošová[1], R. Fialka[1], V. Kovár[1], V. Žilinská[1], Z. Hajdúchová[1], P. Veteška[1], P. Peciar[3], J. Feranc[1], Ľ. Bača[1]

[1]Slovak University of Technology, Faculty of Chemical and Food Technology, Radlinského 9, 812 37 Bratislava, Slovakia
[2]Comenius University, Faculty of Natural Sciences, Department of Physical and Theoretical Chemistry, Ilkovičova 6, Mlynská dolina, 842 15 Bratislava, Slovak Republic
[3]Slovak University of Technology, Faculty of Mechanical Engineering, Nám. slobody 17, 812 31 Bratislava, Slovakia
e-mail: marian.janek@stuba.sk

ABSTRACT

In recent years intensive rise of the additive manufacturing technologies have created new advances and frontier breakthroughs in several multidisciplinary sciences, including inorganic, organic, pharmaceutic and medical sciences in scaffold engineering applications. There are several distinct additive manufacturing technologies such as photo polymerization, powder bed, fused deposition systems and several others, which compete for leading position in 3D printing of ceramic objects. In our study were investigated tensile and compression strength properties of composite filaments applicable in fused deposition ceramics systems, containing hydroxyapatite particles of different sizes and size distributions. Such material may find its application as small dimension implants required for dental and specific bone-part replacements. Filaments for fused deposition of ceramics technology used in any equipment, must fulfil several specific physical-chemical requirements allowing its successful utilisation in commercial 3D printers. One of these requirements include filament mechanical behaviour during feeding in current fused deposition of ceramics, based on broadly used fused deposition modelling equipment.

Keywords: hydroxyapatite, 3D printing, composite filament, mechanical properties, FDC

INTRODUCTION

The attractivity of fused deposition of ceramics (FDC) is related to simplicity of fused deposition modelling (FDM) technology. The functional equipment requires for operation just a platform positioning system in cartesian space, feeding system with liquefier applicable for broad range of polymers available and computer aided design (CAD) software for creation of virtual 3D model in personal computer. This explains the success and the application potential of FDM technology operating with production-grade thermoplastics [1, 2]. Therefore, FDM as melt extrusion technology proved its value in manifold applicability to solve practical and technical tasks in production chain thanks to continuous developing and validating new materials and novel parts applications. The FDM belongs to melt extrusion technology and similarly are successfully produced ceramic parts by well-established ceramic injection moulding process since last century [3-5].

For successful 3D printing of ceramic objects, the additive manufacturing technology must challenge the feature demanding by the nature of the ceramic materials. This includes the two-stage processing: i) the production of green body objects and ii) object firing without its significant shape deformation [6-8]. Prior the part processing, the successful and reliable printout of green parts must be established as failproof. This requires the correct adjustment of processing parameters from very beginning in filament production. In current FDM equipment, the melt feeding part is based on heated tube, where moving filament act as plunger for extrusion of already melted filament portion through nozzle of desired diameter. Such easy solution brings the danger of filament buckling in the case that feeding rate, filament strength, operating temperature and rheological properties are not sufficiently optimised. From these reasons we focused on the mechanical strength of composite containing hydroxyapatite (HAp) particles as inorganic filler as indicator of filament suitability for FDC during development of future novel formulations [9-12].

EXPERIMENTAL

Mechanical testing of filament tensile and compressive strength was done on Micro-Epsilon SZ-3000 (Czech Republic) 3kN mechanical tester equipped with three-point claw gripping heads. The non-desired filament buckling may occur during filament feeding into the liquefier described by the Euler buckling analysis [13] as expressed by Equation 1:

$$p_{cr} \geq \frac{\pi^2 d_f^2 E}{16 l_{FL}^2} \tag{1}$$

Here, p_{cr} is critical pressure achieved during pressing of filament with diameter d_f into the liquefier nozzle, while free filament length l_{FL} defined by the feeder to liquefier construction distance, E is the elastic modulus, hence filament elasticity parameter affecting buckling. The ratio of l/d defines here the slenderness ratio. Along with experimental HAp filled filaments commercial sample made from pure thermoplastic polylactic acid was measured for comparison (philament, Hungary). The investigated filaments with diameter ~1.75 mm were cut to different lengths and mechanical properties were measured at nominal gripping heads distance 20, 40 and 80 mm defining the free filament length and its slenderness. For statistical evaluation of mechanical properties at least 50 force loading measurements were done for tensile or compressive measurements. The filling grades with inorganic components were determined by thermogravimetric analysis in the flowing air atmosphere of 150 ml/min and heating ramp of 5 °C/min up to temperature 550 °C are summarized in Table 1.

Table 1: List of investigated filaments for their tensile and compressive strength behavior.

Filament	Material	Filling mass %
HAT00	Hydroxyapatite	49.4
HAT10	Hydroxyapatite	49.3
Commercial PLA	-	0

RESULTS

The force loading dependences of selected data measurement from the whole matrix corresponding to tensile and compressive measurements of commercial PLA and laboratory prepared HAT00 filaments are shown in the Figure 1. In the case of tensile measurements for PLA, almost linear material force resistance can be observed for small elongation displacements. The slope of this curve part indicates the Young´s modulus of material. At further force increase, the material reaches maximal value and plastic deformation starts. This corresponds to the tensile strength of PLA with zero filling by inorganic particles. For the testing of laboratory prepared HAT00 filaments the stress-strain curves indicate parabolic dependence for small elongation displacements. Thus, only extrapolated tangent slope for zero elongation displacement can be a close estimation of Young´s modulus for the deformation of this type filament. Clearly, both elastic and plastic deformations of HAT00 filaments are taking place after the force load of material starts prior maximum force is reached. Finally, plastic material deformations occur until total material failure at higher elongations.

The compressive strength test revealed similar dependence for PLA as observed during tensile tests. However, the filament resisted up to triple applied force loading than in tensile measurements prior to its buckling. During buckling one and less frequently two maxima were observed on the stress-strain curves. After the point the material resisted its buckling only continuous force decay was observed, indicating material resistance during its bending. The analogous situation was observed for laboratory prepared HAT00 filaments, while for smaller compressions parabolic dependence was observed until the maximum compressive load force was reached and filament buckling started. Here only extrapolated tangent slope for zero compressive displacement can be considered as a close estimate of Young´s modulus for deformation of this type filament. Similarly, as during the tensile HAT00 measurements, both elastic and plastic deformation of filaments is taking place prior to maximum compressive force load is reached. Interestingly, after this point, periodic consolidation of the polymer composite filled by solid inorganic particles was observed by wavy form of stress-strain dependence (Figure 1).

For comparison of maximal forces during tensile and compressive measurements and verification of their distribution during testing, all HAT00 maximal force load values and their distribution around mean values are shown in the Figure 2. For evaluation of filament suitability for 3D printing using feeder – nozzle systems, the maximal compressive force indicates practical filament buckling limits at the simulated feeder – nozzle distance which was in this case 20 mm. The real systems may have usually shorter l_{FL} values or may have any form of Bowden tubing solution to support printing with more flexible filaments. Both distributions of maximal forces revealed dependences which were close to the normal Gauss distribution (Figure 2). Very similar dependences were found also for HAT10 sample, therefore only HAT00 are further discussed only.

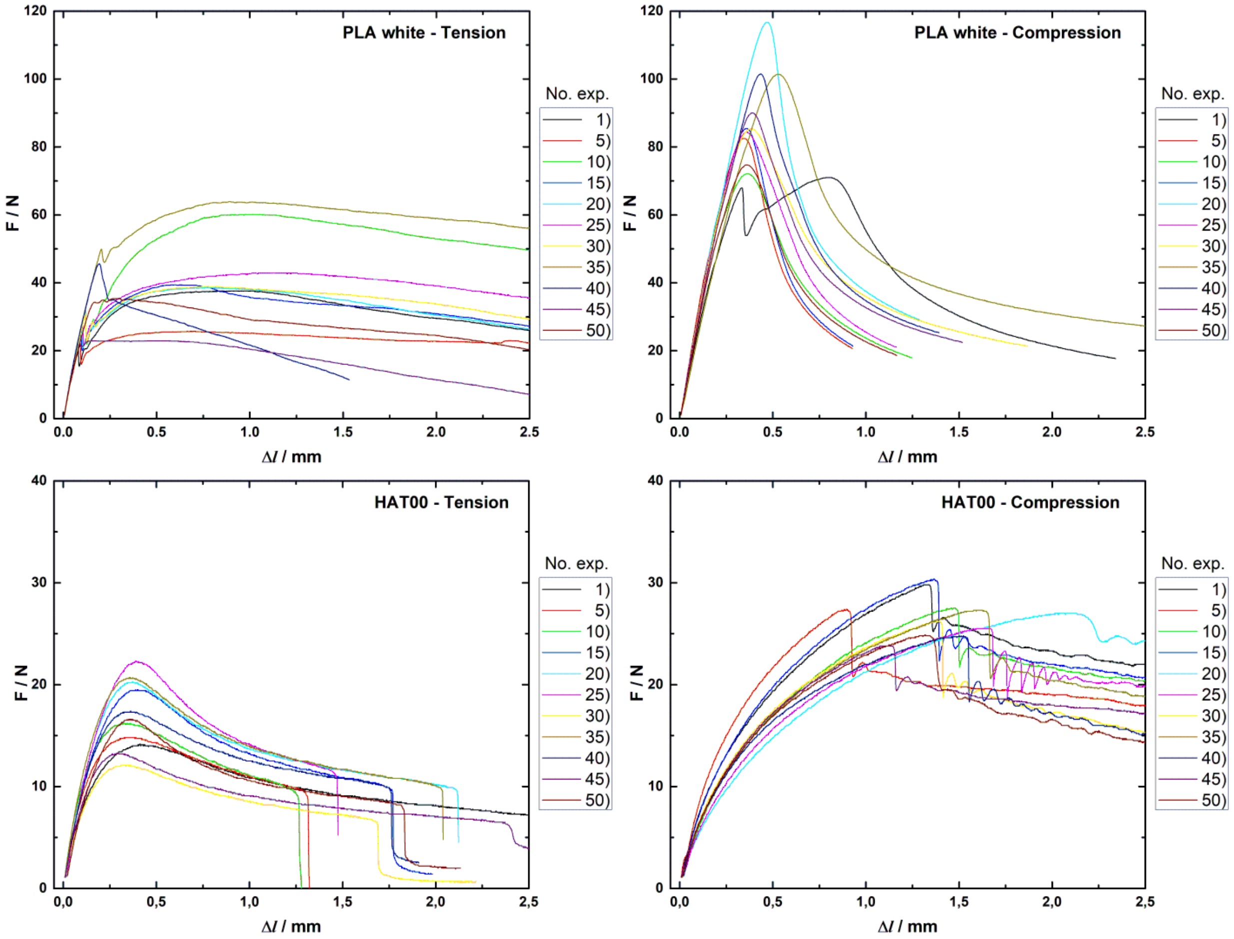

Figure 1: Tensile and compression force loading dependences of PLA and HAT00 filaments.

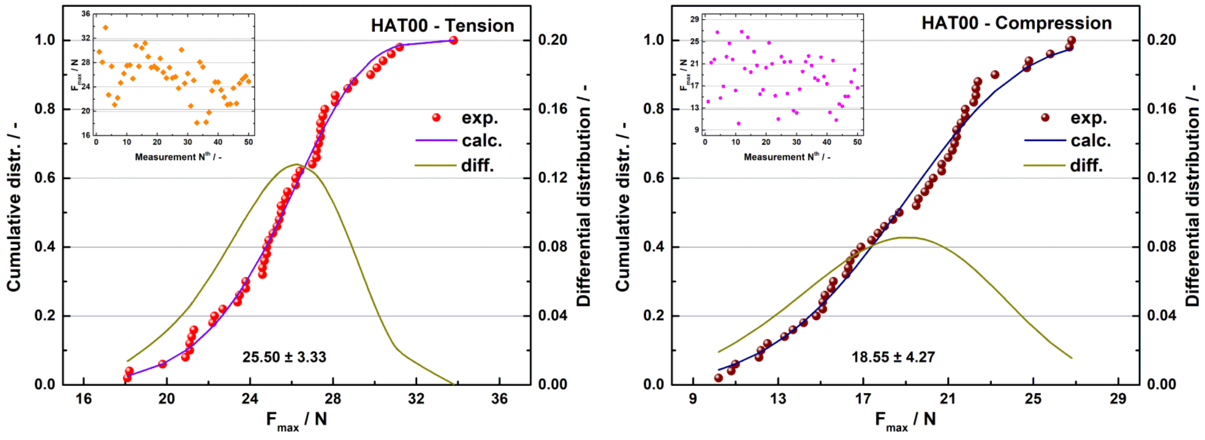

Figure 2: Distributions of maximal forces values during tensile and compressive strength measurements (mean force values indicated with respective standard deviations in the graphs).

The summary of maximal forces during tensile and compressive measurements on all investigated filament lengths for HAT00, hence 20, 40 and 80 mm is shown in the Figure 3. The maximal compressive force load decreased substantially with the free filament length l_{FL} which agrees with Euler buckling theory. On the other hand, the maximal tensile force load almost did not change or slightly increased its value with increasing of l_{FL} values. Comparison of Young´s modulus of HAT00 filaments as determined from tensile or compressive strength measurements shows comparable decreasing tendency for increasing l_{FL} values, however, the values determined from compressive experiments shows systematically higher values than were found from tensile strength measurements (Figure 3).

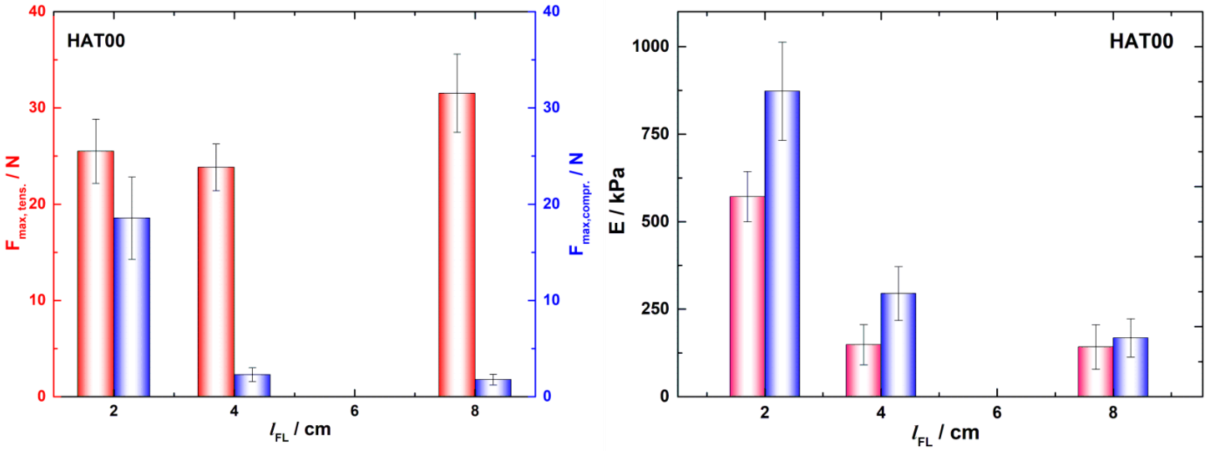

Figure 3: Maximal forces and Young´s modulus during tensile and compressive measurements as function of free filament length.

CONCLUSIONS

The tensile and compressive strength measurements of experimental and commercial filament applicable in additive manufacturing for FDC/FDM technology were investigated. Depending on the free length of filament (20, 40, 80 mm) the longer the specimen used the closer values for Young´s modulus were determined from both tensile and compressive measurements. However, the values increased exponentially if shorter filament free lengths were used. The critical pressure achieved from Euler analysis from tensile Young´s modulus of HAT00 was 270 kPa, while experimentally determined buckling force from compressive measurement achieved 7.71 MPa. This indicates a difficulty if filament suitability should be considered for feeder – nozzle systems used in FDC/FDM equipment by the linear Euler buckling analysis. Evaluation of maximal force required for filament buckling during compressive measurements can be considered as an experimentally directly available indicator of filament utilization at the given feeder – nozzle construction. In comparison, the maximal tensile strength of material changed only slightly with the increasing length of filament tested.

ACKNOWLEDGMENT

The financial support of the Slovak Grant Agency for Science VEGA grant No. 1/0906/17 and Slovak Research and Development Agency APVV-16-0341 are greatly appreciated. This work is based on the results of the project Center for Applied Research of New Materials and Technology Transfer, ITMS 26240220088, supported by the Science and Research Operational Program by the European Regional Development Fund.

REFERENCES

[1] Crump, S. (1989) Apparatus and Method for Creating Three-Dimensional Objects. 30 October 1989, US Patent 07/429,012.

[2] Gibson, I.; Rosen, D.; Stucker, B. (2015) Additive Manufacturing Technologies. 3D Printing, Rapid Prototyping, and Direct Digital Manufacturing, 2nd ed.; Springer: New York, NY, USA, 498p. ISBN: 978-1-4939-2112-6

[3] Ligon S.C., Liska R, Stampfl J., Gurr M. and Mülhaupt R. (2017) Polymers for 3D Printing and Customized Additive Manufacturing. Chem. Rev. 117(15) 10212−10290.

[4] Dimitrov D., Schreve K. and de Beer N. (2006) Advances in three dimensional printing – state of the art and future perspectives. Rapid Protot. J., 12(3), 136–147.

[5] Hammel E.C., Ighodaro O.L.-R., Okoli O.I. (2014) Processing and properties of advanced porous ceramics: An application based review. Ceram. International 40, 15351–15370.

[6] Bengisu M., Engineering ceramics, Springer-Verlag Berlin Heidelberg 2001. 620p.

[7] Robert B. Heimann. Classic and Advanced Ceramics, From Fundamentals to Applications. WILEY-VCH Verlag GmbH & Co. KGaA, Weinheim 2010. 553p.

[8] Hwa L.C., Rajoo S., Noor A.M., Ahmad N., Uday M.B. (2017) Recent advances in 3D printing of porous ceramics: A review. Current Opinion in Solid State and Materials Science 21, 323–347.

[9] Fielding, G. A., Bandyopadhyay, A., and Bose, S. (2012) Effects of silica and zinc oxide doping on mechanical and biological properties of 3D printed tricalcium phosphate tissue engineering scaffolds. Dental Materials, 28,113–122.

[10] Mota C., Puppi D., Chiellini F., Chiellini E. (2012) Additive manufacturing techniques for the production of tissue engineering constructs. Journal of Tissue Engineering and Regenerative Medicine 9, 174-190.

[11] Narayan R. (editor) Rapid prototyping of biomaterials - Principles and applications. Woodhead Publishing Series in Biomaterials: No. 70, Cambridge (2014) 323pp.

[12] Adel-Khattab D., Giacomini F., Gildenhaar R., Berger G., Gomes C., Linow U., Hardt M., Peleska B., Günster J., Stiller M., Houshmand A., Ghaffar K.A., Gamal A., EL-Mofty M., Knabe Ch. (2018) Development of a synthetic tissue engineered 3D printed bioceramic-based bone graft with homogenously distributed osteoblasts and mineralizing bone matrix in vitro. Journal of Tissue Engineering and Regenerative Medicine 12, 44–58.

[13] Turner B.N., Strong R. and Gold S.A. (2014) A review of melt extrusion additive manufacturing processes: I. Process design and modeling. Rapid Prototyping Journal 20(3), 192–204. DOI 10.1108/RPJ-01-2013-0012

MEZOPORÉZNE BIOAKTÍVNE SKLÁ DOPOVANÉ TERAPEUTICKÝMI IÓNMI

MESOPOROUS BIOACTIVE GLASS DOPED WITH THERAPEUTIC IONS

M. Michálek[1], F. Kurtuldu[1], Z. Neščáková[1], L. Liverani[2], D. Galusek[3], A. R. Boccaccini[2]

[1] *Department of Biomaterials, FunGlass, Alexander Dubček University of Trenčín, Študentská 2, 911 50 Trenčín, Slovakia*
[2] *Department of Materials Science and Engineering, University of Erlangen – Nuremberg, 910 58 Erlangen, Germany*
[3] *Dpt. VILA – Joint Glass Centre of the IIC SAS, TnUAD, FChPT STU, Študentská 2, 911 50 Trenčín, Slovakia, FunGlass, A. Dubček University of Trenčín, Študentská 2, 911 50 Trenčín, Slovakia*

ABSTRACT

In the present study the mesoporous bioactive glass (MBG) particles were prepared by microemulsion assisted sol-gel technique. Incorporation of therapeutic inorganic ions (TII) enhance the biological impact of MBG materials. Metallic ions such as strontium, copper, gallium, cerium, magnesium and boron have been incorporated to the binary system SiO_2 / CaO with the nominal composition of 60/40 mol %. The effect of TII doping on the morphology and chemical composition of MBG nanoparticles was investigated. The results show significant difference in the nominal and experimental chemical composition of the obtained MBG particles in attendance from the used metallic ion, moreover the TII affect the size and shape of the materials.

Keywords: sol-gel, mesoporous bioactive glass, therapeutic ions, morphology, bioactivity

INTRODUCTION

The term sol-gel was first used by Graham [1] 1864 and sol-gel derived bioactive glass (BG) was first produced in the early 90`s by Li et al. [2]. The sol-gel approach is a chemical-based process performed at lower temperatures than the melting technique [3], which attracts attention of researchers due to the increased specific surface area of sol-gel derived BG over traditional melt-derived BG leading to enhanced bioactivity and degradability. Moreover, the sol-gel approach overcomes some limitations of the melting process; namely, the maintenance of the high purity required for the bioactivity and the compositional limitations imposed on BG made by the melting quench method [2]. There are several sol-gel based strategies, including base- catalysis [4, 5], acid/base co-catalyse [6] and microemulsion assisted sol-gel method [7, 8], to synthesize MBG. The concentration of surface active agents affects the pore size, pore volume and size of the particles [7]. Other parameters such as pH, temperatures or type and concentration of precursors also play an important role in the formation of the particles [9].

In the present work, the diverse dopants including the Sr, B, Mg, Cu, Ga and Ce were incorporated into the binary system of SiO2-CaO. The microemulsion assisted sol-gel method has been selected to prepare doped glasses. The effect of the dopants on the morphology, chemical composition, in vitro bioactivity and biocompatibility of the prepared bioactive glass powders have been evaluated.

EXPERIMENTAL

The mesoporous bioactive glass nanoparticles (MBG) were synthesized by a microemulsion- assisted sol-gel approach described elsewhere [7] and is shown in Fig 1. In the first case, the nominal composition of MBG was (in mol %) 60 SiO_2 / 40 CaO and by first set of doped materials 62 SiO_2 / 32 CaO / 6 X, where X = SrO, B_2O_3, MgO, CuO, Ga_2O_3. All chemicals were used as delivered without any treatment. The synthesized particles are noted as MBG, MBG+6Sr, MBG+6B, MBG+6Mg, MBG+6Cu and MBG+6Ga, according to the nominal volume of used therapeuticion.

In the second trial cerium doped MBG and gallium doped MBG of 60 SiO_2 - (40 - y) CaO - yX system (where y stands for 1, 3 and 5 mol % and X for the particular ion) were investigated. In this case the materials are noted as MBG-yX.

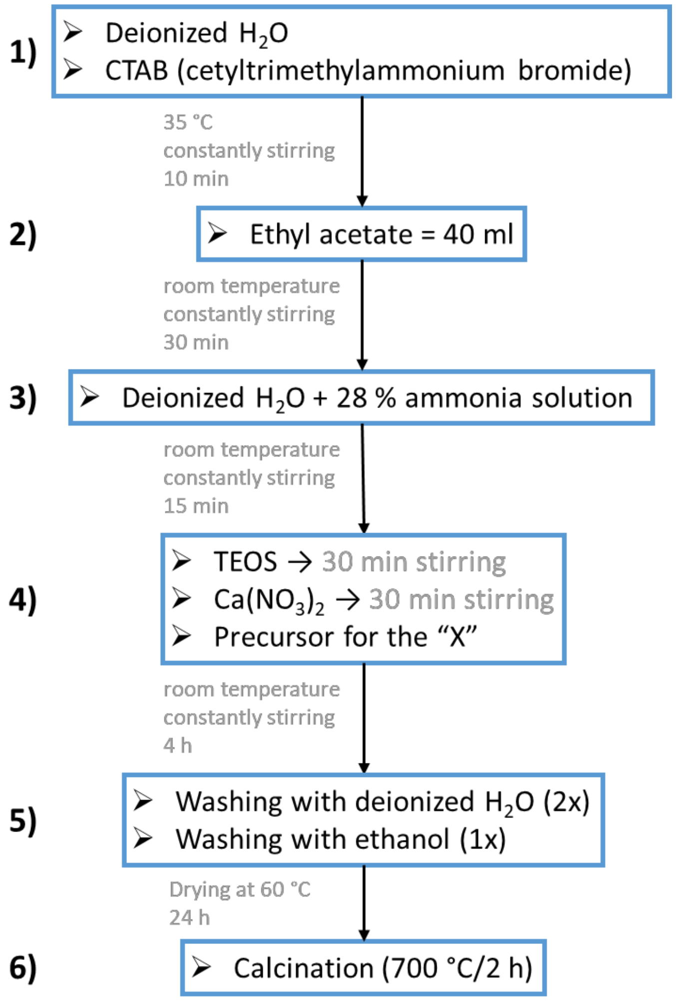

Figure 1: Schedule of the microemulsion assisted sol-gel process used to synthesise the MBG.

Morphology analysis was performed by scanning electron microscope (SEM) equipped with an EDX detector. Particle size was determined using the ImageJ software. The quantitative analysis of the chemical composition was utilized by inductively coupled plasma optical emission (ICP-OES) spectroscopy.

RESULTS

The micro-emulsion assisted sol-gel method was used in order to prepare MBG with and without doping by therapeutic inorganic ions. In the first case the 6 mol % of Sr^{2+}, B^{3+}, Mg^{2+}, Cu^{2+} and Ga^{3+} was added to the initial MBG matrix. The real compositions of MBG determined by the ICP-OES measurement are listed in Table 1 together with the size and shape of MBG. It is clearly visible that the 6 mol % nominal doping with diverse elements leads to considerable differences in the overall compositions. The differences in the shape and chemical composition may influence the bioactivity and biocompatibility of the materials.

Table 1: Experimental chemical composition in mol % of the MBG particles with and without doping determined by ICP-OES with particle size d50 and shape of the particles.

Sample	**SiO_2 #**	**CaO**	**"X"**		**Size d50 (nm)**	**Shape**
MBG	*91.48 ±0.92*	*8.52±0.13*	-	-	*114 ±18*	*Sphere*
MBG+6Sr	*88.11 ±0.88*	*10.73±0.3*	*1.16±0.11*	SrO	*157 ±19*	*Sphere*
MBG+6B	*70.73 ±0.7*	*16.78±0.5*	*12.49±0.27*	B2O3	*265 ±29*	*Pineal*
MBG+6Mg	*79.60 ±0.83*	*10.53±0.2*	*9.87 ±0.06*	MgO	*530 ±92*	*Pineal*
MBG+6Cu	*76.56 ±0.72*	*4.68±0.01*	*18.76±0.07*	CuO	*171 ±15*	*Sphere*
MBG+6Ga	*87.52 ±0.13*	*6.24±0.47*	*6.24 ±0.14*	Ga2O3	*185 ±19*	*Sphere*

 # Not measured, calculated.

In the second trial, nanoparticles with 1 mol % of Ce^{3+} and Ga^{3+} were in size, shape and surface pore structure similar to those of the undoped MBG. Increasing the content of dopants to 3 and 5 mol % resulted in deformation of the spherical shape of the nanoparticles. The resulted pineal shape of particles was with the aspect ratio 5:3. In addition, content of calcium decreased significantly (down to 2 at. %), most likely due to replacement of Ce^{3+} and Ga^{3+} in the glass structure with the ions of the dopants.

CONCLUSIONS

Using the microemulsion assisted sol-gel preparation technique the influence of Sr^{2+}, B^{3+}, Mg^{2+}, Cu^{2+}, Ga^{3+} and Ce^{3+} dopants on the morphology and chemical composition has been studied. The used dopants have a significant effect on the size, shape and chemical composition when the conditions of the sol-gel process are fixed. The presented results will help to better understand the effect of therapeutic inorganic ions incorporation into the bioactive glasses, in aim to fully reveal their potential in the field of biomedical applications such as bone, soft tissue engineering, drug loading, etc.

ACKNOWLEDGMENT

This paper is a part of dissemination activities of the project FunGlass. This project has received funding from the European Union′s Horizon 2020 research and innovation programme under grant agreement No 739566. Financial support of this work by the grants SAS-MOST JRP 2018/02 and VEGA 1/0098/19 is gratefully acknowledged.

REFERENCES

[1] T. Graham, Journal of the Chemical Society 17 (0) (1864) 318-327.

[2] R. Li, A. E. Clark and L. L. Hench, J Appl Biomater 2 (4), (1991) 231-239.

[3] L. L. Hench, R. J. Splinter, W. C. Allen and T. K. Greenlee, Journal of Biomedical Materials Research 5 (6) (1971) 117-141.

[4] O. Tsigkou, S. Labbaf, M. M. Stevens, A. E. Porter and J. R. Jones, Adv Healthc Mater 3 (1), (2014) 115-125.

[5] K. Zheng, N. Taccardi, A. M. Beltran, B. Y. Sui, T. Zhou, V. R. R. Marthala, M. Hartmann and A. R. Boccaccini, Rsc Adv 6 (97) (2016) 95101-95111.

[6] X. F. Chen, C. L. Guo and N. R. Zhao, Appl Surf Sci 255 (2) (2008) 466-468.

[7] Q. M. Liang, Q. Hu, G. H. Miao, B. Yuan and X. F. Chen, Mater Lett 148 (2015) 45-49.

[8] K. Zheng, J. Kang, B. Rutkowski, M. Gawęda, J. Zhang, Y. Wang, N. Founier, M. Sitarz, N. Taccardi and A. R. Boccaccini, Frontiers in Chemistry 7 (2019) 497.

[9] J. Eastoe, M. J. Hollamby and L. Hudson, Advances in Colloid and Interface Science 128, (2006) 5-15.

POSÚDENIE POČIATOČNEJ FÁZY ROZPÚŠŤANIA NOVODOBÝCH BIOMATERIÁLOV V SB KVAPALINE

ASSESMENT OF ION RELEASE AT EARLY STAGE OF IMMERSION IN SB FLUID FOR NOVEL BIOMATERIALS

D. Galusková[1], H. Kaňková[1], A. Švančárková[1,2], D. Galusek[1, 3]

[1] *Centre for Functional and Surface Functionalized Glass, Alexander Dubček University of Trenčín, Študentská 2, 91150 Trenčín, Slovakia*
[2] *Faculty of Chemical and Food technology, Slovak University of Technology, Bratislava,*
[3]*Joint Glass Centre of the IIC SAS, TnUAD and FChPT STU, FunGlass, Trencin, Slovakia*

ABSTRACT

Identification of a test setting including evaluation procedure of data sets, which is predictive in respect to bioactivity at the early stage of immersion testing was studied and verified on selected novel bioactive materials. The experimental parameters of flow through test synchronized with an inductively coupled plasma optical emission spectrometer were optimized to continuously measure the concentration profile of the ions dissolving from studied glass in simulated body fluid. The method was tested using the bioactive glass reflecting composition of the 45S5 bioglass 23Na_2O, 23CaO, 6P_2O_5, 48SiO_2 (wt%). In our study we observed that calcium and silicon are congruently released from the powder glassy sample at the same rate already in the initial period of time starting at 5 min. Phosphorus released from tested glass powder was detected below the concentration monitored in the SBF blank solution.

Keywords: bioactive glass, ion release, SB fluid, ICP OES

INTRODUCTION

The evaluation of apatite-forming ability on implant material in SB (simulated body) fluid relies on appropriate methodology of in vitro tests together with the methods for diagnosing group of calcium-phosphates responsible for bridging the tissue with material. For decades, the Kokubo recipe [1, 2] has been included in bioactivity and degradation testing to identify a material with *in vivo* bone reactivity or tissue regeneration ability as reliably as possible. It is also cited in the International Standard ISO/FDIS 23317:2007 describing the method for detecting apatite formed on surface of a material in SB fluid based on evaluation of a diffraction pattern obtained by X-ray with small incident angle against the surface of the sample [3]. In the Standard [3] the soaking time is recommended to be 4 weeks. Most studies rely only on detecting apatite-forming ability based on XRD pattern and observation of the surface. Other, include also ICP results to demonstrate that material dissolves in SB fluid. In most of static tests usually performed at different S/V ratios the sampling starts after 1 day. Since SB fluid is already metastable, the ability to form apatite is very probable already in the initial period of soaking the material. Therefore the information about ion release in the initial period can significantly contribute to assessment of early stage kinetics of material dissolution.

Therefore in this work we tested and verified an experimental setting facilitating in line testing of early stage dissolution of biomaterials. As a reference medium deionized water with only dissolved TRIS (tris-(hydroxymethyl) aminomethane) buffer was utilized. Identification of a test setting including evaluation procedure of data sets, which is predictive not only in respect to bioactivity at the early stage of immersion testing but also to assessment of controlled release of various ions from bioactive material was studied and verified on the novel bioactive materials. The method was tested using the bioactive glass reflecting composition of the 45S5 Bioglass 23Na_2O, 23CaO, 6P_2O_5, 48SiO_2 (wt%).

EXPERIMENTAL

For the *flow-through* test the thermostatic bath, corrosion cell, peristaltic pump and tubing were assembled and connected directly to the introduction system of the optical emission spectrometer (ICP OES, Agilent 5100 SVDV). Internal standard scandium (10 mg/L) was included in inline sampling in order to deal with non-spectral interferences. SBF buffer solution with pH 7.4 was prepared according to the protocol described by Kokubo et al. [1] at 36.5 °C. Limit of detection for therapeutic ions (Co, Cu, Sr, Zn) together with silicon, as the elements not dissolved in SBF solution, was determined. Limit of quantification with precision calculated as RSD% was considered to be < 5%. The bioactive glass (23Na_2O, 23CaO, 6P_2O_5, 48SiO_2 (wt%)) reflecting the composition of 45S5 Bioglass [4] was prepared by conventional melt quenching at 1300°C. The glass powder with the particle size ≤ 25 μm was used for optimization of the experimental parameters for continuous measurement of the concentration of ions released into SB fluid. The sample weighing ~ 200 mg was soaked in the corrosion cell with the volume of ~ 1mL, through which continuously flew fresh SBF solution at the temperature held constant at 37±1 °C at a flow rate of 0.56 mL/min. Concentration of released ions in time interval of 2 min was directly monitored using ICPExpert software. The total amount of leached elements (*Q)* was determined by the following equation [1] and normalized to the content of the element in the initial sample:

$$Q_i^t = c_i \frac{F}{m_i} \Delta t + {Q_i}^{t-\Delta t} [\mathrm{mg/g}] \tag{1}$$

where c_i (mg/L) is concentration of particular leached element at the time t (min) subtracted from the concentration of the element in blank, and F (10^{-3}mL/min) is the flow rate, m_i (g) the content of element in the initial sample. Values of the initial leaching rate can be evaluated from experimental time dependencies of Q_i.

RESULTS AND DISCUSSION

The interval of calcium and phosphorus variation in the SB fluid were determined by analysing the solution flowing through the reactor without the sample (*blank*) repeatedly in different days. The calcium and phosphorus concentration in SBF solution determined at the ambient temperature with the precision 0.2% fall to the interval starting from 95 to 98 mg/L and from 29 to 31 mg/L respectively. Only the determined values of Ca and P outside of these intervals would be considered as relevant for evaluation of bioactivity. The concentration of the Ca and P above the maximal values would be considered as the amount of dissolved ion originated from dissolution process. The concentration of Ca and P falling to the interval of reliability or determined below minimal value detected for both elements would possibly indicate the precipitation of apatite-like phases. The limit of quantification (LOQ) 0.49 mg/L was determined for Si in SB fluid with precision <5%, calculated as *3xsd* from all acquired

SBF-blank analysis. Limits of detection and quantification for considered therapeutic ions are shown in the Table 1.

Table 1: Limits of detection (LOD) and limits of quantification (LOQ) for potential therapeutic elements dissolved in the simulated body fluid (SBF).

element [nm]	B *249.772*	Co *228.615*	Cu *324.754*	Sr *216.596*	Sr *421.552*	Zn *202.548*
LOD [mg/L]	0.007	0.02	0.02	0.008	0.001	0.02
LOQ [mg/L]	**0.02**	**0.07**	**0.06**	**0.03**	**0.004**	**0.05**

The bioactive glass with the composition of 45S5 dissolves in aqueous solutions easily. Their dissolution performance in early stage was monitored only for deionized water with TRIS buffer and also in acidic environment at pH 4 [7]. So far the interactions of 45S5 glass with SB fluid for time interval < 1 hour have not been documented in literature. In our study we observed that calcium and silicon are congruently released from the powder glassy sample at the same rate already in the initial period of time starting at 5 min (Fig. 1). Phosphorus released from 45S5 sample was detected below the concentration monitored for the SBF blank solution. Although we could distinguish calcium release from the material into SB fluid, it is also highly probable that it precipitated together with phosphorus and magnesium forming phases close to apatite composition. Test performed at the same conditions only in deionized water buffered with TRIS support this hypothesis, while amount of released calcium is 5 times higher in 10 min interval comparing to SBF test results (Fig. 2).

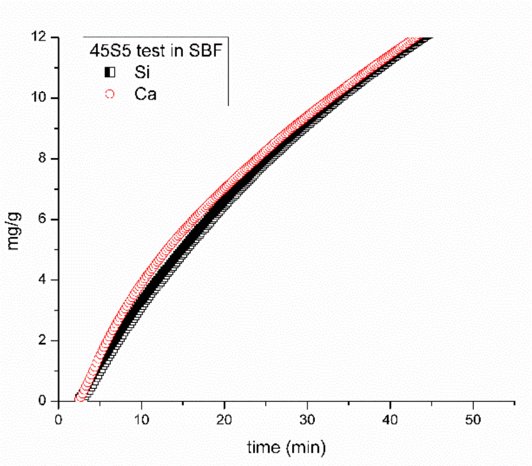

Figure 1: Dissolution of 45S5 expressed in terms of release Ca and Si in SB fluid in the initial 2 minutes time interval.

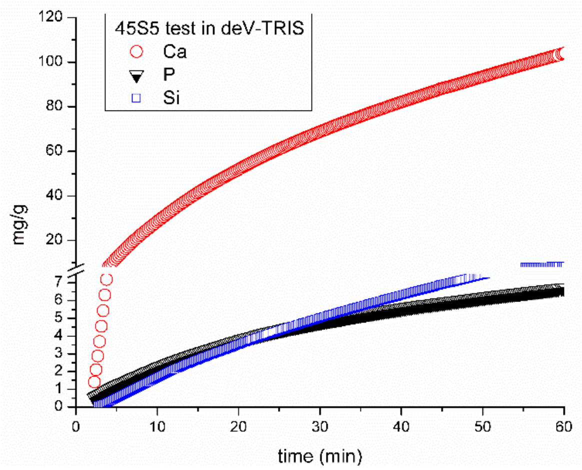

Figure 2: Dissolution of 45S5 expressed in terms of release Ca and P in deionized water buffered with TRIS.

CONCLUSIONS

The early stage dissolution of Bioglass could be reliably monitored starting from 2 min of the test, taking into account the retention time of sample and fluid as well filling up the tubing system, before the solution is nebulized and aspirated to plasma. Limits of quantification for considered therapeutic ions (Co, Cu, Sr, Zn) in SB fluid were determined <0.08 mg/L with precision <5%. In SBF the release of calcium from dissolved 45S5 glass material can be evaluated with respect to bioactivity in terms of cumulative normalized amounts. However the flow through tests performed in deionized water buffered with TRIS with direct determination of ion release are more reliable in order to assess the kinetics in early stage of dissolution for strongly bioactive materials in contact with the SB fluid.

ACKNOWLEDGMENT

This paper is a part of dissemination activities of project FunGlass. This project has received funding from the European Union´s Horizon 2020 research and innovation program under grant agreement No 739566.

REFERENCES

[1] Kokubo T, Ito S, Shigematsu M, Sakka S, Yamamuro T. Fatigue and life-time of bioactive glass-ceramic A-W containing apatite and wollastonite, J Mater Sci 22, 4067–70, 1987

[2] Kokubo T, Takadama H. How useful is SBF in predicting in vivo bone bioactivity? Biomaterials 27, 2907-15, 2006

[3] The International Standard ISO/ 23317:2007, Implants for surgery – In vitro evaluation for apatite-forming ability of implant materials

[4] Hench, L.L., Splinter, R.J., Allen, W.C. Bonding mechanisms at the interface of ceramic prosthetic materials, J.Biomed. Mater. Res. 5 (1971) 117-141

[5] Bohner M., Lemaitre J., Can bioactivity be tested in vitro with SBF solution, Biomaterials 30: 2175-2179, 2009

[6] Rohanova D., Boccaccini A.R., Yunos D.M., Horkavcová D., Brezovská I., Helebrant A., TRIS buffer in simulated body fluid distorts the assessment of glass–ceramic scaffold bioactivity, Acta Biomaterialia 7 2623–2630, 2011

[7] Fagerlund S., Ek P., Hupa L., Hupa M., Dissolution kinetics of a bioactive glass by continuous measurement, J. Am. Ceram. Soc. 95 [10] 3130-3137, 2012

BIOLOGICKÉ VLASTNOSTI KERAMIKY NA BÁZE SI_3N_4 PO OPRACOVANÍ POVRCHU KYSLÍKOVO-ACETYLÉNOVÝM PLAMEŇOM

BIOPROPERTIES OF Si_3N_4 - BASED CERAMICS AFTER OXY-ACETYLENE FLAME TREATMENT

M. Hičák[1], M. Hnatko[1, 4], M. Labudová[2], D. Galusková[3], J. Sedláček[1], Z. Lenčéš[1], P. Šajgalík[1]

[1]*Institute of Inorganic Chemistry, Slovak Academy of Sciences, Dúbravská cesta 9, 842 36 Bratislava, Slovakia*
[2]*Biomedical Research Center of the Slovak Academy of Sciences, Dúbravská cesta 9, 84505 Bratislava, Slovakia*
[3] *Centre for Functional and Surface Functionalized Glass, TnU AD, Študentská 2, 911 50 Trenčín, Slovakia*
[4] *Centre of Excellence for Advanced Materials Application, Slovak Academy of Sciences, Dúbravská cesta 9, 84511, Bratislava, Slovakia*

ABSTRACT

Silicon nitride-based ceramics with SiO_2, CaO and $Ca_3(PO_4)_2$ as sintering additives, have been prepared in order to study the bioactivity. Dense ceramic bodies were oxidized by an oxy-acetylene flame at approx. 1475°C for 60 seconds, in order to modify the surface in terms of bioactivity enhancement and the formation of optimal porosity for cell viability. The best bioactivity was obtained for oxy-acetylene flame treated Si_3N_4 ceramics with $Ca_3(PO_4)_2$ sintering additive.

Keywords: silicon nitride, surface modification, flame oxidation, bioactivity

INTRODUCTION

Silicon nitride-based ceramics are characterized by high chemical resistance and a superior combination of fracture toughness, strength, hardness, tribological and thermomechanical properties. These features are not only important for engineering applications such as cutting tools, ball bearings, sealing elements, engine components, etc., but they are also attractive for medical applications such as implants in the human body [1-2]. Owing to the biocompatibility of Si_3N_4 ceramics there is a wide range of bio-applications of Si_3N_4 ceramics. However, the majority of biological applications require not only biocompatibility but also bioactivity, which results in the formation of good bonding between tissues and the implanted material [3].

The mechanical properties of a biomaterial are mainly governed by the bulk of the material, while the bioactivity is determined by the surface properties. Therefore, the enhancement of the bioactivity of bioinert material requires some modifications of the surface to enable the host tissue to interact with the implant. Bio-coatings are applied by a variety of surface engineering techniques, such as thermal spraying (plasma spraying, high velocity oxy-fuel coating, cold spraying etc.), pulsed laser deposition (PLD), chemical and physical vapour deposition (CVD and PVD), ion beam sputtering, electrophoretic deposition, radio frequency magnetron sputtering, and sol-gel techniques [4]. As the compatibility of bioactive hydroxyapatite (HAP) is better with oxide ceramics compared to nonoxides, also the high temperature oxidation can be used for the surface modification of non-oxide ceramics instead of laborious coating.

Si_3N_4 is thermodynamically unstable in an oxidizing atmosphere at high temperatures (T > 1100 °C). Oxidation of Si_3N_4 grains causes the formation of a silica layer. This intergranular silica-based glassy phase, when molten, serves as a path for outward diffusion of cations (such as cations deriving from sintering aids or impurities) and inward diffusion of oxygen [5-9]. The surface of Si_3N_4 grains is covered by this protective silica layer and grain boundary species, which can form either amorphous or crystalline phases adjacent to the silicon nitride bulk [10-12]. Bock et al. prepared a bioactive Si_3N_4 with Y_2O_3 and Al_2O_3 sintering additives by heat-treatment of this material in N_2 atmosphere [13]. Si-Y-Al-O-N compounds formed by the migration of grain-boundary phase to the surface, which exhibited improved bone healing capacity [14]. Very similar processes occur in a short timeframe during the ablation and oxidation tests of ultrahigh temperature ceramics by oxyacetylene torch with a flame temperature of about 3000°C [15-16].

This paper deals with the characterization of oxidized surface layer on Si_3N_4-based ceramics using an oxyacetylene torch flame. The chemistry of the surface layers will be controlled by the composition of the sintering additives used for the preparation of Si_3N_4-based ceramic substrates. The cell viability and bioactivity of the flame-treated materials will be tested in simulated body fluid (SBF).

EXPERIMENTAL

Preparation of dense Si3N4 substrates

The ceramic substrates were prepared using a commercial Si_3N_4 powder (grade SN-E10, >95% α-Si_3N_4, d_{50} = 0.5 µm, 1.3 wt.% O, Ube Industries Ltd., Japan) and SiO_2 (SSA. = 50 m2·g^{-1}, Aerosil OX-50, Degussa, Germany), together with a bioactive phase acting also as a sintering aid, either CaO or $Ca_3(PO_4)_2$ (p.a. purity, both produced by Lachema, Czech Republic). The chemical compositions of the initial powder mixtures are given in Table 1.

Table 1: Chemical compositions of the initial powder mixtures and sintering temperatures.

Sample	Si_3N_4 (wt.%)	SiO_2 (wt.%)	CaO (wt.%)	$Ca_3(PO_4)_2$ (wt.%)	sintering *T* (°C)
SNSi	90	10	-	-	1750
SNSiCa	90	6.4	3.6	-	1600
SNCaP	90	-	-	10	1630

Samples with a diameter of 20 mm and height of approx. 5 mm were prepared by hot pressing at temperatures between 1600°C and 1750°C (Table 1) applying a pressure of 30 MPa for 60 min under nitrogen atmosphere. The relative densities of the prepared samples, determined using the Archimedes method, were above 97 % of the corresponding theoretical density. The sample surfaces were grinded (80 µm → 15 µm) and polished with diamond suspensions (9 µm → 1 µm) to mirror finish. An oxyacetylene torch flame with constant O_2:C_2H_2= 1:1.1 ratio was used for thermo-oxidative treatment of Si_3N_4 substrate surfaces for 60 sec. The sample surface temperature was kept at approx. 1475°C, measured with an optical pyrometer, and controlled by changing the distance between the nozzle tip of the burner and the surface. Microstructure and the chemical composition of the surface and cross sections were characterized by scanning electron microscopy attached with X-ray spectrometers (JEOL JSM-7600 F/EDS/WDS/EBSD). The phase composition was determined by X-ray diffraction analysis (Bruker AXS D8 Discover, CuK_α radiation) and low angle grazing incidence X-ray diffraction (GIXD) technique at $\alpha = 6°$. The detailed preparation of Si_3N_4-based substrates is described in [17].

Viability assay

Human pulmonary fibroblast cells MRC5 (ATCC®; CCL17™) were used for all the biocompatibility assays as they are approved by the International Organization for Standardization (ISO) for tests of *in vitro* cytotoxicity (ISO10993-5:2009). The cells were cultured in a complete Dulbecco´s modified Eagle´s medium (DMEM, Lonza, Belgium) with 2 mM of L-glutamine supplemented with 10% fetal bovine serum (Lonza) and 160 µg/ml gentamicine (Lek, Slovenia) at 37°C under humidified air atmosphere containing 5% CO_2. The conditions were kept constant for cultivation of cells on ceramics.

Prior to analysis with a polarization microscope, samples were stained with Briliant Blue R (Merck, Darmstadt, Germany) in 70% ethanol for 20 min at room temperature and washed in a physiological buffer.

The viability tests were performed on sterilized samples. The steam sterilization was carried out at 120°C for 20 min after 24 hours of incubation at 37°C under humidified air and 5% CO_2 atmosphere in an appropriate volume of DMEM cultivation medium (keeping the ratio of 1 ml of DMEM to 100 mg of sample). After the separation of DMEM an extract was obtained. Meanwhile, 5000 MRC5 cells were seeded in a 96-well plate in four parallel replicas and incubated at the same conditions for 24 hours. After 24 hours, 100 µl of ceramic extract per well was added to the cells. The viability was assessed with a CellTiter Blue® viability assay (Promega, Madison WI, USA). The assay is based on the ability of living cells to convert a redox dye (resazurin) into a fluorescent end product (resorufin). Therefore, 20 µl of CellTiter Blue® solution was added to the cells with 100 µl of medium and further incubated at 37°C and 5% CO_2 for 3 hours. The fluorescence was measured at A590 on a Synergy Multi-mode reader (BioTek). The average fluorescence value of the culture medium was subtracted from the average fluorescence values from four parallel lines of experimental wells. The percentage of the viability was assessed against control cells. For significance evaluation the Student's *t*-test was used and values of $p < 0.05$ were considered as significant. Two more ceramic extracts (referred to as the 2nd and 3rd extracts) from the same sample were analysed under the same conditions, to see if extensive washing of the biomaterial would improve the effect on the biological properties of the cells.

The real-time cell analysis method (RTCA), a method for non-invasive measurement of electrical impedance, was used to determine the proliferation of the cells in the presence of the studied material using an xCELLigence RTCA instrument (ACEA Biosciences Inc., USA). Either extract or control media, 100 µl in volume was added into each well of the 96-well E-plate and the background was measured. Then 5000 MRC5 cells in 100 µl of extract or media were added and the cell impedance was measured every 15 min for 95 h. Each measured extract and control media were analysed at least four times. The cell proliferation and the doubling time were evaluated by the RTCA software.

Bioactivity determination

The *in vitro* bioactivity of the samples was determined using a procedure described in detail by Kokubo et al. [18]. The samples were inserted into prepared SBF with a pH value of 7.32 and left in an incubator for four weeks at a constant temperature (36.5 ± 0.1°C). The SBF solution had a similar composition and component concentrations to those of human plasma. The ionic concentration of used SBF (in mM) is as follows: Na^+: 142.0; K^+: 5.0; Ca^{2+}: 2.5; Mg^{2+}: 1.5; Cl^-: 148.8; HCO^{3-}: 4.2; HPO_4^{2-}: 1.0; SO_4^{2-}: 0.5. The soaking period was 21 days. After soaking, the specimens were removed from the fluid, washed with distilled water and the surfaces were studied by SEM (JEOL JSM-7600). The ionic concentrations of Ca^{2+} and PO_4^{3-} ions in the SBF after soaking were determined using an optical emission spectrometer with inductively coupled plasma ICP OES (5100 SVDV ICP-OES, Agilent), as the bioactivity can be proven by the formation of hydroxyapatite (HAP). The formation of HAP is accompanied by decreased concentration of Ca^{2+} and PO_4^{3-} ions in SBF solution after leaching.

RESULTS

The substrate surfaces after thermal treatment with acetylene-oxygen flame

The substrate surfaces after thermal treatment with acetylene-oxygen flame (C_2H_2: O_2 ratio 1.1:1) at 1475°C ± 25°C for 60 s are shown in Fig. 1. The flame exposed front faces of the substrates were covered by a strongly bonded oxide layer. The substrate surfaces are eroded and have a porous structure (Figs. 1A-C). Less erosion was observed on the SNSi sample surface, because this system contains SiO_2 with a melting point of 1660°C, above the flame temperature, as well as Si_2N_2O (Table 2), exhibiting a very good oxidation resistance up to 1400°C [19].

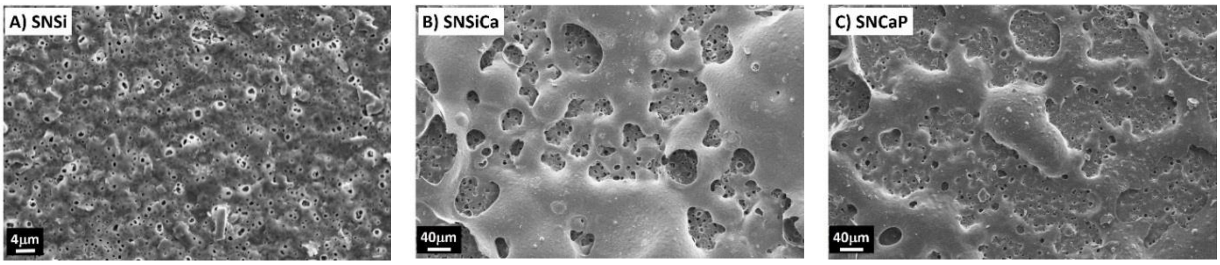

Figure 1: Structures of substrate surfaces after oxy-acetylene flame treatment.

The surface of SNSiCa sample is different from that of SNSi after the thermal treatment, showing an erosion in evidently different manner. The image magnification of Fig. 1A is 10× higher than Fig. 1B, as the surface damage of the SNSi substrate was not sufficiently visible and higher magnification was needed. This was not the case for substrate SNSiCa after flame oxidation. CaO itself has a high melting temperature (2572°C), but in the system CaO-SiO_2 the lowest melting point is 1437°C for the molar eutectic composition $CaO/SiO_2 = 0.61$. The flame temperature was high enough to melt this eutectic mixture. The temperature gradient from the flame exposed surface to the center of samples caused the migration of grain boundary phase, enhanced by capillary forces, to the surface of substrate.

This motion results in the formation of large oxide phase droplets, which become interconnected on the SNSiCa substrate surface (Fig. 1B). The surface topology of sample SNCaP (Fig. 1C) is similar to that of SNSiCa, large interconnected droplets and the porous nature of the surface are clearly visible.

Low angle GIXD analysis of substrate surfaces after flame thermal treatment

The phase composition of the oxy-acetylene flame treated surface layers was also investigated by the low angle grazing incidence X-ray diffraction technique at α = 6° and the results are summarized in Table 2. In the case of SNSi and SNSiCa samples, the phase composition did not change compared to the “bulk” XRD analysis of the substrates, only the portion of oxide phases (Si_2N_2O and SiO_2) was higher compared to Si_3N_4 (roughly 60% : 40%). In the diffractograms of SNSiCa and SNCaP also a remarkable hump was observed in the range $2\theta = 17° - 30°$ (Fig. 2), showing the presence of SiO_2-based amorphous phase.

The surface layer of SNSiCa sample contains except of amorphous phase (~15 %) also crystalline Si_2N_2O and β-Si_3N_4 major phases and SiO_2, $CaSiO_3$ (< 5%) minor phases.

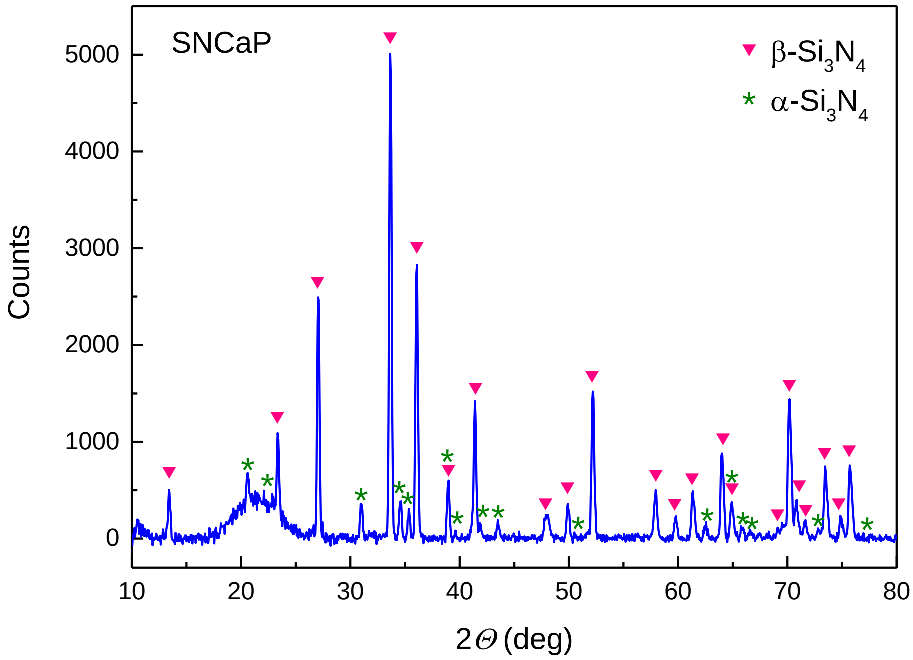

Figure 2: Low angle (α= 6°) GIX diffraction pattern of SNCaP sample.

The surface layer of the SNCaP sample contains the starting Si_3N_4 and minor $CaSiO_3$ and SiO_2 crystalline phases. Similar to SNSiCa, also this case a hump was observed in the diffraction pattern, indicating the presence of silica-based amorphous phase. A weak diffraction of CaO were identified by the High Score Plus software, but the intensities were close to the noise of background, therefore it is difficult to determine the quantity (<3%). Also in this case, like in the bulk XRD analysis, the presence of $Ca_3(PO_4)_2$ was not confirmed. The $Ca_3(PO_4)_2$ phase added to the starting mixture most probably dissociates under the oxyacetylene flame treatment through C_2P, CP, C_2P_3, CP_2 (where C = CaO, P = P_2O_5) to P_2O_5 and CaO.

The EDX analysis of sample surface showed a relatively high phosphorus content (13.7 wt.%, Table 3), therefore it should be present also in the amorphous phase.

Table 2: Phase composition of the Si_3N_4 substrate surfaces (GIXD analysis) after oxy-acetylene flame treatment, measured by the grazing incidence X-ray diffraction technique ($\alpha = 6°$).

	SNSi	**SNSiCa**	**SNCaP**
Composition:			
major phases	β-Si_3N_4, Si_2N_2O	β -Si_3N_4, Si_2N_2O, am.SiO_2	β -Si_3N_4, α-Si_3N_4, am.SiO_2
minor phases	SiO_2	SiO_2	SiO_2

Table 3: EDX analyses of Si_3N_4 substrate surfaces after dynamic flame oxidation.

Sample	C (wt.%)	O (wt.%)	Si (wt.%)	Ca (wt.%)	P (wt.%)
SNSi	7.9±0.3	51.2±1.6	40.9±1.4	-	-
SNSiCa	6.0±0.2	51.1±1.5	37.2±1.1	5.7±0.3	-
SNCaP	8.2±0.3	52.9±1.9	10.6±0.9	14.6±0.8	13.7±0.9

The nature of the porous surface layers prepared by oxy-acetylene flame is significantly different to that of layers prepared by traditional techniques such as PVD, CVD, dip-counting, etc. The bonding of the prepared surface layers is stronger, without any spallation. This very fast method can be applied either to the modification of ceramic surfaces (flame exposition only for seconds), or Si_3N_4-based granules of diameter 50 – 200 µm used as a filler in bone cement (kilograms of granules per day).

Biological properties of thin layers

The cell viability (i.e. their ability to proliferate and thrive under certain conditions) was determined using the standard method. The health of the cells is shown by measuring the markers of cellular activity. A cell culture in the presence of non-cytotoxic material will exhibit good viability, usually above 80%. All the substrates prepared in the present study were non-cytotoxic with viability values above 97% in the second and third extracts (Fig. 3).

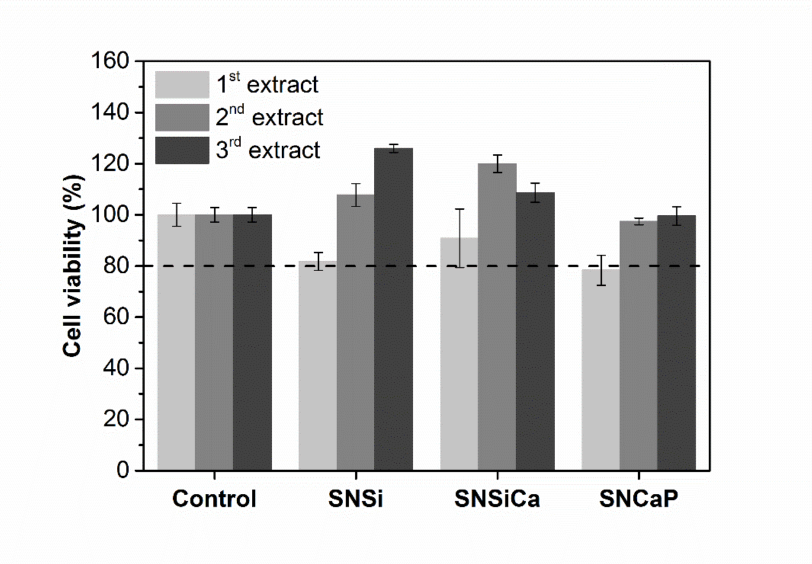

Figure 3: Cell viability assay - the percentage of cell viability of MRC5 cells grown on the flame treated Si3N4-based substrates (SNSi, SNSiCa, SNCaP), extracts after 24 hours.

The first extracts of all the tested ceramic substrates showed lower viability than the control sample (i.e. pure SBF, without ceramics). The lowest viability was 78%, measured for the substrate SNCaP. However, after additional extractions, the viability of the cells in this particular case increased to 97% (Fig. 3). The MRC5 human fibroblast cells were able to grow on all the tested substrates, as it is shown in Fig. 4.

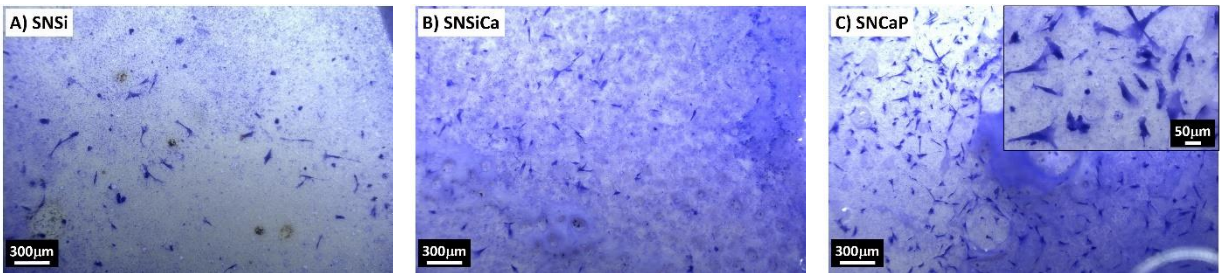

Figure 4: Growth of the MRC5 cells on Si3N4-based substrates (SNSi, SNSiCa and SNCaP) for a period of one week and analyzed by polarization microscope.

The highest amount of cells grew on the material containing Ca and P, while the lowest population of cells was determined on the SNSi substrate. As it was mentioned in the experimental part, the results of control vs. samples were analysed with two-tailed unpaired t-test (Student's test) with a threshold $P < 0.05$ considered for statistical significance. The results are summarised in Table 4 and show a significant difference from the control for samples SNSi and SNCaP.

Table 4: Student's t-tests for the cell proliferation and doubling time of the MRC5 cells on the Si_3N_4-based substrates ($P < 0.05$ is considered as significant difference).

	Cell proliferation			Doubling time		
sample	**SNSi**	**SNSiCa**	**SNCaP**	**SNSi**	**SNSiCa**	**SNCaP**
P	0.0084	0.1107	0.0001	0.0397	0.5200	0.0249
significance	*	ns	*	*	ns	*

* means significant, ns = non significant

Despite this, the growth of the cells was slower, with a doubling time 1-3 hours longer, than for the control (Fig. 5). However, the preparation of ceramic substrates/implants for bio-applications by flame treatment seems to be a very promising and economic method.

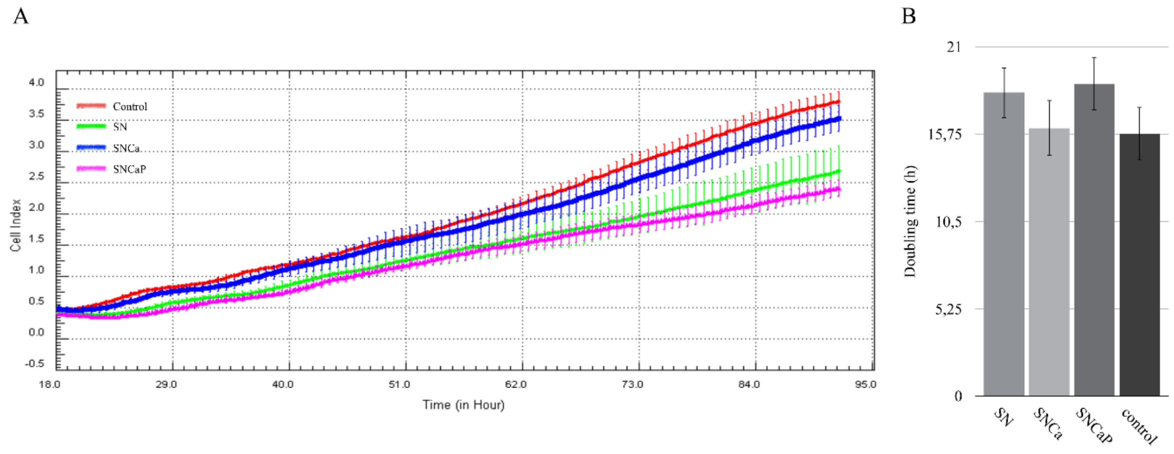

Figure 5: Cell proliferation and doubling time of the MRC5 cells on the Si_3N_4-based substrates (SNSi, SNSiCa, SNCaP). The extracts were monitored by Real Time Cell Analysis (RTCA, xCELLigence software) for 95 hours.

Assessment of bioactivity behaviour

In order for porous bioceramics to be bioactive, the formation of interfacial bond with a surrounding tissue must be possible. Growth of hydroxyapatite (HAP) on the ceramic surface after lengthy submersion in simulated body fluid (SBF) is an indirect indicator of bioactive behaviour. The SBF system is metastable solution supersaturated with respect to apatite [18], and it is a matter of time, when it becomes thermodynamically stable by forming apatite crystals. The addition of an at least partially soluble solid to the SBF can modify the solution composition in a way favouring apatite formation. It is actually quite difficult in a laboratory to prepare pure calcium hydroxyapatite, idealized as $Ca_{10}(PO_4)_6(OH)_2$, by soaking the substrate in simulated body fluids. There are several calcium phosphate phases like HAP, dicalcium phosphate dihydrate, tricalcium phosphate and octacalcium phosphate, which are frequently encountered, depending on pH, ionic strength and the partial pressure of CO_2 [20]. However, the identification of the phase composition of the formed surface layer is rather difficult. Precipitation reactions can result in the initial formation of an “amorphous calcium phosphate” having an apatitic short-range structure, but with a crystal size so small to appear amorphous in XRD analysis [21]. Change in the concentrations of Ca^{2+} and PO_4^{3-} ions in the solution detected after exposure of the substrate to the SBF solution could indirectly prove the formation of HAP or some other phase with an apatitic structure. The stoichiometric molar ratio of calcium to phosphorus required for the thermodynamically favoured formation of HAP is 1.67. The solution used for immersion tests had a Ca/P ratio of around 1.9. Significant changes in the concentrations of Ca^{2+} and PO_4^{3-} ions in the solution were not observed in SBF after 21 days immersion of SNSi sample (Fig. 6). No newly formed phases or visible changes in the surface microstructure were detected by SEM analysis. It can be concluded that the addition of SiO_2 does not result in a formation of bioactive surface layer on the oxyacetylene flame treated Si_3N_4-based substrate.

However, the Ca/P ratio does increase, and indicators of bioactivity are seen, for the SNSiCa and SNCaP samples. These materials release the Ca^{2+} ions into solution, while the amount of PO_4^{3-} ions in solution decreases. In calcium-rich aqueous solutions with Ca/P molar ratios of 1.8-2.5 the formation of HAP can occur through initial formation of amorphous calcium phosphate [21]. Small precipitates of HAP were detected on the surface and in the pores of the SNSiCa sample (arrows in Fig. 7B). The micrograph of the SNCaP sample (Fig. 7C) shows the evidence of larger globular precipitates assembled into an almost compact layer. In addition, the Ca/P ratio in the SBF remarkably increased compared to the SNCa sample (Fig. 6), but presently there is no clear explanation for this effect. More detailed observation of the globular aggregates in Fig. 7C revealed that they consist of acicular, needle-like crystals of nanoscale dimensions (Fig. 8), the structure typical for HAP [18]. Finally, it can be concluded from the preliminary bioactivity tests (21 days) that the oxy-acetylene flame pre-treatment of Si_3N_4–based substrates, together with the incorporation of Ca and P containing sintering additives into the ceramics matrix, boost the bioactivity of this kind of ceramics.

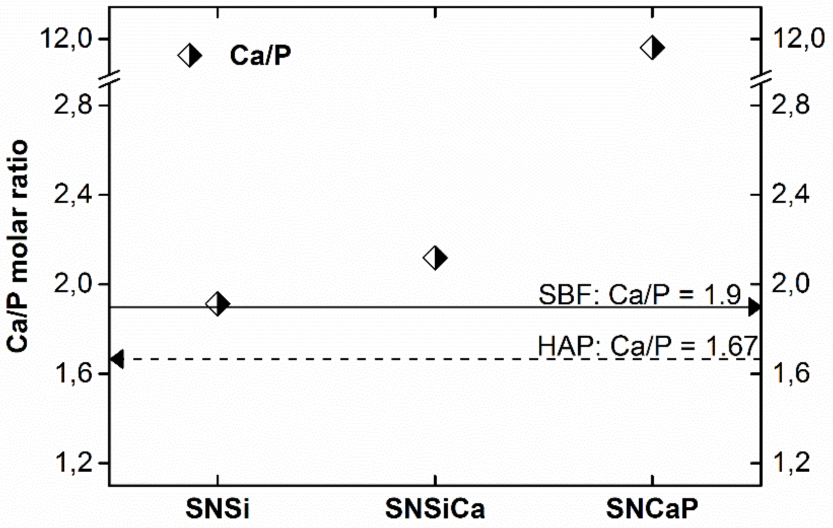

Figure 6: Evolution of the molar Ca/P ratio in SBF solution after 21 days soaking of samples in SBF (in the starting SBF solution the Ca/P ratio was 1.9, the stoichiometric ratio in HAP is 1.67).

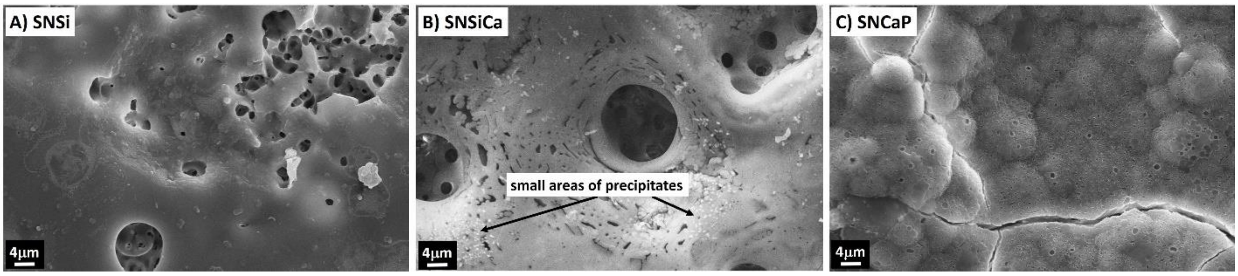

Figure 7: SEM analysis of the surfaces after bioactivity test in SBF for 21 days at 36.5°C.

Due to the nature of the biological SBF solution prepared in laboratory conditions, more attention must be paid to the fate of the calcium released from the biomaterial into SBF solution. The involvement of TRIS (tris-hydroxymethyl aminomethane) in SBF can act not merely as a buffer but as a complexing agent with various cations including Ca^{2+}. This is in addition to the proteins naturally present in serum that might play an essential role in controlling apatite nucleation. These issues, together with pH and ionic strength of solution, need to be addressed in any future bioactivity testing which relies on the formation of HAP.

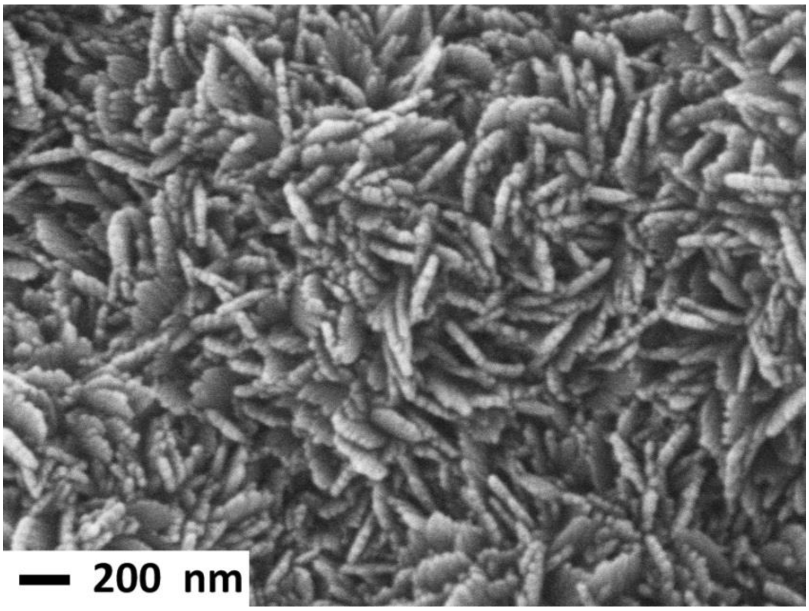

Figure 8: Detailed view of nanoscale crystals grown from globular clusters on the SNCaP.

CONCLUSIONS

Dense silicon nitride materials with different sintering additives of SiO_2, SiO_2 + CaO, and $Ca_3(PO_4)_2$ were prepared by hot-pressing method. The surfaces of the Si_3N_4-based substrates were covered after oxy-acetylene flame-impingement treatment at 1475°C for 60 s by porous oxide surface layer. The bioactivity tests in SBF confirmed the inert character of Si_3N_4 ceramics containing SiO_2 or SiO_2+CaO sintering additives. The surface of the SNCaP sample containing $Ca_3(PO_4)_2$ as sintering aid is bioactive, and considerable formation of HAP nanocrystals was observed on the surface after the test in SBF.

This very fast and cost-effective oxy-acetylene flame treatment method can be applied either to the modification of dense bulk ceramic surfaces, porous bodies, or Si_3N_4-based granules for bio-applications.

ACKNOWLEDGMENT

This work was supported by the Slovak Grant Agency VEGA Project No. 2/0152/18, APVV-18-0542 and MVTS - CERANEA project (in the framework of FLAG ERA II). This study was performed during the implementation of the project Building-up Centre for advanced materials application of the Slovak Academy of Sciences, ITMS project code 313021T081 supported by Research & Innovation Operational Programme funded by the ERDF.

REFERENCES

[1] B. McEntire, B. Bal, M. Rahaman, J. Chevalier, G. Pezzotti, Ceramics and ceramic coatings in orthopaedics. J. Eur. Ceram. Soc. 35 (2015) 4327–4369. https://doi.org/10.1016/j.jeurceramsoc.2015.07.034

[2] G. Pezzotti, E. Marin, T. Adachi, A. Rondinella, F. Boschetto, W. Zhu, N. Sugano, R. M. Bock, B. McEntire, S. B. Bal, Bioactive silicon nitride: A new therapeutic material for osteoarthropathy. Sci. Rep.-UK 7 (2017) 44848. https://doi.org/10.1038/srep44848

[3] L.L. Hench, O. Andersson, Bioactive glasses, in: L.L. Hench (Ed.), An Introduction to Bioceramics, 2nd ed., Imperial College Press, London, 2013. p. 49.

[4] R.B. Heimann, H.D. Lehmann, Bioceramic coatings for medical implants. Wiley-VCH, Weinheim, 2015. https://doi.org/10.1002/9783527682294

[5] V. Medri, M. Bracisiewicz, K. Krnel, F. Winterhalter, A. Bellosi, Degradation of mechanical and electrical properties after long-term oxidation and corrosion of non-oxide structural ceramic composites, J. Eur. Ceram. Soc. 25 (2005) 1723-1731. https://doi.org/10.1016/j.jeurceramsoc.2004.12.002

[6] R. Klein, V. Medri, M. Desmaison Brut, A. Bellosi, J. Desmaison, Influence of additive content on the high temperature oxidation of silicon nitride-based composites, J. Eur. Ceram. Soc. 23 (2003) 603-611. https://doi.org/10.1016/S0955-2219(02)00376-X

[7] M. Bracisiewicz, V. Medri, A. Bellosi, Factors inducing degradation of properties after long term oxidation of Si3N4-TiN composites , Appl. Surf. Sci. 202 [3-4] (2002) 139-149. https://doi.org/10.1016/S0169-4332(02)00498-1

[8] S. Guicciardi, C. Melandri, V. Medri, A. Bellosi, Effect of thermal treatments on properties of a Si3N4-TiN composite, Mat. Sci. Eng. A Struct. 360 [1-2] (2003) 35-45. https://doi.org/10.1016/S0921-5093(03)00501-X

[9] V. Medri, A. Bellosi, Factors inducing degradation of properties after long-term oxidation of Si3N4–MoSi2 electroconductive composites, J. Mater. Res. 19 [5] (2004) 1567-1574. https://doi.org/10.1557/JMR.2004.0210

[10] X. Pan, Atomistic structure of silicon nitride/silicate glass interfaces, J. Am. Ceram. Soc. 79 (1996) 2975-2979. https://doi.org/10.1111/j.1151-2916.1996.tb08737.x

[11] J. Echeberria, F. Castro, Oxidation of silicon nitride sintered with ceria and alumina, Mater. Sci. Tech. Ser. 6 (1990) 497-503. https://doi.org/10.1179/mst.1990.6.6.497

[12] S.K. Biswas, J. Mukerji, P.K. Das, Oxidation of silicon nitride sintered with yttria and magnesia containing nitrogen rich liquid, Key Eng. Mat. 89–91 (1994) 271–274. https://doi.org/10.4028/www.scientific.net/KEM.89-91.271

[13] R.M. Bock, B.J. McEntire, B.S. Bal, M.N. Rahaman, M. Boffelli, G. Pezzotti, Surface modulation of silicon nitride ceramics for orthopaedic applications, Acta Biomater. 26 (2015) 318-330. http://dx.doi.org/ 10.1016/j.actbio.2015.08.014

[14] G. Pezzotti, R.M. Bock, T. Adachi, A. Rondinella, F. Boschetto, W. Zhu, E. Marin, B. McEntire, B.S. Bal, O. Mazda, Silicon nitride surface chemistry: A potent regulator of mesenchymal progenitor cell activity in bone formation, Appl. Mater. Today 9 (2017) 82-95. http://dx.doi.org/10.1016/j.apmt.2017.05.005

[15] C. Vix-Guterl, C. Grotzinger, J. Dentzer, M. P. Bacosb, P. Ehrburger, Reactivity of a C/SiC composite in water vapour, J. Eur. Ceram. Soc. 21 (2001) 315-323. https://doi.org/10.1016/S0955-2219(00)00207-7

[16] E.L. Corral, L.S. Walker, Improved ablation resistance of C–C composites using zirconium diboride and boron carbide, J. Eur. Ceram. Soc. 30 (2010) 2357-2364. https://doi.org/10.1016/j.jeurceramsoc.2010.02.025

[17] M. Hičák, M. Hnatko, M. Labudová, D. Galusková, J. Sedláček, P. Šajgalík, Surface modification of Si3N4 by oxyacetylene torch – influence of grain boundary composition, Processing and properties of advanced ceramics and glasses, Stará Lesná - High Tatras, Slovakia, October 29 - 31, 2018 : conference proceedings, p. 64-71. ISBN 978-80-89782-10-9.

[18] T. Kokubo, H. Takadama, How useful is SBF in predicting in vivo bone bioactivity?, Biomaterials 27 (15) 2006. 2907-2915. https://doi.org/10.1016/j.biomaterials.2006.01.017

[19] J. Persson, P.-O. Kall, M. Nygren, R. Larker, Oxidation studies of Si2N2O, in: R. Carlsson et al. (eds.), 4th Int. Symposium on Ceramic Materials and Components for Engines, Elsevier Science Publ., MPA Stuttgart, 1992, pp. 1187-1194.

[20] M. Bohner, J. Lemaitre, Can bioactivity be tested in vitro with SBF solution?, Biomaterials 30 (2009) 2175-2179. https://doi.org/10.1016/j.biomaterials.2009.01.008

[21] L. Wang, G. H. Nancollas, Calcium orthophosphates: crystallization and dissolution, Chem. Rev. 108 (2007) 4628-4669. https://doi.org/10.1021/cr0782574

PÓROVITÉ BIOAKTÍVNE SKLENÉ MIKROGUĽÔČKY PRIPRAVENÉ PLAMEŇOVOU SYNTÉZOU

POROUS BIOACTIVE GLASS MICROSPHERES PREPARED BY FLAME SYNTHESIS

J. Kraxner[1], M. Michalek[1], A. R. Romero[2], H. Elsayed[2], E. Bernardo[2] and D. Galusek[3]

[1] *FunGlass, Alexander Dubček University of Trenčín,Trenčín, Slovakia*
[2] *Department of Industrial Engineering, Università degli Studi di Padova, Padova, Italy*
[3] *Joint glass centre of the IIC SAS, TnUAD, and FChFT STU, FunGlass, Alexander Dubček University of Trenčín, Trenčín, Slovakia*

ABSTRACT

Low cost processing method to prepare porous bioactive glass (BG) microspheres is presented. Glass powder with composition based on 45S5 BG and exhibiting irregularly shaped particles was fabricated by conventional melting. Glass powder was alkali activated to induce pore formation during the following flame synthesis step. Porous microspheres, with diameters ranging between 45 and 75 µm, were successfully prepared and characterized by X-ray diffraction, Fourier-transform infrared spectroscopy, and scanning electron microscopy with energy-dispersive X-ray spectroscopy. The porous bioactive glass microspheres are promising candidates for applications in bone regeneration, tissue engineering, and as carriers for controlled drug delivery.

Keywords: Bioactive glass, porous microspheres, alkaline activation, flame synthesis.

INTRODUCTION

The field of inorganic bioactive materials started in 1971 with the discovery of 45S5 bioactive glass (BG) by Hench et al. [1]. It is a special composition of silicate glass containing 45% SiO_2, 24.5% CaO, 24.5% Na_2O, and 6% P_2O_5, in wt.% (Table 1). Bioactive glass is able to bond to bone tissue and stimulates bone regeneration by the release of Si, Ca, P ions [2, 3]. Due to the low specific surface area, and the lack of microporosity, the bioactivity of melt-derived glasses mainly depends on the SiO_2 content [4]. Microspheres possess several advantages compared to irregularly shaped materials; therefore, they have become important in many scientific fields, including biomaterials. They can be engineered and manufactured to be solid, hollow, or porous, which provides a larger surface area allowing for sufficient therapeutic coatings, an increase in degradation rate and beneficial ion release profile [5], or encapsulation of various biomedical relevant components [6, 7]. Recently, porous calcium phosphate glass microspheres were fabricated by Hossain et al. [6] via the cost-effective flame spheroidisation process. Careful selection of the glass, pore-forming agent, and a manufacturing method with the required processing window enabled the production of porous glass microspheres via a single-stage manufacturing process. Microspheres are already exploited in the pharmaceutical and health care industry. Precise control over pore size is, however, difficult; hence, manufacturing technologies need to be improved to create reproducible porosity and pore sizes [7].

In the present study, a simple, cost-effective, and scalable method for the preparation of porous 45S5 BG microspheres is presented and discussed.

EXPERIMENTAL

Bioactive glass of 45S5 composition was prepared by mixing the analytical grade purity ($\geq$ 99 %) raw materials: SiO_2, $CaCO_3$ (Centralchem, Slovakia), Na_2CO_3 (Penta, Czech Republic), and $Na_5P_3O_{10}$ (Sigma-Aldrich, Slovakia). The mixture was then melted in Pt-10% Rh crucible in a superkanthal furnace at 1300°C for two hours in ambient atmosphere. The homogeneity was ensured by repeated hand mixing of the melt. Then the molten glass was poured onto a stainless steel plate. The sample was tempered in a muffle furnace for 30 minutes at 560°C and then the furnace was switched off. The prepared bulk glass was crushed and sieved through a 45 μm analytical sieve.

The powder was mixed into an aqueous solution containing 1 M NaOH (reagent grade, Sigma- Aldrich, UK), with a solid loading of 65 wt%. The glass powder was subjected to an alkaline attack for 1 h under mechanical stirring at 500 rpm. After alkaline activation, the obtained suspension of glass powders, subjected to surface dissolution, was cast in closed polystyrene cylindrical moulds (60 mm diameter), and cured at 75°C for 24 hours. Finally, the hardened gel was crushed and sieved through analytical sieves to obtained fraction of 45-75 μm in size.

The precursor, prepared by the alkaline activation process, was fed into an oxygen-methane torch with a vacuum powder feeder at a rate of 1.4 g/min using oxygen carrier gas. The spherical melt particles were formed in the flame with the estimated maximum temperature in the range of 1500-1600°C (which was measured in the centre of flame by a thermocouple) and then quenched by distilled water to form porous microspheres. The obtained spherical particles were separated from the distilled water by microfiltration through a ceramic filter with the pore size less than 0.3 μm. The as fabricated 45S5 BG powder, the powder after alkaline activation, and porous microspheres were subjected to Fourier-transform infrared spectroscopy (FTIR, FTIR model 2000, Perkin Elmer Waltham, MA). Alkali activated glass was investigated by thermogravimetric analysis (STA449 F1 Jupiter TG/DTA/DSC, Netzsch). The phase analysis was conducted by X-ray powder diffraction using a Bruker D8 Advance diffractometer (Germany – CuKα radiation, λ = 0.15418 nm, 40 kV-40 mA, 2θ = 10-70°, step size 0.05°, 2 s counting time). The phase identification was performed by the Match!® program package (Crystal Impact GbR, Bonn, Germany), supported by the data from the PDF-2 database (ICDD-International Centre for Diffraction Data, Newtown Square, PA). The chemical composition of the glass powder and the microspheres, and the morphology of the microspheres, were examined by scanning electron microscopy (JEOL 7600F with EDS detector).

RESULTS

Alkaline activation with sodium hydroxide as the activation agent was performed to form calcium silicate hydrates (C-S-H) at the surface of the bioactive glass powder. In general, C-S-H are well known products of alkaline attack on any CaO-rich silicate glass [8, 9]. The results of FTIR analysis of the as prepared 45S5 glass powder, alkali activated bioactive glass powder, and microspheres after the flame synthesis process are shown in Figure 1a. The visible absorption band of hydrated calcium silicate centred around 3400 cm^{-1} is attributed to O-H stretching vibrations. This band was not present in the starting glass powder or in the microspheres after the flame synthesis. The decomposition temperature of hydroxyl groups is reasonably lower than the temperature of formation of the spherical particles in the torch. Nevertheless, the time of formation of spherical particles is sufficient to remove all hydroxyl groups formed during the alkali activation: these may then act during the spheroidisation process as blowing and pore-forming agents. Minor contributions to the pore forming could be also attributed to the CO_2 release, which is demonstrated in alkali-activated glass by the presence of C=O stretching vibrations in the region around 1440 cm^{-1}. The thermal stability of the products of alkaline activation is further documented by the results of thermo-gravimetric analysis reported in Figure 1b. The main weight losses (~10.7%) appeared to occur below 500°C as a consequence of decomposition of hydrated compounds, with release of water from removal of –OH groups. Additional losses (~1.0%) at higher temperatures (500-1300°C) could originate from full decomposition of the phases developed upon activation, as previously observed for soda-lime glass [8].

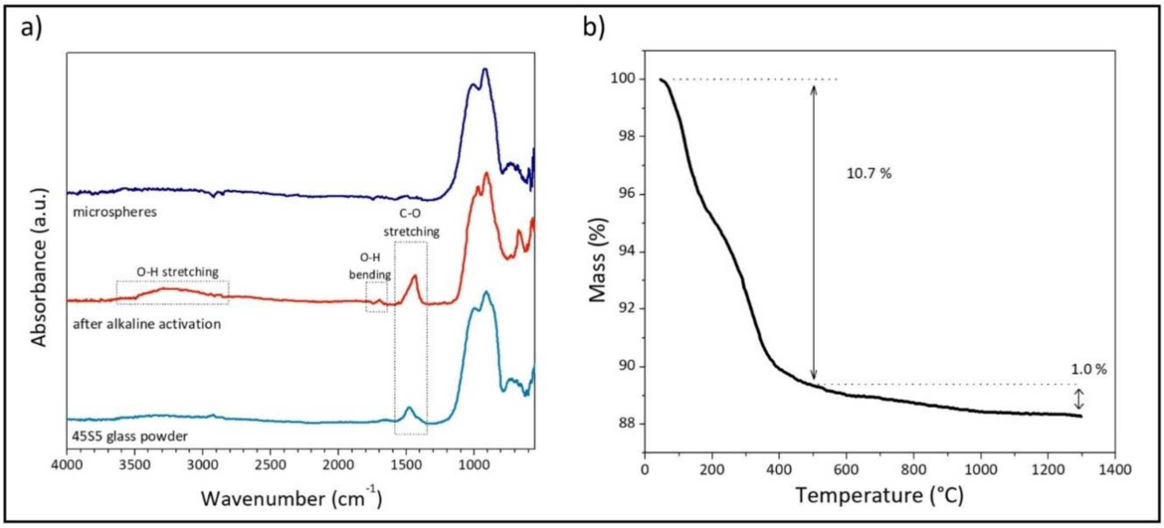

Figure 1: (a) FTIR spectra of the as prepared powder (bottom), alkali activated (middle), and after the spheroidisation process (top) and (b) thermo-gravimetric plot of alkali activated 45S5 glass.

The XRD patterns presented in Figure 2 confirm the data obtained by the FTIR analysis. The diffraction maxima attributed to calcium silicate hydrate (PDF #33-0306), natrite (Na_2CO_3, PDF #77-2082), and sodium hydrogen phosphate heptahydrate (($Na_2HPO_4.7H_2O$), PDF #71-2113) were observed and confirm the efficiency of alkaline activation.

The flame spheroidisation process led to microspheres with high content of residual glass. Observed diffraction maxima were attributed to sodium calcium silicate (combeite, $Na_{4.2}Ca_{2.8}(Si_6O_{18})$, PDF#78-1649), a common product of devitrification of 45S5 BG [101]. No traces of phases created by alkaline activation (natrite or C-S-H) are visible.

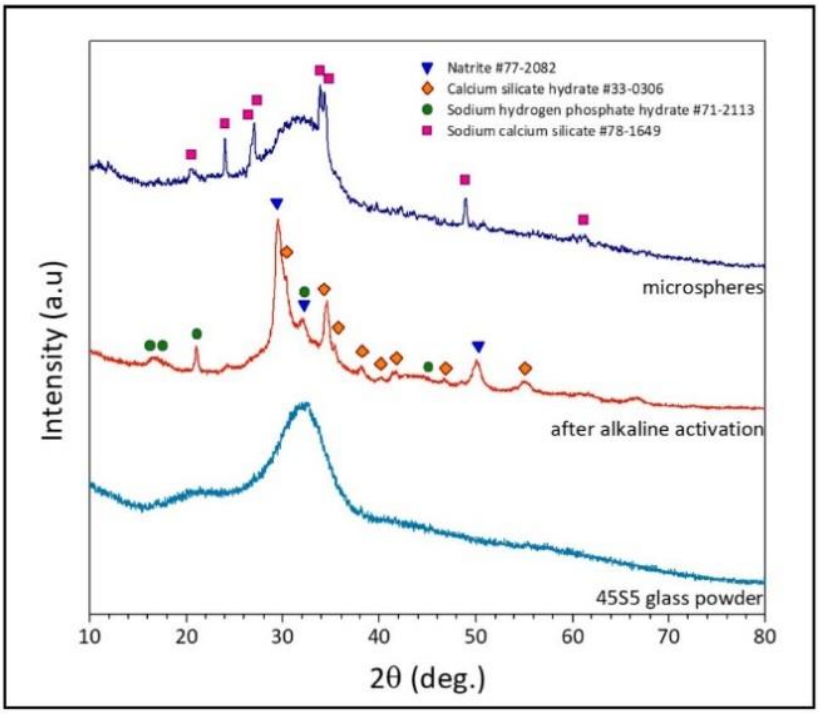

Figure 2: XRD diffraction patterns of the as prepared 45S5 glass powder, alkali activated glass powder, and microspheres.

The morphology of microspheres after flame synthesis is shown in Figure 3. Small solid particles are accompanied by bigger ones, hollow and with numerous openings in the outer walls. The pores are visible at the surface of the spheres as well as in their interior.

Effective employment of the developed porous particles obviously depends on the ability to maintain the chemical composition of 45S5 BG. The results of semi-quantitative EDS analysis performed before and after the flame synthesis are summarized in Table 1. Only slight reduction in the content of Na_2O, P_2O_5, and CaO was observed.

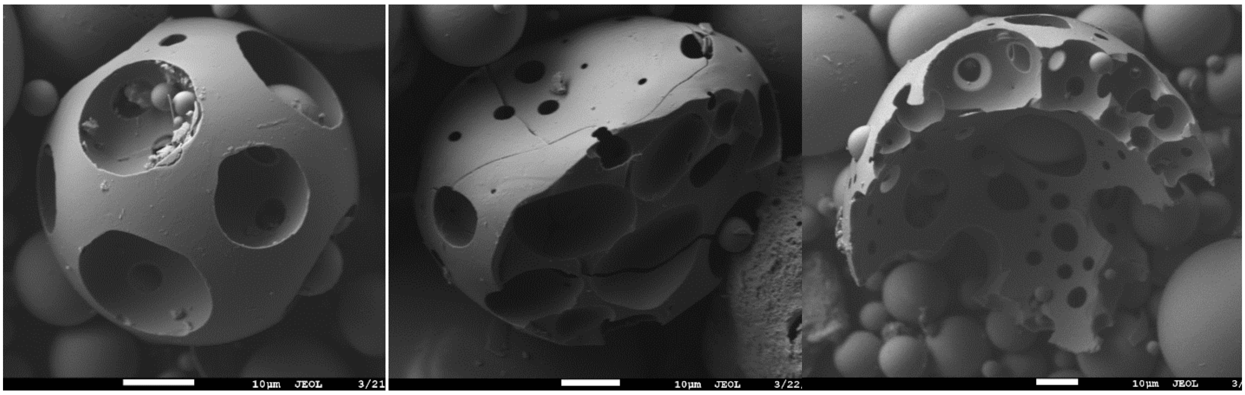

Figure 3: Morphology of the as prepared porous 45S5 BG micro-sphere particles.

Table 1: Comparison of the theoretical composition, in wt.%, of the 45S5 BG with the experimentally determined, values before, and after the flame synthesis process.

Oxide	**Na_2O**	**SiO_2**	**P_2O_5**	**CaO**
45S5 BG (theoretical composition)	24.5	45.0	6.0	24.5
45S5 glass powder (prepared by melting process)	22.9 ± 0.6	45.7 ± 0.2	5.7 ± 0.2	25.7 ± 0.2
Glass microspheres (prepared by flame synthesis)	17.0 ± 0.5	56.7 ± 0.5	4.9 ± 0.2	21.4 ± 0.8

CONCLUSIONS

To the best of our knowledge the paper presents the first successful preparation of porous bioactive glass microspheres based on 45S5 BG composition by flame synthesis process. The microspheres were prepared by alkaline activation of conventionally melted BG powder, followed by flame spheroidisation. C-S-H and natrite, formed during the alkaline activation release volatile species (water vapour and CO_2) during the flame synthesis, which act as pore forming agents yielding to porous microspheres with diameter ranging between 45 and 75 μm. Only slight reduction in the content of Na_2O, P_2O_5, and CaO was observed after the flame synthesis.

ACKNOWLEDGMENT

This paper is a part of dissemination activities of the project FunGlass. This project has received funding from the European Union´s Horizon 2020 research and innovation programme under grant agreement No 739566. Financial support of this work by the grants SAS-MOST JRP 2018/02 and VEGA 1/0098/19 is gratefully acknowledged. Discussions with Prof. Aldo R. Boccaccini, Institute of Biomaterials, University of Erlangen-Nuremberg, Germany, are acknowledged.

REFERENCES

[1] L. L. Hench, et al.: Bonding Mechanisms at the Interface of Ceramic Prosthetic Materials, Journal of Biomedical Materials Research 5 (1971) 117-141.

[2] J. R. Jones: Reprint of: Review of bioactive glass: From Hench to hybrids, Acta Biomaterialia 23 (2015) S53 S82.

[3] A. Hoppe, N. S. Guldal, A. R. Boccaccini: A review of the biological response to ionic dissolution products from bioactive glasses and glass-ceramics, Biomaterials 32 (2011) 2757-2774.

[4] C. T. Wu and J. Chang, Multifunctional mesoporous bioactive glasses for effective delivery of therapeutic ions and drug/growth factors, Journal of Controlled Release 193 (2014) 282-295.

[5] S. Li et al.: Porous-wall hollow glass microspheres as novel potential nanocarriers for biomedical applications, Nanomedicine: Nanotechnology, Biology and Medicine 6 (2010) 127–136.

[6] K. M. Z. Hossain et al.: Porous calcium phosphate glass microspheres for orthobiologic applications, Acta Biomaterialia 72 (2018) 396-406.

[7] K. M. Z. Hossain, U. Patel, I. Ahmed: Development of microspheres for biomedical applications: a review, Progress in Biomaterials 4 (2015) 1-19.

[8] A. Rincon et al.: Novel 'inorganic gel casting' process for the manufacturing of glass foams, Journal of the European Ceramic Society 37 (2017) 2227–2234.

[9] P. R. Monich et al.: Porous glass-ceramics from alkali activation and sinter-crystallization of mixtures of waste glass and residues from plasma processing of municipal solid waste, Journal of Cleaner Production 188 (2018) 871-878.

[10] P. M. Reddy et al.: Synthesis, characterization and formulation of sodium calcium silicate bioceramic for drug delivery applications, Science and Engineering of Composite Materials 23 (2014).

PRÍPRAVA POLYCAPROLKATÓNOVÝCH MEMBRÁN DOPOVANÝCH NANOČASTICAMI BIOAKTÍVNEHO SKLA PRE REGENERÁCIU TKANÍV

ELECTROSPUN POLYCAPROLACTONE MEMBRANES DOPED WITH BIOACTIVE GLASS NANOPARTICLES FOR TISSUE REGENERATION

Z. Neščáková[1], L. Liverani[2], K. Zheng[2], M. Michálek[1], D. Galusek[1], A.R. Boccaccini[2]

[1]*FunGlass - Centre for Functional and Surface Functionalized Glass, Alexander Dubček University of Trenčín, Slovakia*
[2]*Institute of Biomaterials, Department of Materials Science and Engineering, University of Erlangen-Nuremberg, Germany*

ABSTRACT

Bioactive glasses (BGs) represent a group of biomaterials with wide application possibilities in regenerative medicine. In this work, the synthesis of bioactive glass nanoparticles with further fabrication of composite membranes based on poly(ε-caprolactone) (PCL) by electrospinning method was investigated. Influence of addition of BG nanoparticles on the morphology and fiber diameter was studied.

Keywords: bioactive glass, polycaprolactone, electrospinning, fibrous composites

INTRODUCTION

Bioactive glasses (BGs) continue to attract interest for applications in hard tissue engineering for replacement, regeneration and repair bone and teeth. Their application possibilities have covered also the area of soft tissue engineering (angiogenesis, cardiac, lung, nerve, gastrointestinal tissue regeneration) and wound healing [1]. BGs are often incorporated into a polymeric matrix to produce composite which can act as a scaffold or nets for cell adhesion. Biodegradable composite offers a suitable environment for later differentiation, proliferation of the cells and stimulate direct tissue formation *in situ* [2]. Material uses for fabrication of the scaffolds and meshes is usually natural or synthetic biopolymer (polysaccharides, polyester, hydrogels, etc.). The other important component of the composite is bioactive ceramic such a calcium phosphate and bioactive glass or glass-ceramic. The common route to produce fibrous scaffolds and meshes is through electrospinning which uses an electrical charge to draw very fine fibres via a spinning jet from a liquid or sol [3]. BGs incorporated in a polymeric composite could release ionic products in sustained and controlled manner which could be used as a carrier for drugs and molecules delivery. Polymer/BGs fibrous composites meshes can be applied as a multifunctional scaffold in hard and soft tissue applications [4].

The main aim of this work is synthesis of bioactive glass particles, which are subsequently incorporated to PCL-fibres to create multifunctional membranes for tissue regeneration.

EXPERIMENTAL

Bioactive glass powder synthesis

Bioactive glass nanoparticles (BGNs) based on binary system SiO_2-CaO were synthesized by using a microemulsion-assisted sol-gel approach [5]. Briefly, hexadecyltrimethylammonium bromide (CTAB) was dissolved in deionized water. Subsequently, ethyl acetate was slow poured into the solution under continuous stirring. Then, the adequate amount of tetraethyl orthosilicate (TEOS) was added to the mixture and stirred following with the addition of $Ca(NO_3)_2.4H_2O$. Subsequently, the precipitate was dried in an oven at 60 °C for 24 h, followed by calcination at 700 °C for 2 h at a heating rate of 2 °C min^{-1}. All the used chemicals were purchased from Sigma-Aldrich (Darmstadt, Germany) without further purification.

Fibre mats fabrication

The fibre membranes were fabricated by electrospinning method. Poly ε- caprolactone (PCL, 80 kDa) was dissolved in a mixture of formic and acetic acid in the ratio of 1:1 at the room temperature [6]. For the fabrication of composite fibres BGs nanoparticles (30 wt% respect to PCL) were added to the polymer solution. The polymer solution used for electrospinning containing 20 % w/v of PCL in solvent. The optimized electrospinning parameters (15 kV, 2.9 mL/h flow rate, 11 cm distance from collector), were applied for fabrication of PCL fibre and PCL-BGs fibre composites.

RESULTS

The morphology of the prepared BG particles was analysed by SEM observation. Figure 1a shows well dispersed and spherical (ovoidal) particles with visible nanoporosity. The average particle size was in the range 130 ± 10 nm. Dispersion of nanoparticles was reached by using microemulsion assisted sol-gel method, which also explained the homogeneity in the size and shape. XRD spectra shown in Figure 1b indicating the amorphous nature of the sample. The broad band in the range of 20° - 34° (2Θ) could be ascribed to the amorphous silicate, while no other diffraction peaks are visible. The qualitative chemical composition analysis performed by SEM-EDX confirmed presents of Si and Ca elements (Figure 1c).

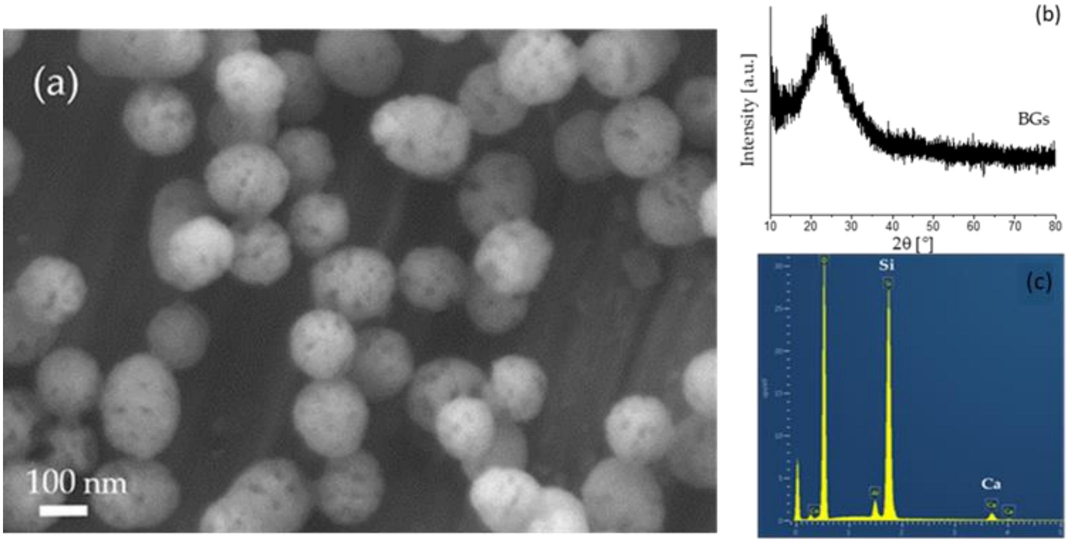

Figure 1: Morphology (a) and elemental composition (c) of synthesized BGs particles obtained by SEM-EDX. X-ray diffraction (XRD) pattern of BGs (b).

PCL-BGs fibre membranes were produced by electrosspinning process. The morphology of the mats was investigated by SEM (Figure 2). The size of BG particles allowed their incorporation into the fibers and affect the surface morphology of PCL-BGs fibres. Compared to control rough surface on PCL-BGs was obtained. The BG nanoparticles were heterogenously distibuted in long fibres and some clusters of particles were also observed. Obtained results confirmed that BG nanoparticles are sucessfully placed inside of the fibres.

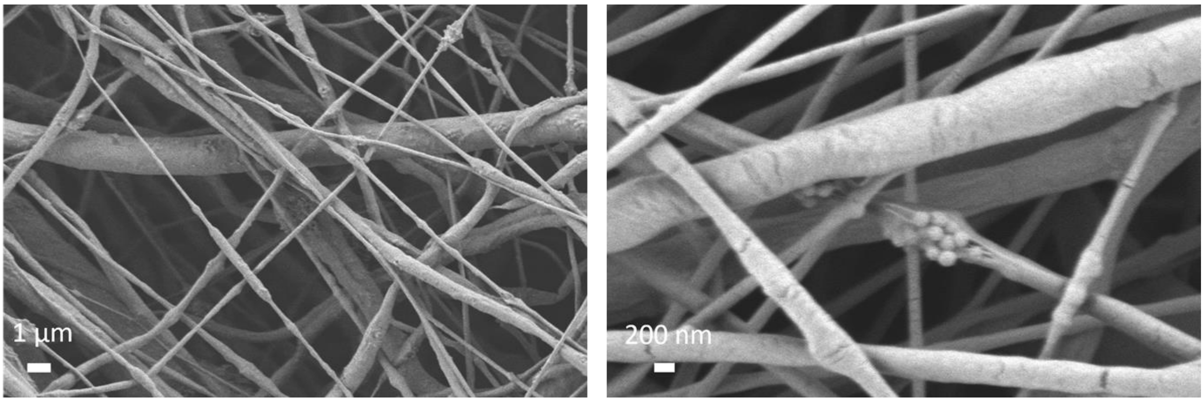

Figure 2: SEM micrographs of PCL-BGs electrospun nanofibers.

CONCLUSIONS

Bioactive glass nanoparticles based on simple binary system SiO_2-CaO were produced by the microemulsion sol-gel route. The size of well dispersed, spherical particles was in the range of 130 ± 10 nm. Subsequently, electrospun fibers containing BGs nanoparticles dispersed in a polymeric matrix were produced. Fibers mats were fabricated by electrospinning using poly(ε-caprolactone) (PCL) dissolved in benign solvents for the electrospinning (i.e. acetic acid). The BG nanoparticles were successfully incorporated into the structure and we developed smart multifunctional materials which can be used for tissue regeneration and wound healing.

ACKNOWLEDGMENT

This paper is a part of dissemination activies of project FunGlass. This project has received funding from the European Union´s Horizon 2020 research and innovation program under grant agreement No 739566 and in the frame of the project Centre for Functional and Surface Functionalized Glass (CEGLASS), ITMS code is 313011R453, operational program Research and innovation, co-funded from European Regional Development Fund.

REFERENCES

[1] V. Miguez-Pacheco, L. L. Hench, and A. R. Boccaccini, ‘Bioactive glasses beyond bone and teeth: Emerging applications in contact with soft tissues’, Acta Biomater., vol. 13, pp. 1–15, 2015.

[2] K. Rezwan, Q. Z. Chen, J. J. Blaker, and A. Roberto, ‘Biodegradable and bioactive porous polymer / inorganic composite scaffolds for bone tissue engineering’, Biomaterials, vol. 27, pp. 3413–3431, 2006.

[3] Z. Huang, Y. Zhang, M. Kotaki, and S. Ramakrishna, ‘A review on polymer nanofibers by electrospinning and their applications in nanocomposites’, Comp. Si. Tech.,vol. 63, pp. 2223–2253, 2003.

[4] S. Labbaf, A. B. Houreh, M. Rahimi, and H. Ting, ‘Bioactive glass-polycaprolactone fiber membrane and response of dental pulp stem cells in vitro’, Biomed. Glasses, pp. 123–130, 2018.

[5] Q. Liang, Q. Hu, G. Miao, B. Yuan, and X. Chen, ‘A facile synthesis of novel mesoporous bioactive glass nanoparticles with various morphologies and tunable mesostructure by sacrificial liquid template method’, Mater. Lett., vol. 148, pp. 45–49, 2015.

[6] L. Liverani and A. R. Boccaccini, ‘Versatile Production of Poly (Epsilon-Caprolactone) Fibers by Electrospinning Using Benign Solvents’, Nanomaterials, vol. 6, pp. 1-15, 2016.

PRÍPRAVA B_4C-TiB_2 KOMPOZITOV SPEKANÍM ZA ASISTENCIE ELEKTRICKÉHO PRÚDU

DENSIFICATION OF B_4C-TiB_2 COMPOSITES BY FIELD ASSISTED SINTERING

H. Ünsal[1], I. Shepa[2], B. Matovic[3], O. Hanzel[1], E. Múdra[2], P. Tatarko[1]

[1]*Institute of Inorganic Chemistry, Slovak Academy of Sciences, Dubravska cesta 9, 845 36 Bratislava, Slovak republic*
[2] *Institute of Materials Research, Slovak Academy of Sciences, Watsonova 47, 040 01 Košice, Slovak republic*
[3] *Institute of Nuclear Sciences, Centre of Excellence-CextremeLab Vinca, University of Belgrade, Serbia*

ABSTRACT

The B_4C/TiB_2 composites were fabricated by in situ reaction of B_4C, TiO_2 and carbon black using Field Assisted Sintering Technology (FAST). The effect of different processing parameters on the sintering behaviour of B_4C was studied in the temperature range of 1800 °C to 2000 °C and the pressure of 70 MPa. Fully dense B_4C -10 vol.% TiB_2 materials were obtained using the sintering regime with a degassing step at the temperature of 1800 °C, followed up by the applying of a pressure of 70 MPa for 30 s. Only B_4C and TiB_2 phases were identified, which confirmed that the reaction between TiO_2 and B_4C was completed and no residual TiO_2 was found in the materials. The mechanical properties of B_4C, such as hardness, and fracture toughness, were improved by the addition of in-situ formed TiB_2 particles.

Keywords: B_4C-TiB_2 composites, Reaction sintering, FAST, mechanical properties

INTRODUCTION

Due to its high hardness, high wear resistance and low density, boron carbide (B_4C) is used in many structural applications, such as personal ballistic armors, wear-resistant components and neutron absorbing parts in nuclear power plants [1-2]. However, the commercial applications of B_4C were limited due to the two main reasons, namely, its low fracture toughness and very high temperatures required for sintering [3]. On the other hand, both limitations can be mitigated using appropriate additives.

It was found that the preparation of B_4C–TiB_2 composites via in situ reaction of TiO_2, carbon and B_4C significantly reduces sintering temperature, while the presence of TiB_2 may increase the fracture toughness and strength [3-4]. The sintering process involves the conversion of TiO_2 to TiB_2 according to the following reaction 1:

$$2TiO2 + 3C + B4C \rightarrow 2TiB2 + 4CO \qquad (1)$$

Recently, Field Assisted Sintering process has received considerable attention to produce poorly sinterable materials, such as borides, carbides and nitrides. This sintering technique has the advantage of higher heating rates and shorter dwell times than conventional methods. The process is a kind of pressure sintering method, in which the samples are heated up directly by the electric current (in case of conductive materials) or indirectly via graphite die (in the case of isolating materials). Usually, the FAST process allows a material to be densified at lower temperatures and shorter times than would be required if the same material was sintered using one of the conventional techniques, such as Hot pressing, and Pressureless sintering [5-7].

The aim of the present work was to utilize the direct effect of electric current to in-situ synthesize B_4C-TiB_2 composites with 10 vol.% TiB_2 at a lower sintering temperature and a shorter processing time than normally used in the literature. The effect of the processing temperature and time on the densification, phase constitution, as well as microstructure of the sintered compacts was investigated.

EXPERIMENTAL

B_4C-TiB_2 composites were prepared by the in-situ reaction of B_4C (Grade HD20, H.C. Starck, Germany, d50 = 0.5 μm), TiO_2 (Anatase, Sigma Aldrich, - 325 mesh) and carbon black, which were used as raw materials. The powder mixture containing the appropriate amounts of the individual compounds to form 10 vol% of TiB_2 was prepared by planetary ball milling (Retsch PM 100, Germany) in isopropyl alcohol for 2 h using ZrO_2 milling balls.

The dried milled powders were uniaxialy pressed in a graphite die with a diameter of 20 mm at a pressure of 70 MPa. The sintering was performed using a Field Assisted Sintering apparatus (DSP 507, Dr. Fritsch GmbH., Germany) at the temperature range of 1800°C to 2000°C in vacuum atmosphere. Both the heating and cooling rates were 100°C/min, while the dwell time varied from 10 minutes to 30 seconds.

The density was measured by the Archimedes method. The microstructure was investigated using Scanning Electron Microscopy (AURIGA Compact, Zeiss). The hardness and the indentation fracture toughness were evaluated using a Vickers indentation (Zwick Roell Z2,5), at the load of 9.81 N. The crystalline phases were identified using X-ray diffraction (Panalytical Empyrean, Cu Kα radiation).

RESULTS

The effect of different sintering conditions on the final material density and microstructures was investigated for the B_4C-10 vol.% TiB_2 composition. In these experiments, conventional sintering conditions were applied as first. The maximum temperature was 2000°C and the pressure increased progressively to 70 MPa with increasing temperature. The dwell time was kept to 10 minutes. The sintering regime with the corresponding shrinkage curve is shown in Fig 1a.

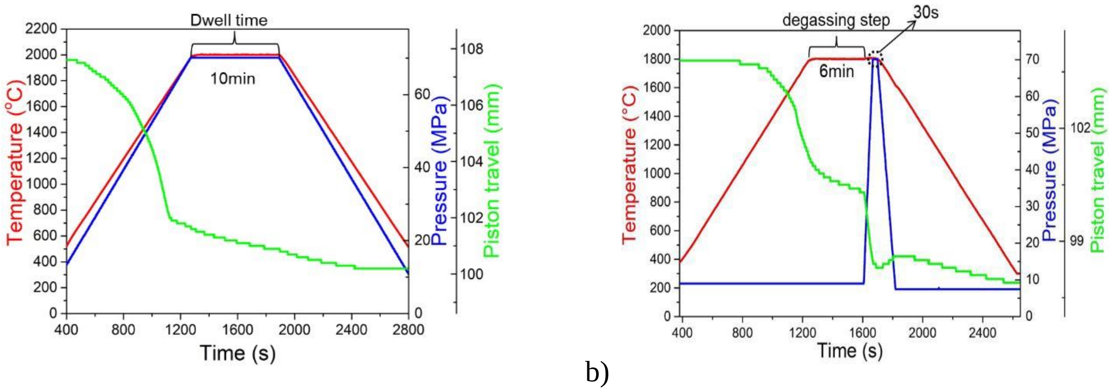

a) b)

Figure 1: Sintering regimes for B4C-10 vol.% TiB2 without a degassing step a); and with a degassing step and a dwell time of 30 seconds b).

The relative density of the sample sintered at 2000 °C was 93.3%. The SEM analysis of the sample (Fig. 2a) confirmed the presence of uniformly distributed TiB_2 particles (white particles) in the matrix of B_4C (grey phase in Fig. 2a). In addition, some oxide residues (EDX not shown here) were found forming a network-like structure. In order to remove the residual oxides from the final microstructure, a degassing step was added to the sintering process. This means that the temperature was increased with a constant minimum pressure of ~ 7 MPa. When the maximum temperature of 1800°C was reached, the sample was kept at the temperature for 6 minutes while keeping the minimum pressure to enable gasses to volatilize from the sample. After this degassing step, the pressure increased to 70 MPa within a minute and the sample was densified for 30 seconds. The sintering regime is given in Fig 1b.

The SEM analysis revealed that the degassing step was effective to remove all the oxide residues from the microstructure, as no network-forming oxide layer was found after the sintering with a degassing step. Instead, the SEM image of the fracture surface showed a dense, homogenous microstructure of B_4C-10 vol.% TiB_2 composite (Fig. 2b). The relative density of the sample was 99.9%. It should be pointed out that if a longer dwell time was used (the results not shown here), the decomposition of B_4C was observed, leading to a lower density of the materials.

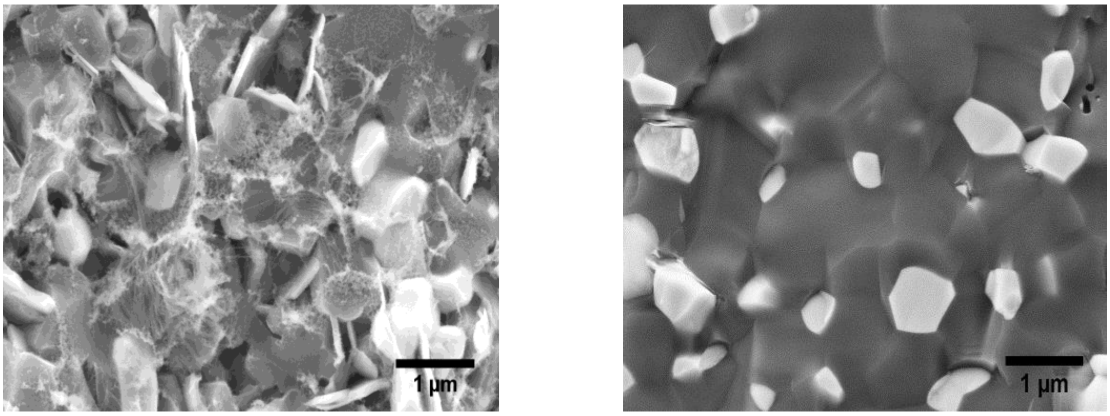

Figure 2: SEM images of the fracture surfaces of B_4C-10 vol.% TiB_2 samples sintered without a) and with degassing step b).

The hardness and indentation fracture toughness of the fully dense, homogenous B_4C-10 vol.% TiB_2 sample were compared to the properties of pure B_4C, sintered under the same conditions. After the addition of TiB_2, the hardness significantly increased from ~30 to 38 GPa, while the fracture toughness increased from ~ 2.1 to 3.0 MPa.m$^{1/2}$. This clearly confirms that the mechanical properties of B_4C ceramics can be significantly improved by the in-situ formation of TiB_2 in the microstructure. At the same time, the present results showed that by the direct effect of the electric current, a fully dense B_4C-10 vol.% TiB_2 composite can be obtained at lower temperatures and shorter processing times than usually used in the literature.

CONCLUSIONS

A fully dense B_4C-10 vol.%TiB_2 material was obtained after a modified sintering regime, which included a degassing step (6 min) at the temperature of 1800 °C, followed up by the applying of maximum pressure (70 MPa) for 30 s. Due to the direct effect of electric current, the material was sintered at a lower temperature and a shorter processing time than usually reported in the literature. The hardness and fracture toughness of B_4C were improved by the addition of in-situ formed TiB_2 particles.

ACKNOWLEDGMENT

This work was supported by the Slovak Research and Development Agency under the contract no. APVV-17-0328 and APVV-SK-SRB-0022. The support of the MVTS project of SAS "UltraCom" within the scheme of "Support of the Seal of Excellence projects" is also acknowledged.

REFERENCES

[1] Kim, K.H., Chae, J.H., Park, J.S., Ahn, J.P., Shim, K.B., "Sintering behavior and mechanical properties of B4C ceramics fabricated by spark plasma sintering", Journal of Ceramic Processing Research, vol. 10, no. 6, pp. 716-720 (2009).

[2] Yamada, S., Hirao, K., Yamauchi, Y., Kanzaki, S., "High strength B4C–TiB2 composites fabricated by reaction hot-pressing" Journal of the European Ceramic Society, vol. 23, pp. 1123-1130 (2003).

[3] Yu-jin, W., Hua-xin, P., Feng, Y., Yu, Z., "Effect of TiB2 content on microstructure and mechanical properties of in-situ fabricated TiB2/B4C composites", Trans. Nonferrous Met. Soc. China vol. 21, s369-s373 (2011).

[4] V. Skorokhod, Jr., V. D. Krstic, "High strength-high toughness B4C-TiB2 composites" Journal of Materials Science Letters, vol. 19, p.237– 239 (2000).

[5] S.G. Huang, K. Vanmeensel, O. Van der Biest, J. Vleugels "In situ synthesis and densification of submicrometer-grained B4C–TiB2 composites by pulsed electric current sintering" Journal of the European Ceramic Society, vol. 31, pp. 637–644 (2011).

[6] Suárez, M., Fernández, A., Menéndez, J.L., Torrecillas, R., Kessel, H.U., Hennicke, J., Kirchner, R., Kessel, T., "Challenges and Opportunities for Spark Plasma Sintering: A

Key Technology for a New Generation of Materials”, Sintering Applications, (2013) ISBN: 978-953-51-0974-7

[7] Kessel, H.U., Hennicke, J., Schmidt, J., Weißgärber, T., Kieback, B.F., Herrmann, M., Räthel, J.“ "FAST" field assisted sintering technology- a new process for the production of metallic and ceramic sintering materials” Powder Metallurgy in Science and Practice, vol. 22, pp.201-37 (2006).

KERAMICKÉ MATERIÁLY NA BÁZE ZrB_2-SiC S PRÍSADAMI OXIDOV PRVKOV VZÁCNYCH ZEMÍN

ZrB_2-SiC CERAMICS WITH RARE-EARTH OXIDE ADDITIVES

Z. Fürdősová[1], H. Ünsal[1], A. Kovalčíková[2], I. Dlouhý [3], P. Tatarko[1]

[1]*Institute of Inorganic Chemistry, Slovak Academy of Sciences, Dúbravska cesta 9, 845 36, Bratislava, Slovak Republic*
[2]*Institute of Materials Research, Slovak Academy of Sciences, Watsonova 49, 04001, Košice, Slovak Republic*
[3]*Institute of Physics of Materials, Academy of Sciences of the Czech Republic, Žižkova 22, 61662 Brno, Czech Republic*

ABSTRACT

The effect of different amounts (2wt.% and 5wt.%) of various rare earth oxides (Eu_2O_3, Yb_2O_3, Lu_2O_3) on the sintering, microstructure evolution, phase composition, and mechanical properties of ZrB_2-25vol.% SiC ceramics was investigated. All the samples achieved a relative density above 98% when sintered at 2000°C/70MPa/7min in Ar using Field Assisted Sintering Technology. The room temperature mechanical properties slightly increased with the addition of rare-earth oxide additives. The ablation rate decreased by ~ 30% after the use of 5wt.% of Yb_2O_3 and Lu_2O_3, when compared to the reference ZrB_2-25vol.% SiC material without sintering additives. On the other hand, the material with the Eu_2O_3 additive showed the ablation rate at the same level as that of the reference material.

Keywords: zirconium diboride, rare-earth oxides, ultra-high temperature ceramics, field assisted sintering technology, mechanical properties

INTRODUCTION

Zirconium diboride (ZrB_2), similar to other so-called Ultra High Temperature Ceramics (UHTCs), has high melting temperature (above 3000°C), good thermal and electric conductivity, good oxidation resistance and strength at elevated temperatures [1]. Such materials are used for applications performing at high temperatures, such as rocket propulsion, or thermal protection system for sharp leading edges of hypersonic vehicles [1-2]. Although ZrB_2 has extremely high melting temperature (3246°C), monolithic material has limited oxidation resistance [3-4], as during oxidation in air above 1000°C, B_2O_3 starts evaporating, and the porous ZrO_2 layer is the only phase remaining after the oxidation at 1500°C [5]. The phase transformation of ZrO_2 (1000-1200°C) also leads to the volume change and the increase of ZrO_2 layer porosity, which accelerate the oxidation rate [6].

Silicon carbide (SiC) is one of the most commonly used additives to improve the oxidation resistance of monolithic ZrB_2 ceramics. During oxidation it forms a borosilicate glass on the surface of ZrB_2-SiC, which reduces the oxygen permeation [1]. For this reason, a ZrB_2 - 25 vol.% SiC system has been considered as the most promising material system for ultra-high temperature environments [7]. However, new materials for hypersonic applications need to meet strict requirements of aerospace industry to survive temperatures above 2000°C.

The aim of the work was to develop a new diboride material for extreme applications by introducing rare-earth oxide additives (Eu_2O_3, Yb_2O_3, Lu_2O_3) into the commonly used ZrB_2 - 25 vol.%SiC material system. The effect of different content of the individual additives on the sintering, microstructure evolution, phase composition, and mechanical properties of ZrB_2-SiC ceramics at room as well as high temperatures was investigated.

EXPERIMENTAL

Commercially available powders of ZrB_2 (d50 ~1.5-3.0 μm, grade B, H.C. Starck), β-SiC (d50 ~0.6 μm Superior Graphite, β-SiC) and rare earth oxides, such as Eu_2O_3, Yb_2O, and Lu_2O_3, (d50 ~3.0-15.0 μm, Treibacher,) were used as raw materials. The ZrB_2/SiC ratio was kept constant (75 vol.% ZrB_2/25 vol.% SiC), while the amount of rare-earth oxides (RE_2O_3) was either 2 or 5 wt.%. The powder mixtures were prepared by a planetary ball mill (Retsch PM 100) using tungsten carbide (WC) milling media and the following conditions: 150 rpm for 6 hours (h). The reference ZrB_2-25vol.%SiC sample without sintering additives was also prepared for the sake of comparison.

The dried milled powders were uniaxialy pressed in a graphite die with a diameter of 20 mm at a pressure of 30 MPa. The sintering was performed using a Field Assisted Sintering Tehcnology (DSP 507, Dr. Fritsch GmbH.) at the temperature of 2000°C and the pressure of 70 MPa in Argon atmosphere. Both the heating and cooling rates were 100°C/min, while the dwell time was 7 minutes. The density was measured by the Archimedes method.

The microstructure of the materials was investigated using SEM (AURIGA Compact, Zeiss). The hardness and the indentation fracture toughness were evaluated using a Vickers indentation (ZWICK ROELL Z2,5), at the load of 9.81 N. The crystalline phases were identified using X-ray diffraction (Panalytical Empyrean, Cu Kα radiation), followed up by Rietveld analysis. The ablation resistance of the materials was investigated by an oxyacetylene flame up to the temperature of about 2600-2650°C, measured by the optical pyrometer. The dwell time at the maximum temperature was 1 minute. The ablated surface was observed by a confocal microscope (Lext OLS 3100, Olympus) in order to measure the depth of the ablated zone and calculate the linear ablation rate of the materials.

RESULTS

The sintering regime was effective to produce fully dense ZrB_2-SiC materials, as the relative densities of all the samples was above 98 %, Table 1. The SEM analysis of the microstructures revealed the presence of uniformly distributed SiC particles (dark grey phase in Fig. 1) in the ZrB_2 matrix (light grey phase in Fig. 1). In good agreement with the relative density, almost pores-free microstructure was observed for the ZrB_2-SiC with Lu_2O_3 (Fig. 1c, 1f), while a very few pores were found in the other compositions (shown by arrows in Fig. 1). The rare-earth oxide additives were uniformly distributed at the grain boundaries of ZrB_2 and could be seen at higher magnifications (SEM images not shown here).

Table 1: The relative densities and room temperature mechanical properties of the ZrB_2-SiC reference material (ZS) as well as the ZrB_2-SiC with different content of various RE additives (Eu, Yb, Lu)

Material	**Relative density [%]**	**Hardness HV1 [GPa]**	**Fracture toughness [MPa.m$^{1/2}$]**
ZS	99.8	17.6 ± 0.5	2.2 ± 0.2
ZS2Eu	99.0	17.8 ± 0.9	2.4 ± 0.2
ZS2Yb	99.1	16.9 ± 0.9	2.4 ± 0.1
ZS2Lu	99.3	19.4 ± 0.6	2.4 ± 0.2
ZS5Eu	98.3	16.3 ± 0.4	2.8 ± 0.2
ZS5Yb	98.9	18.6 ± 1.0	2.5 ± 0.1
ZS5Lu	99.8	19.6 ± 0.6	2.5 ± 0.2

The room temperature mechanical properties of the ZrB_2-25vol.%SiC materials with different RE additives, such as hardness, and indentation fracture toughness, are given in Table 1. The results showed that no significant change in the mechanical properties of the ZrB_2-SiC materials was observed after the addition of RE additives. The hardness even increased from 17.6 GPa to 19.6 GPa when the reference ZrB_2-SiC and ZrB_2-SiC with 5wt.% Lu_2O_3 are compared. It must be pointed out that the RE oxides were used mainly to improve high temperature properties of ZrB_2-based materials. At the same time, their addition should not lead to the deterioration of mechanical properties at room temperatures. It can be concluded that the room temperature mechanical properties retained the same level or were even improved after the addition of 5 wt.% RE_2O_3.

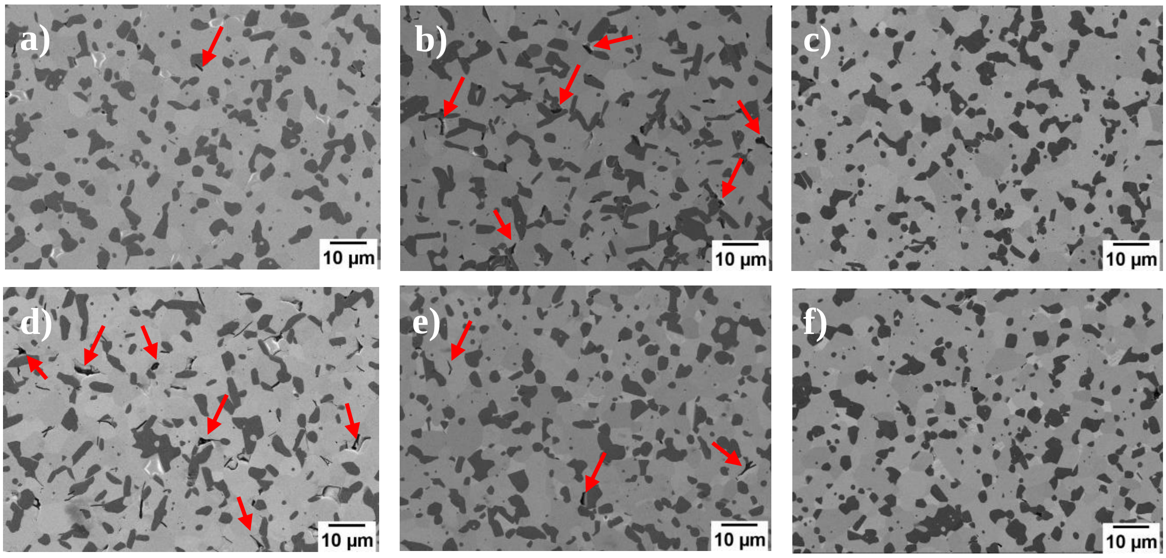

Figure 1: SEM microstructures of ZrB_2 - 25vol.% SiC with different RE_2O_3 additives: a) 2wt.% Eu_2O_3; b) 2wt.% Yb_2O_3; c) 2wt.% Lu_2O_3; d) 5wt.% Eu_2O_3; e) 5wt.% Yb_2O_3; f) 5wt.% Lu_2O_3

The high temperature properties of the materials were evaluated in terms of the ablation tests up to the temperature of ~ 2600°C using an oxyacetylene flame. Fig. 2 shows an example of 3D-surfaces (obtained by a confocal microscopy) of the ZS and ZS2Lu and ZS5Lu samples, respectively. It is obvious that the amount of the ablated material was significantly lower with the increasing amount of sintering additive, as the ablated hole in the middle was smaller with a less material removed as the content of the additives increased.

The linear ablation rate was calculated from the depth of the ablated region for all the samples. It decreased from ~ 7.5 x 10^{-3} mm/s for the reference ZS material to ~ 4.8 x 10^{-3} mm/s for ZS5Yb and ZS5Lu materials. This constitutes around 30 % improvement of the ablation resistance obtained for the materials with the addition of 5wt.% of Lu_2O_3 and Yb_2O_3. On the other hand, the Eu_2O_3 additive was not effective to improve the ablation resistance, as the ablation rate of this material was at the same level as that of the reference material (7.2 x 10^{-3} mm/s). This was caused by the higher porosity of the material, as well as the less refractory nature of the grain boundary phase. It is well known that the refractory nature of the glassy phase increases with the decreasing ionic radius of RE^{3+}. The Eu^{3+} cation has the largest ionic side among all of the investigated additives; thereby the lowest refractory nature. It can be concluded that a significant reduction of the ablation rate was obtained by the addition of appropriate RE additives, while the room temperature mechanical properties were retained at the same level as that of the reference material with additives.

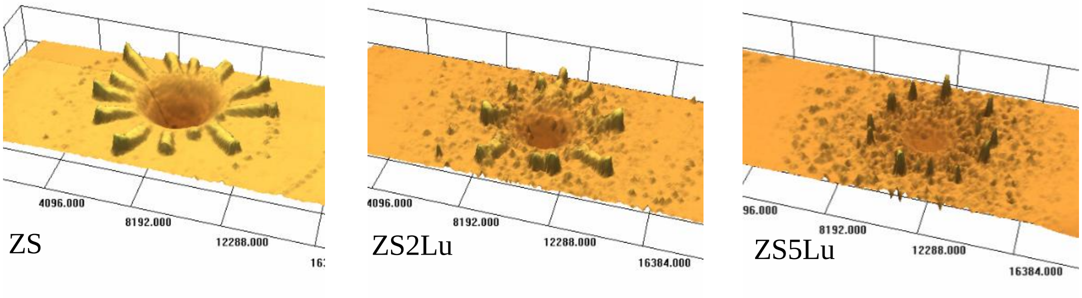

Figure 2: 3D-ablated surfaces of the reference (ZS) and the ZrB_2-SiC with 2wt.% Lu_2O_3 (ZS2Lu) and 5wt.% Lu_2O_3 (ZS5Lu) samples after the ablation tests at ~ 2600°C

CONCLUSIONS

The fully dense ZrB_2 - 25vol.% SiC materials with different amounts (2 and 5wt.%) of rare-earth oxide additives (Eu_2O_3, Yb_2O_3, and Lu_2O_3) were prepared using Field Assisted Sintering Technology at the temperature of 2000°C and the pressure of 70 MPa. The room temperature mechanical properties, such as hardness, and indentation fracture toughness, were not only at the same level as that of the reference ZrB_2-SiC material without the additives, but they even slightly increased. At the same time, the ablation rate was significantly decreased after the use of additives, and further decreased with the increasing amount of the additives. The improvement of ~ 30% was achieved when 5 wt.% of Yb_2O_3 and Lu_2O_3 additives was used, while no significant improvement was observed for the Eu_2O_3 additive.

ACKNOWLEDGMENT

This project has received funding from the European Union's Horizon 2020 research and innovation programme under the Marie Sklodowska-Curie grant agreement No 798651. This work was also supported by the Slovak Research and Development Agency under the contract no. APVV-17-0328 and APVV-SK-CN-2017-0040. The support of the Joint Mobility Project MAD SAV-AVCR 18-12 under the ASCR-SAS agreement is also acknowledged.

The link to a repository to access the research data needed to validate the results will be sent upon a request made to peter.tatarko@savba.sk.

REFERENCES

[1] W.G. Fahrenholtz, E.J. Wuchina, W.E. Lee, Y. Zhou: Ultra-high temperature ceramics – Materials for extreme environment applications, John Wiley & Sons, Inc., Hoboken, New Jersey (2014), ISBN 978-1-118-70078-5

[2] B. Berton, M. Bacos, D. Demange and J. Lahaye, "High-temperature oxidation of silicon carbide in simulated atmospheric re-entry conditions", J. Mater. Sci. vol. 27, pp. 3206-3210, 1992.

[3] M. A. Levinstein, in Proceedings of Metallurgical Society Conference on Refractory Metals and Alloys, Chicago, edited by M. Semchysen and I. Perlmutter (Interscience Publishers, New York, London, 1963).

[4] A. K. Kuriakose and J. L. Margrave, "The oxidation kinetics of zirconium diboride and zirconium carbide at high temperatures," J. Electrochem. Soc., vol. 111, no. 7, pp. 827-831, 1964.

[5] L. Kaufman, E. V. Clougherty and J. B. Berkowitz-Mattuck, "Oxidation Characteristics of Hafnium and Zirconium Diboride," Trans. Metall. Soc. AIME, vol. 239, no.4, pp.458–66, 1967.

[6] T. A. Parthasarathy, R. A. Rapp and M. Opeka, "Effects of phase change and oxygen permeability in oxide scale on oxidation kinetics of ZrB_2 and HfB_2," J. Am. Ceram. Soc., vol. 92, no.5, pp. 1079-1086, 2009.

[7] D.D. Jayaseelan, E. Zapata-Solvas, P. Brown, W.E. Lee: In situ formation of oxidation resistant refractory coatings on SiC-reinforced ZrB_2 ultra high temperature ceramics, J. Am. Ceram. Soc. 95[4] (2012)

SINTERING

BEZTLAKOVÉ SPEKANIE JEMNO-ZRNNÉHO KARBIDU BÓRU DOPOVANÉHO UHLÍKOM

PRESSURELESS SINTERING OF FINE-GRAINED BORON CARBIDE POWDERS DOPED WITH CARBON

M. Vozárová [1], Z.Kováčová [1,2], E. Neubauer [2], V. Trembošová [3,4], Ľ. Bača [1], M. Kitzmantel [2], M. Janek [1,5]

[1] *Department of Inorganic Materials, Faculty of Chemical and Food Technology, STU, Radlinského 9, 81237 Bratislava, Slovakia*
[2] *RHP-Technology GmbH, Forschung- und Technologiezentrum, 2444 Seibersdorf, Austria*
[3] *Institute of Materials and Machine Mechanics, Slovak Academy of Science, Dúbravská cesta 9/6319, 845 13 Bratislava, Slovakia*
[4] *Faculty of Materials Science and Technology in Trnava, STU, Jána Bottu 2781/25, 917 24 Trnava, Slovakia*
[5] *Comenius University, Faculty of Natural Sciences, Department of Physical and Theoretical Chemistry, Mlynská dolina Ch1, 842 15 Bratislava*

ABSTRACT

Boron carbide is a material of great interest to modern industry. However, its densification using conventional sintering techniques without applying external pressure or using sintering additives is challenging. The present study is focused on the pressureless sintering of a commerical available boron carbide powder with a high specific surface area and submicron size. The B_4C powder was doped by graphite or phenolic resin with concentrations varying from 0.5 to 3 wt.%. Moreover, the influence of the cold pressing pressure on densification was evaluated. Generally, a higher cold pressing pressure resulted in an improved densification for the selected powder. The graphite addition can be assessed as more effective considering the measured values of relative density. It has been observed that – depending on how the carbon is added - an improvement of the densfication can be achieved.

Keywords: B_4C, carbon, grain size, pressureless sintering, additive manufacturing

INTRODUCTION

Boron carbide (B_4C) is the third hardest material next to diamond and cubic boron nitride, having a Vickers hardness of 3770 kg/mm^2. Due to its low density (2.52 g/cm^3), it is the leading material for personal armor, typically in the form of front and back inserts of ballistic vests made from B_4C plates. B_4C is also used for nuclear shielding applications as a result of boron’s high neutron absorption cross-section. It is used in particulate form as an abrasive, and as a nozzle material for slurry pumping and grit blasting because of its excellent abrasion resistance [1]. Unfortunately, a high densification without application of additives or high external pressure is impossible due to the covalent B-C bond and the low self-diffiuson coefficient. Moreover, the presence of boron oxide as surface oxide layer also inhibits the densification [2]. A typical method to enhance the densification of boron carbide is pressure assisted sintering such as hot pressing, but it is applicable only to rather simple shapes. Currently, additive manufacturing is one of the most promising technologies for preparation of complex near-net shaped 3D objects. Due to its simplicity, the shaping of ceramic parts is more accessible. However, the densification is restricted to pressureless sintering. Currently, there is a wide offer of commercially available boron carbide powders with different properties, which have crucial effect on sinterability as well as the properties of the final product. Within this work the focus was to assess the use of a very fine powder (particle size of <1 μm) and a high specific surface area (22 – 25 m^2/g) and to study the sinterability of the powder taking into account different additives.

Besides the use of pressure another alternative to promote the densification of boron carbide is the use of sintering additives. Carbon is one of the most studied sintering additive for boron carbide. Generally, carbon can be added either as an admixture or produced in-situ and it reacts with the boron oxide layer as described in equation (1).

$$2B_2O_{3(g)} + 7C_{(s)} \rightarrow B_4C_{(s)} + 6CO_{(g)} \quad (1)$$

According to literature, carbon is typically used in the form of phenolic resin, carbon black or from organic precursors, e.g. glucose. It has been shown in [3], that the phenolic resin activates sintering of B_4C already at 1350°C. Another study showed the beneficial effect of phenolic resin on the densification performed at 2280°C. Doping of the B_4C with 1.5-3 wt% resin resulted in a relative density of more than 97% by minimizing of oxygen impurity effect using micron sized powders [1, 4-5]. Generally, the properties of polycrystalline materials depend on several factors such as grain size, porosity, inclusions and impurities or agglomerates present in starting material. These factors (and many others) have an essential influence on the sinterability and mechanical properties of the final material and affect the application. Therefore, they have to be properly considered to controll or tailor the properties of engineered material [6]. This knowledge would open the possibility for shaping of the B_4C also by using additive manufacturing technologies for industrial applications. The aim of present work was to assess the sinterability of a powder with a high specific surface area and particle size of 0,5μm by pressureless sintering. The effect of doping this type of powder with graphite as well as phenolic resin on the densification by using an amount of 0.5 – 3 wt.% was studied. Additionally, effect of cold-pressing pressure was investigated to determine the material with the best shaping and sintering behaviour. This work is the basis for subsequent steps to employ additive manufacturing for the shaping. The sinterability was assessed by the measurement of the relative density. Additionally the material loss during the sintering is reported.

EXPERIMENTAL

Commercially available powder (labelled as Grade A) was used as starting material. The main characteristic are listed in Tab 1. The graphite and phenolic resin was changed in a quantity ranging from 0.5 to 3 wt. % and were added as source of carbon.

Table 1: Characterisation of boron carbide powder

	Grade A
Surface Area	22 – 25 m^2/g
Particle size / D50	0.5 μm
Total oxygen	3.06 %
Total carbon	21.9 %
B/C atomic ratio	3.7 - 3.9

The powder mixtures consisting of B_4C powder and additives were homogenized in organic solvent using using hard metal balls in a tumbling mixer. The wet mixtures were consequently dried in an evaporator and sieved. The as received B_4C powder was used as a reference. The powder mixtures were uniaxially cold-pressed using a pressure of 100 MPa and 150 MPa. The cylinders with diameter of 20 mm and height of 5 mm were prepared and the densities of the green bodies were measured. The sintering was performed at temperature of 2200°C in vacuum for 4 hours. The relative density of samples was calculated from the ratio of the Archimedes density measured in mercury to the theoretical density of B_4C (2,5 g/cm^3).

RESULTS

The Fig. 1 compares the influence of graphite addition and cold-pressing pressure on relative densities for the studied B_4C grade. Generally, higher pressure resulted in higher relative density after sintering, which is more significantly visible for graphite doped samples. It must be noted, that the effect of cold-pressing pressure on undoped powders was negligible. The cold-pressed bodies with additives appeared to be more compact and easier to handle.

The addition of carbon in the form of graphite resulted in a slightly increase of green body relative densities (approx.3 % higher compared to undoped powder) as well as higher densities of samples after sintering. The impact of the investigated additives on the green body densities is shown in the following Fig.1.

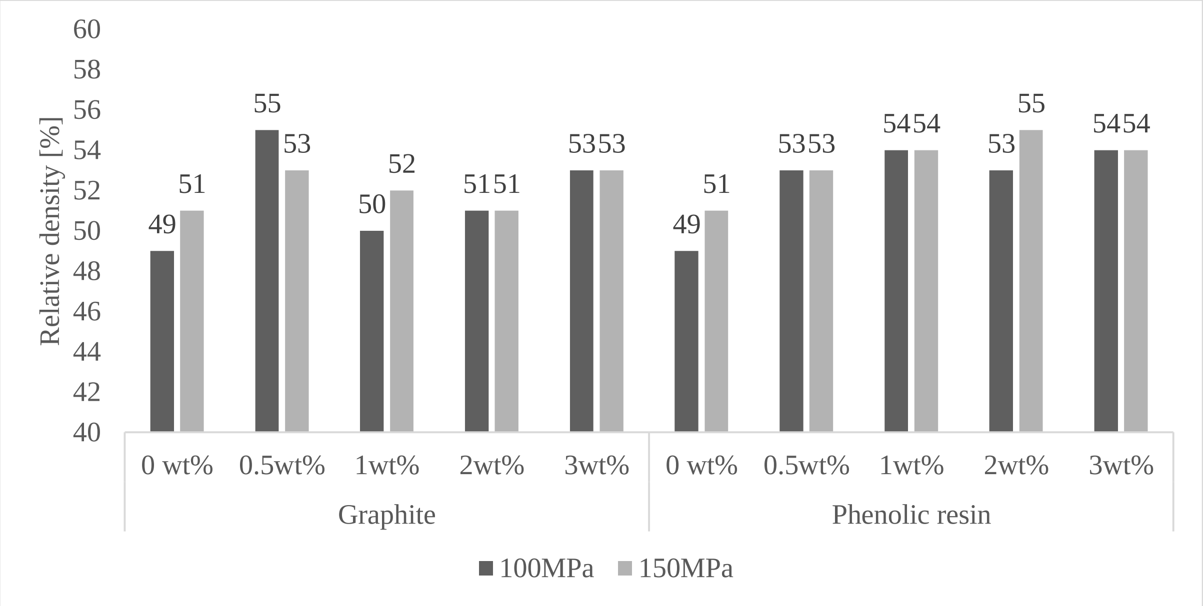

Figure 1: Impact of the addition of graphite addition (left) and phenolic resin addition (right) on the green body density for two different cold compaction pressures

It can be seen from Fig 1 that there is slight increase of the green body density with increasing graphite content with the exception of 0,5 wt.%. In this case higher densifications are observed. The increase of the cold compaction pressure has mainly a positive influence on the green body density for the as received powder.

After sintering of the green bodies the densification increased with increasing graphite content. While the reference samples showed a relative density of 87 % an increase by 5 % is observed at a graphite content of 3 wt.%. The achieved final relative densities ranged from approx. from 90 to 92% and were independent on the used amount of graphite especially, if a content of more than 1 wt.% was used. In some of the samples a delamination of the samples was observed, especially when higher cold compaction pressures were applied.

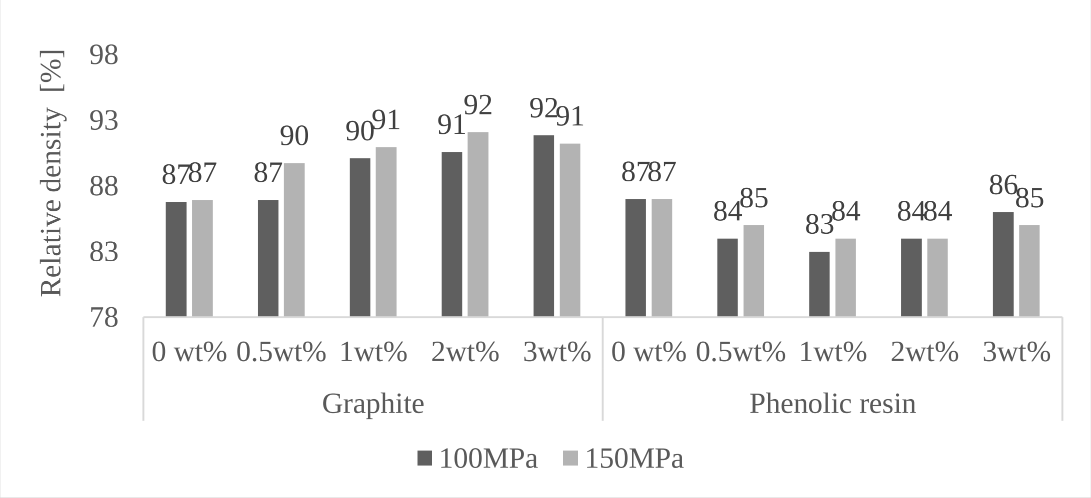

Figure 2: The comparison of the final relative densities of investigated boron carbide samples doped with graphite (left) and phenolic resin (right) cold-pressed using different pressures.

The influence of phenolic resin addition as well as cold-pressing pressure on B_4C powder was compared as the second part of the work. The phenolic resin was used as additional source of carbon to investigate its effect on cold compaction behavior and densification. Green density was comparable to the graphite doped powders and Fig. 1 (right) shows the results of the green body densities. The samples had tendency for a slighty higher green body density compared to undoped boron carbide and were easier to handle.

However, the relative densities achieved after sintering were inferior to the samples achieved by the addition of the graphite. A possible explanation is that the phenolic resin udergoes a decomposition to volatile organic products resulting in formation of volatile products resulting in pores formation and defects in the material. All samples showed delamination and cracking, as presented in Fig. 3. This phenomenon could be avoided by reducing the heating rate. It can allow to controll the successive release of residues and to minimze the material degradation.

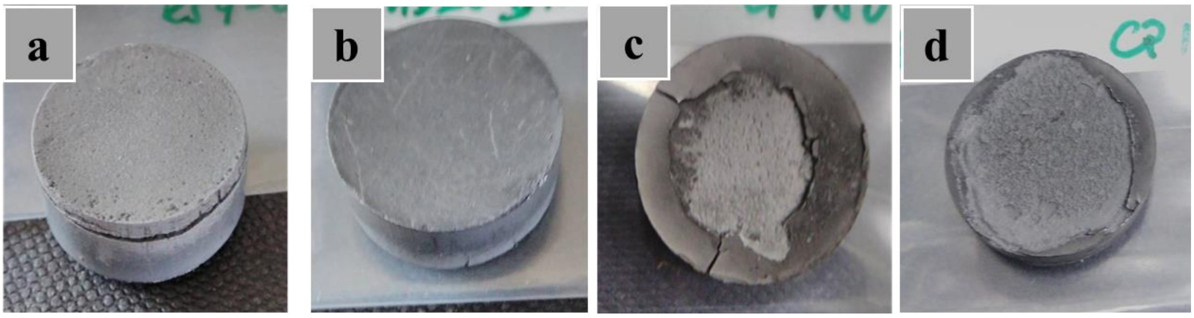

Figure 3: B_4C sample after sintering doped with 0.5 wt.% (a) and 3 w.t% (b) of graphite compared with samples doped with 0.5 wt.% (c) and 3 wt.% (d) phenolic resin, cold-pressed using 150 MPa

The densification of the phenolic resin doped powders was even lower compared to the reference without doping. All samples - even if 3 wt.% of resin were used - were even less dense than the undoped material.

CONCLUSIONS

The present study was focused on pressureless sintering of submicron sized B_4C powders using two different doping elements. The influence of graphite or phenolic resin as an additive was used in various contents up to 3 wt.%. Additionally, the green bodies were prepared in two different cold-pressed conditions using a pressure of 100 and 150 MPa. The sintering behavior was assessed by measurement of the relative density. The results show, that the application of a higher pressure during the formation of the green bodies, a slightly improved green density as well as final density is observed. The addition of graphite enhances the densification of the doped powder grades. However, the densification is strongly depending on the sintering additive. The phenolic resin resulted in green bodies with higher densification and also higher green body strength. On the other hand, the phenolic resin appeared to be not suitable since samples after sintering were damaged due to the formation of volatile products during decomposition, which is also indicated by a material loss. Based on these results, the addition of carbon in form of graphite showed a positive trend to increase the densification during the sintering. The next step is to apply additional gas pressure in order to obtain a full densification.

ACKNOWLEDGMENT

This work is based on the results of the project Centre for Applied Research of New Materials and Technology Transfer. ITMS 26240220088. supported by the Science and Research Operational Program by the European Regional Development Fund. The financial supports of the Slovak Research and development Agency APVV-16-0341 and Slovak Grant Agency for Science VEGA grant No. 1/0906/17 are also greatly appreciated.

REFERENCES

[1] R.F. Speyer, H. Lee, Advances in pressureless densification of boron carbide, J. Mater. Sci. 39 (2004) 6017–6021. doi:10.1023/B:JMSC.0000041698.23052.b9.

[2] M. Asadikiya, C. Rudolf, C. Zhang, B. Boesl, A. Agarwal, Y. Zhong, Thermodynamic modeling and investigation of the oxygen effect on the sintering of B4C, J. Alloys Compd. 699 (2017) 1022–1029. doi:10.1016/j.jallcom.2016.12.315.

[3] H. Lee, R.F. Speyer, Hardness and Fracture Toughness of Pressureless-Sintered Boron Carbide (B4C), J. Am. Ceram. Soc. 85 (2004) 1291–1293. doi:10.1111/j.1151-2916.2002.tb00260.x.

[4] X. Shi, J. Cao, Z. Li, D. Yan, Effect of the Addition of Carbon on the Sintering Properties of Boron Carbide Ceramics prepared by Pressureless Sintering, (2015) 392–398. doi:10.2991/ic3me-15.2015.77.

[5] K.A. Schwetz, W. Grellner, The influence of carbon on the microstructure and mechanical properties of sintered boron carbide, J. Less-Common Met. 82 (1981) 37–47. doi:10.1016/0022-5088(81)90195-8.

[6] P. Barick, D.C. Jana, N. Thiyagarajan, Effect of particle size on the mechanical properties of reaction bonded boron carbide ceramics, Ceram. Int. 39 (2013) 763–770. doi:10.1016/j.ceramint.2012.06.089.

SPÁJANIE SiC KERAMICKÝCH MATERIÁLOV SO ZLIATINAMI NA BÁZE Ti POMOCOU SPS

JOINING OF SiC CERAMICS WITH Ti-BASED ALLOYS BY SPS

P. Tatarko[1], X. Zhou[2], A. Kovalčíková[3], I. Dlouhý[4]

[1]*Institute of Inorganic Chemistry, Slovak Academy of Sciences, Dúbravska cesta 9, 845 36, Bratislava, Slovak Republic*
[2]*Engineering Laboratory of Specialty Fibers and Nuclear Energy Materials, Ningbo Institute of Materials Technology and Engineering, Chinese Academy of Sciences, Ningbo, Zhejiang 315201, China*
[3]*Institute of Materials Research, Slovak Academy of Sciences, Watsonova 49, 04001, Košice, Slovak Republic*
[4]*Institute of Physics of Materials, Academy of Sciences of the Czech Republic, Žižkova 22, 61662 Brno, Czech Republic*

ABSTRACT

Monolithic CVD-SiC materials were successfully joined with different Ti-based interlayers (pure Ti, Ti_3SiC_2 and Ti/Ti_3SiC_2) using Spark Plasma Sintering. A significant volume change, along with the extensive reaction of the filler with the matrix resulted in the significantly lower bending strength of the CVD-SiC/Ti and CVD-SiC/Ti/Ti_3SiC_2 joints, when compared to the CVD-SiC/Ti_3SiC_2 joint. On the other hand, the solid state diffusion bonding without any reaction with the matrix or significant volume change led to the bending strength of CVD-SiC/Ti_3SiC_2 joints comparable to the intrinsic strength of CVD-SiC materials (~ 220 MPa).

Keywords: monolithic CVD-SiC, joining, Spark Plasma Sintering, microstructure, strength

INTRODUCTION

Silicon Carbide (SiC) monolithic materials are primarily used as materials for aerospace and nuclear applications due to their excellent combination of properties, such as low density, high strength, good thermal stability, high thermal conductivity, good irradiation resistance and low induced-activation. In the nuclear field the most important application of SiC is for cladding materials in pressurised water reactors and flow channel insert materials in thermonuclear fusion reactors [1]. The fully ceramic cladding usually consists of the combination of fibrous SiC composites with a single layer or multiple layers of monolithic SiC coatings; and this material is considered for the next generation reactors [2].

In recent years, electric field assisted technology, such as SPS, has attracted considerable interest as a new advanced technique for joining of SiC-based materials [3]. In this case, both rapid heating and short processing time may inhibit the reactions between interlayers and base materials. At the same time, the electric field can accelerate self-diffusion, and promote the migration of ions through the joining interface [4].

Besides the joining technology, another critical issue is to develop new joining materials with high melting points, good oxidation and irradiation resistance. Recently, Ti_3SiC_2 (MAX phase) has attracted considerable attention as a joining filler for SiC materials [5-6], due to a unique combination of metallic and ceramic properties, such as damage tolerance, machinability, high temperature oxidation resistance, good electrical and thermal conductivities, thermal shock resistance, and wear resistance [7]. Since MAX phases also possess excellent irradiation/corrosion resistance, they are regarded as promising structural materials for fusion reactors and lead-cooled fast reactors. On the other hand, the coefficient of thermal expansion (CTE) of Ti_3SiC_2 (~ 9.2 x 10^{-6} K^{-1}) is twice of SiC (~ 4.4 x 10^{-6} K^{-1}), which is a critical problem because the thermal mismatch stresses always cause the formation of cracks [6]. Therefore, it has recently been suggested that TiC could also be considered as a joining material for SiC because of its better lattice and thermal matching with SiC than Ti_3SiC_2 (CTE is ~ 7.7 x 10^{-6} K^{-1}) [6].

The aim of this work was to join monolithic CVD-SiC ceramics with Ti and Ti_3SiC_2 joining materials using SPS. The properties, such as mechanical strength of the joints, were compared with the aim to propose a reliable joining material to assemble SiC into a more complex structures.

EXPERIMENTAL

The starting material was the high-purity (99.9995 %), fully dense (3.21 g/cm^3) CVD β-SiC (The Dow Chemical Company). The joining pairs of CVD-SiC blocks, rectangles with a dimension of 15 x 6 x 25 mm, were joined along the 15 x 6 mm cross-section. Three different joining materials were used: a commercially available Ti foil (with a thickness of ~ 120 μm), a pre-sintered Ti_3SiC_2 foil, and a combination of both Ti and Ti_3SiC_2. The Ti_3SiC_2 foils were pre-sintered from a synthesized Ti_3SiC_2 powder (with Al_2O_3 additives) using the SPS process at 1300°C with an external pressure of 60 MPa and a dwell time of 5 min in vacuum. The Ti_3SiC_2 bulk samples were then ground to a final thickness of between ~ 30 and 100 μm and polished using a final diamond suspension of 3 μm. As regards the Ti/Ti_3SiC_2 joining material, a thin layer of pure Ti (~ 10 μm) was first PVD deposited on both SiC surfaces to be joined. The pre-sintered Ti_3SiC_2 foil was then interposed between the two Ti-coated CVD-SiC matrices, as done for the cases where only Ti or Ti_3SiC_2 foils were used.

The assembly was then inserted into a cylindrical graphite die with a diameter of 30 mm. The external pressure was applied through the graphite punches inserted in the cylindrical die. The joining assembly was indirectly heated to the joining temperature by the Joule heating of the graphite die in vacuum in an SPS furnace (HPD 25/1, FCT systems, Germany). The SiC couples with Ti foil were joined at the temperature of 1700°C (above the melting point of Ti ~ 1668°C). The temperature was lowered to 1300°C for the case when Ti_3SiC_2 foil was used to avoid reactions and decomposition to take place. In all cases, the pressure of 50 MPa was used and the dwell time was 5 minutes. The heating and cooling rates were 100°C/min.

After the joining, three beams with a dimension of 4 x 6 x 50 mm were cut out of each joined blocks along their long axis. The 4-point bending strength was measured using a universal electro mechanical testing machine (Instron 8862). The inner and outer spans were 20 and 40 mm, respectively. The cross-head speed was 0.5 mm/min. The polished cross-sections of the joints and the fracture surfaces after the mechanical tests were characterized using Scanning Electron Microscopy (SEM) FEI Inspect-F equipped with Energy Dispersive Spectroscopy (EDS) detector.

RESULTS

The SEM images of the cross sections of the SiC joints with pure Ti and Ti_3SiC_2 foils are shown in Fig. 1a and 1b, respectively. It is clear that in both cases the joining interlayers showed a homogenous thickness. It can also be seen that the joining material strongly reacted with the CVD-SiC matrix, leading to the so-called “nail-like” interface in both cases, despite the fact that the surface of CVD-SiC was polished to the final 1 μm before the joining. This interaction was more significant when the pure Ti foil was used as a joining filler (Fig. 1a). More importantly, a significant shrinkage was observed for the CVD-SiC/Ti joints, as the Ti foil with a thickness of ~ 120 μm was used, while the final interlayer had a thickness of ~ 35 μm. Such a significant volume change, along with the mismatch in thermal expansion coefficients (CTE) between Ti and CVD-SiC, led to the formation of transverse cracks in the interlayer. These cracks never propagated into the CVD-SiC matrix. It is well known that the presence of transverse cracks has much lower impact on the mechanical performance of the joints, when compared to the cracks propagated along the interface [3, 4, 6]. On the other hand, no transverse or parallel cracks were observed for the CVD-SiC/Ti_3SiC_2 joints (Fig. 1b). No obvious shrinkage of the Ti_3SiC_2 foil during joining was observed. Similarly, much less significant reaction of the Ti_3SiC_2 joining filler with the matrix was revealed. This led to the formation of crack-free interlayer. While the TiC layer was observed in the middle of CVD-SiC/Ti joint (EDX results not shown here), the rest of the interlayer was composed of Ti_3SiC_2 phase. No unreacted Ti remained in the interlayer. On the other hand, the interlayer of CVD-SiC/Ti_3SiC_2 joints consisted of the uniformly distributed Al_2O_3 particles (dark grey phase in the interlayer in Fig. 1b) in the Ti_3SiC_2 matrix. The alumina was added to the Ti_3SiC_2 powder during the preparation of the foil in order to improve the densification and mechanical properties of the Ti_3SiC_2 matrix. No other phases were detected, confirming that no significant reaction of the filler with the matrix occurred during the joining process.

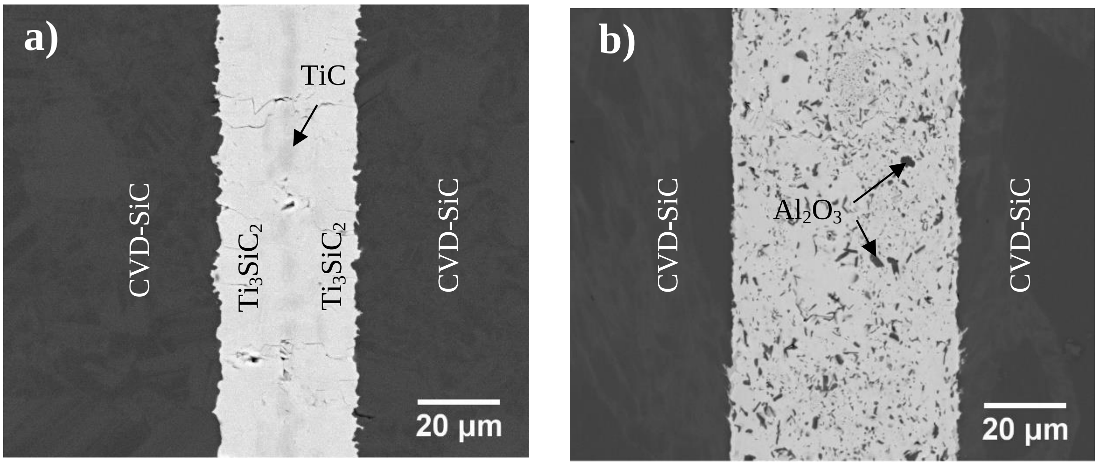

Figure 1: SEM images of the CVD-SiC joints with a) pure Ti; and b) Ti_3SiC_2/Al_2O_3

The SEM image of the joining interface of the CVD-SiC/Ti/Ti_3SiC_2 joint is shown in Fig. 2. Similar to the CVD-SiC/Ti_3SiC_2 case, no significant shrinkage and no presence of cracks were observed. The in-situ reaction layer with a thickness of ~ 10 μm was clearly formed as the transition layer between the CVD-SiC matrix and the Ti_3SiC_2 interlayer. The in-situ reaction layer consists of two distinct parts, i.e. the transition layer of TiC at the interface with the CVD-SiC matrix (with a thickness of ~ 4 µm), and the in-situ formed Ti_3SiC_2 layer with Ti_5Si_3 particles (the EDX and XRD analysis are not shown here) at the interface between TiC and the initial Ti_3SiC_2. The difference between the in-situ reaction zone and the initial Ti_3SiC_2 foil was the absence of Al_2O_3 particles in the in-situ formed layer (Fig. 2).

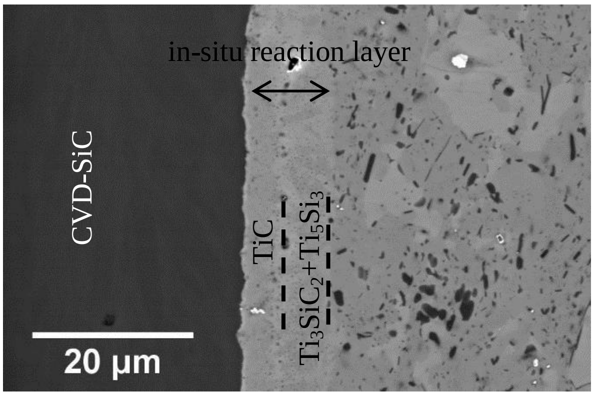

Figure 2: SEM images of the CVD-SiC joint with the Ti/Ti_3SiC_2 interlayer

In order to characterize the mechanical performance of the joints, the four-point bending strength of the joints was investigated and compared to the strength of the reference unjoined CVD-SiC materials, Fig. 3. When Ti was present in the joining interlayer, the strength of the joints was 50% lower (~ 110-120 MPa) than the intrinsic strength of the unjoined material (~ 215 MPa). On the other hand, when only Ti_3SiC_2 pre-sintered foil was used, the strength of the joints reached the value of the intrinsic strength of CVD-SiC (214 ± 13 MPa). In this case, the failure always occurred in the matrix, close to the joining interface. This confirmed that the strength of the joint was higher than the intrinsic strength of the CVD-SiC. Most probably, a significant volume change and extensive reaction for the joints where Ti was present resulted in the formation of large residual stresses in the joined couples. This caused a significant reduction of the mechanical performance of the joint. On the other hand, pre-sintering of Ti_3SiC_2 helped to use the filler in a solid state. Neither reaction nor shrinkage occurred during the joining, which was the reason of a significantly higher strength of the joints, comparable with the intrinsic strength of the CVD-SiC.

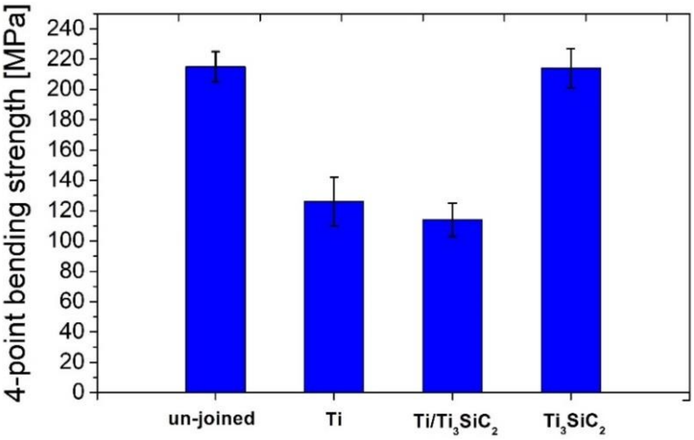

Figure 3: Four-point bending strength of the CVD-SiC joints with the Ti; Ti/Ti_3SiC_2 and Ti_3SiC_2 interlayers, compared to the reference unjoined material

CONCLUSIONS

The SPS process was successfully used to join monolithic CVD-SiC with Ti-based interlayers via reaction bonding (when Ti and Ti/Ti_3SiC_2 joining filler were used) or solid state diffusion bonding (when pre-sintered Ti_3SiC_2 foil was used). The reaction bonding led to a significant volume change and extensive reaction, which most probably resulted in the formation of large residual stresses, leading to a significant deterioration of the strength. On the other hand, when the CVD-SiC was joined via solid state diffusion, the strength of the joints was at the same level as the intrinsic strength of the CVD-SiC materials.

ACKNOWLEDGMENT

This work was supported by the Slovak Research and Development Agency under the contract no. APVV-SK-CN-2017-0040 and APVV-17-0328. The work was also supported by the MVTS project of SAS "UltraCom" within the scheme of "Support of the Seal of Excellence projects". The support of the Joint Mobility Project MAD SAV-AVCR 18-12 under the ASCR-SAS agreement is also acknowledged.

REFERENCES

[1] L. L. Snead, T. Nozawa, Y. Katoh, T. S. Byun, S. Kondo, D. A. Petti: J. Nucl. Mater. 371 (2007) 329-377

[2] Y. Katoh, L. L. Snead, T. Cheng, C. Shih, W. D. Lewis, T. Koyanagi, T. Hinoki, C. H. Henager Jr., M. Ferraris: J. Nucl. Mater. 448 (2014) 497-511

[3] S. Rizzo, S. Grasso, M. Salvo, V. Casalegno, M.J. Reece, M. Ferraris: J. Eur. Ceram. Soc. 34 (2014) 903-913

[4] X. Zhou, Y. H. Han, X. Shen, S. Du, J. Lee, Q. Huang: J. Nucl. Mater. 466 (2015) 322-327

[5] P. Tatarko, Z. Chlup, A. Mahajan, V. Casalegno, T.G. Saunders, I. Dlouhy M.J. Reece: J. Eur. Ceram. Soc. 37 (2017) 1205-1216

[6] M. Li, X. Zhou, H. Yang, S. Du, Q. Huang: Scr. Mater. 143 (2018) 149-153

[7] W. Barsoum (2013) MAX phases: properties of machinable ternary carbides and nitrides, Wiley-VCHVerlag GmbH & Co. KGaA, Germany; ISBN: 978-3-527-33011-9

POTLAČENIE RASTU ZŔN V Al_2O_3 KERAMIKE PRÍDAVKOM ZrO_2

ZIRCONIA INCLUSIONS AS AN INHIBITOR OF ALUMINA GRAIN GROWTH

L. Húlek[1], M. Orlovská[1], Ľ. Bača[1], V. Kovár[1], M. Janek[1]

[1] Department of Inorganic Materials, Institute of Inorganic Chemistry, Technology and Materials FCHPT STU, Radlinského 9, 812 37 Bratislava, Slovakia

ABSTRACT

Alumina is one of the widely used ceramic materials for different kinds of applications. In order to improve the strength of alumina after sintering one of the strategies is to eliminate the growth of grains at high temperatures, especially in the case of translucent ceramics where fully dense material is a must. The aim of this work was to study the effect of the small addition of pure zirconia on the sintering and microstructure, especially the growth of alumina grains. The alumina ceramics were prepared by casting of stable suspension with the addition of ZrO_2 inclusions in amount up to 0.5 wt. %. It was proved that even a small addition of ZrO_2 reduces grain growth during the sintering at 1400 °C for 1 h. However, a significant grain growth for both pure Al_2O_3 and alumina-doped ZrO_2 samples at the final stage of sintering (at 1600 °C) was observed.

Keywords: zirconia inclusions, alumina, grain growth, sintering, microstructure

INTRODUCTION

For the toughening of alumina ceramics, zirconia is one of the best choices due to the tetragonal to monoclinic phase transformation of Y stabilized ZrO_2 (t-YSZ) connected with the volume change [1]. Another possibility is the improvement of strength by a design of microstructure with fine grains (~ 1 μm) during pressureless sintering [2-3] two-step sintering [4-6] or fast sintering [7-10]. Seidel et al. [11] investigated the grain size dependence of fracture strength and Weibull modulus of alumina using high purity commercially available powders. They found out that the fracture strength in alumina increases with decreasing average grain size from 564 MPa at 1.7 μm to 320 MPa at 11 μm. Zhao et al. [12] studied the influence of 10 vol. % of ZrO_2 particles (stabilized with 6 mol. % Y_2O_3) on the sintering of submicron Al_2O_3 powder at 1620 °C. They observed that alumina grain sizes decrease significantly with zirconia or MgO addition compared to pure alumina. However, the addition of such dopants has a negative impact on the sintering process, but longer dwell time can compensate it. Lange et al. [13] investigated the effect of ZrO_2 inclusions in the amount of 2 vol. % and 10 vol. % on the sintering behavior of alumina. Two different zirconia inclusions were used, one cubic, stabilized with 6.6 mol. % Y_2O_3 and pure amorphous ZrO_2 powder. They prepared Al_2O_3/ZrO_2 composite specimens by consolidating of flocced slurries by filtering (slip casting) in cylindrical Teflon molds on casting plaster. After drying, the cylindrical powder compacts were isostatically pressed at 350 MPa. Their study demonstrates that the two-phase Al_2O_3/ZrO_2 powder compacts require a higher sintering temperature to achieve a comparable density relative to their constituents. In another study the same authors [14] prepared Al_2O_3/cubic-ZrO_2 (1 to 10 vol. %) composite powders which were consolidated by a colloidal method, sintered to > 98 % theoretical density at 1550 °C, and subsequently heat-treated at temperatures up to 1700 °C for grain-size measurements. They observed abnormal grain growth when the inclusion distribution was not sufficiently uniform to hinder the growth of all Al_2O_3 grains. This condition was observed for compositions containing less than 2.5 vol. % ZrO_2, where the inclusions did not fill all 4-grain junctions. On the other hand, no abnormal grain growth was achieved when a majority (or all) 4-grain junctions contained a ZrO_2 inclusion, viz., for compositions containing ≥ 5 vol. % ZrO_2. Based on the state of the art it seems that there exists a border when ZrO_2 inclusions are effective for the hindrance of alumina grain growth. However results in the literature are not always consistent because various phases and amounts of ZrO_2, exceeding 1 %, were used for investigations.

In our study, we have focused on the preparation of Al_2O_3 ceramics doped with pure monoclinic ZrO_2 in the amount up to 0.5 wt. % by the casting of suspensions. The effect of neat zirconia inclusions on the sintering and grain growth of alumina was studied.

EXPERIMENTAL

For the preparation of zirconia-doped alumina samples, commercial powders were used:

- Taimicron TM-DAR for Al_2O_3 (Taimei Chemicals Co., Ltd.), particle sizes 0.1 μm – 0.3 μm
- TZ-0 for pure ZrO_2 (Tosoh Corporation), particle size 0.04 μm

Samples were prepared by casting of suspensions into molds. Water suspensions were prepared by homogenization of 74 wt. % of the powder content using 0.8 wt. % of Dolapix CE64 (ZSCHIMMER & SCHWARZ, Germany) as a dispersing agent (with respect to the powder content) and distilled water. Pure zirconia powder was used for doping of alumina samples in the amount of 0.1, 0.15, 0.2, 0.3, 0.5 wt. % denoted here as AZ-0.1, AZ-0.15, AZ-0.2, AZ-0.3 and AZ-0.5. After homogenization, suspensions were poured into molds, dried and sintered in air at 850 °C, 1200 – 1450 °C in 50 °C steps and 1600 °C for 1 h. The density of all samples was determined using an application of the Archimedes´ method. The double weighting technique was performed to determine volume, i.e. weighting in air and in mercury using the density kit for precise balances. The theoretical density for each sample was calculated based on the densities of individual components of corundum 3.99 $g.cm^{-3}$ and monoclinic zirconia 5.68 $g.cm^{-3}$. The microstructural observation was done using both secondary and backscatter electron images taken using a scanning electron microscope JEOL JSM 7500F. The image analysis of SEM micrographs using Image J software allowed determination of the grain size. For the determination of the grain size a minimum 100 grains were taken into account.

RESULTS

In Fig. 1a, bulk density measurements for samples sintered up to 1450 °C for 1 h are displayed. In order to check if undoped and ZrO_2 doped Al_2O_3 samples are uniformly prepared, the first sintering/calcination temperature was set at 850 °C. At this temperature, samples were strong enough to withstand the manipulation and density measurements. Also, the bulk densities of brown bodies were determined. Results showed, that relative densities (RD) around 67 % independent on zirconia content were obtained. By this check, the homogeneous preparation of samples with different content of zirconia was proved as the starting point for our study (Fig. 1b). The increase of sintering temperature to 1200 °C led to the improvement of relative densities for all samples. At higher sintering temperatures (up to

1350 °C) relative density of samples decreases with increasing of zirconia content. The relative density of pure alumina at 1300 °C is higher about 7.7 % and 11.4 % in comparison to the AZ-0.2 and AZ-0.5 respectively. At this temperature, pure alumina achieved around 95 % of the theoretical density. Above this temperature, the difference in relative densities decreases and at 1400 °C all samples achieved more than 96 %. Moreover at 1450 °C the final stage of sintering seem to be finished with the RD above 98 % though still small variance among pure alumina and doped samples is present.

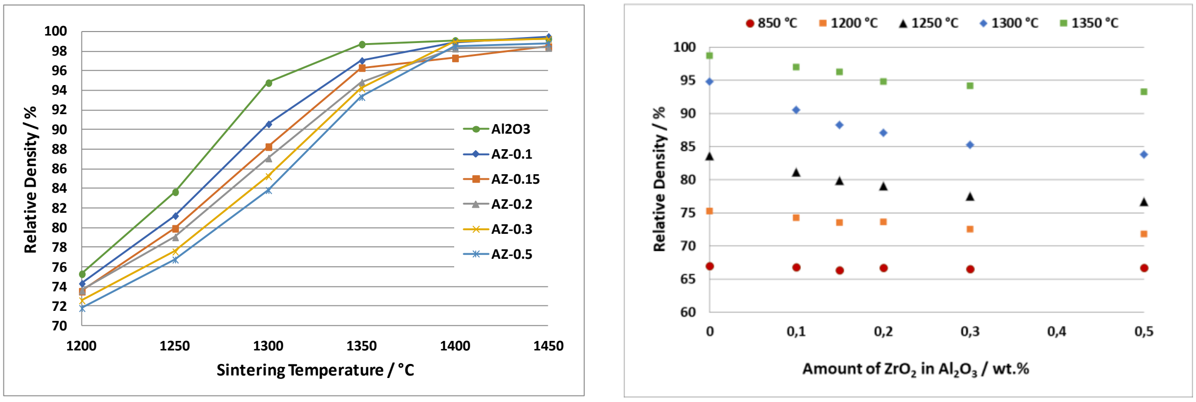

Figure 1: Results of relative density measurements in mercury a) for samples sintered up to 1450 °C; b) the dependence of RD vs. concentration of dopants for each sintering temperature.

Scanning electron microscopy (SEM) analysis of samples containing 0, 0.2 and 0.5 wt. % of pure zirconia showed that already 0.2 wt. % of ZrO_2 addition suppress the grain growth of Al_2O_3 (Fig. 2) though the RD of pure alumina reached 99.1 % when as sample AZ-0.2 just 98.3 %.

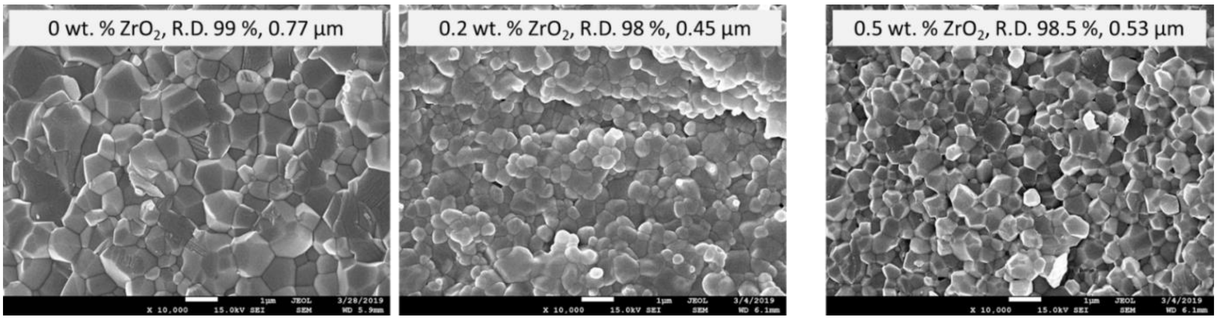

Figure 2: Fracture surface of samples sintered at 1400 °C for 1 h, magnification 10000x.

After sintering at 1600 °C, exaggerated grain growth was observed for all samples no matter how much ZrO_2 inclusions were used (Fig. 2). However, the measurement of grain size revealed that 90 % of grains of pure alumina fall into the interval of 1.24 µm - 7.60 µm. On the other hand, for sample AZ-0.2, 90 % interval contains grains with a size of 1.44 µm – 5.16 µm.

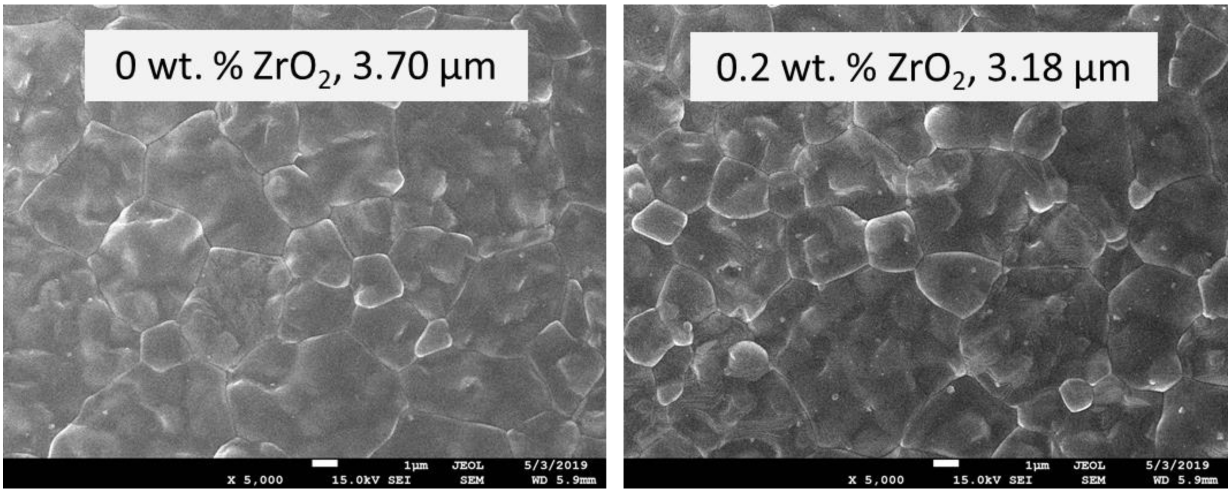

Figure 3: SEM pictures of samples sintered at 1600 °C for 1 hour, magnification 5000x.

The average grain size of pure alumina and sample AZ-0.2 was 3.26 ± 1.85 μm and 2.97 ± 1.27 μm, respectively. From these measurements can be concluded that sample AZ-0.2 contains narrower size distribution and smaller grains on the upper border of grain size distribution as pure alumina (Fig. 4).

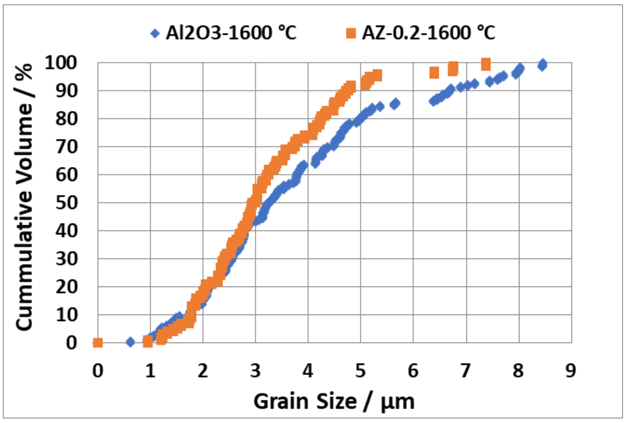

Figure 4: Grain size distribution of the pure alumina and alumina doped with 0.2 wt. % ZrO_2 (AZ-0.2) sintered at 1600 °C for 1 hour.

In other words, the suppression of grain growth is much smaller at 1600 °C, but the narrower distribution of grains can be an advantage for the strength of the alumina ceramics. As the grain growth can be explained as a migration of grain boundaries, then certain energy is needed for the moving of grain boundaries of single phases. If we consider the melting temperature of pure zirconia (2715 °C) against alumina (2072 °C) than the sintering temperature for alumina should be also lower in comparison to the zirconia. From this point of view, the grain boundary mobility of alumina should be higher. Subsequently, when the zirconia particles are used as inclusions and they don´t react with alumina (e.g. don´t form eutecticum), then the grain boundary mobility of alumina grains are pinned on the zirconia grains. As a result of the grain boundary pinning is the inhibiting of alumina grains.

CONCLUSIONS

In this work, we focused on preparation high-dense alumina with a low content of zirconia inclusions – up to 0.5 wt. %. The results unambiguously confirmed that ZrO_2 inclusions in such a small amount suppress reliably the alumina grain growth. Average grain size after sintering at 1400 °C was 0.77 ± 0.35 µm for pure Al_2O_3 compared to 0.45 ± 0.15 µm for zirconia-doped alumina (0.2 wt. %). Moreover, results from Lange et al. [2] were confirmed that the sintering process in this two-phase system (Al_2O_3-ZrO_2) is shifted to higher temperatures. To obtain similar results it was necessary to use 50 °C higher sintering temperature than it is for pure alumina. On the other hand, after sintering at 1400 °C, all samples achieved relative density 98 ~ 99 %. Due to the pinning of grain boundaries by zirconia grains the grain size distribution of ZrO_2 doped alumina after sintering at 1600°C is narrower as for pure alumina.

ACKNOWLEDGMENT

The financial support of the Slovak Grant Agency for Science VEGA grant No. 1/0906/17 and Slovak Research and Development Agency APVV-16-0341 are greatly appreciated. This work is based on the results of the project Center for Applied Research of New Materials and Technology Transfer, ITMS 26240220088, supported by the Science and Research Operational Program by the European Regional Development Fund.

REFERENCES

[1] F. Sommer, R. Landfried, F. Kern, R. Gadow, Mechanical properties of zirconia toughened alumina with 10–24 vol. % 1.5 mol % Y-TZP reinforcement, J. Eur. Ceram. Soc. 32 (2012) 3905–3910. doi:10.1016/j.jeurceramsoc.2012.02.057.

[2] P. Chantikul, S.J. Bennison, B.R. Lawn, Role of Grain Size in the Strength and R-Curve Properties of Alumina, J. Am. Ceram. Soc. 73 (1990) 2419–2427. doi:10.1111/j.1151-2916.1990.tb07607.x.

[3] A. Krell, P. Blank, The Influence of shaping method on the grain size dependence of strength in dense submicrometre alumina, J. Eur. Ceram. Soc. 16 (1996) 1189–1200. doi:10.1016/0955-2219(96)00044-1.

[4] C.-J. Wang, C.-Y. Huang, Y.-C. Wu, Two-step sintering of fine alumina–zirconia ceramics, Ceram. Int. 35 (2009) 1467–1472. doi:10.1016/j.ceramint.2008.08.001.

[5] K. Bodišová, P. Šajgalík, D. Galusek, P. Švančárek, Two-Stage Sintering of Alumina with Submicrometer Grain Size, J. Am. Ceram. Soc. 90 (2007) 330–332. doi:10.1111/j.1551-2916.2006.01408.x.

[6] S. Yan, Z. Yin, J. Yuan, W. Xu, M. Chen, J. Ye, Microstructure and properties of submicron grained alumina ceramic tool material prepared by two-step microwave sintering, Ceram. Int. 44 (2018) 17479–17485. doi:10.1016/j.ceramint.2018.06.217.

[7] J.-C. M'Peko, Flash sintering in well-dispersed insulator-ionic conductor composites: The case of diphasic alumina-zirconia (Al2O3-3YSZ) system, Scr. Mater. 175 (2020) 38–42. doi:10.1016/j.scriptamat.2019.09.004.

[8] V. Prajzler, D. Salamon, K. Maca, Pressure-less rapid rate sintering of pre-sintered alumina and zirconia ceramics, Ceram. Int. (2018). doi:10.1016/j.ceramint.2018.03.132.

[9] M. Biesuz, V.M. Sglavo, Flash sintering of alumina: Effect of different operating conditions on densification, J. Eur. Ceram. Soc. 36 (2016) 2535–2542. doi:10.1016/j.jeurceramsoc.2016.03.021.

[10] R.R. Menezes, P.M. Souto, R.H.G.A. Kiminami, Microwave fast sintering of submicrometer alumina, Mater. Res. 13 (2010) 345–350. doi:10.1590/S1516-14392010000300011.

[11] J. Seidel, N. Claussen, J. Rödel, Reliability of alumina ceramics: Effect of grain size, J. Eur. Ceram. Soc. 15 (1995) 395–404. doi:10.1016/0955-2219(95)91430-V.

[12] J. ZHAO, M.P. HARMER, Effect of Pore Distribution on Microstructure Development: II, First- and Second-Generation Pores, J. Am. Ceram. Soc. 71 (1988) 530–539. doi:10.1111/j.1151-2916.1988.tb05916.x.

[13] F.F. LANGE, T. YAMAGUCHI, B.I. DAVIS, P.E.D. MORGAN, Effect of ZrO2 Inclusions on the Sinterability of Al2O3, J. Am. Ceram. Soc. 71 (1988) 446–448. doi:10.1111/j.1151-2916.1988.tb05892.x.

[14] F.F. LANGE, M.M. HIRLINGER, Hindrance of Grain Growth in Al2O3 by ZrO2 Inclusions., J. Am. Ceram. Soc. 67 (2006) 164–168. doi:10.1111/j.1151-2916.1984.tb19734.x.

PRÍPRAVA A KORÓZIA KERAMICKÝCH VRSTIEV PRIPRAVENÝCH Z ORGANOKREMIČITÝCH PREKURZOROV S PASÍVNYMI PLNIVAMI

PREPARATION AND CORROSION BEHAVIOUR OF PDC LAYERS WITH PASSIVE FILLERS

M. Parchovianský[1], I. Parchovianská[1], P. Švančárek[2], G. Motz[3], D. Galusek[2]

[1]*FunGlass, Alexander Dubček University of Trenčín, Študentská 2, 911 50 Trenčín, Slovakia*
[2]*Joint Glass Centre of the IIC SAS, TnUAD and FChFT STU, FunGlass, Študentská 2, 911 50 Trenčín, Slovakia*
[3]*University of Bayreuth, Ceramic Materials Engineering, D-95440 Bayreuth, Germany*

ABSTRACT

The work is aimed at development of a protective, dense and well adherent coating system on steel. For that purpose, four compositions of a double layer coating consisting of a polymer derived ceramic (PDC) bond coat, and a PDC top coat with glass and ceramic fillers were prepared. Two PDC layers (D2, D3) are studied with respect to their corrosion resistance at temperatures up to 950 °C. YAG, c-ZrO_2, and $Ba(AlSiO_4)_2$ are identified at the corroded surface of the coatings using X-ray diffraction. A significant weight gain of the unprotected steel is measured after all experiments. Corrosion tests of the protected steel show a zero or negligible weight gain after oxidation at 850 °C and 950 °C.

Keywords: polymer derived ceramics, passive fillers, corrosion

INTRODUCTION

Polymer derived ceramic (PDC) coatings have been intensively studied in the last years. PDC are an extremely promising class of materials with unique features [1]. Aspects such as the relatively low preparation temperatures (typically between 700 and 1000 °C), a wide choice of relatively low cost precursors, easy handling, a wide range of achievable compositions and simple deposition methods (dip coating [2], spray coating [3], spin coating [4], tape casting [5]) are beneficial. PDC coatings are also promising materials for high temperature applications as they have an excellent corrosion and thermal shock resistance and are stable at high temperatures [6]. Hence these PDC coatings can protect metallic components from corrosive combustion gases, e.g. used for the construction of heat exchangers in thermal power plants or waste incinerators, However, the high coating shrinkage during the polymer-to-ceramic conversion is a serious problem. It can be as high as 80 vol. % and leads to cracks and delamination from the substrates [7]. The protective effect is also significantly reduced if the coatings are too porous. A solution has been proposed in the pioneering work of Greil [8] on active and passive fillers. Active fillers, which increase in volume during pyrolysis, include $ZrSi_2$, $TiSi_2$ or powders such as Al, Cr, Fe, Si. Passive fillers include ZrO_2, BN, and various types of commercially available glass frits and remain inert during pyrolysis. Double layer coatings of a PDC bond coat below a PDC top coat with glass and ceramic fillers appear to be also an efficient solution [9].

The presented work is focused on the preparation of glass/ceramic composite coatings on stainless steel substrates by a hybrid process of the preparation of ceramics from organosilicon precursors based on polysilazanes. The prepared coatings were studied in terms of their microstructure, phase composition and corrosion resistance.

EXPERIMENTAL

Stainless steel (AISI 441) was cut into sheets with the dimensions of 10x15x1 mm^3. The corners and edges of the steel samples were chamfered with sandpaper. After cutting, the stainless steel was cleaned in an ultrasonic bath using acetone, ethanol a deionized water for 20 min and then dried. Two different commercially available polysilazanes, PHPS (perhydropolysilazane) and Durazane 1800 (both Merck KGaA, Germany) were used as pre-ceramic precursors. The pre-treated substrates were dip-coated (Relamatic RDC 15, Switzerland) in the PHPS solution to obtain the bond-coat. The curing of the PHPS bond-coat was carried out in air at 450 °C for 1h with heating rate of 3 K/min (N41/H, Nabertherm, Germany). The subsequently applied top coat was prepared by mixing defined volume fractions of a liquid polysilazane HTT1800, ceramic filler particles: yttria-stabilized zirconia (8-YSZ, Inframat, USA), Al_2O_3-Y_2O_3-ZrO_2 (AYZ) precursor powder prepared by sol gel Pechinni method and commercial glass G018-281 (Schott, Germany). In the final step, the pyrolysis of the all prepared coatings was performed in air at 850 °C with the heating and cooling rate of 3 K/min and a holding time 1 h. The prepared compositions are listed in the Tab. 1. The SEM/EDXS examination of the coatings after pyrolysis was conducted with the use of a JEOL JSM 7600 F (JEOL, Japan) scanning electron microscope at an acceleration voltage of 20 kV and was focused at evaluation of homogeneity, adhesion and possible failures of the coatings. X-ray powder diffraction analysis (CuKα, 2θ range 10-80°, Empyrean DY1098, PANalytical B.V., Netherlands) was used to investigate the phase composition of the coatings after corrosion tests. The corrosion tests were performed in a high temperature horizontal electric tube furnace (Clasic 0213T, Clasic, Praha, Czech Republic) in flowing atmosphere of synthetic air (purity 99.5, Siad, Slovakia) at the temperature of 950 °C with heating rate of 10 °C/min and exposure time of 24h.

Table1: Compositions of the composite top coats after pyrolysis (vol. %).

COMPOSITIONS	HTT1800	YSZ	G018-281	AYZ20
C2c	30	35	35	-
C2d	35	32,5	32,5	-
D2	25	20	35	20
D3	30	20	30	20

RESULTS

SEM micrographs illustrating the cross-sections of all prepared compositions after pyrolysis are shown in Fig. 1. After a thermal treatment in air at 850 °C, uniform, almost dense and crack-free composite coatings on stainless steel were achieved. Furthermore, the fillers particles (YSZ, AYZ) within the coating were distributed homogeneously. The filler particles are embedded and surrounded by molten glass, and porous precursor matrix. The filler particles are well coated with the HTT1800 precursor, which builds up the matrix, and also acts as an adhesive between the particles. In the case of compositions C2c and C2d, small closed pores were observed within the coatings. On the other hand, no pores were observed in the samples containing AYZ filler (compositions D2 and D3). On the basis of the analyzed cross sectional micrographs of the coatings D2 and D3 (Fig. 1), it can be concluded that the addition of the AYZ powder precursor was effective in preventing the formation of cracks and pores. The results of EDXS mapping on the cross-section of D3 sample including the steel substrate are shown in (Fig. 1). The main components of the coating D3 detected by EDXS were silicon, zirconium, yttrium, aluminium, barium and oxygen. Intact PHPS bond-coat with a thickness of approximately 1 µm is also visible.

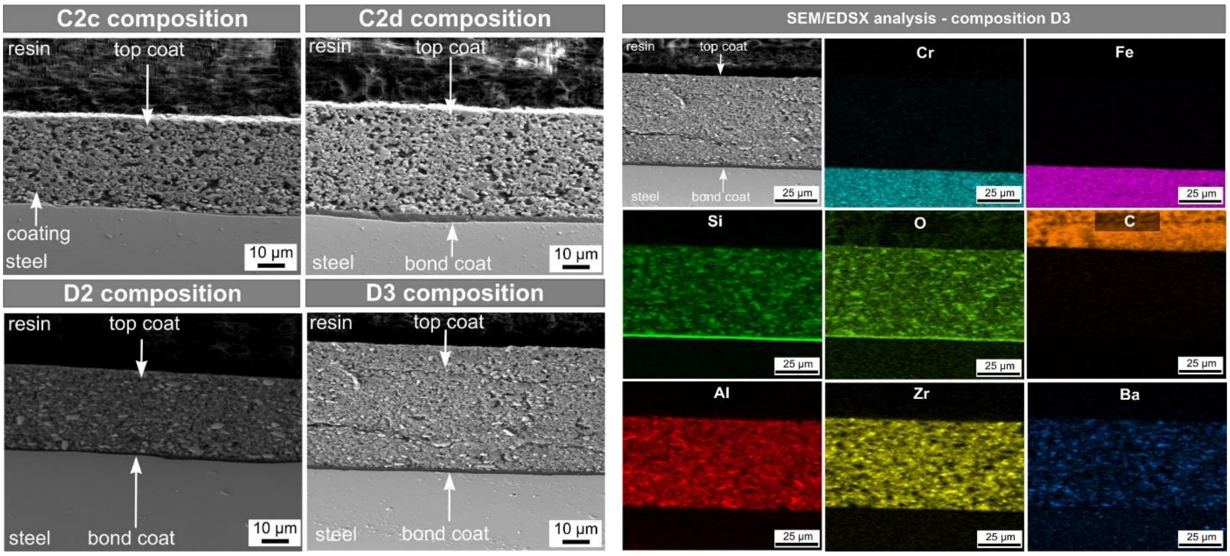

Figure1: Cross-sectional SEM micrographs of the prepared coatings after pyrolysis in air and SEM/EDXS analysis of D3 composition

To assess the protective function of the coatings in this work, weight changes of the coated and uncoated samples after the oxidation tests were determined. Weight changes of uncoated and coated samples after different exposures at temperature 950 °C are shown in Table 2. A significant weight gain of the unprotected steel was measured after all experiments due to the oxide scale growth. Corrosion tests of the protected steel showed a zero or negligible weight gain after 950 °C compared to the uncoated stainless steel.

Table 2: Mass gain of AISI 441 steel and selected coatings after exposure to temperature 950 °C and various exposure times of corrosion

	D2	**D3**	**Uncoated steel**
1h	0	0	0.238
24 h	0	0	0.486
48 h	0.024	0.051	0.613

After oxidation tests, the selected compositions were further examined by the XRD to identify the formation of various phases at different temperatures and duration of heat treatment during corrosion tests. XRD patterns after corrosion tests of compositions D2 and D3 are shown in Fig. 2 a, b. The XRD patterns acquired from the D2 and D3 coated steel only shows the presence of the fillers c-ZrO_2, as well as the crystallization product YAG after all experiments. $Ba(AlSiO_4)_2$-celsian is additionally observed after corrosion after 24 h exposure at 950 °C. The results of the XRD measurements along with weigh gain measurement indicated that the coated stainless steel substrates were not oxidized at the applied tested temperatures.

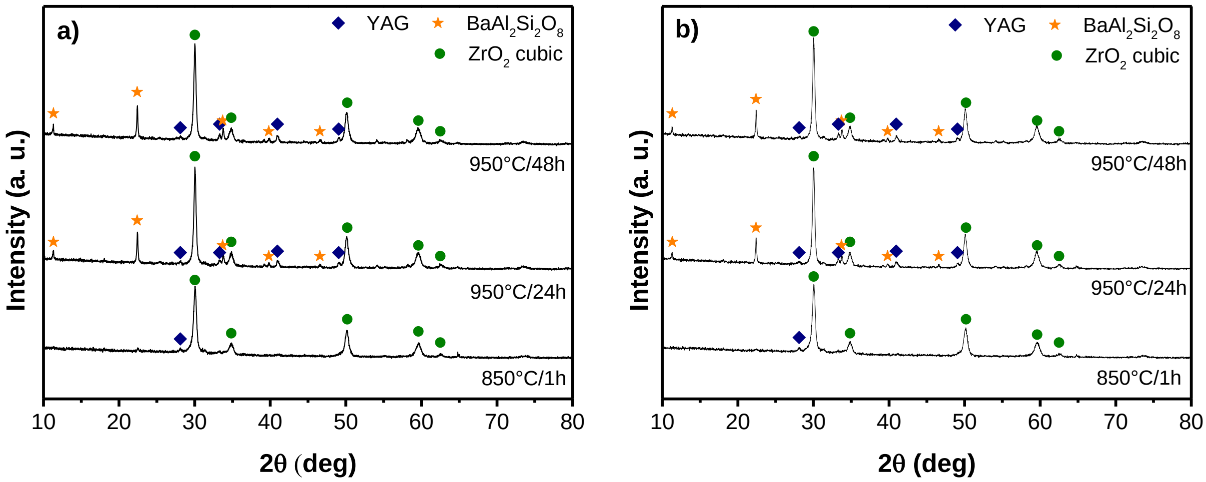

Figure 2: XRD-patterns after corrosion tests a) D2 composition, b) D3 composition

CONCLUSIONS

Protective coatings with a low porosity and a good adhesion to the stainless steel substrates were produced. Measurable weight changes were achieved by exposure of steel and coatings to corrosion in synthetic air. Their protective effect up to 950 °C is demonstrated by the presented results. No corrosion products were identified on coated samples.

ACKNOWLEDGMENT

Financial support of this work by the grant APVV 0014-15, and the Deutscher Akademischer Austauschdienst (DAAD) grant scheme is gratefully acknowledged. This paper was also created in the frame of the project Centre for Functional and Surface Functionalized Glass (CEGLASS), ITMS code is 313011R453, operational program Research and innovation, co-funded from European Regional Development Fund.

REFERENCES

[1] Greil P. Polymer Derived Engineering Ceramics. Adv Eng Mater. 2000;2(6):339–48.

[2] Kappa M, Kebianyor A, Scheffler M. A two-component preceramic polymer system for structured coatings on metals, Thin Solid Films. 2010;519:301–305.

[3] Goerke O, Feike E, Heine T, Trampert A, Schubert H. Ceramic coatings processed by spraying of siloxane precursors (polymer-spraying). J Eur Ceram Soc. 2004;24(7):2141–7.

[4] Morlier A, Cros S, Garandet JP, Alberola N. Thin gas-barrier silica layers from perhydropolysilazane obtained through low temperature curings: A comparative study. Thin Solid Films. 2012;524:62–66.

[5] Cromme P, Scheffler M, Greil P. Ceramic tapes from preceramic polymers, Adv Eng Mater. 2002;4:873–7.

[6] Wang K, Günthner M, Motz G, Bordia RK. High performance environmental barrier coatings, Part II: Active filler loaded SiOC system for superalloys. J Eur Ceram Soc. 2011;31(15):3011–20.

[7] Günthner M, Wang K, Bordia RK, Motz G. Conversion behaviour and resulting mechanical properties of polysilazane-based coatings. J Eur Ceram Soc. 2012;32(9):1883–92.

[8] Greil P. Near Net Shape Manufacturing of Ceramic Components. J Eur Ceram Soc. 1998;18:1905-1914.

[9] Barroso GS, Krenkel W, Motz G. Low thermal conductivity coating system for application up to 1000 °C by simple PDC processing with active and passive fillers. J Eur Ceram Soc. 2015;35(12):3339–48.

CORROSION

ŠTÚDIUM SKLOKERAMICKÝCH PDC POVLAKOV APLIKOVANÝCH NA RÔZNE ČISTENÉ OCEĽOVÉ SUBSTRÁTY

INVESTIGATION OF PDC GLASS/CERAMIC COATINGS APPLIED TO DIFFERENT PRE-TREATED STAINLESS STEEL SUBSTRATES

I. Parchovianská[1], M. Parchovianský[1], P. Švančárek[1], G. Motz[2], D. Galusek[1]

[1]*FunGlass - Centre for Functional and Surface Functionalized Glass, Študentská 2, 911 50 Trenčín, Slovakia*
[2] *University of Bayreuth, Ceramic Materials Engineering (CME), D-95440 Bayreuth, Germany*

ABSTRACT

This study describes the development of a corrosion resistant environmental barrier coatings on AISI 441 stainless steel substrates. For this purpose, double layer polymer derived ceramic (PDC) coating systems consisting of a bond coat and a top coat were developed. In order to achieve well adherent coatings without failures, stainless steel substrates were cleaned by three different cleaning procedures. Pre-treatment by ultrasonic cleaning in acetone, ethanol and deionised water was found to be the most effective and the resultant D2-AYZ coating, pyrolysed at 850 °C, showed good adhesion since no gaps or cracks propagating along the metal/coating interface were detected.

Keywords: bond coat, PDC coating, stainless steel

INTRODUCTION

The preparation of ceramics and ceramic composites by controlled thermal decomposition (pyrolysis) of organosilicon polymeric precursors has received attention over the past two decades due to their benefits over traditional methods for ceramic processing [1]. Polymer-derived ceramics (PDCs) provide a simple way to produce a number of technologically important ceramic components, such as fibers, coatings, porous media and complex bulk parts, which, in principle, cannot be prepared using powder technology [2]. The properties of PDCs can be also successfully utilized in anti-corrosion coatings on metals, especially steels, used in construction of heat exchangers in power plants and communal waste incinerators, where they undergo a long exposure to corrosive combustion gases at high temperatures [3-4]. However, the high volume shrinkage and density increase of the coatings during the polymer-to-ceramics conversion of organosilicon precursors poses a serious problem. The accompanying release of gases not only leads to unwanted and uncontrollable porosity but also to significant shrinkage resulting in crack formation and delamination of the protective coating from the metallic substrate [5-6]. The effective method to reduce the volume change due to polymer-to-ceramics conversion is the incorporation of active or passive fillers. Active fillers, which are based on metals, intermetallics or ceramics (e.g. Fe, Si, Al, Cr [7], $ZrSi_2$ [8], $TiSi_2$ [9]), may increase their volume during pyrolysis by reacting with the products released during the polymer decomposition. The main functions of active fillers are to provide a stabilizing network of filler reaction products and to increase the ceramic yield. As the name implies, passive fillers remain completely inert throughout the

PDC preparation process. Their function is to eliminate the presence of macro-defects by filling the free space in the material without changing its volume. Typical examples of passive fillers are YSZ [10], Si_3N_4 [11], Al_2O_3 [12] and BN [13] or various types of commercially available glass frits [7]. By incorporation of glass fillers, it is also possible to generate coatings with additional functionalities and increase the efficiency as environmental barrier coating (EBC).

The presented work is focused on the preparation of passive fillers loaded glass/ceramic composite coatings on stainless steel substrates by a hybrid process of the preparation of ceramics from organosilicon precursors based on polysilazanes. The influence of different cleaning procedures on the adhesion of the PDC coating to the stainless steel substrates was also examined.

EXPERIMENTAL

Stainless steel (AISI441) plates were cut into 10 x 15 mm sheets. In order to achieve well adherent coatings without failures, stainless steel substrates were cleaned by three different cleaning procedures, such as 3-steps ultrasonic vibration cleaning in acetone, ethanol and deionised water, sandblasting with glass beads and chemical etching with Kroll's reagent. The pre-treated substrates were then dip-coated (dip-coater RDC 15, Relamatic, Switzerland) in perhydropolysilazane (PHPS, Merck KGaA, Germany) solution to obtain bond-coat. The annealing of the PHPS bond-coat was carried out in air at 450 °C for 1 h with heating and cooling rates of 5 °C/min (Nabertherm® N41/H, Nabertherm, Germany). The subsequently applied top-coating, denoted as D2-AYZ, consisted of defined volume fractions (see Tab. 1) of ceramic, matrix forming liquid, polysilazane HTT1800 precursor (Merck KGaA, Germany), ceramic filler particles yttria-stabilized zirconia (YSZ, H. C. Starck GmbH, Germany), Al_2O_3-Y_20_3-ZrO_2 powder (AYZ) prepared via Pechini method and commercial glass frits (G018-281, Schott AG). The resulting mixture was applied by spray-coating technique. All coated samples were heat treated in air at 850°C for 1 h with heating and cooling rates of 5 °C/min.

Table 1: Compositions of the D2-AYZ coating before pyrolysis (vol. %) and estimated thermal expansion coefficient (10^{-6}/K)

	HTT1800	**YSZ**	**G018-281**	**AYZ**	**CTE**
D2-AYZ	25	20	35	20	8.7

The surface morphology of pre-treated samples was examined by scanning electron microscopy (SEM, JEOL JSM 7600 F) and roughness parameters were observed using atomic force microscope (Renishaw InVia). For detailed examination of the coating/metal interface, the samples were cold-mounted in polymeric resin and carefully polished to prepare cross sections. Then the examination of the coatings was conducted with the use of SEM and was focused at evaluation of adhesion, homogeneity and possible failures of the coatings.

RESULTS

In order to achieve well adherent and homogeneous coatings without failures, different cleaning procedures of the steel substrates were investigated. The results of SEM analysis

(Fig. 1) showed that chemical etching results in a surface with irregular morphology with slight roughening of the surface (Rz = 0.88 µm) compared to ultrasonically cleaned substrates (Rz = 0.27 µm). More uniform and compacted surface was achieved by the sandblasting with glass beads, while the average surface roughness Rz increased to a value of 1.7 µm.

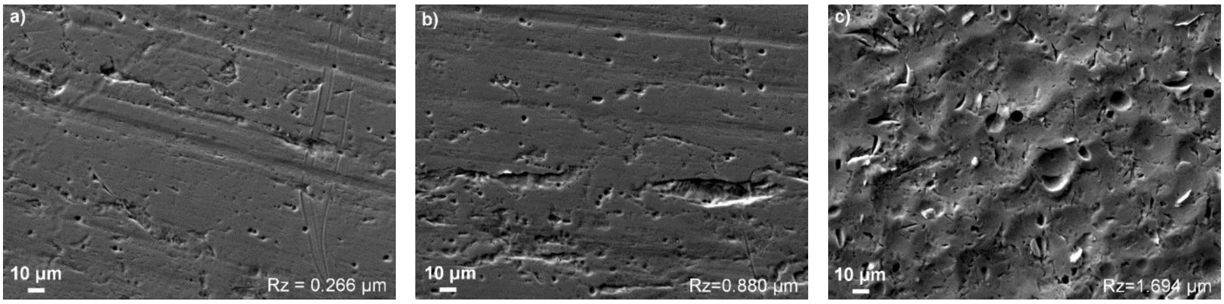

Figure 1: SEM micrographs of steel surfaces treated by different cleaning procedures: a) ultrasonic cleaning, b) chemical etching, c) sandblasting

To investigate the bonding between the bond coat and steel substrate treated by different cleaning procedures, cross-sections of the optimized composition D2-AYZ were prepared for SEM examination (Fig. 2). The chemical etching with the Kroll´s reagent caused considerable changes in the microstructure and the chemistry of stainless steel and as a result, the bond coat peeled off the substrate (Fig. 2b). In the case of sandblasted samples, the sharp borders and peaks initiated the formation of cracks and spallation of the bond coat in the coatings (Fig. 2c). On the other side, pre-treatment by ultrasonic cleaning in acetone, ethanol and deionized water was found to be the most effective, since no spallation or cracking was observed in the whole cross section (Fig. 2a). Moreover, ultrasonically cleaned steel surface is uniformly wetted and covered by the about 1 µm thick PHPS bond coat. In order to clarify the bonding between the coating and steel, the D2-AYZ coating was tested under prolonged static exposure for 24 hours in air at 850 °C. After heat treatment, all D2-AYZ coatings, except for those applied to substrates cleaned in ultrasonic bath, delaminated or significant cracking was observed in the bond coat.

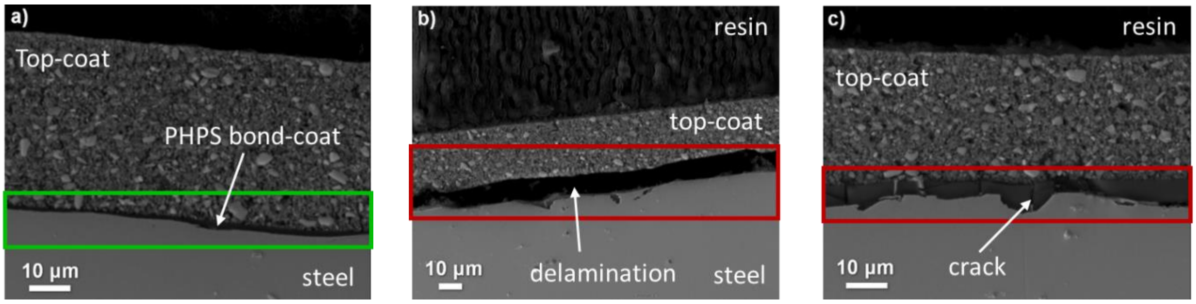

Figure 2: SEM cross-sectional micrographs of the coating D2-AYZ applied to different pre- treated steel substrates: a) ultrasonic cleaning, b) chemical etching, c) sandblasting

As can be seen in Fig. 2a), the resultant coating with the thickness up to 41 µm applied to ultrasonically cleaned substrates is almost fully dense, with no cracking or delamination and it is expected to prevent the access of aggressive environment to the steel substrate at elevated temperatures. The PHPS-based bond coat increased the adhesion of top coatings and acted as a diffusion barrier against oxidation during the pyrolysis of the coating system due to the formation of a SiON-based ceramics [5]. Additionally, this microstructure system with residual porosity is beneficial to the thermal stability of the coatings, as it contributes to the reduction of the thermal stresses during heating and cooling cycles.

CONCLUSIONS

The investigations showed that the pre-treatment as well as the application of a PHPS bond coat on stainless steel substrates are very important to achieve well adherent composite coatings. It was found that the most effective pre-treatment is 3-steps ultrasonic vibration cleaning in acetone, ethanol and deionized water. The results confirmed that the combination of PDC with tailored fillers and glass systems enable the processing of dense and crack free coating system on stainless steel.

ACKNOWLEDGMENT

This paper is a part of dissemination activities of project FunGlass. This project has received funding from the European Union´s Horizon 2020 research and innovation programme under grant agreement No 739566. This paper was created in the frame of the project Centre for Functional and Surface Functionalized Glass (CEGLASS), ITMS code is 313011R453.

REFERENCES

[1] Colombo P, Mera G, Riedel R, Sorar GD. Polymer-derived ceramics: 40 Years of research and innovation in advanced ceramics. J Am Ceram Soc. 2010;93(7):1805–37.

[2] Riedel R, Passing G, Schonfelder H, Brook RJ. Synthesis of dense silicon-based ceramics at low-temperatures. Nature. 1992 (355) 714-717.

[3] Wang K, Unger J, Torrey JD, Flinn BD, Bordia RK. Corrosion resistant polymer derived ceramic composite environmental barrier coatings. J Eur Ceram Soc. 2014;34(15):3597–606.

[4] Wang K, Günthner M, Motz G, Bordia RK. High performance environmental barrier coatings, Part II: Active filler loaded SiOC system for superalloys. J Eur Ceram Soc. 2011;31(15):3011–20

[5] Günthner M, Kraus T, Dierdorf A, Decker D, Krenkel W, Motz G. Advanced coatings on the basis of Si(C)N precursors for protection of steel against oxidation. J Eur Ceram Soc. 2009;29(10):2061–8

[6] Günthner M, Wang K, Bordia RK, Motz G. Conversion behaviour and resulting mechanical properties of polysilazane-based coatings. J Eur Ceram Soc. 2012;32(9):1883–92

[7] Schütz A, Günthner M, Motz G, Greißl O, Glatzel U. Characterisation of novel precursor-derived ceramic coatings with glass filler particles on steel substrates. Surf Coatings Technol. 2012;207:319–27

[8] Parchovianský M, Barroso G, Petríková I, Motz G, Galuskova D, Galusek D. Polymer derived glass ceramic layers for corrosion protection of metals. Ceram Trans. 2016;256:187–200.

[9] Torrey JD, Bordia RK. Mechanical properties of polymer-derived ceramic composite coatings on steel. J Eur Ceram Soc. 2008;28(1):253–7.

[10] Barroso GS, Krenkel W, Motz G. Low thermal conductivity coating system for application up to 1000 °C by simple PDC processing with active and passive fillers. J Eur Ceram Soc. 2015;35(12):3339–48

[11] Bernardo E, Colombo P, Hampshire S. SiAlON-based ceramics from filled preceramic polymers. J Am Ceram Soc. 2006;89(12):3839–42

[12] Labrousse M, Nanot M, Boch P, Chassagneux E. Ex-polymer SiC coatings with Al2O3 particulates as filler materials. Ceram Int. 1993;19(4):259–67

[13] Kraus T, Günthner M, Krenkel W, Motz G. cBN particle filled SiCN precursor coatings. Adv Appl Ceram. 2009;108(8):476–82

VPLYV SUBSTITÚCIE ZINKU A BÓRU NA PROCES ROZPÚŠŤANIA 45S5 V RÔZNYCH KORÓZNYCH MÉDIÁCH

INFLUENCE OF ZINC AND BORON SUBSTITUTION ON DISSOLUTION PROCESS OF 45S5 IN DIFFERENT CORROSIVE MEDIA

A. Švančárková[1,2], D. Galusková[2], H. Kaňková[2], D. Galusek[2], M. Michálek[2]

[1]*Fakulta chemickej a potravinárske technológie STU, Radlinského 9, 812 37 Bratislava*
[2]*TnUAD-FunGlass Študentská 2, 91150 Trenčín*

ABSTRACT

In this study, the effect of different solution media to the corrosion behavior of 45S5 bioactive glass (BG) and 45S5 dopped with boron (4 wt%) or zinc (4 wt%) was investigated. In vitro tests were carried out in the following solutions: simulated body fluid (pH 7.4), deionized water (pH 6.5, conductivity 0.054 $\mu s/cm^3$), acetic acid buffered with sodium acetate (pH 4) solution simulating inflammatory environment. The fastest ion release from glass was observed in acidic environment. The release of zinc as a potential antibacterial inhibitor, was detected mainly in acetic acid/sodium acetate solution, in other solutions was meeting the limit of quantification.

Keywords: bioactive glass, dissolution, acetic acid/sodium acetate buffer, simulated body fluid

INTRODUCTION

The 45S5 bioglass (BG) by Hench [1] with weight composition 45% SiO_2, 24.5%CaO, 24.5 Na_2O and 6% P_2O_5 is a bioactive material that stimulates bone repair. In aqueous environment, this material undergoes a series of reactions to create a surface layer of hydroxy-apatite (HA) and hydroxy-carbonate apatite [2]. The incorporation of ions in BG can enhance the therapeutic effects of material. For example, zinc is important element of enzyme alkaline phosphataze and co–factor for over other 400 enzymes. Zinc is also key mediator of bone matrix mineralization [3] and plays significant role in bone formation [4]. Additionally, zinc is well known for its antibacterial effects. Boron represents a potential element to improve the properties of bioglass. In some studies was reported that deficiency of boron resulted in the alteration or loss of important physiological functions associated with the metabolism of calcium and formation and remodeling of bone tissue [5, 6]. Recent studies showed the increasing of angiogenesis in bioglass containing boron [7]. The objective of this study is therefore to characterise the behavior of the bioglass 45S5 as a model glass system as well the bioactive glass dopped with therapeutic ions in different environment simulating either human plasma or inflammantory environment.

EXPERIMENTAL

Glass preparation

Glass powders with theoretical composition (in wt%) described in Tab.1. were fabricated by conventional melting. Bioactive glass of 45S5 composition, 45S5+4B and 45S5+4Zn were prepared by mixing raw materials of the analytical grade purity (≥99%): SiO_2, $CaCO_3$, ZnO, Na_2CO_3, H_3BO_3 and $Na_5P_3O_{10}$. The mixture was melted in Pt-10%/Rh crucible in a furnace at 1300°C for two hours in ambient atmosphere. The homogeneity was ensured by repeated hand mixing of the melt. Then the molten glass was poured onto a stainless steel plate. The sample was tempered in a muffle furnace for 30 min at 560°C (45S5+ 4B and 45S5 + 4Zn glass 1 hour at 540˚C) and then the furnace was switched off. The prepared bulk glass was crushed and sieved to achive particle size ≤ 25µm. Schott Vitrixx® Bioactive Glass with the grain size 4-20µm was commercially purchased.

Table 1: Comparison of the theoretical and experimental composition (ICP OES analyses of samples decomposed in mineral acids) of tested bioactive glass in wt%.

wt%	**45S5 Schott**		**45S5**		**45S5+4B**		**45S5+4Zn**	
Oxide	Theor Comp.	Experim. comp.	Theor. Comp.	Experim. comp.	Theor. Comp.	Experim .comp.	Theor. Comp.	Experim .comp.
SiO_2	45	45.3±1*	45	42±5*	44.5	42.9±2*	44.5	42,3±2*
P_2O_5	6	6±1	6	6.1±1	5.9	8.5±3	5.9	9±3
CaO	24.5	25.6±2	24.5	23.5±2	21.4	21.7±1	21.4	21.7±1
Na_2O	24.5	23.1±4	24.5	23.4±2	24.2	23.1±1	24.2	23.3±2
ZnO	-	-	-	-	-	-	4	3.7±0.8
B_2O_5	-	-	-	-	4	3.9±0.6	-	-

**normalized to 100%*

Dissolution experiments

Dissolution studies were performed at the static conditions in the neutral and acidic environment. Acetic acid/sodium acetate (HAc/NaAc) buffer solution was prepared according to Blochberger [8] by adding 6.03ml of 99.5% acetic acid to 900 ml of deionized water with the conductivity 0.054µs/cm^3 and adjusting the pH value to 4±0.05 by adding 1M NaOH solution and filling the volume to 1 liter. The SBF solution was prepared according to Kokubo and Takadama [9]. The 35 mg of glass powder was immersed in 25 ml of solution at 37˚C for 1, 2, 4, 8 and 24 hours. After each time period, samples were filtred through porosity filter paper and concentrations of corrosion solutions were analysed using inductively coupled plasma optical emission spectrometer (ICP-OES, Agilent 5100). Each experiment was performed in three parallels and released ions (in mg/L) were also presented as normalized leached values of elements -NL (in mg of element/g of element in initial powder).

NL values were calculated based on the following equation:

$$NL = \frac{c_i * V}{w_i * m_s} \tag{1}$$

where NL is the normalized leached value of element (*i*) in $mg.g^{-1}$, V is volume of corrosion medium, w_i - mass fraction of an element in sample, c_i - concentration of an element in sample and m_s - is weight of the initial powder.

RESULTS

In deionized water, we observed increase of Na, Si and Ca into solution (Fig.1). Phosphorus concentration decreased gradually during dissolution process in all studied glass systems. For the sample 45S5 dopped by Zn was observed the slowest ion release comparing to undopped systems. Sodium was released from the tested glass at the high speed, this trend has occurred in all materials. It could be caused by rapid exchange of Na^+ with H^+ or H_3O^+ from solution, typical for bioglass in aqueous solutions:

$$\text{Si–O–Na}_{(aq)} + H^+_{(aq)} + OH^-_{(aq)} = \text{Si–OH}_{(aq)} + Na^+_{(aq)} + OH^-_{(aq)}$$

results in producing silanols [2]. The pH value increased quickly at the beginning of the test in deionized water to the value 10.4 due to increase of OH^- groups in the solution.

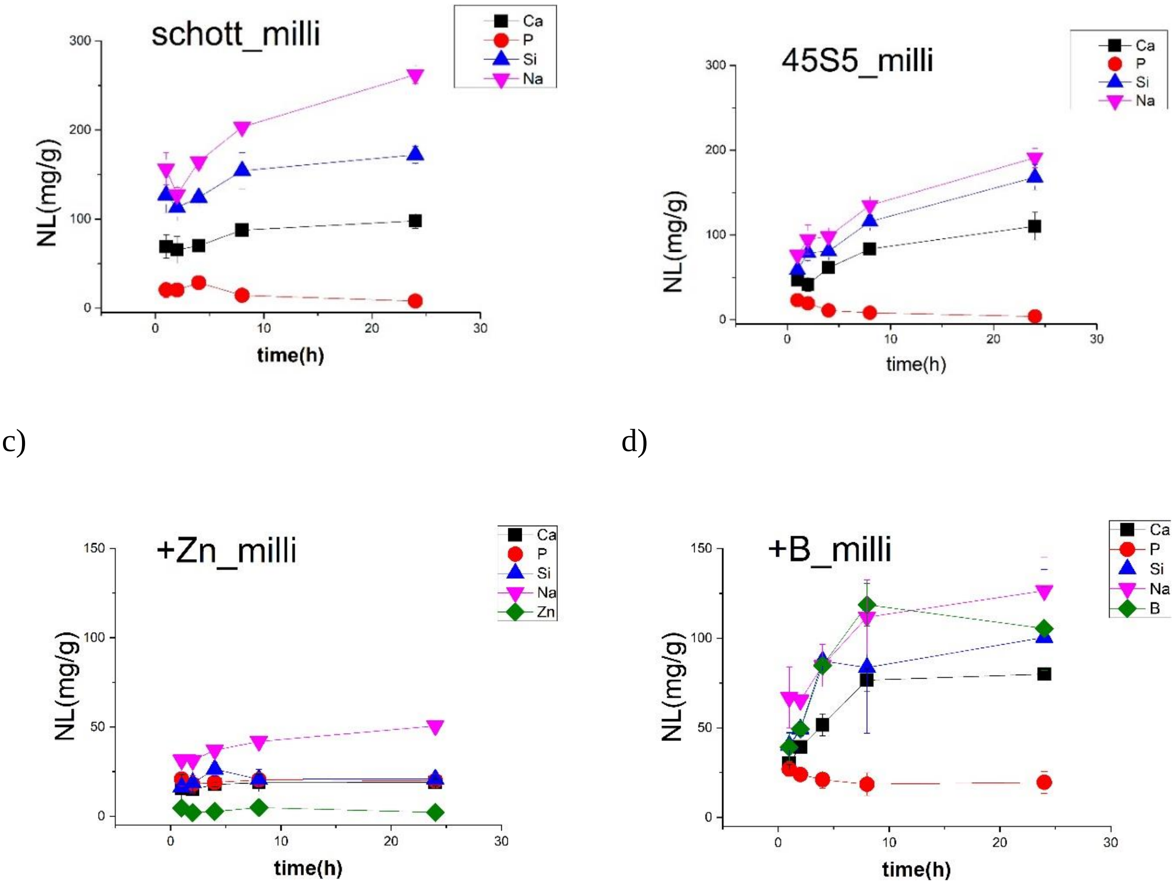

a) b) c) d)

Figure 1: Time dependence of the ions released from the studied glass systems into deionized water of a) Schott, b) 45S5, c) 45S5+4Zn, d) 45S5+B.

In SBF solution, silicon concentration increased in all material rapidly during the first 1-2 h (Fig.2). This initial faster release of Si occurs during the second stage of the deposition of HA layer on the surface of BG [10]. During this second stage Si–O–Si bonds are broken and soluble silica is release to the solution. Rapidly release of Na^+ ions to solution in the first step we did not monitor because of problem to analyze sodium in SBF trustworthy. The main cause is the high sodium content in the solution of simulated body fluid. The third stage of the surface deposition of HA consists form of a hydrated silica-rich layer on the surface. The reason for decrease of phosphorous in solution is the strong adsorption of phosphorus ions from SBF solution to the glass surface [11]. Adsorption of phosphorus ions from SBF is due to exceeding solution saturation concentrations necessary to form Ca–P rich reaction layer (the fourth stage of the deposition of HA layer [10]). In samples 45S5+Zn or in 45S5+B we did not observed so significant decrease of phosphorus. The reason can be higher content of phosphorus in this untreated samples (Tab.1), also it is not necessary to pump so much ions of phosphorus for creating HA layer from the SBF.

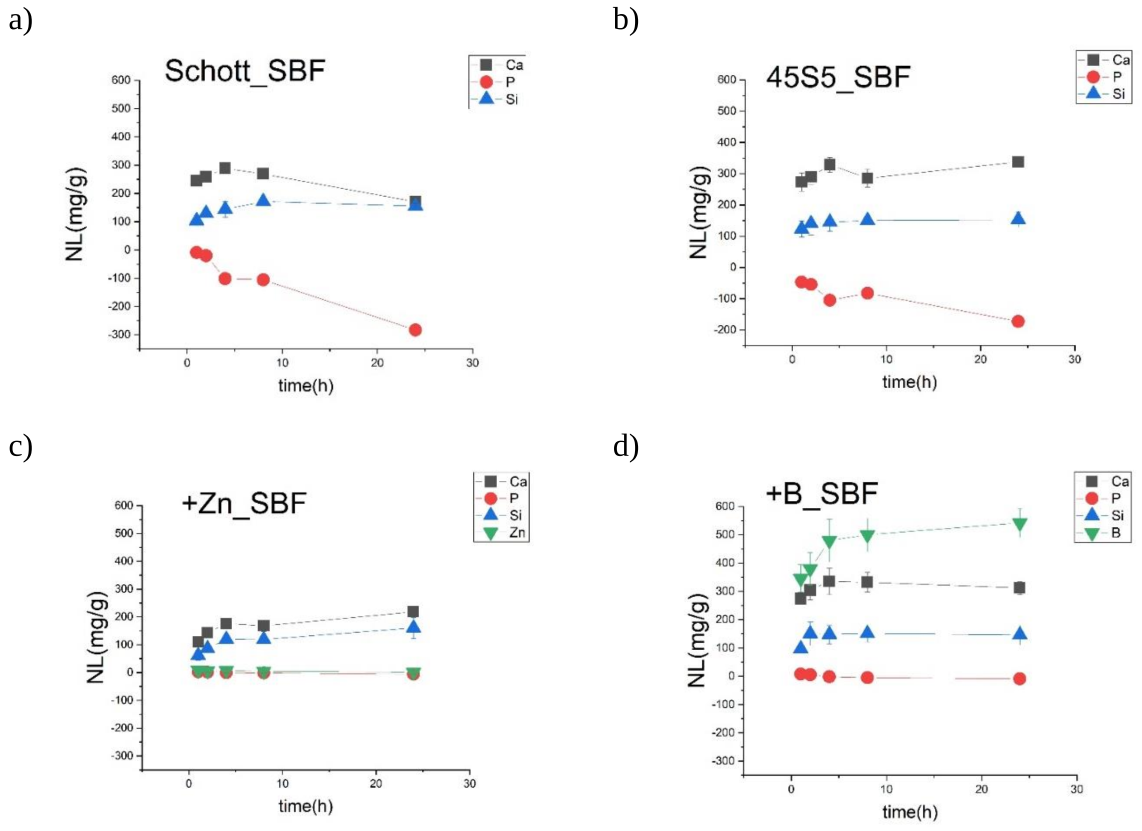

Figure 2: Time dependence of the ions released from the studied glass systems into SBF a) Schott, b) 45S5, c) 45S5+4Zn, d) 45S5+B.

In HAc/NaAc buffer, all tested bioglasses showed the fastest ion release (Fig.3). Only silicate network looks quite stable in acidic enviroment while network modifiers Na, Ca, P and Zn or B leached out from the material very quickly. This behaviour is very favorable to cure and stop the inflammation process in the body through rapid dissolution of the bioactive glass and releasing the zinc to fight bacterial infection. Incorporation of zinc to the glass structure increase its network connectivity [8], however when zinc is leached out already in the early stage, the glass tends to dissolve rapidly in acidic enviroment. We observed silicon concentration increased in all bioglass during the first 1-2 h (Fig.3) like in SBF. Silanol formation can be the key step to create inter-bond between substrate and apatite phase formed on the surface also in acidic environment. Some studies confirmed HA layer formation on the 45S5 surface in HAc/NaAc buffer at the static condition [8,12].

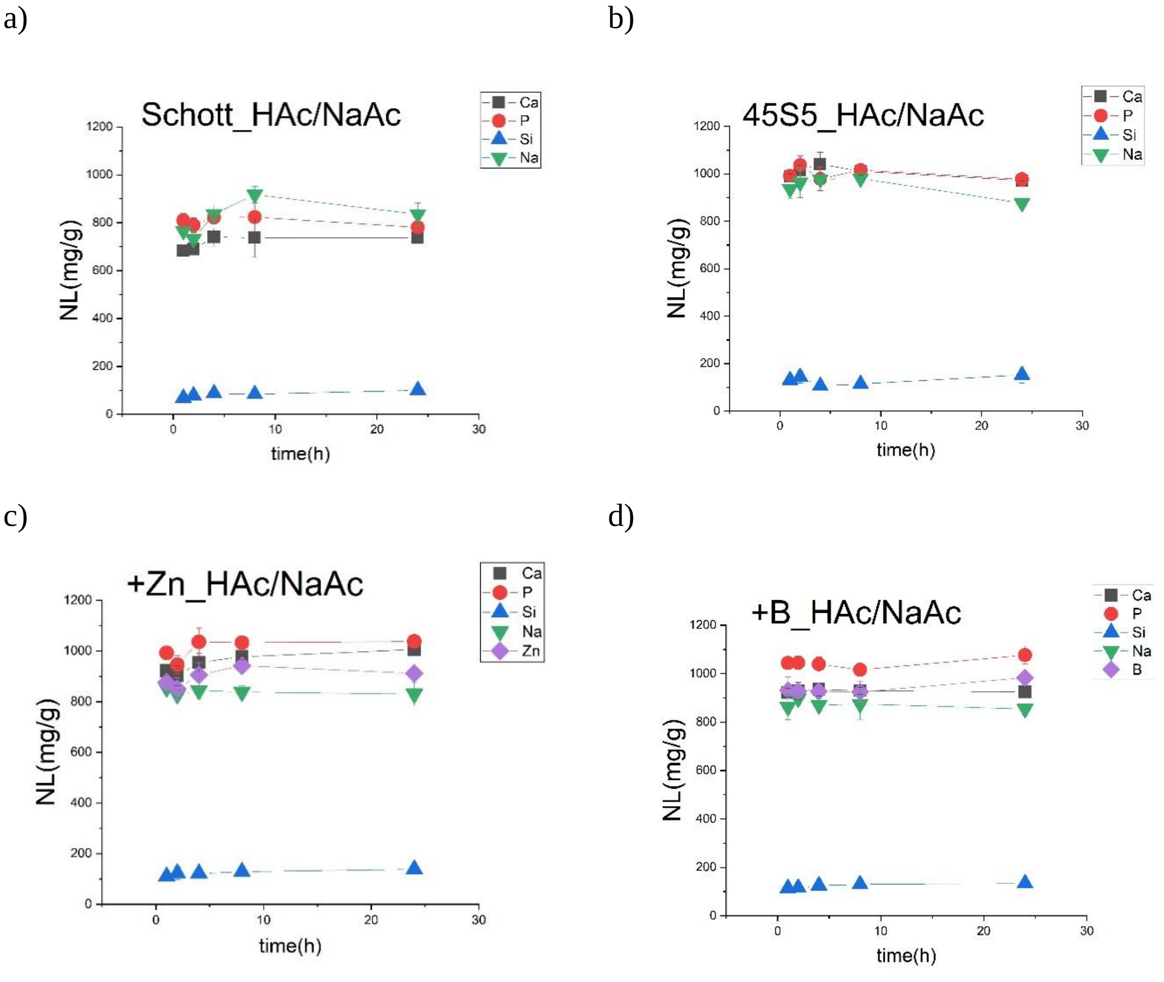

Figure 3: Time dependence of the ions released from the studied glass systems in acetic acid/sodium acetate buffer (pH4) of a) Schott, b) 45S5, c) 45S5+4Zn, d) 45S5+B.

CONCLUSIONS

Interaction of studied glass systems based on the 45S5 bioglass composition, in the acidic enviroment resulted in rapid release of all network modifiers and dopped ions. Stable behaviour of the glass dopped with Zn was observed in neutral media (pH 6.5 – 7.4). Zinc release was detected only in acidic environment. Therefore, the glasses dopped with Zn show interesting behaviour to be useful dealing with the inflammatory process, when the pH value of the body environment decreases.

In several studies [8] has been found that zinc enters the silicate network to a much larger extent, with most or possibly all zinc forming Si-O-Zn bonds, thereby increasing the silica network polymerisation. This fact we noticed in SBF and deionized water when the elution of ions was the slowest in 45S5+Zn. In SBF and acetic acid/sodium acetate buffer we can expect HA layer formation.

ACKNOWLEDGMENT

This paper is a part of dissemination activities of project FunGlass. This project has received funding from the European Union´s Horizon 2020 research and innovation programme under grant agreement No 739566.

REFERENCES

[1] Hench, L.L., Splinter, R.J., Allen, W.C. Bonding mechanisms at the interface of ceramic prosthetic materials, J.Biomed. Mater. Res. 5 (1971) 117-141.

[2] Filgueiras, M.R, Torre, G.L., Hench L.L. Solution effects on the surface reactions of a bioactive glass, J.Biomed. Mater. Res. 27 (1993) 445-453.

[3] Hall, S.L., Dimai, H.P., Farley, J.R. Calcif. Tissue Int. 64 (1999) 163-172.

[4] Lakhkar N.J., Lee, I.H., Kim, H.W., Salih, V., Wall, I.B., Knowles, J.C. Adv. Drug Delivery Rev. 65 (2013) 405-420.

[5] Devirian, T.A., Volpe, S.L. The physiological effects of dietary boron, Critical Reviews in Food Science and Nutrition 43 (2003) 219-231.

[6] Wu, Y.Y., Ye, S., Yao, A.H. et al Effect of gas-foaming porogen-NaHCO3 and citric acid on the properties of injectable macroporus borate bioactive glass cement, Jornal of Inorganic Mater. 32 (2017) 777-784.

[7] Chen, X., Zhao, Y., Geng S. et al In vivo experimental study on bone regeneration in critical bone defects using PIB nanogels/boron-containing mesoporous bioacive glass composite scaffold, International Journal of Nanomedicine 10 (2015) 839-846.

[8] Blochberger, M., Hupa, L., Brauer, D.S. Influevce of zinc and magnesium substitution on ion relaese from Bioglass 45S5 at physiological and acidic pH, Biomed.Glasses 1 (2015) 93-107.

[9] Kobuko, T., Takadama, H. How useful is SBF in predicting in vivo bone activity? Biomaterials 27 (2006) 2907-2915.

[10] Clark, A. R., Pantano, C.G., Hench, L.L. Auger spectroscopic analysis of Bioglass corrosion films, J.Am. Ceram. Soci.59 (1976) 279-284.

[11] Plewinsky, M., Schickle, K., Lindner, M. et all The effect of crystallization of bioactive bioglass 45S5 on apatite formation and degradation, Dental materials 29 (2013) 1256-1264.

[12] Bingel, L., Groh, D., Karpukhina, N., Brauer, D.S., Influence of dissolution medium pH on ion release and apatite formation of Bioglass ® 45S5, Materials Letters 143(2015) 279-282.

BIELE SVETLO EMITUJÚCE FLUORESCENTY NA BÁZE Y_2O_3 DOPOVANÉHO POMOCOU ZnO

WHITE LIGHT EMITTING Y_2O_3 BASED FLUORESCENTS DOPED WITH ZnO

P. Švančárek[1], R. Klement[2], M. Parchoviansky[2] and D. Galusek[1, 2]

[1] *Joint Glass Centre of the IIC SAS, TnUAD, FChPT STU, FunGlass, Študentská 2, 911 50 Trenčín, Slovakia*
[2] *Centre for Functional and Surface Functionalized Glass, Alexander Dubček University of Trenčín, 911 50 Trenčín, Slovakia*

Keywords: Y_2O_3 ceramics, ZnO, Fluorescence, Pressure filtration

ABSTRACT

The fluorescence properties of the Y_2O_3 ceramic materials doped with ZnO were investigated. We observed high intensity broad emission band in visible part of electromagnetic spectra centered at 534 nm (warm white light). The detailed study of microstructure revealed ZnO grains dispersed in Y_2O_3 matrix. The possible fluorescence mechanism is based on electrons that are excited to conductive band of ZnO and subsequently relax through energy levels made by oxygen vacancies to valence band.

INTRODUCTION

Modern and more energy saving light sources depend on research of new materials. Other than for special applications the polychromatic light (e.g. visible part of electromagnetic radiation consisting of a broad range of wavelengths) is usually desired. There are two ways how to produce white light using fluorescent materials:

1. Using a mixture of three phosphors- one emitting blue, one green and one red radiation when irradiated by UV radiation. Alternatively a blue light source can be used to produce fluorescence in green and red part of spectra which together with excitation source produces white light emission [1].
2. Using fluorescent materials able to emit broad range of wavelengths in visible part of electromagnetic spectra under UV excitation [2].

In this work we investigated fluorescence (white light emission) produced by yttrium oxide (Y_2O_3) ceramic materials modified by various amounts of zinc oxide (ZnO).

EXPERIMENTAL

The Y_2O_3 green bodies were prepared by pressure filtration of isopropanol ($(CH_3)_2CHOH$, p.a., 99.7%+, CentralChem, Slovakia) based suspension containing 5 vol% of Y_2O_3 (PENGDA, 150 nm Fig. 1.), stabilized by 1 wt.% of PEG (Polyethylene Glycol 400 Ultra-pure, Fluka, Germany) based on the Y_2O_3 mass.

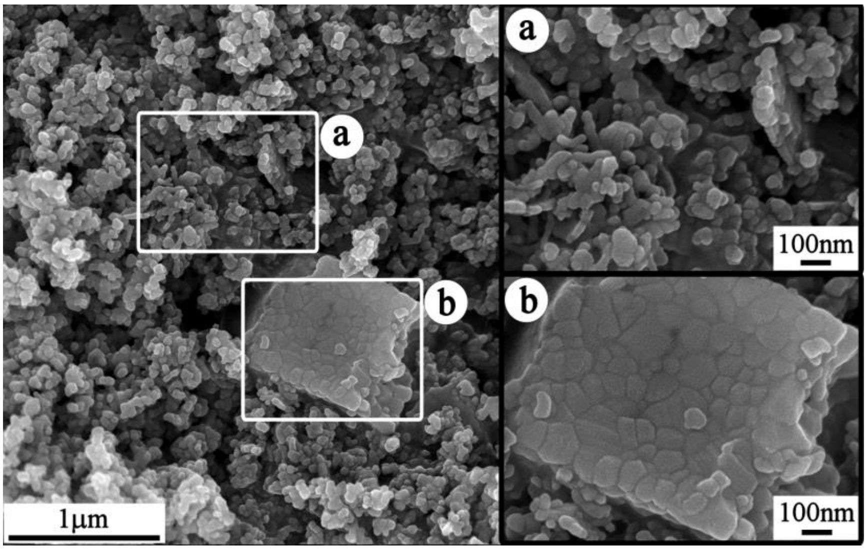

Figure 1: Y_2O_3 PENGDA. a) 250- 400nm aglomerates, b) 1.1µm compact agglomerate.

After drying, the green pellets were pre-sintered using the following regime: ramp 10°C/min to 1000°C with 1 hour holding time followed by free cooling in furnace as to obtain porous but sufficiently stable pellets able to withstand infiltration procedure in water based solutions. The density of pre-sintered samples was determined using mass (balance) and dimensions (micrometer screw) measurements. Water solutions of zinc acetate ($Zn(CH_3COO)_2 \cdot 2H_2O$ p.a.,. CentralChem, Slovakia) with concentrations calculated individually according to porosity of pre-sintered pellets to obtain 0.25, 0.5, 1.0, 2.0, 3.0, 3.5 and 4 atomic percent of Zn^{2+} dopant were used for infiltration of pre-sintered pellets. The infiltrated pellets were then sintered in ambient atmosphere using superkanthal furnace (Classic, Czech republic) using the following regime: ramp 10°C/min to 80°C with 2 hours holding time, then ramp 10°C/min to 250°C with 2 hours holding time and finally, ramp 10°C/min to 1400°C with 2hour holding time followed by free cooling. To confirm the role of vacancies on fluorescence intensities, the final sintering step temperatures 1300°C and 1500°C were also used for the sample compositions with the strongest fluorescence activity. Density of sintered specimens was determined using Archimedes method by weighing the specimens in air and in water.

X-ray diffraction (XRD) was performed using a PANalytical Empyrean DY1098 X-ray powder diffractometer with $Cu_{K\alpha}$–radiation in the θ-2θ arrangement.

Cross sections for SEM were prepared by cutting the pellets in half and embedding them in Buehler KonductoMet (pressure molding at 150 °C for 1 min). The cross sections were ground and polished on diamond wheels using decreasing grain sizes from 45µm down to 0.5 µm in a Buehler AutoMet 300 polisher. A final finish of 2-6 h of vibration polishing was applied using a Buehler VibroMet 2 (200 g static load) and a MasterPrep polishing suspension (50 nm sol-gel alumina). Polished cross sections were coated by thin layer of Au/Pd (80/20) alloy at about 5 Pa to avoid surface charging.

SEM analyses were performed using a Jeol JSM 7600F SEM equipped with an X-Max $50mm^2$ EDXS detector (Oxford Instruments) and a Nordlis Max EBSD-camera. EDXS-spot measurements were acquired using acceleration voltages of 15-20 kV. EBSD-scans were performed using an acceleration voltage of 15 kV and a current of up to ca. 3 nA. The EDXS and EBSD scans were captured using the Oxford Instruments software Aztec 3.1 coupled with Channel5 software for more detailed evaluation.

Both emission (PL) and excitation (PLE) fluorescence spectra were measured using a Fluorolog 3 (FL3-21, Horiba) fluorescence spectrometer in the front-face mode with a Xe-lamp (450 W) as the excitation source.

RESULTS

The relative green body (37.5% ±0.2) and presintered (40.2% ± 1%) sample density was determined from mass and dimensions of pellets. Sintered specimens reached average relative density of 98.7% ± 0.6% when measured in water by Archimedes method. The phase composition was determined by XRD measurements: cubic Y_2O_3 was the only identified crystalline phase. The SEM examination revealed porous cross section of polished sample (Fig 2a).

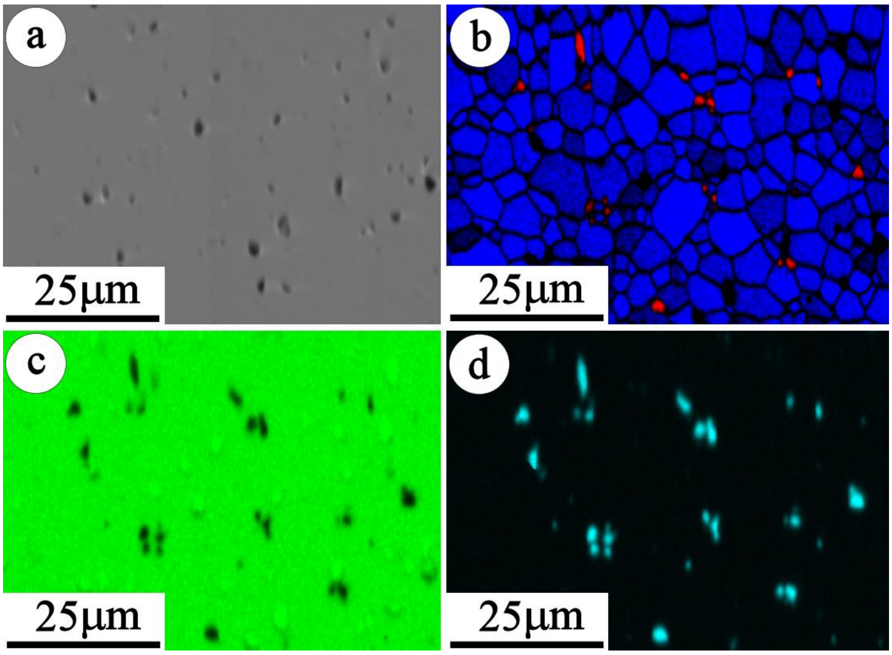

Figure 2: a) SEM, b) EBSD phase map and EDXS element maps c) Y Lα1, d) Zn Lα 1_2

The same region mapped by EDXS (Fig 2c, d) shows zinc concentrated in the form of ZnO grains randomly distributed in the Y_2O_3 matrix (probably localized in former pores, no zinc signal was observed in intergranular boundaries) indicating that ZnO does not react with Y_2O_3 forming additional phases. The EDXS element mapping shows mainly random signal of zinc where Y_2O_3 grains are located, attributed to instrumental noise, and indicating low solubility of Zn in Y_2O_3 matrix. The EBSD (Fig 2b) identified two crystalline phases, namely cubic Y_2O_3 and hexagonal ZnO (zincite). Several places were detected where EDXS revealed the presence of zinc but no zincite was indexed by EBSD. The result was attributed to greater volume and measurement depth of EDXS. In some cases, the superposition of Y_2O_3 and ZnO Kikuchi patterns during EBSD measurements made the phase indexing impossible. To avoid the necessity of thermal etching at high temperature Band Contrast maps from EBSD measurements for determination of the grain size distribution were used (Fig. 3). The median grain size grows with increasing sintering temperature from 0.84 μm (1300°C/2h) through 1.38 μm (1400°C/2h) to 3.10 μm (1500°C/2h).

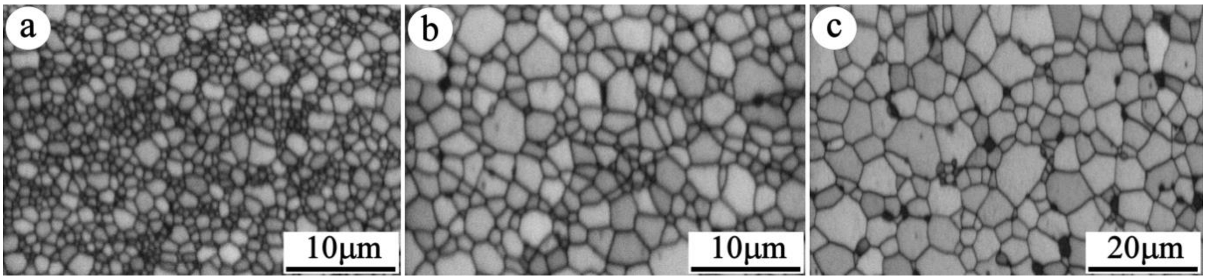

Figure 3: Y_2O_3 : 3.5 at% Zn^{2+}- Microstructure vs sintering temperature. a) 1300°C/2h, b) 1400°C/2h, c) 1500°C/2h

The PLE and PL spectra were measured in a backscattering mode. Emission spectra were corrected for spectrometer optics and excitation lamp response, while PLE spectra were corrected only for spectrometer optics. All spectra were recorded at the same conditions (slit width, integration time, monitored wavelength, cut-off filter). The Fig. 4 represents emission spectra of specimens with different content of Zn^{2+} sintered for 2h at 1400°C. It should be noted that Zn-free sample (pure Y_2O_3) was found to be PL silent and no signal was observed. From SEM/EDXS/EBSD analyses and from fluorescence spectra measurements we tentatively deduce that the luminescence is produced by the same mechanism as found in ZnO:Zn [3]. The mechanism of luminescence consists most probably of excitation of electrons from valence band to conductive band and then relaxation through intermediate states of oxygen vacancies V_O^0, V_O^{+1} and V_O^{+2} These vacancies emerge at the interface between ZnO and Y_2O_3 grain. As documented in Fig. 4, the highest emission intensities were observed for specimens with Zn concentration between 3 and 4 at. %.

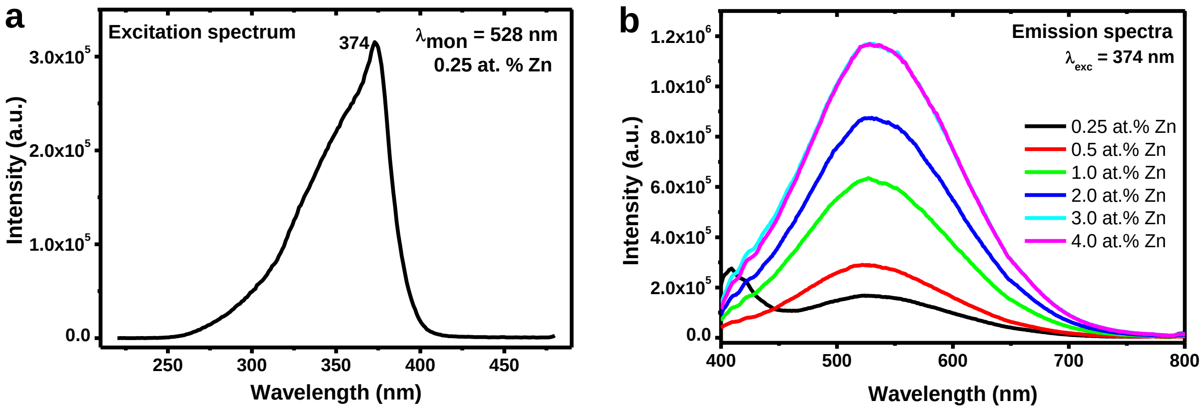

Figure 4: Excitation (a) and emission spectra (b) of Zn^{2+} doped Y_2O_3 sintered for 2h at 1400°C.

The photoluminescence intensities for different dopant concentrations at emission wavelength of 534 nm are shown in Fig. 5.

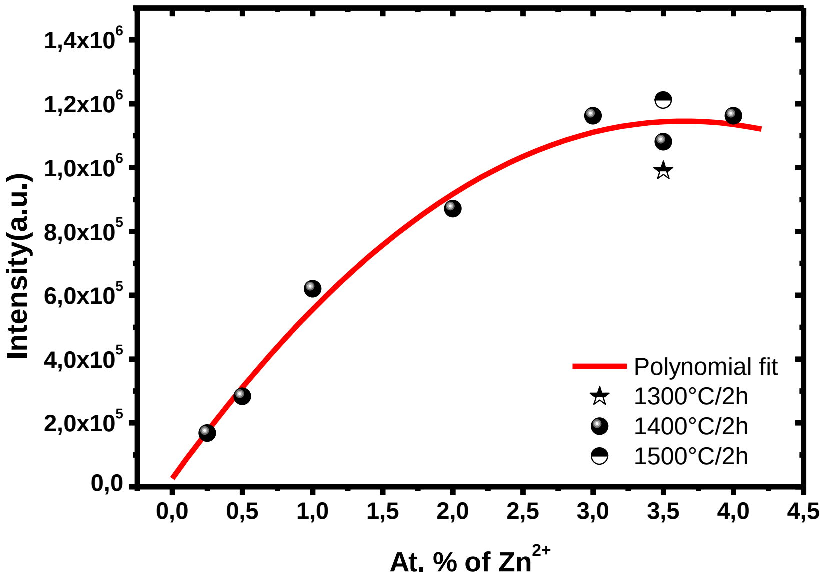

Figure 5: A comparison of emission intensities in dependence of Zn^{2+} additive concentration.

The maximum intensity of luminescence was achieved at 3 to 4 at.% of Zn^{2+} additive. The emission decay times could not be measured due to short decay times which, according to the literature range in the order of magnitude of nanoseconds or less [3].

CONCLUSIONS

The Y_2O_3 ceramic material doped by ZnO was prepared and tested. The microstructural characteristics as well as luminescence properties were investigated. Microstructure examination revealed discreet ZnO grains distributed at boundaries between Y_2O_3 grains. No other ZnO containing phases were detected. The material shows strong emission in broad range of electromagnetic wavelengths in visible part of spectra centered around 534 nm. The observed photoluminescence is attributed to similar mechanism as in the system ZnO: Zn due to similarities in luminescence spectra.

ACKNOWLEDGMENT

This paper is a part of dissemination activities of the project FunGlass. This project has received funding from the European Union's Horizon 2020 research and innovation programme under grant agreement No 739566. This work was also supported by the Slovak Research and Development Agency under the contract No. APVV-17-0049 and by grants VEGA 1/0527/18, VEGA 2/0026/17. We also wish to thank Dr. Wolfgang Wisniewski for his help with EBSD measurements.

REFERENCES

[1] Lei Chen, Chun-Che Lin, Chiao-Wen Yeh and Ru-Shi Liu: Light Converting Inorganic Phosphors for White Light-Emitting Diodes, Materials 3, 2172-2195. 2010

[2] Sufen Wei, Chi-Yu Lin, Cheng-Fu Yang, Yi-Kai Wang, Shang-Te Tsai: Investigations of the crystalline phase and photoluminescence properties of white-light CaxZnMoO4+x phosphors, J. Mater. Res. Technol. 8(5):3772–3782. 2019

[3] P. A. Rodnyi, K. A. Chernenko, and I. D. Venevtsev: Mechanisms of ZnO Luminescence in the Visible Spectral Region, Optics and Spectroscopy, 2018, Vol. 125, No. 3, pp. 372–378. 2018

OPTICAL PROPERTIES

ANALÝZA OPTICKÝCH VLASTNOSTÍ Al_2O_3:Cr^{3+} POKRYŠTALICKEJ TRANSPARENTNEJ KERAMIKY EMITUJÚCEJ ČERVENÉ SVETLO

ANALYSIS OF OPTICAL PROPERTIES OF Al_2O_3:Cr^{3+} POLYCRYSTALLINE TRANSPARENT RED LIGHT EMMITING CERAMICS

R. Klement[1], K. Drdlíková[2], D. Drdlík[2,3], K. Maca[2,3], D. Galusek[1,4]

[1] *FunGlass, Alexander Dubček University of Trenčín, Študentská 2, 911 50 Trenčín, Slovak Republic*
[2] *CEITEC BUT, Brno University of Technology, Brno, Purkynova 123, Brno 612 00, Czech Republic*
[3] *Institute of Materials Science and Engineering, Brno University of Technology, Technicka 2, 616 69 Brno, Czech Republic*
[4] *Joint Glass Centre of the IIC SAS, TnUAD and FChFT STU, Študentská 2, 911 50 Trenčín, Slovak Republic*

ABSTRACT

Transparent Cr^{3+}-doped alumina ceramics was prepared by slip casting, followed by pre-sintering in ambient atmosphere and hot isostatic pressing. The effect of dopant concentration on optical (transmission and photoluminescence-PL) properties was studied. Two approaches were used for treatment and comparison of the transmission data, one based on simple total background correction and other based on Rayleigh-Gans-Debye approximation that includes birefringent grain scattering effect. The PL spectra of studied samples exhibit intensive deep red narrow emissions under violet/green light excitation, R-lines ($^2E_g \rightarrow {}^4A_{2g}$ transition), observed at 692.5 and 693.8 nm, that are very close to ruby single crystal. The highest emission was achieved at the Cr^{3+} concentration of 0.4 at. %. The luminescence decay curves exhibit single-exponential behaviour with decay times of ~3.6 ms.

Keywords: Cr^{3+}-doped Al_2O_3, transparent polycrystalline ceramics, optical properties, luminescence

INTRODUCTION

Single crystals doped with various rare earth (RE = Yb^{3+}, Nd^{3+}, Er^{3+}) or transition metal ions (TM = Ti^{3+}, $Cr^{2+/3+/4+}$) have been widely applied in solid state lasers for applications in optics and photonics. The most important host materials are yttrium aluminium garnet (YAG, $Y_3Al_5O_{12}$), sapphire (Al_2O_3), yttrium vanadate (YVO_4). Tungstates and fluorides have been also used. However, the main disadvantage of single crystals is that large size and high quality crystals with homogeneous distribution of optically active ions in a host are still difficult and expensive to produce. This opens space for alternative approach based on preparation of transparent polycrystalline ceramics (TPCC) for a wide range of applications, from mechanically strong, hard, abrasion and corrosion resistant materials suitable for extreme conditions to optical components and ceramic laser materials. Moreover, compared to single crystals, polycrystalline ceramics (PCC) also provides the flexibility in preparation of products with various size and shape design at reduced cost. On the other hand, difficulties connected with preparation of high quality transparent ceramics still limit this approach, and preparation process of TPCC has to be carefully adjusted and optimized; the optical properties strongly depend on final microstructure. The crucial problem is the light scattering in prepared PCC that significantly affects the final transparency. The main factors affecting the degree of transparency are residual porosity and pore size (especially in isotropic ceramics e.g. YAG), second phase inclusions, grain size, grain boundary misorientation (small differences in refractive indices at interfaces of optically anisotropic crystallites). For example, only 0.1 % of residual porosity can completely eliminate the transparency of a material. In case of optically anisotropic materials like α-Al_2O_3 the degree of birefringence, i.e. the difference from ordinary to the extraordinary refractive indices, is small, $\Delta n = 0.008$ ($n_o = 1.7638$, $n_e = 1.7556$ at 700 nm), but sufficient to turn most alumina ceramics opaque. Highly transparent polycrystalline alumina ceramics (PCA) with good mechanical properties, must simultaneously meet the following requirements: extremely low porosity (< 0.05 %) and fine grain size (< 1μm).

Recently, several studies on PCA doped with Cr^{3+} ions (Ruby) using different preparation techniques were reported, however, only very few of them provide the accurate information on the material transparency that is significantly related to the Cr^{3+} dopant concentration [1]. Detailed analysis of optical properties, including calculation of absorption/scattering coefficients, was described only by Penilla et.al. [2] for two concentrations of Cr^{3+} ions in a ruby (0.5 and 1.0at. %).

In the present work, we report on the analysis of optical properties of Al_2O_3 polycrystalline ceramics doped with Cr^{3+} ions at different concentration level ranging from 0.1 up to 0.5 at.%. Two approaches have been applied to obtain the absorption coefficients for optical transitions of the Cr^{3+} ions in the visible spectral range. The first is based on the total background correction of the measured transmission spectra corrected for reflection losses from 2 surfaces of polished samples, the second approach relies on the Rayleigh-Gans-Debye (RGD) approximation previously used by Apetz and Van Bruggen and others [3-4] for transparent non-doped PCA and Penilla et. al. [2] for polycrystalline ruby ceramics. The absorption parameters are compared with those obtained for Cr-doped PCA and also single crystals. Moreover, the luminescence properties of prepared Cr^{3+}-doped PCA was studied in detail as a function of dopant concentration.

EXPERIMENTAL

Chromium doped alumina was prepared from commercial high purity Al_2O_3 powder (TM-DAR, Taimei Chemicals Co., Japan, purity of 99.99%) with the primary particle size of ~150 nm and nano-Cr_2O_3 powder (purity of 99%, GNM – Getnanomaterials, USA) with the primary particle size of ~60 nm. The content of chromium ranged from 0.10 to 0.50 at.% with respect to Al_2O_3 (Fig. 1). Preparation of the samples was carried out according to the procedure described in detail in our recently published papers [5-6]. The designation of the samples in the work reflects the content of Cr^{3+}; e.g. Cr 0.1 means 0.10 at.% of Cr with respect to alumina.

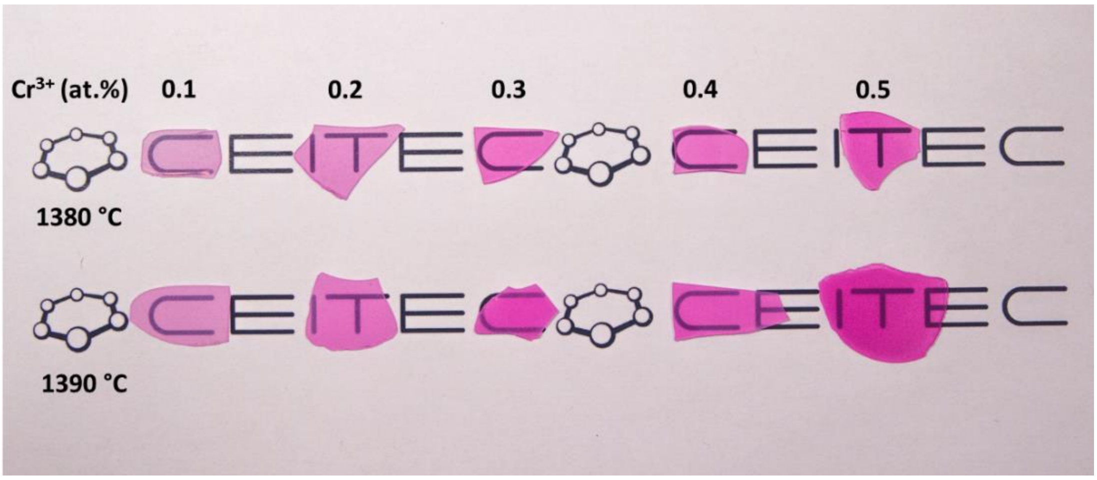

Figure 1: The photographs of the Al_2O_3:Cr^{3+} ceramics at different Cr^{3+} doping level

The UV-VIS-NIR spectra (optical transmission spectra) of the polished samples were measured on a Cary 5000 spectrometer (Agilent, USA) in the spectral range of 200-2500 nm. The samples were placed at normal incidence to the beam path. The spectra were obtained at a scan rate of 300 nm/min. The transmission spectra were corrected for the reflection losses that in the case of alumina corresponds to ~ 14 %, and recalculated to the 0.8 mm sample thickness to compare experimental data with literature reported data.

The photoluminescence excitation and emission spectra were recorded using a Fluorolog FL3-21 spectrometer (Horiba, Japan). The Xe-lamp (450 W) was used as an excitation light source. The luminescence spectra of studied samples presented herein were recorded at room temperature in backscattering geometry. The luminescence decay curves were recorded at room temperature with the same instrument using a phosphorescence module of the spectrometer. The flash Xe-lamp was used as an excitation source.

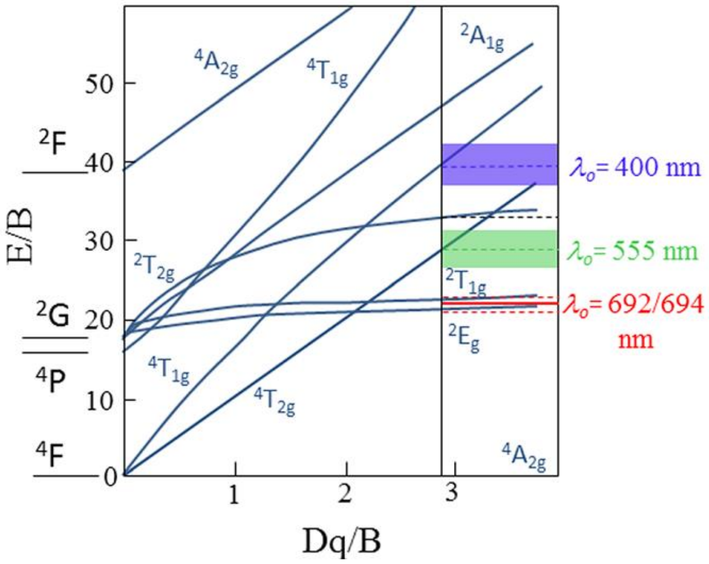

Figure 2: Tanabe-Sugano energy level diagram for Cr^{3+} ions in an octahedral crystal field. The vertical black line corresponds to Dq/B = 2.8 for ruby; B = 918 cm-1. Taken form ref. [2].

RESULTS AND DISCUSSION

In terms of Tanabe-Sugano energy level diagram (Fig. 2) that shows the splitting of the Cr^{3+} free ion levels (d^3 configuration) in an octahedral crystal field as the ratio of crystal field strength to interelectronic repulsion (measured in D_q/B units), five absorption transitions are possible for the ruby with Dq/B value of 2.8 and B = 918 cm^{-1}; five absorption lines correspond to $^4A_{2g}(^4F) \rightarrow {}^4T_{1g}(^4F)$, $^4A_{2g}(^4F) \rightarrow {}^2T_{2g}(^2G)$, $^4A_{2g}(^4F) \rightarrow {}^4T_{2g}(^4F)$, $^4A_{2g}(^4F) \rightarrow {}^2T_{1g}(^2G)$, $^4A_{2g}(^4F) \rightarrow {}^2E_g(^2G)$ electronic transitions [2, 7]. Three dominant bands commonly observed in absorption spectra are violet, green and red centred at ~400, 555 and 692/694 nm (R-lines). The violet ($^4A_{2g}(^4F) \rightarrow {}^4T_{1g}(^4F)$) and green ($^4A_{2g}(^4F) \rightarrow {}^4T_{2g}(^4F)$) transitions as a spin-allowed transition result in intensive broad absorption bands; the red $^4A_{2g}(^4F) \rightarrow {}^2E_{2g}(^2G)$ is spin-forbidden transition of much lower intensity. The weak spin-forbidden quartet-doublet transitions $^4A_{2g}(^4F) \rightarrow {}^2T_{1g}(^2G)/{}^2T_{1g}(^2G)$ are rarely observed and resolved in the absorption spectra [2, 7].

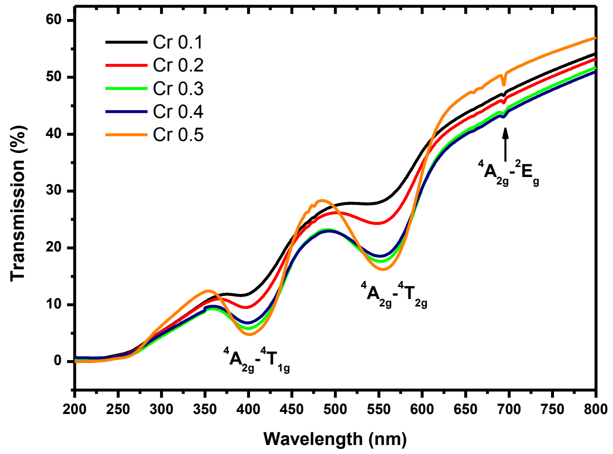

Figure 3: Transmission spectra of polycrystalline Cr^{3+}-doped alumina transparent ceramics recalculated for sample thickness of 0.8 mm, prepared using pre-sintering regime 1380°C/2min and HIP 1200°C/3h.

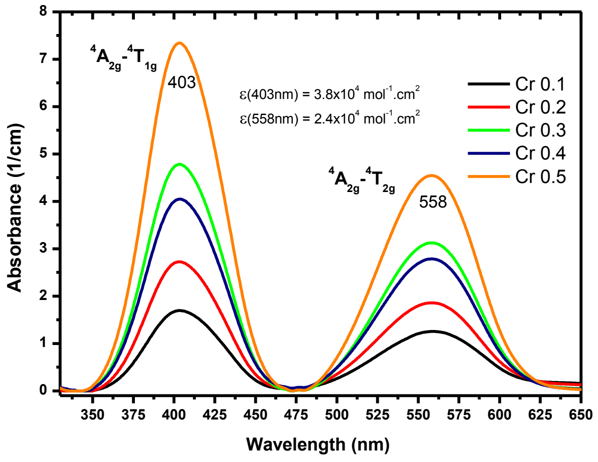

Figure 4: Absorption spectra of Cr^{3+}-doped transparent PCA.

The optical transmission spectra of the studied Cr^{3+}-doped transparent alumina with various Cr^{3+} concentrations pre-sintered at 1380°C are shown in Fig. 3. The transmission spectra exhibit two broad bands with the maxima at 403 and 558 nm and one "line" band of low intensity at 694 nm corresponding to absorption of Cr^{3+} ions.

Compared to the alumina single crystal with almost constant transmission (~86%) in the whole visible spectral range, the transmission of prepared transparent polycrystalline Cr^{3+}-doped alumina samples decreases with decreasing wavelength due to the scattering of the incident light at grain boundaries, which is wavelength dependent. The transmission of prepared samples was found to be similar to the data published previously on the Al_2O_3:Cr^{3+} doped transparent polycrystalline ceramics [1, 2]. Samples pre-sintered at 1390°C exhibit lower transmission compared to the samples pre-sintered at 1380°C because of larger grain size and larger scattering affect. The transmission spectra were corrected for reflection losses, converted into absorbance scale and normalised to 1 cm thickness. Then, the background correction applying the exponential function in the range of 350-800 nm was used to eliminate the light scattering effects at grain boundaries and at pores. The absorption spectra are shown in Fig. 4. The absorbance increased with increasing Cr^{3+} concentration and calculated molar absorption coefficients, ε, (using the linear fit according to the Lambert-Beer law $A/l = \varepsilon c$, with Adj. $R^2 = 0.99$ or better) for violet and green absorption were found to be $3.8 \pm 0.1 \times 10^4$ $mol^{-1}cm^2$ ($38\ L^{-1} \cdot mol^{-1}cm$) and $2.4 \pm 0.1 \times 10^4$ $mol^{-1}cm^2$ ($24\ L^{-1} \cdot mol^{-1}cm$), respectively. It should be noted, that sample containing 0.4 at.% of Cr^{3+} was excluded from the linear fit due to the lower absorption than sample with 0.3 at.% of Cr^{3+}. This is most likely due to the lower overall transparency of the sample. Almost identical values were found for samples pre-sintered at 1390°C (36 and 24 $L^{-1} \cdot mol^{-1} \cdot cm$). The red absorption was too weak to determine the molar absorption coefficient reliably. Absorption cross-section (ACS) values, σ, for violet and green absorption were calculated (from molar absorption coefficients) to be 1.45×10^{-19} cm^2 and 9.22×10^{-20} cm^2, respectively. The absorption coefficient α (in cm^{-1}), as defined in Eqn. (1), for each sample was also calculated from experimental transmission data and the values are summarised in Table 1. The α values can easily be converted to the ACS for particular concentration of a dopant ($\sigma = \alpha/c$). As follows from Table 1, the data for ACS calculated form each value of α are very similar for different Cr^{3+} concentration in the sample. The obtained absorption-cross section data corresponds quite well with the average ACS data reported by Dodd et at. [8] for ruby single crystal doped with different concentration of Cr^{3+} ions; 1.98×10^{-19} cm^2 and 1.20×10^{-19} cm^2. Somewhat higher ACS data for ruby single crystal was reported by Cronemeyer [9]. The differences between our data and data reported by Dodd et al. and Cronemeyer are most likely due to sample processing, either caused by Cr loss and/or by partial reduction of Cr^{3+} species to Cr^{2+} [2]. The peak absorption coefficients of our sample Cr 0.5 obtained from background corrected absorption spectra are in a good agreement to those reported by Penilla et.al. [2] for the same concentration of Cr^{3+} in Al_2O_3 polycrystalline transparent ceramics (see Table 1).

Table 1: Optical data for ruby samples. The peak absorption coefficients were obtained from measured data and absorption cross-section were calculated using relation $\sigma = \alpha/c$.

Cr concentration		**Grain size (nm)**	**Peak absorption coefficient (cm^{-1})[#,§]**		**Peak absorption cross-section (cm^2)[#,§]**	
c(at.%)	**c(ions/cm^3)**		α_V	α_G	σ_V	σ_G
0.1	2.370×10^{19}	450±80	**3.954** (7.899)	**2.983** (5.425)	**1.668×10^{-19}** (3.333×10^{-19})	**1.259×10^{-19}** (2.889×10^{-19})
0.2	4.737×10^{19}	420±60	**6.186** (11.139)	**4.131** (6.992)	**1.306×10^{-19}** (2.351×10^{-19})	**8.719×10^{-20}** (1.476×10^{-19})
0.3	7.102×10^{19}	420±60	**10.978** (17.286)	**7.197** (11.049)	**1.546×10^{-19}** (2.434×10^{-19})	**1.013×10^{-19}** (1.556×10^{-19})
0.4	9.464×10^{19}	390±40	**9.249** (17.072)	**6.359** (11.287)	**0.977×10^{-19}** (1.804×10^{-19})	**6.719×10^{-20}** (1.193×10^{-19})
0.5	1.182×10^{20}	380±50	**16.894** (21.580)	**10.448** (13.137)	**1.429×10^{-19}** (1.825×10^{-19})	**8.837×10^{-20}** (1.111×10^{-19})
				Average	**1.49×10^{-19}** **$\pm 0.16\times10^{-19}$**	**1.00×10^{-19}** **$\pm 0.18\times10^{-19}$**
				Least squares	**1.45×10^{-19}** **$\pm 0.04\times10^{-19}$**	**9.22×10^{-20}** **$\pm 0.45\times10^{-20}$**
Data Penilla [2]						
0.5	1.180×10^{20}	344±43	14.2	9.0	1.09×10^{-19}	7.03×10^{-20}
1.0	2.357×10^{20}	337±46	27.7	16.9	1.12×10^{-19}	6.87×10^{-20}
Data Dodd [8][∃]					1.98×10^{-19}	1.20×10^{-19}
Data Cronemeyer [9][∃]					2.78×10^{-19}	1.76×10^{-19}

[#] The data obtained from background corrected absorption spectra (in bold).

[§] The data in parentheses refer to a calculation of absorption coefficient α and κ using RGD approximation, eqn. (1) and (3).

[∃] The data were calculated from single crystal absorption coefficients ($\alpha_{//}$ and $\alpha_{\perp}$ using equation $\alpha=\alpha_{//}/3+2\alpha_{\perp}/3$) and are averaged from values for several concentrations

Penilla et al. [2] reported detail analysis of transmission spectra of polycrystalline Al_2O_3:Cr^{3+} transparent ceramics at Cr^{3+} doping level of 0.5 and 1.0 at.% and grain size similar to our samples. The applied modified analytical model is based on Rayleigh-Gans-Debye approximation, that was already employed for transparent alumina ceramics [3-4].

Generally, for light transmitted through material, including the effect of light reflection at sample surface, scattering and absorption, can be written as:

OPTICAL PROPERTIES

$$T(\lambda) = [1 - 2R]e^{-l(\kappa+\alpha)} \tag{1}$$

$$R = \left(\frac{\bar{n} - 1}{\bar{n} + 1}\right)^2 \tag{2}$$

where l is the sample thickness, R is the reflectivity, κ is the scattering coefficient, and α is the absorption coefficient. In terms of RGD approximation, the scattering coefficient, κ, can be expressed by the formulae

$$\kappa = d\frac{3\pi^2}{\lambda^2}\Delta n^2\chi \tag{3}$$

where d is maximum grain size, $\Delta n = 0.008$ for alumina, and χ is a texture parameter that depends on the degree of texturing in the ceramics. When there is no texture and grains are randomly oriented, as expected for PCA, the texture parameter $\chi = 0.28$.

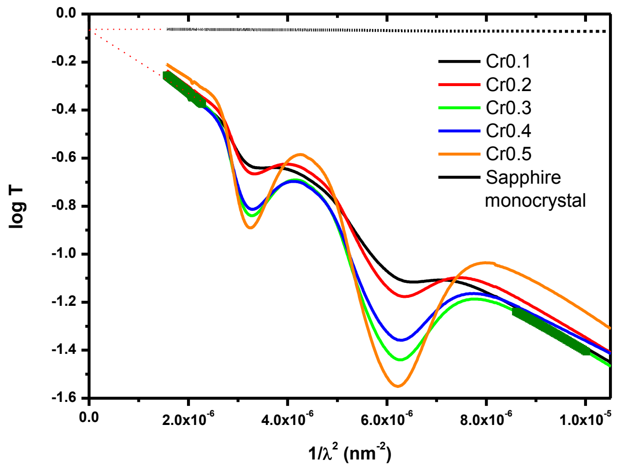

Figure 5: Logarithm of transmittance (absorbance) vs. the inverse of the wavelength square. The green dots denote the wavelength range that was used for linear fit.

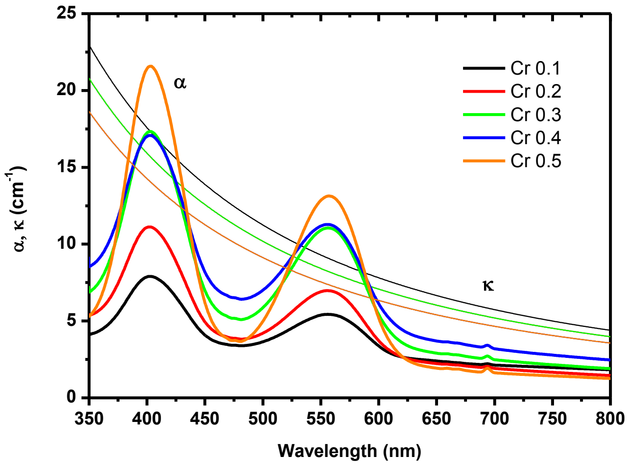

Figure 6: Absorption, α, and scattering, κ, coefficients of Cr^{3+}-doped alumina ceramics.

Excluding the absorption by optically active species and taking into account only scattering at the grains, the Eqn. (1) can be rearranged to Eqn. (4)

$$\log T(\lambda) = \log T_0(\lambda) - \frac{3\pi^2}{\lambda^2} d\Delta n^2 \chi \tag{4}$$

so that, a fit of $\log T(\lambda)$ vs. λ^{-2} should produce a line. The slope of the line is proportional to the value of χ and because other quantities in Eqn. (4) can be experimentally measured, the texture parameter can be estimated. The intercept, $\log T_0$, thus represents the logarithm of the transmittance of scattering-free sample.

The $\log T(\lambda)$ vs. λ^{-2} plot for all studies samples including sapphire single crystal is presented in Fig. 5; the wavelength range for linear fit was selected as 315-340 and 660-800 nm so that the range is not affected by the Cr^{3+} absorption. Very good linear fit (with Adj. R^2~0.99) suggests that transmission is most likely dominated by birefringence scattering, although also residual porosity may play some role. The T_0 values determined from the intercept for sample thickness of 1 mm was found to be around 75% while the typical value for optical quality sapphire is 87%. The texture parameter was estimated to be ~0.17, which means that the preferential texture angle is 38°that is not so far from the random grain orientation (45°) [4]. The absorption (α) and scattering (κ) coefficient obtained using Eqn. (1) and (3) from measured transmission spectra are shown on Fig. 6. The grain size used in the calculations were the maximum values (average plus standard deviation, see Table 1) for the corresponding sample. The texture parameter for random grain orientation ($\chi = 0.28$) and the experimental transmission spectra corrected for reflection losses and recalculated for the sample thickness of 1 mm were used for estimation of coefficients α and κ. So that absorption coefficients are corrected both for reflection and scattering. Especially scattering correction is often omitted in spectra treatment in the literature. This approach is acceptable only in the low porosity isotropic polycrystalline materials, while in the case anisotropic ceramics scattering correction is necessary. Otherwise, the analysis leads to the overestimation of absorption in a sample. The values for particular Cr^{3+} concentration in the sample are summarised also in Table 1. Obtained α values are however significantly higher than the values obtained by the spectra treatment using exponential background correction. As seen in the Fig. 6, the absorption curves still have significant non-constant (exponential like) background that overestimates the absorption coefficients. This is most likely due to the scattering effect of pores that are usually present in low amounts and dimensions in polycrystalline ceramics. As theoretically analysed by Peelen and Metselaar [10], who applied the Mie theory of light scattering in the case of PCA, the porosity and pore size significantly affect the scattering coefficient especially at lower wavelength below 1000 nm, i.e. in the visible range. The other reason is also the absorption of the pure host matrix (Al_2O_3) that was not subtracted. The transmission data obtained from the measurements of polycrystalline transparent/translucent ceramics have to be carefully evaluated and critically reviewed. In this light, the simple background correction using exponential function that eliminates matrix absorption, birefringent grain and pores scattering (see Fig. 4) is more plausible method for transmission data treatment than the second method based on RGD approximation, especially when material contains strongly absorbing species like Cr^{3+} ions.

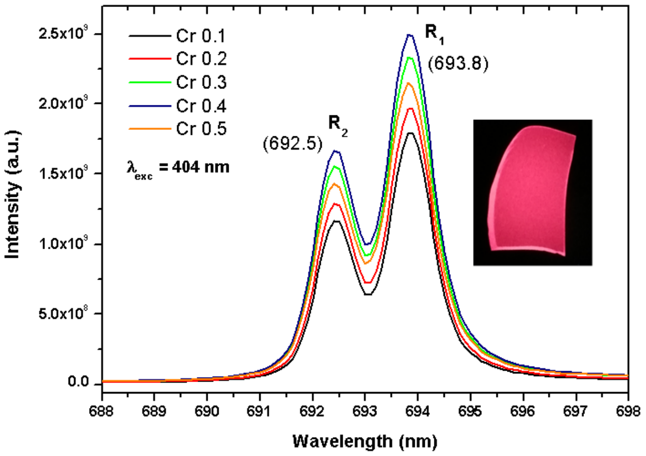

Figure 7: Emission spectra of Al_2O_3:Cr^{3+} ceramics with different concentration of Cr^{3+} ions (0.1-0.5 at.%) in host matrix under excitation at 404 nm..

The photoluminescence emission (PL) spectra Cr^{3+} doped Al_2O_3 under excitation at 404 nm (Fig. 7) exhibited very narrow (with FWHM 23 and 19 cm^{-1}) so-called zero-phonon R-lines (Raman lines R_1 and R_2) at 692.5 nm (14442 cm^{-1}) and 693.8 nm (14412 cm^{-1}) assigned to spin-forbidden $^2E_g(^2G) \rightarrow {}^4A_{2g}(^4F)$ transition originating from isolated Cr^{3+} ions in octahedral sites, [11,12] e.g. Cr^{3+} ions substituting Al^{3+} ions in the α-Al_2O_3 lattice. Two observed R-lines, the R_1 and R_2 lines, are separated by 30 cm^{-1}. For comparison, the R line positions of Cr^{3+} ions in bulk ruby single crystal are 694.3 nm (R_1) and 692.9 nm (R_2) with separation of 29 cm^{-1}. It is evident that emission intensity strongly depends on doping concentration. The PL intensity increases with increasing Cr^{3+} concentration approaching the maximum at 0.4 at.% (Fig. 7). At higher chromium concentration the PL intensity decreases due to the concentration quenching as the distance between Cr^{3+}-Cr^{3+} ions decreases and energy transfer between the Cr^{3+} ions becomes more favourable. The fitted fluorescence lifetime values for Al_2O_3:Cr^{3+} transparent ceramics samples are about 3.60 ± 0.05 ms and are not significantly affected by the Cr^{3+} concentration in the host matrix within the studied concentration range. The values are similar to the value reported in literature of about 3 ms at 300K for ruby single crystal.

CONCLUSIONS

Transparent polycrystalline Cr^{3+}-doped alumina (ruby) with photoluminescent properties were prepared and characterised. The optical transmittance is strongly related to the grain size: proper adjustment of sintering conditions limiting the grain growth is crucial for achieving the transparency. Even mild grain size increase results in the significant transparency decrease. The transmission spectra exhibit two broad bands with the maxima at 403 and 558 nm and one “line” band of low intensity at 694 nm corresponding to absorption of Cr^{3+} ions. The absorbance increases with increasing Cr^{3+} concentration in the samples and calculated molar absorption coefficients (using the linear fit) for violet and green absorption were found to be 3.8×10^4 $mol^{-1}cm^2$ (38 $L^{-1}.mol^{-1}.cm$) and 2.4×10^4 $mol^{-1}cm^2$ (24 $L^{-1}.mol^{-1}.cm$), respectively. Absorption cross-section values, σ, for violet and green absorption were calculated to be 1.45×10^{-19} cm^2 and 9.22×10^{-20} cm^2. The simple background correction using exponential function, that eliminates matrix absorption, birefringent grain and pores scattering is more plausible method for transmission data treatment especially for materials containing strongly absorbing species like Cr^{3+} ions. The intensive deep red narrow emissions under violet/green light excitation, R-lines ($^2E_g \rightarrow {}^4A_{2g}$ transition), were observed at 692.5 and 693.8 nm, that are very close to ruby single crystal. The optimal Cr^{3+} doping concentration was found to be 0.4 at.%. The luminescence decay curves exhibit single-exponential behaviour with decay times of ~3.6 ms, similar to ruby single crystal, and decay is only slightly affected by the Cr^{3+} concentration.

ACKNOWLEDGMENT

This work is part of the project 5SA14857, which has acquired the financial contribution from the EU Framework Programme for Research and Innovation Horizon 2020 within the scope of the Marie Sklodowska-Curie Actions co-financed by the South Moravian Region according to the Grant Agreement no. 665860. This research was carried out under the project CEITEC 2020 (LQ1601) with financial support from the Ministry of Education, Youth and Sports of the Czech Republic under the National Sustainability Programme II. This work was also supported by the Slovak Research and Development Agency under the contract No. APVV-17-0049 and by grants VEGA 1/0527/18 and VEGA 2/0026/17. This paper is a part of dissemination activities of the project FunGlass. This project has received funding from the European Union´s Horizon 2020 research and innovation programme under grant agreement No 739566.

REFERENCES

[1] C.Wang, Z. Zhao, Transparent polycrystalline ruby ceramic by spark plasma sintering, Mater. Res. Bull. 45 (9) (2010) 1127-1131, and references cited therein.

[2] E.H. Penilla, C.L. Hardin, Y. Kodera, S.A. Basun, D.R. Evans, J.E. Garay, The role of scattering and absorption on the optical properties of birefringent polycrystalline ceramics: Modeling and experiments on ruby ($Cr:Al_2O_3$), J. Appl. Phys. 119 (2) (2016) 023106.

[3] R. Apetz, M.P.B. van Bruggen, Transparent alumina: A light-scattering model, J. Am. Ceram. Soc., 86 (3) (2003) 480-486.

[4] C. Pecharromán, G. Mata-Osoro, L.A. Díaz, R. Torrecillas, J.S. Moya, On the transparency of nanostructured alumina: Rayleigh-Gans model for anisotropic spheres, Opt. Express 17 (8) (2009) 6899-6912.

[5] K. Bodišová, R. Klement, D. Galusek, V. Pouchlý, D. Drdlík, K. Maca, Luninescent rare-earth-doped transparent alumina ceramics, J. Eur. Ceram. Soc. 36 (12) (2016) 2975-2980.

[6] K. Drdlíková, R. Klement, D. Drdlík, T. Spusta, D. Galusek, K. Maca, Luninescent Er^{3+}-doped transparent alumina ceramics, J. Eur. Ceram. Soc. 37 (7) (2017) 2695-2703.

[7] M.G. Brik, S.J. Camardello, A.M. Srivastava, N.M. Avram, A. Suchocki, Spin-Forbidden transitions in the spectra of transition metal ions and nephelauxetic Effect, ECS J. Solid State Sc. 5 (1) (2016) R3067-R3077, and references cited therein.

[8] D.M. Dodd, D.L. Wood, R.L. Barns, Spectrophotometric determination of chromium concentration in ruby, J. Appl. Phys. 35 (4) (1964) 1183-1186.

[9] D.C. Cronemeyer, Optical absorption characteristics of pink ruby, J. Opt. Soc. Am. 56 (12) (1966) 1703-1706.

[10] J.G.J. Peelen, R. Metselaar, Light scattering by pores in polycrystalline materials: Transmission properties of alumina, J. Appl. Phys. 45 (1) (1974) 216-220.

[11] F. Liu, B.A. Goodman, X. Tan, X. Wang, D. Chen, W. Deng, Luminescence and EPR properties of high quality ruby crystals prepared by the optical floating zone method, Opt. Mater. 91 (2019) 183-188.

[12] D. Liu, Effects of Cr content and morphology on the luminescence properties of the Cr-doped alpha-Al_2O_3 powders, Ceram. Int. 39 (5) (2013) 4765-6769.

OPTICAL PROPERTIES

SPEKANIE SKLA SO ZLOŽENÍM HLINITO-YTTRITÉHO GRANÁTU POMOCOU SPS

SPARK PLASMA SINTERING OF GLASS MICROSPHERES WITH YAG COMPOSITION

M. Michálková[1], J. Kraxner[2], V. Pouchlý[3], K. Maca[3], D. Galusek[2]

[1]*Dpt. VILA – Joint Glass Centre of the IIC SAS, TnUAD, FChPT STU and FunGlass, Študentská 2, 911 50 Trenčín, Slovakia*
[2]*FunGlass, A. Dubček University of Trenčín, Študentská 2, 911 50 Trenčín, Slovakia*
[3]*CEITEC BUT, Brno University of Technology, Purkynova 123, Brno, Czech Republic*

ABSTRACT

The work deals with the preparation of bulk glass with yttrium aluminium garnet (YAG) composition from glass microspheres prepared by flame synthesis. Viscous flow sintering of the microspheres was performed to prepare bulk glass in a SPS. Dense translucent YAG glass were successfully prepared at temperatures below 950°C without isothermal heating.

Keywords: flame synthesis, microspheres, glass-ceramic, SPS, YAG

INTRODUCTION

A glass, whether in bulk, fibre, or film form, is a non-crystalline solid (NCS) which undergoes a glass transition, to which a glass transition temperature- T_g, is associated. In principle, any substance can be vitrified by quenching from the liquid state into a solid glass, with the melt structure becoming “frozen” below T_g [1]. Sintering of conventional glass frit into coherent, dense, bulk forms is a well-known method in which free surfaces are eliminated by viscous flow, at temperatures above T_g. For glasses that do not devitrify, there is little restriction on the sintering temperatures. However, many quenched glasses, including YAG, crystallize rapidly at their crystallization temperatures - T_x, when the supplied thermal energy mobilizes the structure and the latent heat previously trapped during quenching is released. The working temperature of such glasses is thus restricted to the temperatures between T_g and onset of the crystallization temperature T_0 [1] (kinetic window), which is, in the case of glass with YAG composition, very narrow (between 20 and 25 °C) [2-5]. Due to the narrow kinetic window and rapid crystallization of YAG the densification of glass with pure YAG composition was up to now not successfully prepared by viscous-flow sintering. Therefore, the presented work deals with the preparation of bulk YAG glass and glass-ceramic from glass microspheres by pressure assisted viscous-flow sintering in SPS. The main aim of the work is to overcome the problem of narrow kinetic window by using high heating and cooling rate in SPS and consequently prepare bulk glass with YAG composition.

EXPERIMENTAL

Glass microspheres with YAG composition were prepared according to process described elsewhere [6]. Dense YAG glass and glass/ceramic samples were prepared by SPS (spark plasma sintering technique Dr Sinter SPS-625 from Fuji Electronic Industrial CO., LTD.). Carbon foil (0.5 mm thick) cladded graphite dies were filled with prepared YAG glass microspheres and sintered under vacuum at different conditions (see Tab. 1).

Table 1: Summary of SPS sintering conditions and dilatation of the samples.

Sample	Pressure [MPa]	Heating rate [°C/min]	Dilatation of sample [mm]	max T [°C]
SPS 921	60	50	1.91	902.1
SPS 922	70	50	2.02	898.9
SPS 924	80	50	2.28	904.1

The density of sintered samples was measured by Archimedes' method in water.

The phase composition of sintered samples was determined by X-ray powder diffraction (XRD) using a Panalytical Empyrean DY1098 diffractometer, operated at 40 kV and 45 mA with Cu Kα radiation (λ = 0.15405 nm). The data were acquired over a 2θ range of 10-80° (step size 0.01 °, 50 s/step). The data were evaluated using the High Score Plus software with the crystallographic open database (COD 2018).

RESULTS

The XRD analysis of SPS sintered samples at different uniaxial pressures (60, 70 and 80 MPa) revealed that all samples are XRD amorphous (Fig. 1). Hence, the densification temperature was set below the onset of the crystallization temperature. The shrinkage of the samples mentioned in Tab. 1 together with XRD analysis leads towards the conclusions that the densification was successfully done by viscous-flow sintering.

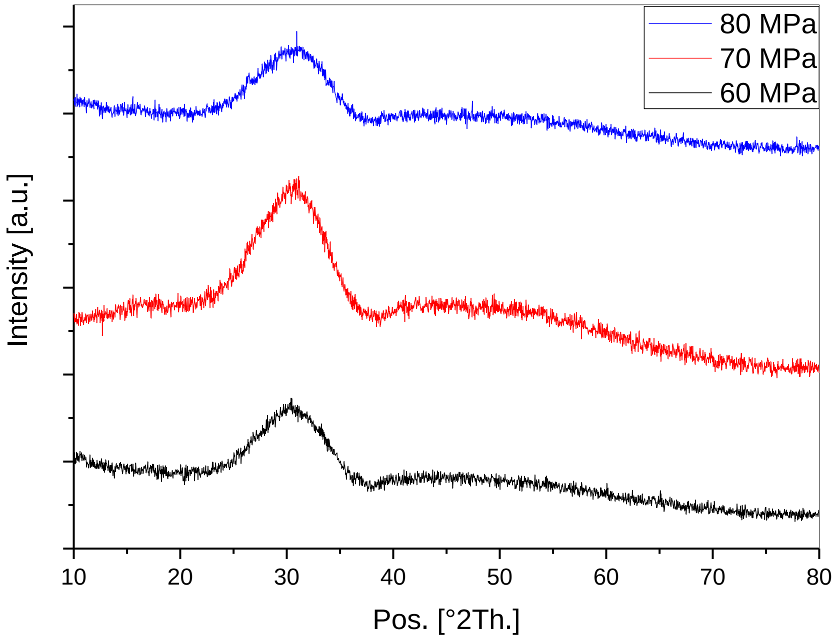

Figure 1: XRD patterns of glasses with YAG composition SPS densified at different pressures.

Additionally, Fig. 2 presents the photography of prepared translucent YAG glass/ceramic samples with diameter of 12 mm placed directly on the text. The translucency was achieved in two cases: (a) at the pressure of 60 MPa and temperature 902 °C and (c) 80 MPa and temperature 904 °C. Opacity in the sample shown in Fig. 2 (b) was ascribed to the lower densification temperature 899 °C compare to the 902 °C used in the (a) case despite of the fact that higher pressure of 70 MPa to the 60 MPa between the (b) and (a) trials, was applied.

Figure 2: The photograph of the prepared translucent YAG glass/ceramic with diameter 12 mm placed on the text. Pressure used during densification a) 60 MPa; b) 70 MPa; c) 80 MPa.

CONCLUSIONS

This work describes successful preparation of translucent glass with YAG composition at temperatures below 950 °C without dopants widening the kinetic window. Lower temperature leads to opaque white sample while increasing of the densification temperature resulted in translucent samples.

ACKNOWLEDGMENT

This paper is a part of dissemination activities of project FunGlass and was supported by VEGA grant no. 2/0026/17. This project has received funding from the European Union´s Horizon 2020 research and innovation programme under grant agreement No 739566. This research has also been financially supported by the Ministry of Education, Youth and Sports of the Czech Republic under the project LTT18013.

REFERENCES

[1] Almeida, R.M.; Gonçalves, M.C. Crystallization of Solgel-Derived Glasses, Int. J. Appl. Glas. Sci. 5 (2014) 114–125. doi:10.1111/ijag.12075.

[2] Ma, X.; Li, X.; Li, J.; Genevois, C.; Ma, B.; Etienne, A.; Wan, C.; Véron, E.; Peng, Z.; Allix, M. Pressureless glass crystallization of transparent yttrium aluminum garnet-based nanoceramics, Nat. Commun. 9, 1175 (2018). doi:10.1038/s41467-018-03467-7.

[3] He, G.; Li, Y.; Bu, C.; Liu, G.; Jiang, W.; Li, J. Preparation of Ce-doped $(Y,Gd)_3Al_5O_{12}$ nanoceramics by sintering and crystallization of glass microspheres, Mater. Res. Bull. 66 (2015) 45–50. doi:10.1016/j.materresbull.2015.02.021.

[4] Wang, L.L.; Mei, L.; He, G.; Liu, G.H.; Li, J.T.; Xu, L.H.; Jiang, Z.J. Preparation of infrared transparent YAG-based glass-ceramics with nano-sized crystallites, J. Eur. Ceram. Soc. 32 (2012) 3091–3096. doi:10.1016/j.jeurceramsoc.2012.03.023.

[5] Wang, L.; Mei, L.; He, G.; Li, J.; Xu, L. Preparation of Ce: YAG glass-ceramics with low SiO_2, J. Am. Ceram. Soc. 94 (2011) 3800–3803. doi:10.1111/j.1551-2916.2011.04700.x.

[6] Chovanec, J.; Svoboda, R.; Kraxner, J.; Černá, A.; Galusek, D. Crystallization kinetics of the $Y_3Al_5O_{12}$ glass. Journal of Alloys and Compounds 725 [25] (2017), pp. 792-799.

OPTICAL PROPERTIES

PRÍPRAVA Ce^{3+} - DOPOVANÝCH LUMINOFOROV SPEKANÍM SKLENÝCH MIKROGUĽOČOK – PREDBEŽNÉ ŠTÚDIUM

PREPARATION OF Ce^{3+} - DOPED PHOSPHORS BY SINTERING OF GLASS MICROSPHERES – PRELIMINARY STUDY

A. Akusevich[1], I. Parchovianská[1], M. Parchovianský[1], A. Prnová[2], R. Klement[1]

[1] *FunGlass, Alexander Dubček University of Trenčín, Študentská 2, 911 50 Trenčín, Slovak Republic*
[2] *Joint Glass Centre of the IIC SAS, TnUAD and FChFT STU, Študentská 2, 911 50 Trenčín, Slovak Republic*

ABSTRACT

The sintering by viscous flow at temperatures above glass transformation temperature T_g, in the so called kinetic window between T_g and T_x (onset of crystallization) was used to prepare the bulk glass/glass-ceramics phosphors from glass microspheres, emitting blue and yellow light when excited by UV or blue light. The effect of processing temperature/dwell time and glass composition on luminescence of compact bulk samples prepared by hot-press technique from glass microspheres was studied in detail.

Keywords: Ce^{3+}, phosphors, solid state lighting, pc-WLED

INTRODUCTION

White light-emitting diodes (LEDs) are realised via combination of blue LED chip covered with yellow-emitting $Y_3Al_5O_{12}:Ce^{3+}$ (YAG:Ce) phosphor powder dispersed in organic binder. However, commercial LEDs are currently limited due to the efficiency drop when increasing input current density. As a result it is difficult to realise high-brightness white light sources using laser diode excitation chips. To survive from high-flux laser irradiation and thermal attack, the thermal performance of the phosphor converter is a principal technical parameter for the laser lighting. The excellent phosphor for white lighting application is YAG:Ce having many favourable properties, such as efficient absorption of blue light (also possibility of excitation in UV range), broadband emission in the visible spectral range with high quantum yield, good thermal quenching properties up to 200°C and excellent chemical and thermal stability. The current phosphor converter is made by embedding YAG:Ce powders in organic binders, but the low heat-resistance (polymer resin degradation at higher temperatures/light flux in LEDs) and thermal conductivity (0.1-0.4 $Wm^{-1}K^{-1}$) of this mixture greatly hinder its application in high-power, high-brightness solid state lighting (SSL). To overcome these problems, composite phosphor-in-glass (PiG), where the phosphor is dispersed in a glass, has been developed [1]. Later on, the ceramics attracted increased attention due to its excellent thermal and mechanical properties. One of the most versatile ceramics in structural and optical applications is Al_2O_3 because of its unique properties, and thus alumina may serve as a matrix in combination with luminescence active phase e.g. YAG:Ce in composite. For example Al_2O_3 has a higher thermal conductivity (32-35 $Wm^{-1}K^{-1}$) at room temperature than YAG (9-14 $Wm^{-1}K^{-1}$) and thus alumina may effectively dissipate heat from the heat source such as YAG:Ce [1]. In addition, Al_2O_3 and

YAG have similar thermal expansion coefficients (the linear thermal expansion coefficient is 8.4×10^{-6} K^{-1} for Al_2O_3 and 8.0×10^{-6} K^{-1} for YAG, respectively). The good match between these two components will not cause imperfect mechanical contact or interfacial separation. The other key parameter for SSL is a luminous efficiency that is determined by the quantum efficiency of the phosphor ceramics. This impose some requirements on matrix material that should not have absorption in the visible spectral range and after sintering provides transparency or translucency; e.g. Al_2O_3 ceramics prepared by the spark plasma sintering method provide the maximum transmittance of 85%, that is very close to the theoretical value of 86% for Al_2O_3 single crystal [1]. Based on these facts it is reasonable to expect that YAG-Al_2O_3 composites will be promising candidates for SSL applications with good thermal and optical properties.

In the present work we report on preparation and preliminary characterisation of compact samples prepared by hot pressing of glass microspheres powders in the Ce^{3+} doped Y_2O_3-Al_2O_3 system with different ratio of YAG to Al_2O_3 phase in a composite. First, the thermal properties of prepared glass microspheres were studied by differential scanning calorimetry (DSC). Based on the thermal behaviour, the hot press conditions were selected and luminescent properties of prepared compacts have been investigated.

EXPERIMENTAL

The precursor powders for preparation of glass microspheres were synthesised by modified Pechini method and glass microspheres by flame spraying technique as described elsewhere [2]. The composition of prepared samples are summarised in Tab. 1.

Tab. 1: Theoretical composition of prepared glass

	Glass composition				
Sample[&]	**Y_2O_3 (mol.%)**	**Al_2O_3 (mol.%)**	**Ce_2O_3 (mol.%)**	**Ce^{3+} (at.%)**	**Ce^{3+} in YAG (at.%)**[#]
30%YAG : 70%Al_2O_3 (eut.)	22.64	76.86	0.50	1.00	3.48
50%YAG : 50%Al_2O_3	18.25	81.25	0.50	1.00	2.00
70%YAG : 30%Al_2O_3	25.75	73.75	0.50	1.00	1.42

[&] Denotes composition of YAG/Al_2O_3 phase in the whole sample in mol.%

[#] Recalculated under assumption that all Ce^{3+} ions are hosted in YAG phase after crystallization (heat treatment)

The phase composition was examined using powder diffractometer Panalytical Empyrean DY1098 operating with CuKα radiation. The thermal properties of prepared glass microspheres were studied by differential scanning calorimetry (DSC) in the temperature range between 35 and 1200°C, at a heating rate of 10°C/min, in nitrogen atmosphere using the Netzsch STA 449 F1 Jupiter simultaneous thermal analyser. Approximately 15 mg of glass microspheres was weighed into Pt crucibles and used for DSC experiments. The individual records were evaluated by the Netzsch Proteus (version 6.0.0.) software.

Table 2: Experimental conditions for hot pressing experiments

Sample denote	**Temperature (°C)**	**Pressure (MPa)**	**Dwell time (min)**
840°C / 0 min	840	40	0
1000°C / 30 min	1000	40	30
1000°C / 60 min	1000	40	60
1100°C / 60 min	1100	40	60

The glass microspheres powder, without any treatment in reducing atmosphere was used for hot-press experiments. The compact samples with diameter 1cm and thickness of about 1mm were prepared by hot pressing (Clasic 0220 ZL) at temperatures and isothermal dwell time as summarised in Tab. 2, and with the maximum applied pressure of 40 MPa in the vacuum. WC foil was used as a high temperature protection and an interface between the sample and the graphite die. The luminescence spectra were measured using a Fluorolog FL3-21 spectrometer equipped with the photomultiplier tube R928 detector (VIS range). The Xe-lamp (450 W) was used as an excitation light source. The luminescence spectra of studied samples were recorded at room temperature in front face mode (backscattering geometry).

RESULTS

The composition of prepared Ce^{3+}- doped glasses is derived from the corresponding un-doped system (Fig.1) by equimolar substitution of Y_2O_3 by Ce_2O_3 and is summarised in Tab. 1. The concentration of Ce^{3+} ions in a glass was kept at constant level of 1.0 at.%. However, the dopant concentration change in particular system after crystallization due to much better solubility of Re^{3+} ions in YAG than in Al_2O_3 phase (see Tab.1). The composition of basic glasses were selected in order to change the YAG:Al_2O_3 phase molar ratio and to test behaviour during hot pressing and compacting of a glass powder. As documented in our previous work [2], when these glasses are crystallised at lower temperature up to 1200°C only YAG phase precipitate from the yttrium-aluminate glass as nano/microcrystals embedded in the Al_2O_3 enriched amorphous matrix. The Al_2O_3 phase starts to crystallize over 1300°C as documented by HT XRD scan [2]. Also due to higher thermal conductivity of Al_2O_3 phase compared to the YAG phase, the Al_2O_3 enriched matrix may serve as heat absorber and dissipate the heat from YAG:Ce^{3+} crystals (worming due to the non-radiative transitions), that is common problem in LED devices emitting the white light; increasing temperature significantly affects the luminescence intensity (thermal quenching).

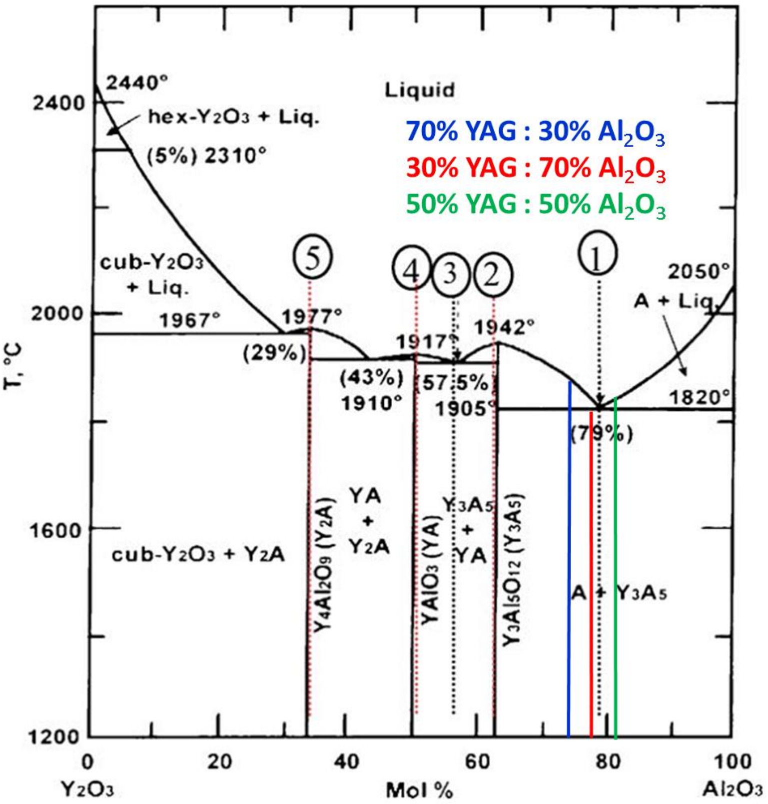

Figure 1: Experimental Y_2O_3-Al_2O_3 phase diagram with the studied compositions. Adopted from ref. [3].

The prepared glass microspheres of given compositions were found to be XRD amorphous within the detection limit of the XRD diffractometer. Thermal properties of prepared glass compositions were examined by DSC analysis. The DSC records for studied samples are shown in Fig. 2. Two exothermic effects are clearly observed in DSC traces, the first one at temperatures around 940°C and the second effect, ranging from 965°C up to 1060°C, that is significantly dependent on the composition of the glass. Based on our previous studies, both effects correspond to the crystallization of the YAG phase, as documented also by high temperature XRD, however, each step takes place through different mechanism [2]. In fact, the peak temperature of the second exothermic effect increases with increasing Al_2O_3 content in glass (see Tab. 1), which point to the important role of matter diffusion in the glass during the crystallization process of the YAG phase from amorphous matrix. In general, closer the glass composition is to the pure YAG phase closer is second peak is to the first exothermic effect. The Al_2O_3 phase as corundum start to crystallize over 1300°C [2]. The T_g temperature estimated from DSC data was found to be around 890°C.

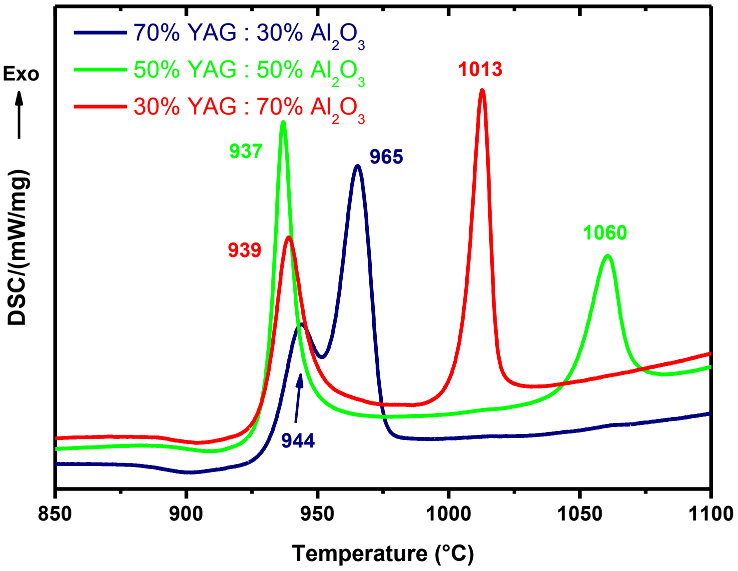

Figure 2: DSC traces of Ce^{3+}-doped glasses recorded at the scan rate of 10°C/min with indicated peak temperatures.

The hot-press experiments were conducted at conditions summarised in Tab. 2. The sintering by viscous flow at temperatures above glass transformation temperature T_g, in the so called kinetic window between T_g and T_x (onset of crystallization), is well-know method to prepare coherent, dense, bulk forms form glass powders e.g. conventional glass frit. This method was also applied by A. Rosenflanz et.al. [4] to prepare bulk glasses and ultrahard nanoceramics based on alumina and rare-earth oxides; the prepared rare-earth aluminate glass microbeads were consolidated by hot-pressing into the bulk glass. The bulk glass from microspheres with eutectic composition was prepared at temperature 840°C with dwell time 0 min, applying the pressure of 40MPa (Fig. 3). These hot-pressing conditions were selected based on preliminary experiments, when at lower temperatures than 840°C almost no bulk samples was possible to prepare, while at higher temperatures the glass starts to crystallise under the applied pressure even at temperatures below the crystallization onset (T_x) estimated from DSC records. Due to high tendency of these type of glasses to crystallize rapidly at and even below T_x, almost zero dwell time (based on the dilatation curve) was selected to retain the consolidated sample in the glassy state. The glass-ceramic samples with YAG crystals embedded in residual glass matrix were prepared at temperatures 1000°C and 1100°C with the dwell time 30 and 60 min. The yellow colour of the consolidated bulk samples (Fig. 3) typical for the YAG:Ce phosphor was observed, indicating crystallization of YAG:Ce from the glass during hot-pressing of glass microspheres. It should be noted, that for hot-press experiments, glass microspheres without any treatment in reducing atmosphere was used. In case when glass was treated before compacting in reducing N_2:10 vol.%H_2 atmosphere (to convert Ce^{4+} to PL active Ce^{3+} ions) the compact bulk samples were visibly contaminated with carbon, that significantly affect their luminescence. Moreover, the composition 70%YAG: 30%Al_2O_3 was not possible to prepare in compact form due to low amount of residual glass phase that holds YAG crystals together.

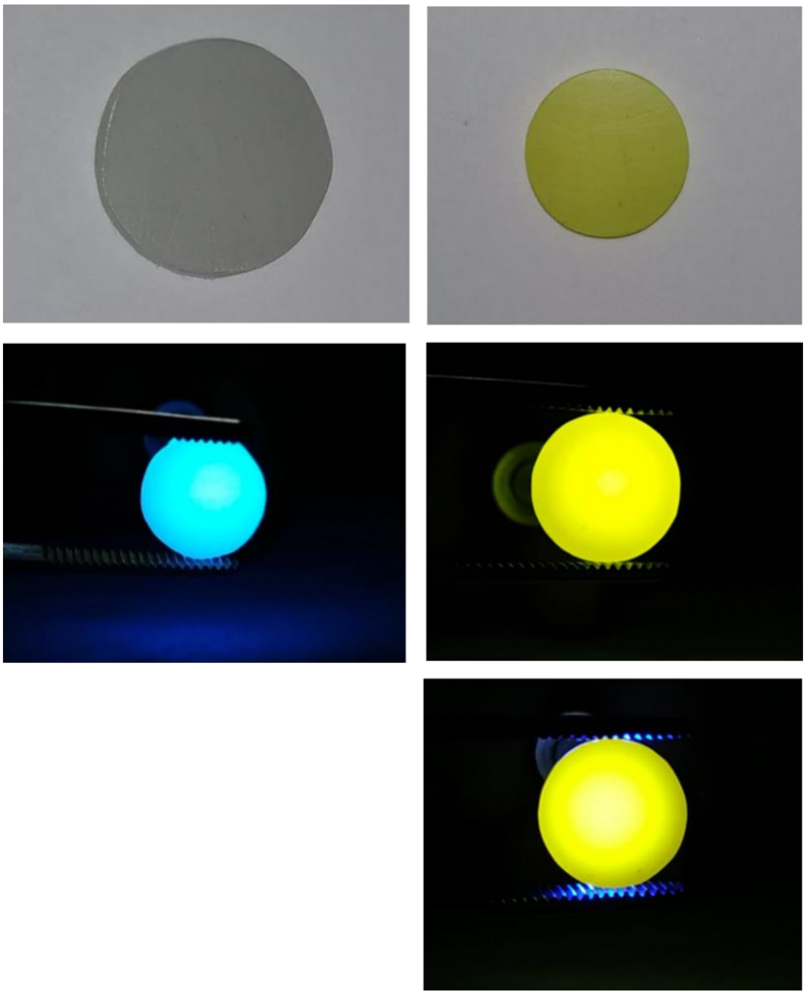

Figure 3: The compact samples (eutectic composition, ∅ 1cm, thickness 1mm) prepared by hot-press of glass microspheres at 840°C/0 min (upper left) and at 1000°C/30 min dwell time and pressure 40MPa (upper right). The compact samples excited by UV light at 350 nm (middle) and 455 nm (down right) blue light.

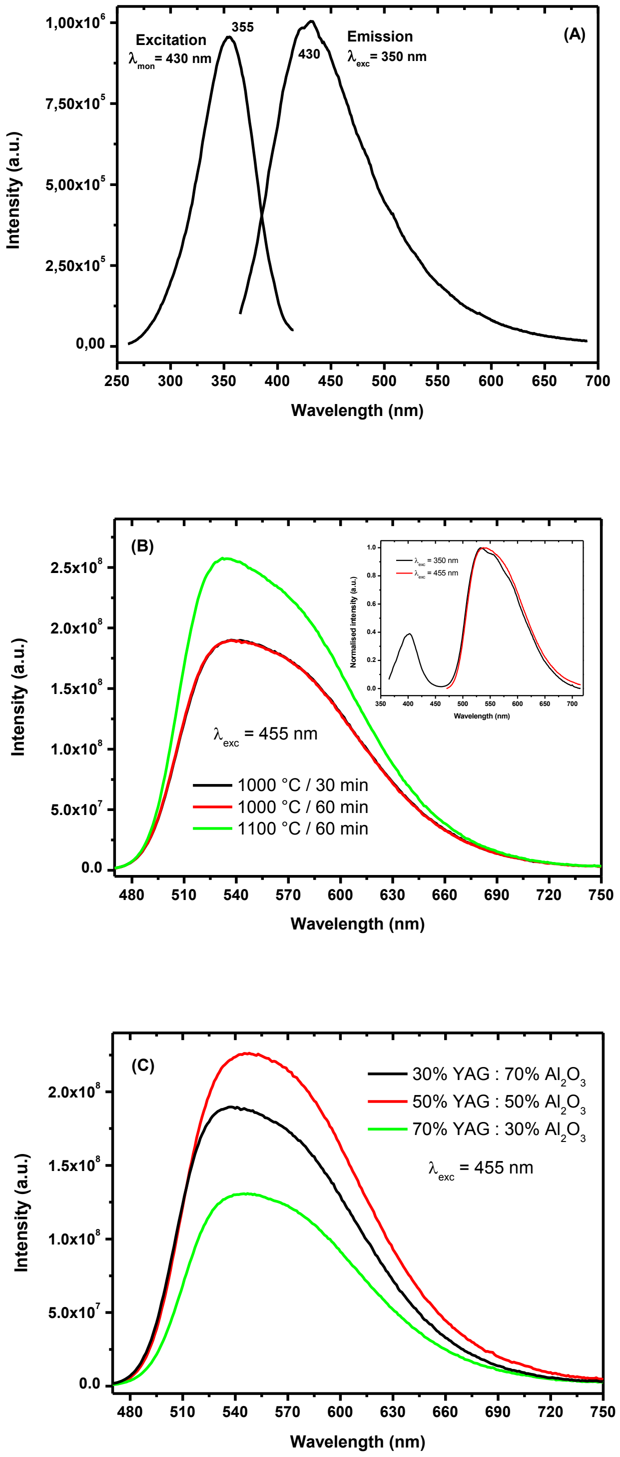

Figure 4: (A) The excitation and emission (PL) spectra of sample with composition 30%YAG-70% Al_2O_3 (eutectic composition) prepared by hot-press of glass microspheres at 840°C/0 min. (B) The PL spectra of sample with composition 30%YAG-70% Al_2O_3 prepared by hot-press of glass microspheres at different temperature and dwell time. Inset represent emission spectra under sample excitation by UV and blue light. (C) The PL spectra of sample with different composition prepared by hot-press of glass microspheres at 1000°C/60 min.

The excitation (PLE) and emission (PL) spectra of the glass bulk sample with eutectic composition is depicted on Fig. 4A. The excitation spectrum was monitored at wavelength 430 nm. The strong absorption with maxima at 355 nm can be ascribed to 4f-5d transition in Ce^{3+} ions. The emission spectrum of the glass compact recorded under UV excitation at 350 nm exhibits broad emission band in spectral range of 365-550 nm with the emission maximum at 430 nm. This emission corresponds to the $5d\rightarrow{}^2F_{5/2}$ and $5d\rightarrow{}^2F_{7/2}$ transitions that are not clearly resolved as in the other Ce^{3+} doped systems with blue emission [5]. This is most likely due to the close energy of the 4f ($^2F_{5/2}$, $^2F_{7/2}$) ground states in Ce^{3+} ions in the yttrium aluminate glass; Ce^{3+} with $4f^1$ electron configuration has two ground states of $^2F_{5/2}$ and $^2F_{7/2}$ due to the spin-orbital coupling. Visible blue light emission from glass compact under UV excitation is clearly shown in Fig. 3. The blue emission point to the weaker crystal field strength around Ce^{3+} ions in prepared glasses compared to the crystal field strength around Ce^{3+} ions in YAG phase (green-yellow emission).

The PL emission spectra ($\lambda_{exc} = 455$ nm) of hot-pressed samples with eutectic composition at different temperatures and dwell time are depicted in Fig. 4B. A typical broad emission band centred at ~550 nm is seen in spectra of samples. The PL emission curves can be deconvoluted into two broad Gaussian bands centred at ~527 nm (peak 1) and ~577 nm (peak 2). These two peaks correspond to the typical $5d^1$-$4f^1$ ($^2F_{5/2}$) and $5d^1$-$4f^1$ ($^2F_{7/2}$) transitions of Ce^{3+} ion, the energy difference between the two energy levels is ~1600 cm^{-1} due to of the spin-orbital coupling in crystal-field [6]. The PL emission intensity depends on the treatment temperature. As the temperature increases from 1000°C to 1100°C, the PL emission intensity significantly increases. The increase of emission intensity with treatment temperature is due to the improvement of crystallinity of samples; most likely more Ce^{3+} doped YAG crystalline phase is formed in the residual glass matrix. The PL spectra of compact samples prepared from different compositions of starting glass sintered at 1000°C/60 min are depicted in Fig. 4C. The emission intensity increases with expected concentration of Ce^{3+} ions in YAG phase for 1.42 and 2.00 at.%, than for concentration 3.48 at.% decreases, most likely due to the energy transfer between Ce^{3+} ions and non-radiative transitions, the effect well known as concentration quenching. Yellow light emission from glass compact under UV/blue light excitation is clearly shown in Fig. 3. The testing of mechanical properties and microstructural study of compact bulk phosphors is currently in progress.

CONCLUSIONS

The sintering by viscous flow at temperatures above glass transformation temperature T_g, in the so called kinetic window between T_g and T_x (onset of crystallization) was used to prepare the bulk glass/glass-ceramics phosphors from glass microspheres, emitting blue and yellow light when excited by UV or blue light. The thermal properties of prepared glass microspheres were studied by DSC analysis. Two exothermic effects are clearly observed in DSC traces, the first one at temperatures around 940°C and the second effect, ranging from 965°C up to 1060°C, that is significantly dependent on the composition of the glass. Both exothermic effects correspond to the crystallization of the YAG phase. The peak temperature of the second exothermic effect increases with increasing Al_2O_3 content, which point to the important role of matter diffusion in the glass during the crystallization process of the YAG phase from amorphous matrix. The blue emission point to the weaker crystal field strength around Ce^{3+} ions in prepared glasses compared to the crystal field strength around Ce^{3+} ions in YAG phase (green-yellow emission). The green-yellow emission intensity form glass-ceramics compacts depends on temperature treatment and composition of glass microspheres (YAG:Al_2O_3 ratio). The highest emission intensity for the given composition (30%YAG-70% Al_2O_3) was found for sintering at 1100°C/60 min, and for constant sintering conditions for composition 50%YAG-50% Al_2O_3. The testing of mechanical properties and microstructural study of compact bulk phosphors is currently in progress. However, the optimisation of Ce^{3+} concentration in host matrix is further necessary to obtain the higher emission intensity.

ACKNOWLEDGMENT

This work was supported by the Slovak Research and Development Agency under the contract No. APVV-17-0049 and by grants VEGA 1/0527/18. This paper is a part of dissemination activities of the project FunGlass. This project has received funding from the European Union´s Horizon 2020 research and innovation programme under grant agreement No 739566.

REFERENCES

[1] S. Li, Q. Zhu, D. Tang, X. Liu, G. Quyang, L. Cao, N. Hirosaki, T. Nishimura, Z. Huang, R.-J. Xie, Al_2O_3-YAG:Ce composite phosphor ceramic: A thermaly robust and efficient color converter for solid state laser lighting, J. Mater. Chem. C 4 (2016) 8648-8654, and references cited therein.

[2] A. Prnová, R. Klement, K. Bodišová, J. Valúchová, D. Galusek, E. Bruneel, I.V. Driessche, Thermal behaviour of yttrium aluminate glasses studied by DSC, high-temperature X-ray diffraction, SEM and SEM EDS, J. Therm. Anal. Calorim. 128 (2017) 1407-1415.

[3] M. Medraj, R. Hammond, M.A. Parvez, R.A.L. Drew, W.T. Thompson, High temperature neutron diffraction study of the Al_2O_3-Y_2O_3 system, J. Eur. Ceram. Soc. 26 (2006) 3515-3524.

[4] A. Rosenflanz, M. Frey, B. Endres, T. Anderson, E. Richards, C. Schardt, Bulk glasses and ultrahard nanoceramics based on alumina and rare-earth oxides, Nature 430 (2004) 761-764.

[5] G. Zhu, Z. Ci, Q. Wang, Y. Wen, S. Han, Y. Shi, S. Xin and Y. Wang, J.Mater. Chem. C, 1 (2013) 4490-4496.

[6] R.R. Jacobs, W.F. Krupke and M.J. Weber, Appl. Phys. Lett. 33 (1978) 410-412.

OPTICAL PROPERTIES

Ni-DOPOVANÉ GELENITOVÉ SKLENÉ MIKROGUĽÔČKY: PRÍPRAVA A CHARAKTERIZÁCIA

Ni-DOPED GEHLENITE GLASS MICROSPHERES: PREPARATION AND CHARACTERIZATION

M. Majerová[1], A. Prnová[2], R. Klement[3], M. Škrátek[1], A. Cigáň[1], A. Dvurečenskij[1],
P. Švančárek[2], J. Kraxner[3], J. Maňka[1], D. Galusek[2,3]

[1] *Ústav merania, Slovenská akadémia vied, Dúbravská cesta 9, 842 19 Bratislava,*
[2] *Vitrum Laugaricio, Centrum kompetencie skla, Spoločné pracovisko ÚAch SAV, TnU AD a FChPT STU, Študentská 2, 911 50 Trenčín*
[3] *Centre for functional and surface functionalized glass, Alexander Dubček University of Trenčín, Študentská 2, 911 50 Trenčín*

ABSTRACT

A flame-spraying technique was applied for preparation of Ni-doped (0.5, 1.0 and 3.0 mol. %) aluminate glass microspheres with gehlenite matrix. In the first step, the precursor powders were prepared from high-purity $CaCO_3$, Al_2O_3, SiO_2 and NiO by a solid-state reaction. The glasses were prepared in the form of microspheres by melting precursor powders in CH_4-O_2 flame and by quenching micro-droplets of the melt by spraying them with deionized water. The structural, photoluminescence and magnetic properties were studied by optical microscopy (OM), scanning electron microscopy (SEM), photoluminescence (PL) spectroscopy and Quantum Design SQUID magnetometer. Phase composition was determined by X-ray diffraction (XRD). The PL emission properties of prepared glasses and their polycrystalline analogues (glass crystallized at 1000 °C for 10 h) were studied in the near-infrared (NIR) spectral range. Glass microspheres did not exhibit luminescence. The polycrystalline samples (excited at 335 nm) exhibited emission band around 1180 nm. The undoped and Ni-doped gehlenite microspheres showed complex magnetic behaviour, which depend on temperature and the magnetic field.

Keywords: Gehlenite, Flame synthesis, Ni^{2+}-doped glasses, PL properties, magnetic properties

INTRODUCTION

The melilites are a large family of tetragonal, non-centrosymmetric materials with a general formula $M_2T_{(1)}T_{(2)2}O_7$ (M are usually the alkaline-earths metals and $T_{(1)}$ and $T_{(2)}$ are usually Al, Ga, Si or Ge) [1]. Since the nineties, the melilite compounds have been intensively studied due to their interesting electrochemical- [2], magnetic- [3, 4], luminescence- [5, 6] and structural-properties [7]. Due to their tetragonal and non-centrosymmetric crystal structure lanthanides can be accepted easily as constituents or dopants by the melilites. Rare-earth (RE) ions doped melilite-type materials represented by gehlenite ($Ca_2Al_2SiO_7$) have been intensively investigated over the past few decades. For example, gehlenite doped with Nd^{3+} ions is a good candidate for diode pumped laser, with a broad absorption around 806 nm [8]. $Ca_2Al_2SiO_7$:Eu^{3+}, Tb^{3+} as potential candidates for phosphor converted light-emitting diodes was reported by Yang et al. [9]. Bernardo et al. compared amorphous gehlenite-based Eu^{3+}-

doped phosphor materials with polycrystalline phosphors of the same composition [10]. It was determined that amorphous phosphor materials contain much more homogeneously distributed dopants (or activators), because they have no grain boundaries to accumulate the dopants.

Currently, most inorganic phosphors contain a significant amount of RE elements. However, the use of RE elements recently threatens the production of inorganic phosphors, due to a sharp increase in their prices, market scarcity and limited raw material resources. The use of RE is also expensive due to the conditions of production (high temperature, high pressure or reducing condition) [9].

3d transition metal ions (Ni^{2+}, Co^{2+}, Cr^{4+}), due to broad photoemission bands in the NIR, have significant and continuous attention for potential applications in tunable lasers, broadband optical amplifiers and optical communications. Nickel takes the divalent state in almost all the hosts, as the divalent nickel is extremely stable [11]. Nickel imparts to oxide glasses probably the widest range of coloration (green, yellow, brown, purple and blue). Ni^{2+} may be present in an inorganic matrix in three different coordination states: tetrahedral (fourfold, $^{IV}Ni^{2+}$), trigonal (fivefold, $^{V}Ni^{2+}$) and octahedral (sixfold, $^{VI}Ni^{2+}$): the modification of the glass colour is related to these three kinds of coordination. NIR luminescence is typically observed in oxide matrices only when a specific coordination is provided, e.g. octahedral for Ni^{2+} [12].

In recent years various materials (glasses, transparent glass-ceramics, ceramics and crystals) were considered for Ni^{2+} doping. The change of Ni^{2+} coordination was found in the case of Li_2O-Al_2O_3-SiO_2, MgO-Al_2O_3-SiO, ZnO-Al_2O_3-SiO glasses doped with TiO_2 and NiO with the increase of the heat-treatment temperature [13]. In parent glasses five-fold coordinated Ni^{2+} sites are present, which are the most reactive species upon liquid phase separation and crystallization. During heat-treatment $^{V}Ni^{2+}$ sites disappear and new distorted $^{VI}Ni^{2+}$ are formed within aluminotitanate, Mg (or Zn) aluminotitanate and Mg (or Zn) aluminate amorphous regions. Botao et al. measured broadband near-infrared emission centred at 1220 nm for Ni^{2+}-doped silicate glass ceramics, with the following composition: MgO-Al_2O_3-Ga_2O_3-SiO_2-TiO_2 [14].

In this work, we investigated the luminescence and magnetic properties of Ni-doped gehlenite glass microspheres, which have been prepared by solid state reaction followed by flame synthesis, and of their polycrystalline analogues.

EXPERIMENTAL

Powder precursors were prepared by solid state reaction, from high-purity SiO_2 (p.a., Polske odczynniki chemiczne, Gliwice), Al_2O_3 (p.a., Centralchem, Bratislava), NiO (99.9 %, STREM Chemicals, USA) and $CaCO_3$ (p.a., Centralchem, Bratislava). The compositions of prepared systems are summarised in the Table 1. At first, suitable amounts of the starting powders were weighed and homogenized in an agate mill in isopropyl alcohol for 4 hours. After drying under infra-red lamp the powders were calcined in a two-step process at 1000 °C for 4 hours in air. In the next step the calcined powders were annealed at 1300 °C for 4 hours in Pt crucible. The synthesized precursors powders were then crushed, and sieved through a 40 μm polyethylene sieve. Flame synthesis was used to prepare glass microspheres from powder precursors. The powders were fed into methane-oxygen flame. The molten particles were quenched by spraying them with distilled water, separated, dried and calcined at 650 °C in air for 4 hours.

To study the influence of crystallinity on magnetic and luminescence properties of prepared glass microspheres and crystallized samples an isothermal crystallization experiments at 1000 °C for 10 h under ambient atmosphere were performed.

Primary information on the morphology of prepared microspheres was obtained by optical microscopy (Nikon ECLIPSE ME 600) in transmitted light at 10-50x magnification. More detailed examination of prepared glass microspheres was carried out by scanning electron microscopy (FEG SEM JEOL 7600F) at accelerating voltage 20 kV. The microspheres were fixed on aluminum sample holder using conductive adhesive graphite tape and sputtered with gold (Carl Zeiss SC 7620 sputter coater) to prevent charging. For the SEM examination of polished cross section of glass microspheres, the microspheres were embedded into polymeric resin (Simplimet 1000, Buehler), carefully polished to prepare cross sections (Ecomet 300, Buehler) and sputtered with carbon to prevent charging. Diameter size distribution of glass microspheres was determined with the use of Mastersizer 2000 instrument (Malvern Instruments).

Phase composition of glass microspheres and of their polycrystalline analogues were studied by X-ray diffraction (Pananalytical Empyrean, CuKα radiation, at ambient temperature in the 2θ range of 10-80°). The software High Score Plus (v. 3.0.4, Pananalytical, The Netherlands) was used to evaluate diffraction data with the use of the COD database.

Magnetic properties were measured by the Quantum Design MPMS XL-7AC SQUID magnetometer. The DC mass magnetization $M(H)$ was measured at 300 K and 2K.

The photoluminescence spectra were recorded by Fluorolog FL3-21 spectrometer (Horiba Jobin Yvon) using Xe (450W) arc lamp as an excitation source.

Table 1: Composition of prepared glass microspheres

Sample	Theoretical composition (mol. %)			
	CaO	Al_2O_3	SiO_2	NiO
GNi0.5	49.76	24.87	24.87	0.5
GNi1.0	49.50	24.75	24.75	1.0
GNi3.0	48.50	24.25	24.25	3.0

RESULTS

Optical micrographs of Ni-doped gehlenite microspheres are shown in Fig. 1. Polydisperse systems have been prepared, with spherical particles transparent in the visible region of the spectrum. A detailed examination of the morphology of the prepared systems was performed by scanning electron microscopy (Fig. 2).

The amorphous character of the prepared glass microspheres was indicated by examining polished cross-sections that contained no morphological features suggesting the presence of crystalline phases.

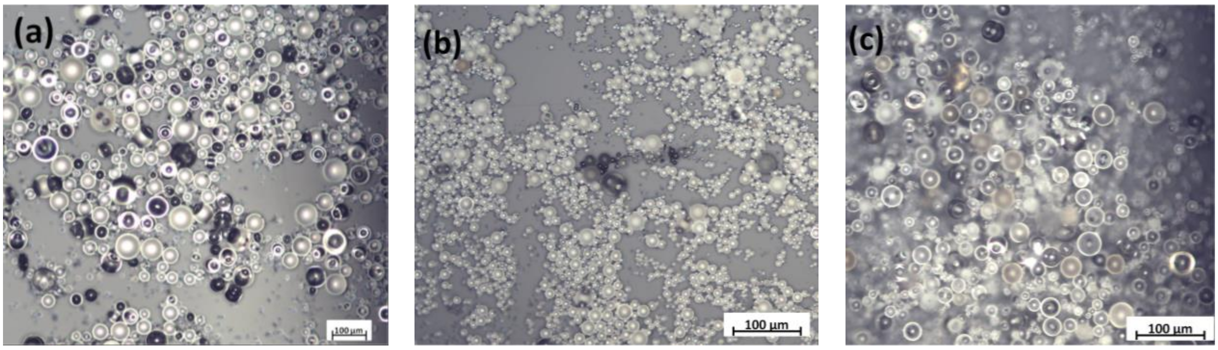

Figure 1: Optical micrographs of (a) GNi0.5; (b) GN1.0; (c) GNi3.0 microspheres.

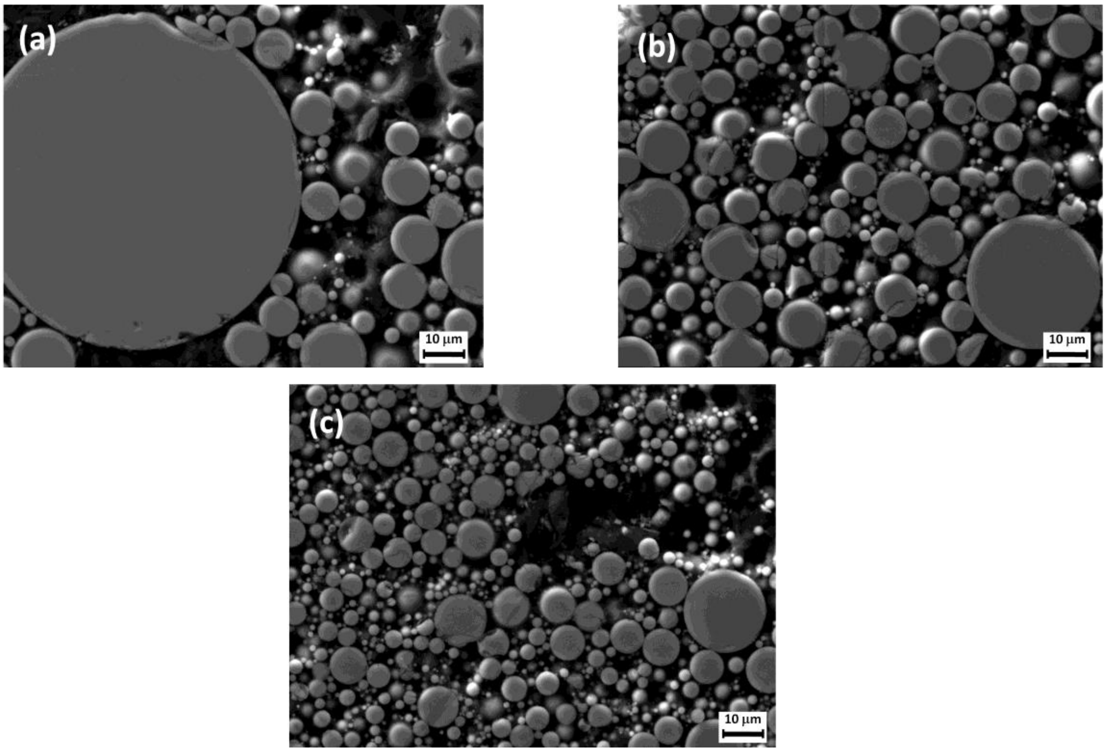

Figure 2: The results of SEM examination of a polished cross sections of (a) GNi0.5; (b) GN1.0; (c) GNi3.0 microspheres.

The particle size distribution analysis (Fig. 3) has shown relatively broad particle size distribution for each sample. The mean particle diameter (d_{50}) was the highest for the GNi0.5 sample and the lowest for the GNi1.0 sample (Table 2). The d_{10} and d_{90} values were obtained from the cumulative diameter distribution curve (the d_n percentile indicates that n % of the particles have a size smaller than shown value). The width of the particle size distribution was the largest for GNi0.5 samples.

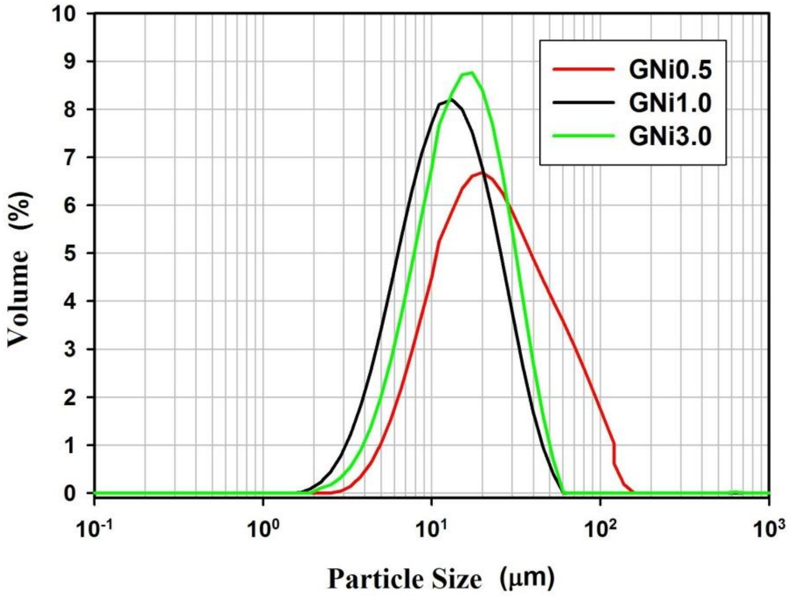

Figure 3: Particle size distribution of Ni doped gehlenite microspheres.

Table 2: Particle diameter for Ni doped gehlenite glass microspheres.

Sample	d_{10} / µm	d_{50} / µm	d_{90} / µm	d_{90}-d_{10} / µm
GNi0.5	8	21	64	56
GNi1.0	5	12	26	21
GNi3.0	6	14	29	23

The phase composition of the prepared Ni doped glass microspheres was studied by X-ray diffraction analysis. The absence of peaks indicating crystalline phases and presence of broad amorphous shoulder (in the range 2θ 24 ° - 36 °) in the XRD diffraction patterns of the prepared microspheres confirmed that the microspheres were X-ray amorphous and the content of any crystalline phase was below the detection limit of X-ray diffraction (Fig. 4).

The XRD patterns of crystallized microspheres (Fig. 5) revealed polycrystalline nature of samples with the presence of gehlenite as the only crystalline phase present (01-074-1607 COD) in case of all samples.

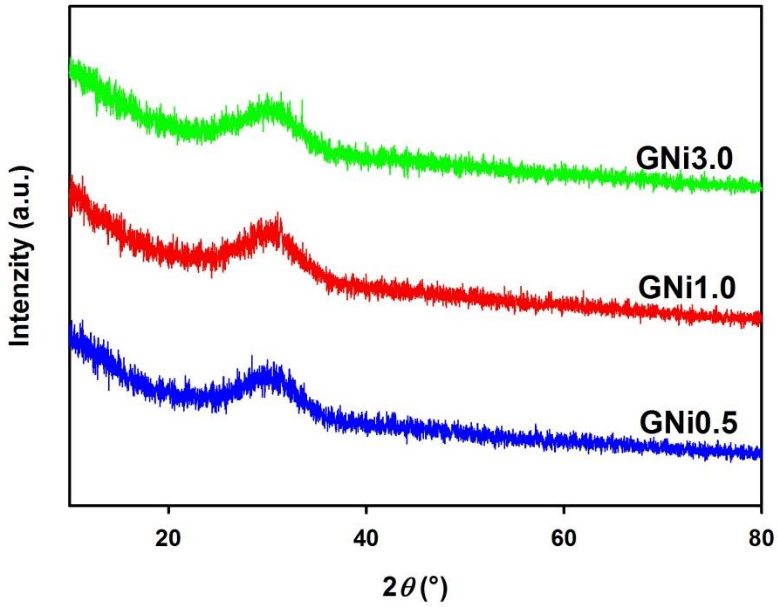

Figure 4: XRD patterns of Ni doped gehlenite glassy particles after flame synthesis.

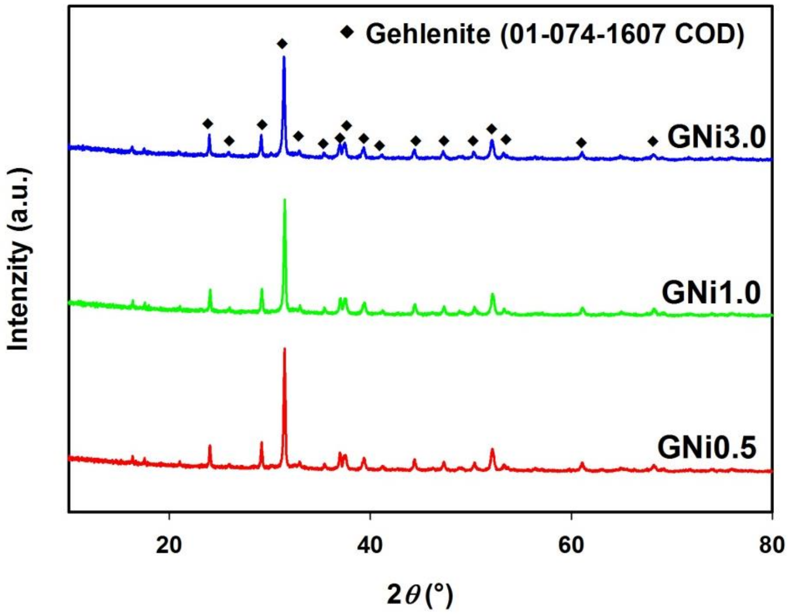

Figure 5: XRD patterns of crystallized Ni doped gehlenite microspheres (1000 °C/10 h).

The PL emission properties of prepared Ni doped glasses and their polycrystalline analogues (glass crystallized at 1000 °C for 10 h) were studied in NIR spectral range. The excitation spectra of the prepared microspheres were monitored at emission wavelengths of 997 nm and 1020 nm. The excitation spectra comprise two individual bands, which are located at about 330 nm and 678 nm, and a shoulder at about 450 nm (Fig. 6a). These excitation bands are assigned to spin-allowed $^3T_1(^3P) \rightarrow {}^3A_2(^3F)$, $^3T_2(^1D) \rightarrow {}^3A_2(^3F)$ and spin-forbidden $^3T_1(^3F) \rightarrow {}^3A_2(^3F)$ transitions, respectively, in $^{VI}Ni^{2+}$. In case of Ni doped glass microspheres no NIR luminescence was detected (Fig. 6b).

In case of crystallized samples, the excitation spectra (λ_{mon} = 1182 nm) show broad absorption bands with maxima at approximately 335 nm and 590 nm. These excitation bands are assigned to spin-allowed $^3T_1(^3P) \rightarrow {}^3A_2(^3F)$ and $^3T_2(^1D) \rightarrow {}^3A_2(^3F)$ in $^{VI}Ni^{2+}$ transitions (Fig. 6c). The absorption band centred at about 335 nm is slightly shifted as the concentration of Ni^{2+} ions increases (from 331 to 337 nm). The most intense excitation band ($^3T_1(^3P) \rightarrow {}^3A_2(^3F)$) was initially used for recording the NIR emission spectra. Then an emission band was detected with a maximum at 1180 nm. The emission intensity is significantly influenced by the concentration of Ni^{2+}: with increasing concentration the intensity decreases, probably due to concentration quenching (Fig. 6d). Similar results are published in Gao et al. [12], who prepared glasses with the composition (mol. %) of $30TiO_2$-$30BaO$-$30SiO_2$-$10Al_2O_3$-xNi (x = 0; 0.05; 0.1; 0.2; 0.4 and 0.8) by conventional melting.

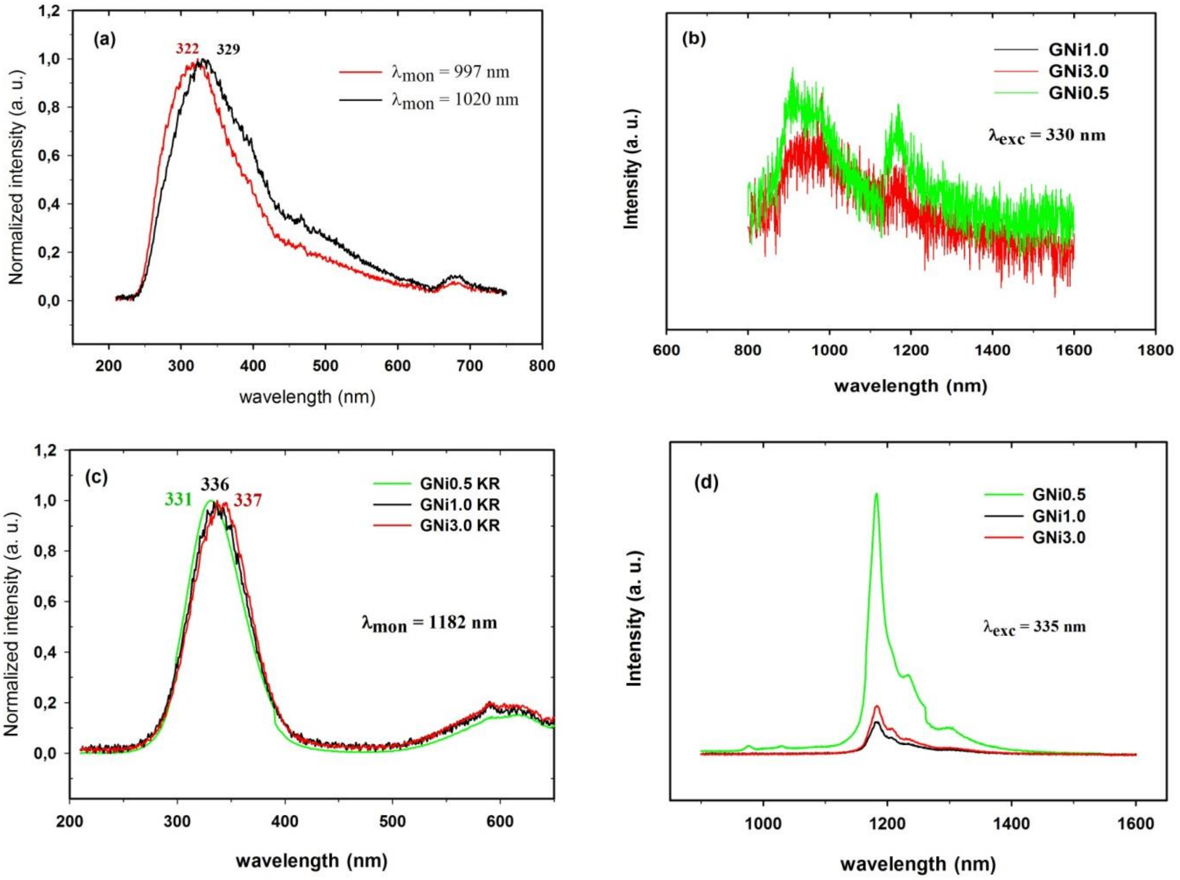

Figure 6: The photoluminescence excitation - PLE (a,c) and emission – PL spectra (b,d) of Ni^{2+} doped samples; (a, c) gehlenite glass microspheres; (b, d) crystallized microspheres

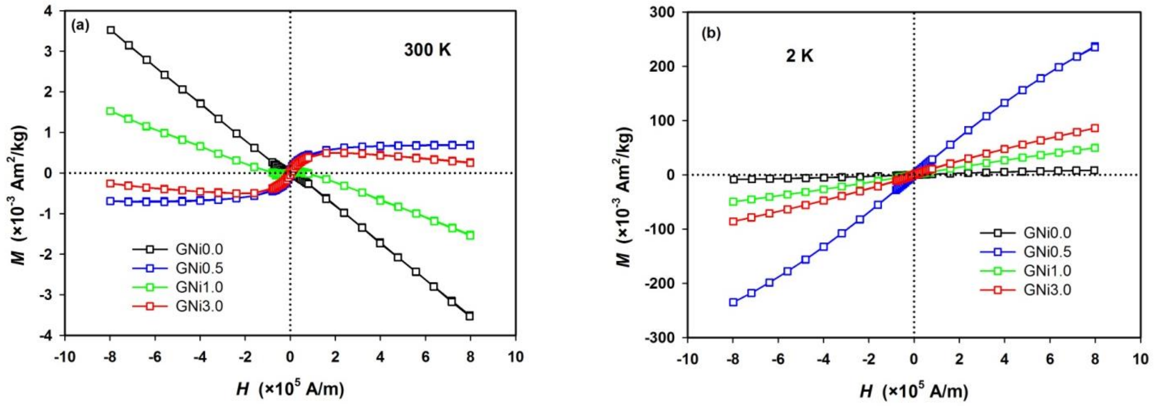

Figure 7: *M*(*H*) dependences of Ni-doped gehlenite glass microspheres measured at the temperature of 300 K (a) and 2 K (b).

Magnetization vs. applied field dependence (*M*(*H*) curve) measured at 300 K (Fig. 7a) shows for the undoped GNi0.0 and doped GNi1.0 gehlenite glass microspheres prevailing diamagnetic state, with small ferromagnetic contribution visible in the low field part of the curve. The influence of the diamagnetic component is significantly lower for the GNi0.5 and GNi3.0 samples. The magnetization significantly increased, when the temperature changed to 2 K. The *M*(*H*) curve for 2 K clearly shows paramagnetic state for all the samples (Fig. 7b). There is slight curvature and hysteresis for the GNi0.5, which could be the sign of the ferromagnetic ordering in this sample.

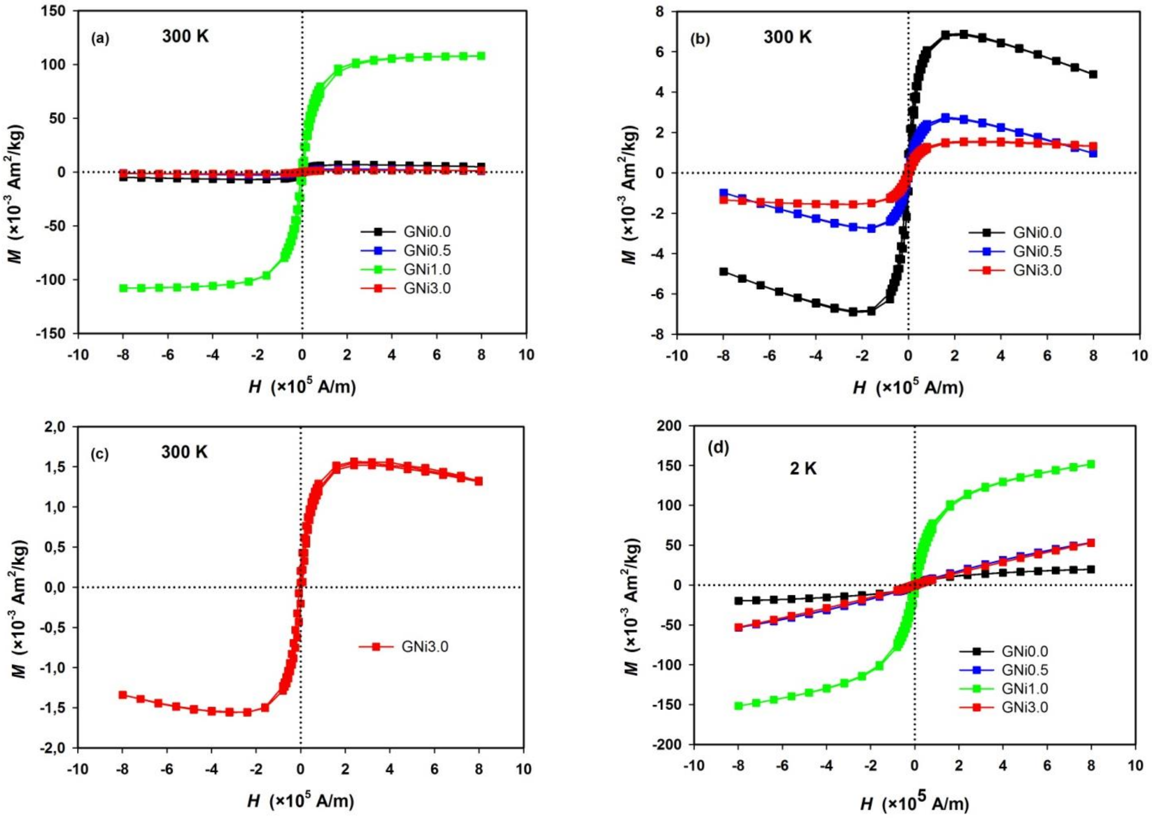

Figure 8: *M*(*H*) dependences of Ni-doped gehlenite crystallized microspheres measured at the temperature of 300 K (a, b, c) and 2 K (d).

The effect of crystallization on the magnetic properties is shown in Fig. 8. Magnetization of crystalline GNi1.0 sample is 10 times higher than magnetization of all other samples. The effect of the diamagnetic component is present in the case of undoped (GNi0.0) and doped GNi0.5 (Fig. 8b), GNi3.0 (Fig. 8c) crystalline samples, with ferromagnetic contribution visible in the low field part of the curve. In case of GNi1.0 sample, there is a significant influence of paramagnetic component in the high field part of the curve. In case of crystallized samples, as well as for amorphous samples, the influence of the paramagnetic component of magnetization is dominant at 2 K. Diamagnetism of the samples originates probably from the gehlenite host matrix, while the paramagnetism and the weak ferromagnetism originate from Ni doping.

CONCLUSIONS

Three Ni-doped gehlenite precursor powders with different concentration of Ni^{2+} ions (0.5, 1, 3 mol. %) were prepared by a solid-state reaction from powder raw materials. X-ray amorphous glass microspheres, with diameters up to 100 μm and transparent in visible light, were then prepared from the precursor powders by flame synthesis.

The PL emission properties of prepared glasses and of their polycrystalline analogues (glass crystallized at 1000 °C for 10 h) were studied in NIR spectral range. For glass microspheres, no NIR luminescence was observed due to predominance of nonradiative relaxation. Crystalline analogues an emission band was detected with a maximum at 1180 nm. The emission intensity is significantly influenced by the concentration of Ni^{2+}.

The Ni doped glass microspheres and their crystallized analogues exhibited complex magnetic properties, which depend on temperature and the magnetic field. Almost every sample showed a relatively strong diamagnetic contribution at the temperature of 300 K. At 2 K the influence of the paramagnetic component of magnetization was dominant.

ACKNOWLEDGMENT.

This paper is a part of the dissemination activities of project FunGlass. This project has received funding from the European Union´s Horizon 2020, research and innovation programme under grant agreement No 739566. The financial support of this work by the projects APVV 0014-15, VEGA 1/0527/18, VEGA 2/0026/17, VEGA 2/0164/17 is gratefully acknowledged.

REFERENCES

[1] Wu, H., Hu, Y., Ju, G., Li, Ch., Wang, X., Yang, Z. Photoluminescence of Ce^{3+} and Eu^{2+} in $Ca_2Al_2SiO_7$ matrix, Journal of Luminescnence, 131 (2011) 2441-2445

[2] Park, H.J., Kim, T.-G., Kwak, C., Lee, S., Lee, K.H. $Sr_2(Mg_{1-x}Ga_x)Ge_2O_{7+0.5x}$: Melilite-type oxygen ionic conductor associated with fivehold coordinated germanium and gallium, J. Power Sources 275 (2015) 884-887

[3] Nöller, R., Knoll, H., Magnetic properties of calcium-silicates (diopsite and gehlenite) doped with iron (III), Solid State Communications Vol. 47, No. 4 (1983) 237-239

[4] Majerova, M., Dvurecenskij, A., Cigan, A., Skratek, M., Prnova, A., Kraxner, J., Galusek, D. Magnetic properties of synthetic gehlenite glass microspheres, Acta Physica Polonica A 131 (2017) 699-701

[5] Shi, Y., Zhu, G., Mikami, M., Shimomura, Y., Wang, Y. Color-tunable $LaCaAl_3O_7$:Ce^{3+}, Tb^{3+} phosphors for UV light- emitting diodes, Materials Research Bulletin, 48 (2013) 114-117

[6] Shih, S.J., Lin, Y.Ch., Lin, S.H., Veteska, P., Galusek, D., Tuan, W.H. Preparation and characterization of Eu-doped gehlenite glassy using spray pyrolysis, Ceramics International 42 (2016) 11324-11329

[7] Yahia, H.M., Essehli, R., Belharouak, I., Gaudin, E. Crystal structure and magnetic properties of $K_2CoV_2O_7$, Materials Research Bulletin, 71 (2015) 7-10

[8] Viana, B., Lejus, A.M., Saber, D., Duxin, N., Vivien, D. Optical properties and energy transfer among Nd^{3+} in Nd:$Ca_2Al_2SiO_7$ crystals for diode pumped lasers, Optical Materials 3 (1994) 307-316

[9] Yang, P., Yu, X., Yu, H., Jiang, T., Xu, X., Yang, Z., Zhou, D., Song, Z., Yang, Y., Zhao, Z., Qiu, J. $Ca_2Al_2SiO_7$:Bi^{3+}, Eu^{3+}, Tb^{3+}: A potential single-phased tunable-color-emitting phosphor, Journal of Luminiscence 135 (2013) 206-210

[10] Bernardo, E., Fiocco, L., Prnova, A., Klement, R., Galusek, D. Gehlenite:Eu^{3+} phosphors from a silicone resin and nano-sized fillers, Optical Materials 36 (2014) 1243-1249

[11] Suzuki, T., Horibuchi, K., Ohishi, Y. Structural and optical properties of ZnO-Al_2O_3-SiO_2 system glass-ceramics containing Ni^{2+}-doped nanocrystals, Journal of Non-Crystalline Solids, 351 (2005) 2304-2309

[12] Gao, G., Reibstein, S., Spiecker, E., Peng, M., Wondraczek, L. Boradban NIR photoluminescence from Ni^{2+}-doped nanocrystalline Ba-Al titanate glass ceramics, Journal of Materials Chemistry, 22 (2012) 2582-2588

[13] Dugue, A., Dymshits, O., Cormier, L., Cochain, B., Lelong, G., Belin, S., Zhili, A. Structural evolution of Ni environment in lithium, magnesium and zinc aluminosilicate glasses and glass-ceramics, Journal of Non-Crystalline Solids, 413 (2015) 24-33

[14] Botao, W., Jiang, N., Zhou, S., Chen, D., Zhu, C., Qiu, J. Transparent Ni^{2+}-doped silicate glass ceramics for broadband near-infrared emission, Optical Materials, 30 (2008), 1900-1904

PRÍPRAVA NANOVLÁKIEN Al_2O_3 A ICH POVRCHOVÁ ÚPRAVA PLAZMOU

PREPARATION OF Al_2O_3 NANOFIBRES AND THEIR SURFACE PLASMA TREATMENT

G. Zrubcová[1], D. Pavliňák[1]

[1]Department of Physical Electronic, Masaryk University, Kotlářská 2, 611 37 Brno, Czech Republic

ABSTRACT

In this work, electrospinning method was used for preparation of ceramic nanofibres from $PVA/Al(NO_3)_3 \cdot 9H_2O$ precursor solution. Six solutions with different concentration of $PVA/Al(NO_3)_3 \cdot 9H_2O$ were prepared and nanofibres from each solution were spun. Precursor nanofibres were treated in DCSBD plasma (diffuse coplanar surface barrier discharge) for 10 minutes. Later were fibres thermally treated in furnance till 100/250/1000 °C. Calcinated nanofibres were studied by FTIR analysis, scanning electron microscopy and thermogravimetry.

Keywords: electrospinning, alumina, nanofibres, plasma

INTRODUCTION

The Al_2O_3 inorganic fibres are widely employed as engineering material used in various application mainly due to high ratio of the surface area to the volume and high desirable porosity. Al_2O_3 nanofibres play an important role as a promising material for a filtration [1], bio-template [2] and catalyst support in high temperature reactions [3]. Nanomaterials in the fibrous form have low basis weight, high permeability and small pore size that make them appropriate for the wide range of filtration application for example reducing NO_x and CO emission [4]. However, more often are Al_2O_3 nanofibres used in high-temperature composites with elastic modulus, thermal and chemical stability as a streighteners [5].

Nowadays, plasma treatment is widely used as an effective tool for physical and chemical modifications of polymer surface, leaving the bulk material unchanged [6-8]. It is a fact that plasma treatment leads to degradation of polymeric chains, chemical bond cleavage, creations of free radicals and release of gaseous degradation products due to irradiation by highly energetic photons (UV, soft X-ray) and substrate bombardment with electrons, ions excited species and radicals. Subsequent chemical reactions of transient, highly reactive species can result into formation of double bonds, large cross-linked and oxidized structures [9].

A needle-free technique was used for preparation nanofibres in this work. Nanofibres were prepared in Nanospider^{TM} NS LAB 500 (Elmarco, Czech Republic), which provides high voltage electrospinning process, spun from free liquid surface

EXPERIMENTAL

Six different polymeric solutions were prepared for spinning. Each solution had different weight concentration of PVA/$Al(NO_3)_3 \cdot 9H_2O$ respectively (see table 1).

Table 1: Sample labelling and composition

Sample labelling	**PVA [wt%]**	**$Al(NO_3)_3 \cdot 9H_2O$ [wt%]**	**Voltage [kV]**
16 PVA_0	20 ml 16%	0	45
14 PVA_0	23 ml 14%	0	65
16 PVA_{15}	20 ml 16%	15	60
14 PVA_{15}	23 ml 14%	15	55
16 PVA_{20}	20 ml 16%	20	60
14 PVA_{20}	23 ml 14%	20	56

Precursor solutions were mixed at 80°C over the night by magnetic stirrer till complete homogenization. Applied voltage varied according to concentrations of solution from 45-60 kV. Distance between electrodes was fixed to 140 mm. Spinning was performed at ambient air, temperature and humidity between 40-60 % RH. Plasma process was held in experimental reactor equipped by a non-isothermal source of plasma (DCSBD electrode). Experiments were done with input power 400 W to electrode at air with flow of gas 5 mL/min. Samples were treated by plasma for 10 minutes before calcination. The calcination process was studied in 100, 250 and 1000 °C temperature steps. The final alumina fibres were obtained by calcination (fig. 1B) in furnace at 1000 °C with the heating rate 9 °C/min.

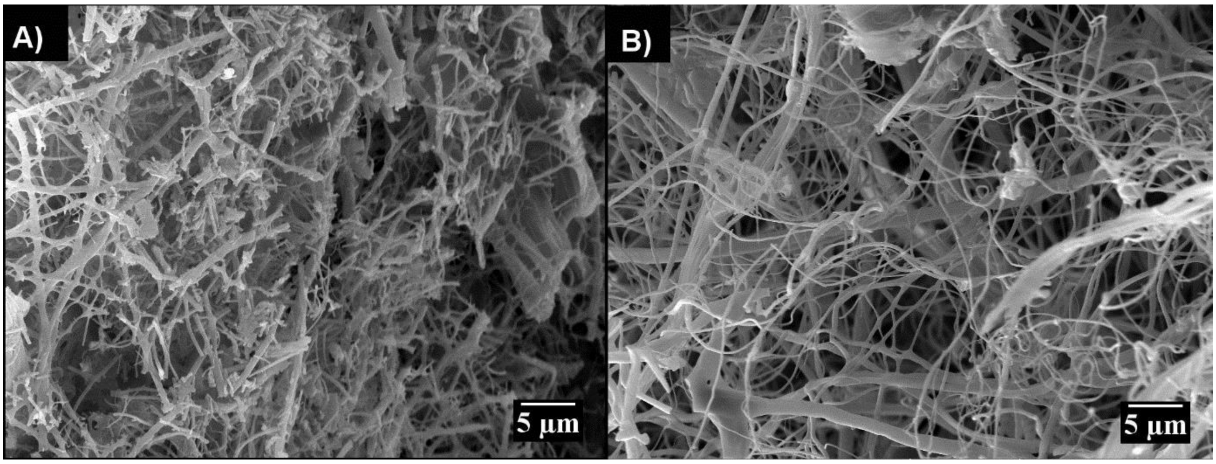

Figure 1: Nanofibres after calcination process till 1000 °C A) without plasma treatment B) with plasma treatment

RESULTS

Non-treated and plasma-treated samples were analysed and compared before and after the calcination process. Due to the plasma etching originally round fibres gradually flattened resulting in increase of their diameter. This phenomenon was explained as a "baking or melting" of nanofibres during plasma process. In case of nanofibres containing aluminium nitrate nonahydrate it was possible, that the water bonded in crystalline structure was released and diluted with PVA like it´s solvent. This could be a key step in the formation a membrane-like structure. Plasma had also a low impact on alumina fibres composition where an increase of oxygen-bonded chemical groups was observed (confirmed by EDX and ATR-FTIR analysis). Furthermore, plasma has a significant effect on the calcination process. Thermogravimetric analysis showed acceleration of calcination in case of plasma treated samples. This effect is not yet fully explained, however, it is assumed that it is caused by reactive groups (radicals, metastable groups) generated by plasma and trapped in the fibre structure. This phenomenon then results in a significant decrease in the temperature required for calcination. Material analysis showed that calcination process up to 1000 °C could not remove all of polymer content. Some carbon (apparently in the graphitic form) remained trapped inside the material.

CONCLUSIONS

In this work were prepared ceramic Al_2O_3 nanofibres using electrospinning method and thermal calcination. Water containing precursor results in formation of alumina nanofibers with membrane-like structure. It was found that, plasma treatment had a significant impact on final structure of material, final composition of nanofibres and it also accelerated the calcination process. Plasma treatment can be considered as a novel method for preparation of ceramic materials.

ACKNOWLEDGMENT

This research has been supported by the project LO1411 (NPU I) funded by Ministry of Education Youth and Sports of Czech Republic.

REFERENCES

[1] C. G. Kang and G. S. Ku, "An Experimental Investigation on Infiltration Limit and the Mechanical Properties of Al2O3 Short Fiber Reinforced Metal Matrix Composites Fabricated by Squeeze Casting," J. Compos. Mater., vol. 29, no. 4, pp. 444–462, Mar. 1995.

[2] T. Fan, B. Sun, J. Gu, D. Zhang, and L. W. M. Lau, "Biomorphic Al2O3 fibers synthesized using cotton as bio-templates," Scr. Mater., vol. 53, no. 8, pp. 893–897, Oct. 2005.

[3] A. A. Herzing, A. F. Carley, J. K. Edwards, G. J. Hutchings, and C. J. Kiely, "Microstructural Development and Catalytic Performance of Au−Pd Nanoparticles on Al 2 O 3 Supports: The Effect of Heat Treatment Temperature and Atmosphere," Chem. Mater., vol. 20, no. 4, pp. 1492–1501, Feb. 2008.

[4] P. Mallick, "Fiber-reinforced composites: materials, manufacturing, and design," 2007.

[5] R. Naslain, “Materials design and processing of high temperature ceramic matrix composites: state of the art and future trends,” Adv. Compos. Mater., vol. 8, no. 1, pp. 3–16, Jan. 1999.

[6] Y. Qiu, C. Zhang, Y. J. Hwang, B. L. Bures, and M. McCord, “The effect of atmospheric pressure helium plasma treatment on the surface and mechanical properties of ultrahigh-modulus polyethylene fibers,” J. Adhes. Sci. Technol., vol. 16, no. 1, pp. 99–107, Jan. 2002.

[7] H.-E. Wagner, R. Brandenburg, K. V. Kozlov, A. Sonnenfeld, P. Michel, and J. F. Behnke, “The barrier discharge: basic properties and applications to surface treatment,” Vacuum, vol. 71, no. 3, pp. 417–436, May 2003.

[8] Z. Gao, J. Sun, S. Peng, L. Yao, and Y. Qiu, “Surface modification of a polyamide 6 film by He/CF4 plasma using atmospheric pressure plasma jet,” Appl. Surf. Sci., vol. 256, no. 5, pp. 1496–1501, Dec. 2009.

[9] M. G. McCord, Y. J. Hwang, Y. Qiu, L. K. Hughes, and M. A. Bourham, “Surface analysis of cotton fabrics fluorinated in radio-frequency plasma,” J. Appl. Polym. Sci., vol. 88, no. 8, pp. 2038–2047, May 2003.

ELEKTROLYTICKY NANÁŠANÉ KOMPOZITNÉ KOVOVÉ VRSTVY SPEVNENÉ PLAZMOVO AKTIVOVANÝMI KERAMICKÝMI PRÁŠKAMI Al_2O_3 A WC

ELECTRODEPOSITED METAL MATRIX COMPOSITE LAYERS REINFORCED BY PLASMA ACTIVATED Al_2O_3 AND WC CERAMIC POWDERS

M. Ilčíková[1], B. Pijáková[1], L.D. Rafailovic[2], A. Stankovic[2], V. Buršíková[1], J. Ráheľ[1]

[1]*Masaryk University, Department of Physical Electronics, Kotlarska 2, Brno, Czech Republic*
[2] *CEST, Centre of Electrochemical Surface Technology, Viktor-Kaplan Strasse 2, 2700 Wiener Neustadt, Austria*

ABSTRACT

Plasma activated tungsten carbide and alumina ceramic powders were evaluated for their impact on electrochemical deposition of Cu and Ni metal matrix composite layers on steel substrate. Plasma activation was done by coplanar dielectric barrier discharge, operating in air at atmospheric pressure. In all experiments surface microstructure involving plasma activated powders was altered. More importantly, plasma treatment provided a statistically significant change in hardness of deposited layers. The effect was most pronounced for Cu metal matrix.

Keywords: electrodepositon; MMC layers; DBD plasma

INTRODUCTION

Electrochemical deposition can be used to fabricate metal layers with fine particles purposely incorporated into the metal matrix. The terms of composite plating, inclusion plating or dispersion coating are commonly used to name this process [1]. The coating itself is often referred to as metal matrix composite (MMC) layer. Polymer particles in metal matrix are used to achieve the effect of self-lubrication, corrosion resistance, or specific structures, e.g. for electrodes of modern batteries or ion membranes of fuel cells. Electrodepositions with dispersed ceramic particles have already found significant technological applications, mostly due to their improved abrasion resistance [2, 3] which may become an alternative to carcinogenic Cr(VI)-based electrolytes required to electrodeposit hard chromium coatings [4]. However, technological production of metallic coatings with dispersed ultra-fine particles suffers from problems associated with the aggregation of nanoparticles and their morphological changes in the aquatic environment. This limits seriously the reproducibility and long-term stability of MMC plating baths. The search for functional solutions to the outlined problems requires verification of new, innovative procedures.

To our best knowledge, the use of plasma activated ceramic powders for the electrodeposition of MMC has not been tested before. However, from the examples below one can reasonably expect that plasma activated powders have a potential to deliver some application-interesting results. Sub-micron Al_2O_3 powders activated in coplanar dielectric barrier discharge (DBD) showed improved aqueous suspension stability by a factor of 1.5 [5]. Multi-walled carbon nanotubes activated in an oxidizing atmosphere showed a zeta potential shift comparable to that achieved by standard chemical functionalization, i.e. 2 hours functionalization in 65% HNO_3 solution at 80°C vs. 20 sec with plasma activation [6]. Our study of electrophoretic deposition (EPD) of sub-micron Al_2O_3 powders dispersed in isopropanol revealed complete reversal of surface charge on plasma activated particles [7]. In addition, obtained internal microstructure of the deposit and its surface morphology improved dramatically.

In the presented contribution we shall report on our first results indicating that the use of plasma activated ceramic powders of Al_2O_3 and WC can have a significant effect on final structure of deposited Ni and Cu layers, and can affect positively the MMC resulting hardness.

EXPERIMENTAL

Plasma activation was performed by Diffuse Surface Dielectric Barrier Discharge (DCSBD) plasma generator [7]. Activation was done at atmospheric pressure air with following set of operational parameters: input power 500 W, discharge excitation frequency 30 kHz, treatment time for single powder batch 30 s, approx. weight of single batch of raw material 0.25 g. Al_2O_3 powders (TM-DAR, Taimei Chemicals Japan, specific surface area 13.7 m^2/g, mean particle size 110 nm) and WC (Nanografi Nanotechnology Co. Ltd., Turkey, 99.99%, 50 nm) were used for the treatment. Electrodepositions were done on steel (34CrMo4) coupons of 60×20×5 mm.

All steel coupons samples were first electrolytically degreased in ENPREP 1012 following the manufacturer instructions. Then pure Ni sub-layer from $NiCl_2$ electrolyte (t=15 min; j=5 A/dm^2) was electrodeposited on all steel coupons. MMC coatings with Cu and Ni metal matrix were investigated on these pre-treated substrates. Ni plating was made from the Watts bath (t=30 min; j=5 A/dm^2; T≈59-64°C); Cu plating from $CuSO_4$ electrolyte (t=30 min; j=3 A/dm^2; ambient temperature). Exact composition of both plating solutions was proprietary. Tested Al_2O_3 or WC powders of 10 g/l were added into the given plating solution 15 min before the actual deposition and dispersed by ultrasonic cleaner. The MMC plating conditions were identical to those of reference pure metal plating specified above. After the deposition, samples were rinsed by deionized water and left to dry at ambient air conditions. Eight sets of distinct deposit compositions were prepared by mutual combination of [Ni; Cu plating matrix] × [Al_2O_3; WC powders; no powders] × [untreated; plasma treated powders]. Scanning electron microscope TESCAN Mira III equipped with EDX was used to observe microstructure and elemental chemical composition of prepared samples. The thickness of deposited layer was not determined. Hardness measurement were done by Hysitron TI950 (Bruker) dual head nanoindentor equipped with Berkovich diamond tip. The tip was calibrated immediately before the hardness measurement using certificated fused silica substrate. The High-Load (maximum load of 2.5 N) measuring head was used. The quasi-static loading function with 20 partial-unloading segments mode was applied in the load range from 5 to 500 mN. The measurement was done by 16 indents and the final value of hardness was determined by statistical data processing.

RESULTS

No apparent improvement in dispersion stability had been observed for any tested combinations of plasma activated powders and/or metal plating bath. Also, there was no change in particle deposition polarity present like in [7]. A control experiment with EPD deposition of plasma activated Al_2O_3 powders in pure water (i.e. not isopropanol like in [7]) revealed, that the presence of aqueous medium removed the reverse polarity deposition effect too. Nevertheless, SEM images of all deposited samples demonstrated some noticeable differences in obtained morphology. Fig.1 shows some representative images illustrating the difference for the Cu + WC system.

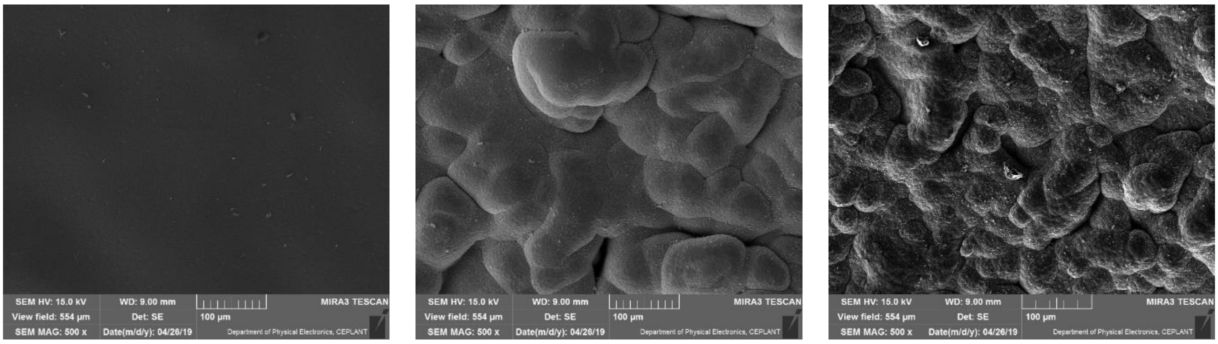

(a) (b) (c)

Figure 1: SEM images for Cu+WC system: (a) Cu layer only; (b) Cu + WC; (c) Cu + plasma activated WC.

Actual impact of these structural changes on hardness and reduced elastic modulus is summarized in Table 1.

Table 1. Hardness and reduced elastic modulus for metal layers doped with ceramics components

		H [GPa]	E_r [GPa]		H [GPa]	E_r [GPa]
	Ni	6 ± 1	90 ± 10	Cu	1.8 ± 0.3	80 ± 5
WC	Ni + WC (ref)	0.25 ± 0.05	15 ± 5	Cu + WC (ref)	1.5 ± 0.5	50 ± 5
	Ni + WC (plasma)	3 ± 1	40 ± 10	Cu + WC (plasma)	3.0 ± 0.7	125 ± 15
Al_2O_3	Ni + Al_2O_3 (ref)	11 ± 1	250 ± 10	Cu + Al_2O_3 (ref)	1.5 ± 1	80 ± 10
	Ni + Al_2O_3 (plasma)	3 ± 1	100 ± 10	Cu + Al_2O_3 (plasma)	2.6 ± 0.5	140 ± 10

For nickel MMC we found that only Al_2O_3 particles led to improved elastic modulus in comparison to pure Ni layer. MMC layers prepared from suspension with WC component exhibited a substantial decline in both hardness and elastic modulus. For both types of particles plasma activation had a noticeable impact, in both positive and/or negative way. Plasma activated WC particles provided layers possessing higher hardness, although not as high as the reference Ni layer. Plasma activated Al_2O_3 showed negative impact on final hardness.

For copper MMC, plasma activation had a pronounced positive effect for both WC and Al_2O_3 powders. Direct addition of non-modified reinforcing particles led to the softer deposited layer in comparison with the pure Cu layer. With plasma activation the obtained hardness was approx. 50% higher than the Cu reference. The reason behind this positive effect is unclear yet, and requires further more detailed study.

CONCLUSIONS

Our pilot set of experiments with electrochemical preparation of plasma assisted metal matrix composite (PAMMC) layers provides a strongly supportive evidence, that further investigation of PAMMC may lead to results of technological significance. The study of actual mechanisms behind the observed improvement would require better control on actual composition of all chemical components. One of the surprising results is that Al_2O_3 particle addition performed better than more common used WC. However, it should be noted that actual deposition process has been realized without any optimization of working conditions, since the work was primary focused on evaluating the impact role of plasma activation only.

ACKNOWLEDGMENT

This work was supported by the project TG02010067 (internal code MUNI/31/63726/2018) of TAČR GAMA program, project CZ.1.05/2.1.00/03.0086 funded by the European Regional Development Fund, and project LO1411 (NPU I) funded by the Ministry of Education Youth and Sports of the Czech Republic.

REFERENCES

[1] Walsh FC, Ponce De Leon C: „A review of the electrodeposition of metal matrix composite coatings by inclusion of particles in a metal layer: An established and diversifying technology“ (2014) *Transactions of the Institute of Metal Finishing*, **92** (2), pp. 83-98.

[2] Simunkova S, Pessenda-Garcia P, Wosik J, Angerer P, Kronberger H, Nauer GE: „The fundamentals of nano- and submicro-scaled ceramic particles incorporation into electrodeposited nickel layers: Zeta potential measurements“ (2009) *Surface & Coatings Technology* **203**, pp. 1806–1814.

[3] Angerer P, Simunkova H, Schafler E, Kerber MB, Wosik J, Nauer GE: „Structure and texture of electrochemically prepared nickel layers with co-deposited zirconia nanoparticles“, (2009) *Surface & Coatings Technology* **203**, pp. 1438–1443.

[4] Lammel P, Whitehead AH, Simunkova H, Rohr O, Gollas B: „Droplet erosion performance of composite materials electroplated with a hard metal layer“ (2011) *Wear* **271**, pp. 1341– 1348.

[5] Szalay Z, Bodišová K, Pálková H, Švančárek P, Ďurina P, Ráheľ J, Zahoranová A, Galusek, D: „Atmospheric pressure air plasma treated alumina powder for ceramic sintering“ (2014) *Ceramics International*, **40** (8 PART B), pp. 12737-12743.

[6] Szalay Z: „Surface modification of powder materials by dielectric barrier discharges“ Dissertation thesis, Comenius University in Bratislava, 2013 (supervisor J. Ráheľ)

[7] Drdlik D, Moravek T, Rahel J, Cihlar J, Drdlikova K, Maca K: „Electrophoretic deposition of plasma activated sub-micron alumina powder“ (2018) *Ceramics International* **44** (8), p. 9787 – 9793.

AUTHOR INDEX

Book of extended abstracts

Workshop „PROCESSING AND PROPERTIES OF ADVANCED CERAMICS AND GLASSES”

November 20-22, 2019, Ráztočno, Slovak Republic

Published by: Institute of Inorganic Chemistry, SAS
Dúbravská cesta 9
845 36 Bratislava
Slovak Republic

Novembre 2019

Book reviewers: doc. Ing. Marián Janek, PhD.
doc. Ing. Robert Klement, PhD.
Ing. Alexandra Kovalčíkova, PhD.
Ing. Monika Michálková, PhD.
doc. RNDr. Jozef Ráheľ, PhD.
Ing. Peter Tatarko, PhD.

Edited by: Ing. Jana Valúchová, PhD.

ISBN 978-80-971648-8-1

ISBN 978-80-971648-8-1